

**Effects of Surface Structure and Wettability Modification on Condensate Mobility  
and Heat Transfer on Flat and Tubular Surfaces**

by

Christopher Martin Duron

A dissertation submitted to the Graduate Faculty of  
Auburn University  
in partial fulfillment of the  
requirements for the Degree of  
Doctor of Philosophy

Auburn, Alabama  
August 5, 2017

Keywords: Condensation enhancement, superhydrophobic, condensate mobility

Copyright 2017 by Christopher Martin Duron

Approved by

Sushil H. Bhavnani, Chair, Professor of Mechanical Engineering  
Roy W. Knight, Assistant Professor of Mechanical Engineering  
Daniel Mackowski, Professor of Mechanical Engineering  
Narendra Govil, Professor of Mathematics and Statistics

## Abstract

Dropwise condensation has long been known to offer heat transfer coefficients potentially an order of magnitude higher than filmwise condensation as mobile droplets can more readily be removed from condenser surfaces (traditionally via gravitational forces) taking with them the thermal resistance imposed by liquid layers on condensers. However most condensers in industrial applications operate under the filmwise condensation mode since traditionally there have not been dropwise condensation promoting materials or surface treatments with the combination of durability and performance necessary for adoption by industry.

Recently, renewed and increased interest in the area of condensation enhancement has led to the development of several types of superhydrophobic surfaces intended to dramatically increase condensate droplet mobility. Many of the surface architectures proposed by literature to produce superhydrophobic surfaces require complex micro and nano fabrication techniques that are not feasible for scale-up to mass production and produce rather delicate surfaces.

This study describes two methods intended to increase droplet mobility and thereby condensation heat transfer coefficients while focusing on durability and feasible fabrication.

In the first method described, custom alumina nano-particle composite hydrophobic coatings were developed from a surface treatment originally designed at

Auburn University for silicon surfaces called Repellix, which uses a vapor deposition process that is readily scalable. These custom coatings were adapted from the original Repellix process to produce surface treatments with increased durability suitable for use on metallic substrates. These custom developed surface treatments were applied to solid hemi-cylindrical test surfaces fabricated from four of the most common power generation plant condenser tube materials, namely, Admiralty brass, cupronickel, titanium and Sea-Cure stainless steel. Flat and hemi-cylindrical 304 stainless steel control surfaces were also fabricated and coated. Results show that the performance enhancement, measured in rate of heat transfer spikes corresponding to condensate roll-off events, was best for the titanium surface which produced 64% more events than the next most active material when coated using the most durable surface treatment tested in this work.

The second method for increasing droplet mobility and thereby condensation heat transfer coefficients presented in this work employs asymmetric triangular saw-toothed profile ratchet surface features in several size, profile and wettability configurations. These surface features while formed in silicon via gray scale lithography for use in this study could easily be formed in metallic surfaces using common modern fabrication techniques. Effects of ratchet size, profile, orientation and surface wettability were examined. Hydrophobic asymmetric ratcheted surfaces studied were observed to produce directional water droplet growth due to surface tension forces during deposited droplet experiments as well as directional water condensate motion during coalescence events under certain conditions. Condensation heat transfer coefficients up to 57% higher on larger ratchets compared to flat surfaces also suggests that some fluid motion is promoted by larger hydrophilic ratchets condensing a highly wetting fluid (FC-72).

Experimental data was compared to a model that predicts dropwise heat transfer coefficients by examining the heat flow through individual droplets to propose a modification to the model that increases its accuracy for predicting heat transfer coefficients on textured hydrophobic surfaces.

Detail on development, fabrication, thermal performance and observations on effects on droplet and condensate motion for the two methods introduced above are presented in this work.

## Acknowledgments

First, I would like to thank my research advisor and advisory committee chair, Dr. Sushil Bhavnani for his patience, support and motivation throughout my time at Auburn University. I would not be where I am today without his guidance and confidence in my abilities. I would also like to thank the other members of my advisory committee Dr. Roy Knight, Dr. Daniel Mackowski, and Dr. Narendra Govil for the insight they provided and for the time they gave to serve on my committee. I also sincerely thank Dr. Allan David for his service as external reader.

I am very grateful for the opportunity I had to work in this field, which was made possible by financial support provided by the NSF, NASA and Southern Company.

I sincerely appreciate the effort, insight and help given by project collaborators Dr. Vinod Narayanan, Dr. William Ashurst and Dr. Allan David and their students Eric Truong, Shashank Natesh and Dr. Jie Zhong. I thank Dr. Charles Ellis, Mr. Drew Sellers, Mr. William Baugh and Dr. Tamara Isaacs-Smith for the much needed knowledge and help they provided during the fabrication of many of the surfaces tested in this study. And to my lab mates: I was very lucky to have such great people to work with.

Finally, I would like to express my utmost gratitude to my family: my parents for their lifelong support, my sister for her motivating competition, and my wife Rachel, daughter Penelope and son on the way for their daily motivation, inspiration and love.

## Table of Contents

Abstract.....	ii
Acknowledgements .....	v
List of Figures .....	ix
List of Tables.....	xvii
List of Abbreviations .....	xix
1 Introduction .....	1
1.1 Enhanced Condensation: Literature Review .....	5
1.1.1 The Quest for Superhydrophobicity .....	5
1.1.1.1 Micro/nano-structured Superhydrophobic Surfaces .....	9
1.1.2 Surfaces Designed to Promote Droplet and Condensate Fluid Motion .....	18
1.2 Summary and Objectives .....	33
2 Fabrication of Test Surfaces and Experimental Facility.....	34
2.1 Test Surface Fabrication .....	34
2.1.1 Flat Silicon Surfaces .....	35
2.1.2 Hemi-cylindrical Condenser Tube Test Surfaces .....	42
2.1.2.1 Hemi-cylindrical Surface Substrate Fabrication .....	42
2.1.2.2 Superhydrophobic Coatings for Hemi-Cylindrical Test Surfaces .....	43
2.1.3 Asymmetric Saw-Toothed Ratcheted Silicon Surfaces .....	50
2.2 Experimental Facility .....	58

2.2.1 Measurement Head .....	65
2.2.2 Heat Flux, Surface Temperature, and Heat Transfer Coefficient Measurements .....	67
2.2.3 Adiabatic Growth/Deposited Drop Experiment Equipment .....	70
2.3 Experimental Procedure .....	71
2.4 Summary .....	73
3 Hemi-Cylindrical Surface Experiments .....	75
3.1 Durability Testing .....	76
3.2 Results and Discussion .....	81
3.2.1 Condensate Morphology .....	81
3.2.2 Heat Transfer Performance .....	83
4 Asymmetric Ratchet Surface Experiments .....	89
4.1 Adiabatic Deposited Drop Mobility Experiments .....	91
4.1.1 Directional Droplet Growth Internal Pressure and Force Calculation .....	95
4.2 Condensation Experiments .....	103
4.2.1 Uncontrolled Pressure Rise Experiments .....	103
4.2.1.1 FC-72 Condensation on Hydrophilic Surfaces .....	104
4.2.1.2 Deionized Water Condensation on Hydrophobic Surfaces .....	107
4.2.2 Controlled Pressure Rise Experiments .....	111
4.3 Dropwise Condensation Heat Transfer Coefficient Model .....	120
5 Conclusions and Recommendations .....	134
5.1 Custom Nano-composite Hydrophobic Coatings on Hemi-cylindrical Condenser Tube Test Surfaces .....	135

5.2 Asymmetric Saw-toothed Ratchet Silicon Surfaces .....	136
5.3 Recommendations for Future Work .....	137
References .....	140
Appendix A: Thermophysical Properties of Water and FC-72 .....	146
Appendix B: Flat Silicon Surface Testing .....	149
Appendix C: Grayscale Photoresist Pattern Layout and Requirements .....	156
Appendix D: Grayscale Photoresist Profile Measurements.....	159
Appendix E: Design Draft Files for Condensation Chamber and Measurement Head..	167
Appendix F: Adhesives and other Consumables.....	184
Appendix G: Heat Transfer Coefficient Plots for Hemi-cylindrical Test Surfaces .....	193
Appendix H: Uncertainty Calculation for Heat Transfer Coefficient Values.....	200



## List of Figures

Figure 1.1: As seen in [4] A. A film of condensation coats a bare copper condenser tube. B. Condensation forms as drops of various sizes on a silane coated copper condenser tube. ....	2
Figure 1.2: From left to right: Droplet on a smooth surface, Droplet in the Wenzel state, Droplet in the Cassie-Baxter state [40]. Wenzel state droplet fills surface texture, Cassie-Baxter state droplet sits on top of surface texture leading to greater droplet mobility.....	9
Figure 1.3: (a-b) One-tier with only micropillars, (c-d) one tier surface with only nanopillars, (e-f) two-tier surface with micro and nano pillars. Images were taken 9 (a, c, e) and 10 (b, d, f) minutes after condensation began [8]......	10
Figure 1.4: Condensation on hexadecanethiol coated two-tier surface, images were captured over the same area. Time of capture is indicated in top left corner [8]......	12
Figure 1.5: Dropwise condensation on (a) a smooth hydrophobic surface and (b) a two-tier superhydrophobic surface [7]......	13
Figure 1.6: Side view of two droplets coalescing and then jumping off of the surface. Notice that the horizontal momentum of the droplets is conserved [7]. ....	14
Figure 1.7: (a) Average drop diameter. (b) Surface coverage, which reached a plateau for both surfaces but fluctuated because of the small field of view [7]. ....	14
Figure 1.8: (a) Filmwise condensation on a smooth hydrophilic copper tube, (b) dropwise condensation on a silane coated smooth copper tube, (c) jumping-drop superhydrophobic condensation on a nanostructured copper oxide tube with inset of magnified view of droplet jumping, (d) flooded condensation on a nanostructured CuO tube [4]. ....	16
Figure 1.9: Schematic of wettability gradient used by Tokunaga et al. [34]. ....	19
Figure 1.10: As seen in [34] moving water droplet on wettability gradient. ....	19
Figure 1.11: Image from [39] of deposited water droplet moving on single wedge shaped hydrophilic track surrounded by superhydrophobic field. ....	20

Figure 1.12: As shown in [43], a deposited water droplet travels up a 15° incline due to surface wettability gradient. ....	20
Figure 1.13: Top: Number of droplets vs. time for each type of surface. Below: Images of each surface and histogram of droplet size during each stage of condensation. Red=Uniform surface. Blue=Gradient surface [44]. ....	22
Figure 1.14: a. Droplets on hydrophobic regions migrate to less hydrophobic regions (darker stripes) drain downward [47]. b. Droplets are removed from condenser tube [48].....	24
Figure 1.15: Diagram of identical droplet model generation from [49]. ....	25
Figure 1.16: (a) Vertical jumping velocity vs. Time. (b) Pressure vs. Time. (pressure of the top and bottom of the droplet) (c) Temperature vs. Time (temperature of surface and droplet fluid) (d) Images of droplet at each stage of jumping (stage transitions are in the second column) [49]. ....	26
Figure 1.17: Time stepped images of coalescing droplets jumping from a Teflon coated copper wire. (a) end view, approximate fiber location is marked with white circle (b) side view [33]. ....	28
Figure 1.18: Schematic of droplet removal with relatively large horizontal velocity. (a) two droplets grow within the microstructure. (b) the droplets have grown large enough to coalesce around a corner. (c) coalesced droplet expands against the pillar and bottom substrate and jumps in a direction almost orthogonal to the pillar. The small vertical velocity is due to the bottom substrate [37]. ....	29
Figure 1.19: Nearly horizontally jumping droplets from the top row sweep the surface removing a total of 15 droplets [37]. ....	30
Figure 1.20: From [14], a. Image of Morpho Deidamia butterfly with radially outward (RO) direction noted. b1. ESEM image of overlapped scales. b2. Illustration of two-tiered asymmetric ratchet structure. c1. Higher magnification ESEM image of nano-ridges. c2. Illustration of nano-ridge structure. d1. Cross section ESEM image of nano-ridges. d2. Illustration nano-ridge cross section. e. Images of directional motion of coalescing condensate drops on butterfly wings. ....	32
Figure 2.1: Layout of 1-D and 2-D flat silicon test surface wettability patterning used for preliminary testing. (white =non-wetting, black=wetting) .....	35
Figure 2.2: Layout of surface wettability patterning for second set of flat silicon test surfaces. (white = hydrophobic, gray= hydrophilic) .....	37

Figure 2.3: Full set of 25mm radial patterned biphilic test sections. The blue/green portions are hydrophilic silicon dioxide the dull gray portions are hydrophobic polymer. ....	40
Figure 2.4: Images used for contact angle measurement on flat silicon test surfaces with measurement marks shown. Above: droplet on hydrophilic areas. Below: Droplet on hydrophobic areas. ....	41
Figure 2.5: Schematics of coating layers for hemi-cylindrical test surfaces with modifications from original Repellix formula circled in red. ....	48
Figure 2.6: Complete set of all hemi-cylindrical condenser tube test surfaces and solid stainless steel control surfaces. ....	49
Figure 2.7: Illustration of some geometric parameters presented in Table 2.4. ....	52
Figure 2.8: Illustration of 25mm square asymmetric ratchet test surface. 500 $\mu$ m pitch shown. ....	53
Figure 2.9: Schematic of biphilic asymmetric ratchet test surface coating application. ..	54
Figure 2.10: Illustration of fabrication steps required to form asymmetric ratchets in silicon. ....	55
Figure 2.11: Microscopic images of wafer at several stages of processing. Top to bottom: Fresh grayscale photoresist before de-scum, During de-scum, De-scum completed, DRIE completed. ....	56
Figure 2.12: Side view of a fully processed 500 $\mu$ m pitch ratchet test surface. Camera is focused on far edge of the surface so the profile can be seen. Some upset material from the dicing operation can also be seen between the ratchets. ...	57
Figure 2.13: Image used for contact angle measurement on NeverWet coated silicon test surfaces with measurement marks shown. ....	57
Figure 2.14: Diagram of experimental facility components. ....	63
Figure 2.15: Top: Side view of experimental equipment in aluminum structure. Bottom: Front view of experimental equipment in aluminum structure. ....	64
Figure 2.16: CAD images of measurement head. Left: Current longer, aluminum measurement head design. Notice the difference in the distance between thermocouple holes. Right: Previous copper measurement head design. ....	66
Figure 2.17: Images of current aluminum core measurement head. Left: Current longer, aluminum measurement head with new type of Delrin filled PTFE insulation. Right: Measurement head core before insertion. Three o-rings are used to provide a good vacuum seal. ....	67

Figure 2.18: Half-cylinder average thickness determination for placement of surface mount thermistor.....	69
Figure 2.19: Deposited drop experiment fixture. ....	71
Figure 3.1: Jig used for holding flat 304 stainless steel surfaces coated with modified Repellix and Repellix 2.0 at 45° under the water stream during coating durability testing. ....	78
Figure 3.2: Contact angle images and values for flat 304 stainless steel surfaces coated with modified Repellix and Repellix 2.0 during coating durability testing. ...	79
Figure 3.3: Plot of contact angle degradation for flat 304 stainless steel surfaces coated with modified Repellix and Repellix 2.0 during coating durability testing. ...	80
Figure 3.4: Comparison images of bare surfaces and both coatings on each material. All images were taken after 10 minutes of condensation activity. ....	82
Figure 3.5: Comparison of droplets present on flat 304 stainless steel surfaces after various amounts of condensation activity. ....	83
Figure 3.6: Heat transfer coefficient as a function of time for SEA-CURE test surfaces for all three surface conditions. Notice that the highest heat transfer coefficients for SEA-CURE were achieved with the bare surfaces and the lowest were achieved with the Repellix 2.0 surfaces. This trend was also true for the Admiralty brass and cupronickel surfaces. Data before 400s is not shown due to interference and therefore unreliable values caused by initial transients. ....	84
Figure 3.7: Heat transfer coefficient as function of time for titanium test surfaces for all three surface conditions. Notice that the highest heat transfer coefficients for titanium were achieved with the Repellix 2.0 coated surfaces and the lowest were achieved with the bare surfaces. This is opposite to the trend observed on the other three tube material test surfaces. Data before 400s is not shown due to interference and therefore unreliable values caused by initial transients. ....	85
Figure 3.8: Average number of roll-off events for each Modified Repellix and Repellix 2.0 coated tube material. ....	87
Figure 3.9: Plot highlighting roll-off events and corresponding heat transfer coefficient spikes. Arrows indicate heat transfer coefficient spike after a roll-off event. Two insets show the surface before and after a roll off event corresponding to a spike in heat transfer coefficient. ....	88
Figure 4.1: Images of deposited water drop growing on 500µm pitch hydrophobic ratcheted surface. ....	93

Figure 4.2: Images taken at each stage of droplet growth on ratcheted surface. Notice that the image for stage 3 was taken just after the ascending edge broke over the crest. The image for stage 4 clearly shows the contact line is on the long face of the ratchet and that the body of the droplet will contact the adjacent ratchet face before the contact line reaches the trough. ....	94
Figure 4.3: Directional growth driving force calculated from equation 4.1 for one growth cycle on 500 $\mu$ m pitch hydrophobic ratcheted surface. ....	96
Figure 4.4: a. Pinned and ascending drop radius data at each growth stage. b. Internal pressure difference calculated from equation 4.3 at each growth stage on 500 $\mu$ m pitch hydrophobic ratcheted surface. ....	97
Figure 4.5: Images used for measurements needed for force and internal pressure calculation for one growth cycle on 500 $\mu$ m pitch hydrophobic ratcheted surface. ....	98
Figure 4.6: Force values calculated from equation 4.1 for deposited droplet on 500 $\mu$ m pitch hydrophobic ratcheted surface growing in preferred direction over several ratchets. Images at stage 1 for each ratchet are given. ....	100
Figure 4.7: Pinned and ascending radii data for deposited droplet on 500 $\mu$ m pitch hydrophobic ratcheted surface growing in preferred direction over several ratchets. Images at stage 1 for each ratchet are given. ....	101
Figure 4.8: Internal pressure difference values calculated from equation 4.3 for deposited droplet on 500 $\mu$ m pitch hydrophobic ratcheted surface growing in preferred direction over several ratchets. Images at stage 1 for each ratchet are given . ....	102
Figure 4.9: Images of FC-72 condensation on a 500 $\mu$ m pitch ratcheted hydrophilic test surface. The diagram above the images shows the orientation of the ratchets. a. Surface just before condensation begins. b. Surface after flooding with condensate. ....	105
Figure 4.10: Condensation heat transfer coefficient as a function of $\Delta T$ for FC-72 on hydrophilic surfaces. ....	106
Figure 4.11: Images of condensation on a 500 $\mu$ m pitch ratcheted hydrophobic test surface. The diagram above the images shows the orientation of the ratchets. a. Surface just before condensation begins. b. several large droplets populate the flat, un-ratcheted, sections of the test section and elongated droplets occupy most of the area in the valleys between ratchet peaks. c. A large droplet has formed on the ratcheted portion of the surface rather than on the flats (second ratchet from the right). d. The droplet coalesces with other smaller droplets becoming almost large enough to spill over the ratchet crest. e. The fluid has spilled over the ratchet crest and coalesced with the droplets filling the neighboring ratchet (third ratchet from the right). Images were	

taken at a rate of 30 frames per second. f. Detail view with dimensions of CAD model of ratchets. ....	108
Figure 4.12: Condensation heat transfer coefficient as a function of $\Delta T$ for deionized water on hydrophobic surfaces. Inset plot shows representative pressure rise for these experiments. ....	110
Figure 4.13: Plot of heat transfer coefficients as a function of $\Delta T$ on horizontally oriented test surfaces for all surface configurations. ....	112
Figure 4.14: Illustration of tilt direction and ratchet orientation for roll-off angle tests. a. (left tilt) Long, shallow slope of ratchet is up. b. (right tilt) Short, steep slope of ratchet is up. ....	113
Figure 4.15: Image of 0.01cc and 0.05cc droplet on 500 $\mu\text{m}$ ratcheted hydrophobic test surface .....	114
Figure 4.16: Heat transfer coefficient as a function of $\Delta T$ for all tilt configurations tested on a. 100 $\mu\text{m}$ hydrophobic ratcheted surfaces and b. 250 $\mu\text{m}$ hydrophobic ratcheted surfaces. ....	116
Figure 4.17: Heat transfer coefficient as a function of $\Delta T$ for all tilt configurations tested on a. 250 $\mu\text{m}$ 9° hydrophobic ratcheted surfaces and b. 250 $\mu\text{m}$ 18° hydrophobic ratcheted surfaces. ....	117
Figure 4.18: Images of condensate removal from 250 $\mu\text{m}$ 18° hydrophobic ratcheted surface notice that the area where the condensate draining occurred remained wet after drainage. Contact line (marked in yellow) doesn't move even after large amount of condensate (yellow ovals) leaves the test surface. ....	118
Figure 4.19: Images of condensate drops on 250 $\mu\text{m}$ hydrophobic ratcheted surface tilted 5 degrees to the right (above) and flat hydrophobic control surface tilted 5 degrees to the left. Irregular droplet perimeters indicate Wenzel state as discussed in [8]. ....	120
Figure 4.20: Images of maximum droplet radius measurement on flat test surface for two data points; 2 minutes elapsed time (left) and 6 minutes elapsed time (right) ... .....	124
Figure 4.21: Heat transfer coefficient as function of time (collected data and model) for flat level hydrophobic silicon surface. ....	125
Figure 4.22: Heat transfer coefficient as function of time (collected data and model) for level 100 $\mu\text{m}$ ratchet pitch hydrophobic silicon surface. ....	127

Figure 4.23: Heat transfer coefficient as function of time (collected data and model) for level 250 $\mu\text{m}$ ratchet pitch hydrophobic silicon surface. ....	127
Figure 4.24: Heat transfer coefficient as function of time (collected data and model) for level 500 $\mu\text{m}$ ratchet pitch hydrophobic silicon surface. ....	128
Figure 4.25: $r_{\text{min}}$ as a function of $r_e$ with trendline for data points on all surfaces considered in this analysis. ....	130
Figure 4.26: Heat transfer coefficient as function of time (collected data, model, and modified model) for flat level hydrophobic silicon surface. ....	131
Figure 4.27: Heat transfer coefficient as function of time (collected data, model, and modified model) for level 100 $\mu\text{m}$ ratchet pitch hydrophobic silicon surface. ...	131
Figure 4.28: Heat transfer coefficient as function of time (collected data, model, and modified model) for level 250 $\mu\text{m}$ ratchet pitch hydrophobic silicon surface. ...	132
Figure 4.29: Heat transfer coefficient as function of time (collected data, model, and modified model) for level 500 $\mu\text{m}$ ratchet pitch hydrophobic silicon surface. ...	132
Figure B.1: Droplets on 1-D patterned test surfaces exhibiting both elongated and irregular shapes from pinning and eventual coalescence. ....	151
Figure B.2: Droplet growth on 2-D patterned surface. From left to right: 1. Schematic of surface patterning black=hydrophilic, white=hydrophobic. 2. Circular droplets with diameters equal to hydrophobic band width. 3. Droplets on hydrophobic bands beginning to elongate. 4. Elongated bands begin to coalesce with droplets on the hydrophobic bands. ....	151
Figure B.3: Plot of elongation ratio as a function of time on two identical 2-D patterned surfaces. ....	152
Figure B.4: Images of condensation on 25mm radial patterned test section with 6mm inner non-wetting island. From left to right. 1. Higher nucleation rate on hydrophilic portions begins to be obvious. 2. Borders of large droplets are affected by patterning. 3. Droplets grow to periphery and leave the surface. 4. Another droplet reaches the periphery and leaves while condensate nucleates and repopulates bare surface where previous droplets left. ....	153
Figure B.5: Droplet coalescence on wedge patterned flat silicon test surface. Top Left: Three droplets sitting on a wetting wedge. Top Right: Droplets coalesce and resulting droplet features larger radius on left side. Bottom Left: Droplet finally achieves circular shape when internal pressures equalize. Bottom Right: Droplet coalesces with others across pattern boundaries. ....	154

Figure D.1: Grayscale exposed and developed photoresist height profile on 100 $\mu$ m ratchet pitch wafer .....	160
Figure D.2: Grayscale exposed and developed photoresist height profile on 250 $\mu$ m ratchet pitch wafer .....	161
Figure D.3: Grayscale exposed and developed photoresist height profile on 500 $\mu$ m ratchet pitch wafer .....	162
Figure D.4: Layout drawing 5mm square unit cells of grayscale processed photoresist on 100mm wafer with photoresist height measurement locations indicated by numbers 1-10. ....	163
Figure G1: Comparison of heat transfer coefficient as a function of time on flat 304 Stainless Steel test surfaces for bare, Modified Repellix coated, and Repellix 2.0 coated .....	194
Figure G2: Comparison of Heat transfer coefficient as a function of time on Round 304 Stainless Steel test surfaces for bare, Modified Repellix coated, and Repellix 2.0 coated .....	195
Figure G3: Comparison of Heat transfer coefficient as a function of time on Admiralty brass test surfaces for bare, Modified Repellix coated, and Repellix 2.0 coated .....	196
Figure G4: Comparison of Heat transfer coefficient as a function of time on Cupronickel test surfaces for bare, Modified Repellix coated, and Repellix 2.0 coated..	197
Figure G5: Comparison of Heat transfer coefficient as a function of time on Titanium test surfaces for bare, Modified Repellix coated, and Repellix 2.0 coated .....	198
Figure G6: Comparison of Heat transfer coefficient as a function of time on SEA-CURE test surfaces for bare, Modified Repellix coated, and Repellix 2.0 coated..	199
Figure H1: Condensation heat transfer coefficient as a function of $\Delta T$ for deionized water on hydrophobic surfaces. Data point used for sample calculation is circled in red. ....	205



## List of Tables

Table 1.1: Contact angle measurements on some non-textured hydrophobic surfaces .....	7
Table 1.2: Contact angle measurements on some textured superhydrophobic surfaces ....	8
Table 2.1: Repellix process parameters .....	47
Table 2.2: Modified repellix process parameters .....	47
Table 2.3: Repellix 2.0 process parameters .....	47
Table 2.4: DRIE process parameters and resulting geometric parameters .....	52
Table 3.1: Contact angle values corresponding to plot points in Figure 3.3 .....	80
Table 4.1: Average roll-off angle .....	114
Table 4.2: $r_e$ , $r_{min}$ , and $r_{max}$ values for flat level hydrophobic silicon surface .....	126
Table 4.3: $r_e$ , $r_{min}$ , and $r_{max}$ values for level 100 $\mu$ m ratcheted hydrophobic silicon surface.....	128
Table 4.4: $r_e$ , $r_{min}$ , and $r_{max}$ values for level 250 $\mu$ m ratcheted hydrophobic silicon surface.....	129
Table 4.5: $r_e$ , $r_{min}$ , and $r_{max}$ values for 500 $\mu$ m ratcheted hydrophobic silicon surface .....	129
Table A.1: Thermophysical properties of saturated water.....	147
Table A.2: Thermophysical properties of saturated FC-72 .....	148
Table D.1: Grayscale processed photoresist thickness measurements on 100 $\mu$ m ratchet pitch wafers.....	164
Table D.2: Grayscale processed photoresist thickness measurements on 250 $\mu$ m ratchet pitch wafers.....	165
Table D.3: Grayscale processed photoresist thickness measurements on 500 $\mu$ m ratchet pitch wafers.....	166

Table G.1: List of figures in Appendix G .....	193
Table H.1: Scale and offset uncertainty values for thermocouples .....	204
Table H.2: Temperature and heat transfer coefficient values for sample calculation .....	206

## List of Abbreviations

### Acronyms

1-D	One Dimension
2-D	Two Dimensions
ALD	Atomic Layer Deposition
CVD	Chemical Vapor Deposition
DRIE	Deep Reactive Ion Etching
ITO	Indium Tin Oxide
PTFE	Polytetrafluoroethylene (Teflon)
RO	Radially Outward
SAM	Self-Assembled Monolayer
SEM	Scanning Electron Microscope
VPD	Vapor Phase Deposition

### Symbols

$c_p$	specific heat, $J/kgK$
$d$	diameter, $m$
$D$	ratchet depth, $m$
$f$	fractional drop size distribution function
$F$	force, $N$
$G$	related drop size distribution function

$h$	heat transfer coefficient, $W/m^2K$
$h_{lv}$	latent heat of vaporization, $J/kg$
$k$	thermal conductivity, $W/mK$
$P$	pressure, $Pa$
$Pr$	Prandtl number
$q$	heat flux, $W/m^2$
$r$	radius, $m$
$R$	specific gas constant, $J/kgK$
$t$	time, $s$
$T$	Temperature, $^{\circ}C$
$u$	uncertainty
$v$	specific volume, $m^3/kg$
$w$	width, $m$

### **Greek Symbols**

$\gamma$	interfacial surface tension, $N/m$
$\Delta P$	pressure difference, $Pa$
$\Delta T$	temperature difference, $^{\circ}C$
$\theta$	contact angle, $^{\circ}$
$\mu$	viscosity, $Ns/m^2$
$\rho$	density, $kg/m^3$
$\sigma$	fluid surface tension, $N/m$
$\hat{\sigma}$	accommodation coefficient
$\omega$	characteristic ratchet angle, $^{\circ}$

## Subscripts

<i>a</i>	ascending
<i>e</i>	equilibrium
<i>l</i>	liquid
<i>max</i>	maximum
<i>min</i>	minimum
<i>p</i>	pinned
<i>r</i>	receding
<i>s</i>	solid
<i>sat</i>	saturation
<i>v</i>	vapor
<i>w</i>	condenser surface

## Chapter 1

### Introduction

Condensation of vapor is an important phase change process that affects many natural phenomena and industrial applications. Power generation, desalination of sea water, water harvesting, and air conditioning are all processes that are affected greatly by the efficiency of heat and mass transfer associated with the condensation of vapor [1]. Most of the world's electrical power is generated in plants that utilize a steam (Rankine) cycle. The wet cooling systems employed in steam cycle power plants account for 41% of all fresh water withdrawals making it the single largest use of fresh water in the United States [2]. Furthermore, the efficiency of these steam cycle systems is directly related to condensation heat transfer performance [3]. Heating Ventilation and Air Conditioning (HVAC) system efficiencies are also highly affected by the mass transfer associated with condensation and these systems account for 10-20% of the total energy usage in developed countries [3]. Needless to say, improvements to heat and mass transfer associated with the condensation of vapor have the potential to lead to considerable energy and natural resource savings [4].

Additionally, the high power electronics industry has a growing interest in condenser performance. Continuing trends of miniaturization and higher power continue place more and more demand on thermal management systems to dissipate higher heat fluxes. As the limits of natural convection and even single phase liquid heat removal are exceeded, more efficient techniques such as liquid to vapor phase change are required

[5]. Liquid to vapor phase change thermal management systems in turn require vapor management sub-systems that are efficient, effective and not overly costly, bulky or delicate in order to become widely used.

The continued interest by the power generation and HVAC industries combined with the recent interest by the electronics industry in condensation dynamics and condenser performance has led to an increased focus on these topics by researchers over the last decade or so. Much of the research effort has been focused on surface modifications to create hydrophobic (contact angle  $> 90^\circ$ ) and superhydrophobic (contact angle  $> 150^\circ$ ) surfaces [6] that promote dropwise condensation which has the potential to greatly increase condensation heat transfer rates.

Condensation can occur in two modes; filmwise and dropwise. Figure 1.1 shows an image of condensation in each of these modes on copper condenser tubes.

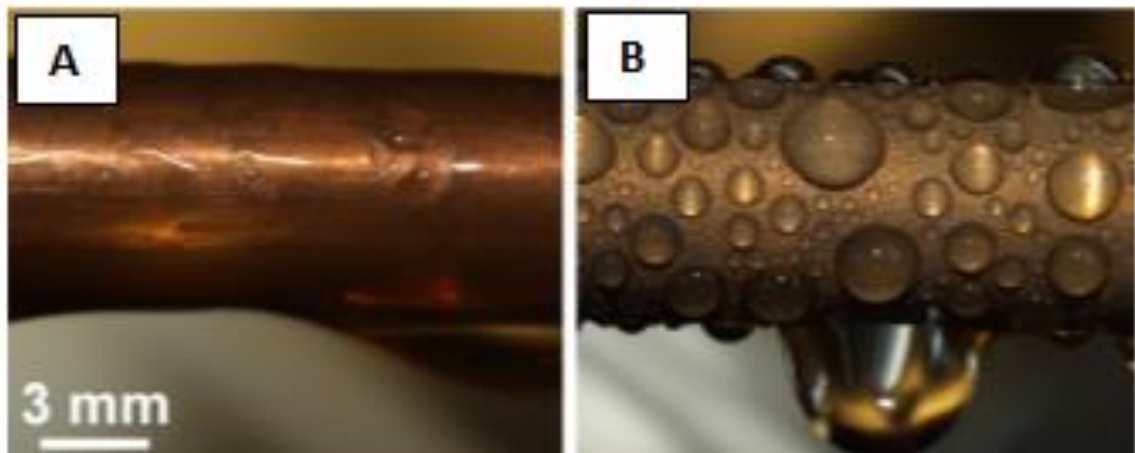


Figure 1.1: As seen in [4] A. A film of condensation coats a bare copper condenser tube. B. Condensation forms as drops of various sizes on a silane coated copper condenser tube.

Condensation heat transfer rates can be up to 10 times higher in dropwise condensation than filmwise condensation [7] because the liquid film in filmwise condensation functions as a thermal barrier that can cover the entire condensing surface [1]. In dropwise condensation droplet mobility greatly affects the rates of heat and mass transfer because as droplets move they expose portions of “fresh” condensing surface that is free of liquid that, just as in filmwise condensation, serves as a thermal barrier. Current condenser design procedures assume filmwise condensation instead of the preferable and more efficient dropwise mode of condensation because traditionally there has been no durable and reliable method of maintaining dropwise condensation for an extended length of time [6].

Given a certain condensation situation—surface material, working fluid and environmental conditions—the only two methods available to increase the condensate mobility and thereby heat transfer performance of a condensing surface are surface structure and wettability modification. The study described in this dissertation focuses on two combinations of these two methods. First, a custom vapor phase deposited nano-composite superhydrophobic surface treatment was developed and applied to hemicylindrical test surfaces fabricated from several commonly used condenser tube materials. This surface treatment deposits a rough nanostructure of alumina particles and hydrophobic silane coating to the smooth tubular surfaces that dramatically decreases the wettability of the surface to which it is applied. And second, silicon surfaces with asymmetric saw-toothed ratchet like microstructure were fabricated and treated with a commercially available hydrophobic coating made by Rust-Oleum called NeverWet. This coating also deposits a small scale rough surface texture.



These combinations of surface structure and wettability modifications were chosen for their potential durability and ability to promote condensate motion during dropwise condensation. The custom vapor phase deposited surface treatment applied to metallic tubular test surfaces was adapted from a similar coating that is currently used on silicon to prevent wetting of sensitive electronics. When applied to silicon this surface treatment has good durability and non-wetting characteristics. This, combined with the highly scalable vapor deposition process that would allow power plant condenser tubes to be treated in-situ provided great motivation to adapt the surface treatment for use on metallic surfaces. Testing was performed mainly on hemi-cylindrical surfaces because the custom surface treatment used was developed specifically for power plant condenser tube materials but a flat bottom surface was needed for test surface installation into the experimental facility. It was expected that gravity would provide the force necessary to promote condensate motion on these round surfaces.

An asymmetric saw-toothed ratchet microstructure was used for the second type of surface studied because it is very likely more durable than the silicon micro-pillar structures employed in other studies [3, 7-9] (the individual ratchets are 100-500 microns wide and extend the entire width of the surface as opposed to a square pillar that is only a few microns wide), and this type of surface structure has been shown to be effective at promoting fluid motion in a preferred direction in Marangoni convection [10], Leidenfrost droplets [11], pool boiling [12], filmwise condensation [13], and dropwise condensation on butterfly wings with a two-tier ratchet structure [14]. The ratchet structure was fabricated in silicon using gray scale lithography as described in [15] to achieve the small feature size desired while maintaining necessary precision. It is

expected that if these surfaces were ever produced on a large scale they would be fabricated from metal by stamping or wire EDM (electrical discharge machining).

## **1.1 Enhanced Condensation: Literature Review**

For any given atmospheric conditions, condensation rates can only be improved through methods that decrease surface wetting and increase droplet mobility and removal rates. Historically methods such as vibrating the condenser surface or adding chemicals to the working fluid that reduces wetting have been used, however this discussion will focus on modifications that can be made to the condenser surface that result in decreased wetting and increased droplet mobility and removal rates.

### **1.1.1 The Quest for Superhydrophobicity**

Several surface coatings have been used to reduce surface wettability and create hydrophobic condenser surfaces. Hydrophobic coating types include self-assembled monolayers (SAMs), polymers, and noble metals. SAMs are thin films that are composed of individual molecules that organize themselves on a surface. The molecules found in SAMs that are used for hydrophobic coatings have two opposing tails one that is attracted and bonds to the surface and the other that repels water and gives the SAM coated surface hydrophobic properties [16]. Many different polymer coatings have been used to create hydrophobic condenser surfaces including Teflon and other fluoropolymers [17, 18], parylene [19], and various silicones [20]. These coatings are usually much thicker than SAMs however recent work using advanced vapor deposition techniques have reported fluoropolymer coating thicknesses of about 50nm [21]. Noble metal

surfaces such as gold plated copper are one of the older methods used for promoting dropwise condensation however they have high surface energies and therefore are actually hydrophilic by nature [22] even though it was originally thought they were naturally hydrophobic [23-25]. While they are not quite hydrophobic by modern standards (contact angle  $> 90^\circ$ ) with measured contact angles of no greater than  $80^\circ$  [26] these surfaces obtain their less wetting properties by collecting organic contaminants from their surrounding atmosphere [26, 27].

Each of these coating types has their own benefits and drawbacks. For SAMs their minute thickness is both a strength and a weakness. Being extremely thin, SAMs impose very little additional thermal resistance to a condenser surface but they also suffer from poor durability. Polymer coatings can be made durable by increasing the coating thickness but the materials from which they are made have very low thermal conductivities and in some cases can actually hinder heat transfer rates [28]. New thin film polymer coatings may show promise if their durability can be enhanced [21, 29]. Even though noble metal surfaces can be made very durable they have largely fallen out of favor due to their expense and the need to periodically replenish the surface contaminants to maintain dropwise condensation [30].

While hydrophobic coatings have been shown to increase heat transfer coefficients during condensation [18, 31], the maximum contact angles achieved by this type of surface treatment are generally around  $120^\circ$ - $130^\circ$  as shown in Table 1.1. Methods have been discovered that can further increase contact angles into the superhydrophobic range ( $>150^\circ$ ) (see Table 1.2) leading to even higher droplet mobility and potential heat transfer gains. For example a droplet with a radius of 1.5mm on a flat

Teflon coated hydrophobic surface will roll off if the surface is tilted  $10^{\circ}$ - $30^{\circ}$  however on a superhydrophobic surface the tilt required for the same droplet to roll off is around  $1^{\circ}$  [32]. The methods used to create superhydrophobic surfaces generally consist of surface micro and nano-structure modification paired with SAM or polymer hydrophobic coatings.

Table 1.1: Contact angle measurements on some non-textured hydrophobic surfaces

Surface Treatment	Working Fluid	Contact angles ( <i>deg.</i> )		Reference
		$\Theta_a$	$\Theta_r$	
Organic SAM on gold coated AL	water	110*	-	31
Silane SAM on copper	water	123	81	4
Teflon coated copper	water	121	108	33
CYTOP coated silicon	water	100*	-	34
Vapor deposited fluoropolymer thin film	water	132	127	21
Gold exposed to air	water	65*	-	26
Gold under vacuum	water	30	0	27

\*Static contact angle

Table 1.2: Contact angle measurements on some textured superhydrophobic surfaces

Surface Treatment	Working Fluid	Contact angles ( <i>deg.</i> )		Reference
		$\Theta_a$	$\Theta_r$	
Silane coated silicon nanopillar	water	164*	-	35
Silane coated nanograssed micropyramids	water	160-165*	-	36
Hexadecanethiol coated micro/nanopillars	water	161	135	37
Hierarchical micro/nanoporous aluminum	water	170*	-	38
PMC coated polished aluminum with TiO <sub>2</sub> nanoparticles	water	151-156*	-	39
<i>Morpho deidamia</i> butterfly wings	water	151*	-	14
Silane SAM on nanostructured CuO	water	171	167	4

\*Static contact angle

Note:  $\theta_a$  and  $\theta_r$  are contact angles measured on an advancing and receding liquid fronts respectively. The hysteresis between  $\theta_a$  and  $\theta_r$  is caused by liquid to surface adhesion forces which cause contact line of a droplet or film to be pinned in place or immobile on the surface. When fluid is added to such a droplet the contact angle increases up to a maximum of  $\theta_a$  before the contact line becomes un-pinned and the liquid front advances. Also when fluid is removed from a droplet the contact angle is reduced to a minimum value of  $\theta_r$  before the contact line becomes un-pinned and the liquid front recedes. Low values of contact angle hysteresis ( $\theta_a - \theta_r$ ) indicate low liquid to surface adhesion. Static contact angles values are always between advancing and receding contact angle values.

### 1.1.1.1 Micro/nano-structured Superhydrophobic Surfaces

There has been much excitement lately on the benefits of superhydrophobic condensing surfaces consisting of nano-scale structures on top of micro-scale structures employed to augment condensation. On textured hydrophobic surfaces, droplets can exist in a Cassie-Baxter, or Wenzel state or both simultaneously. As shown in Figure 1.2 the droplet in the Cassie-Baxter state has a much less contact with the surface than the droplet in the Wenzel state because the Cassie droplet sits on top of the surface texture rather than filling it [32].

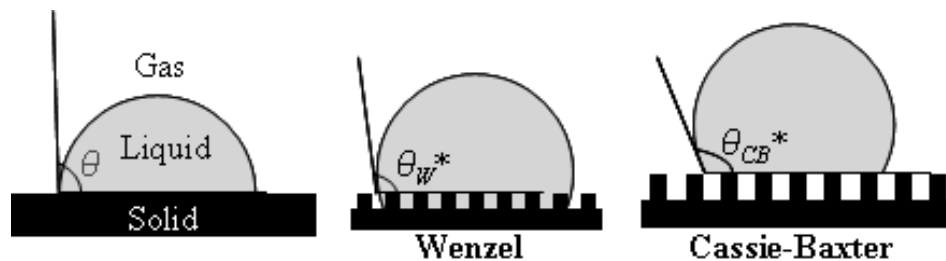


Figure 1.2: From left to right: Droplet on a smooth surface, Droplet in the Wenzel state, Droplet in the Cassie-Baxter state [40]. Wenzel state droplet fills surface texture, Cassie-Baxter state droplet sits on top of surface texture leading to greater droplet mobility.

Because the Cassie droplet has much less contact with the surface than a Wenzel droplet, it also has less contact angle hysteresis and much higher droplet mobility [8]. This higher droplet mobility makes the Cassie state the preferred state for dropwise condensation performance.

One of the earlier papers written on condensation on hydrophobic two-tiered surfaces shows a comparison of condensation performance on three different surfaces,

each with different structures, micromachined silicon pillars, deposited carbon nanotube pillars, and carbon nanotube pillars deposited on top of micromachined silicon pillars [8]. The two tier structure was designed to mimic the structure of a lotus leaf, so the carbon nanotubes used (i) did not have the catalyst removed so they essentially had catalyst caps that prevented liquid from wetting the interior of the tube effectively creating pillars instead of tubes and (ii) they had an average length of about 400 nm which is closer to the length of the nano-structures on a lotus leaf than the average length of carbon nanotubes used in other studies. Images comparing condensation on the three surfaces studied are shown in Figure 1.3.

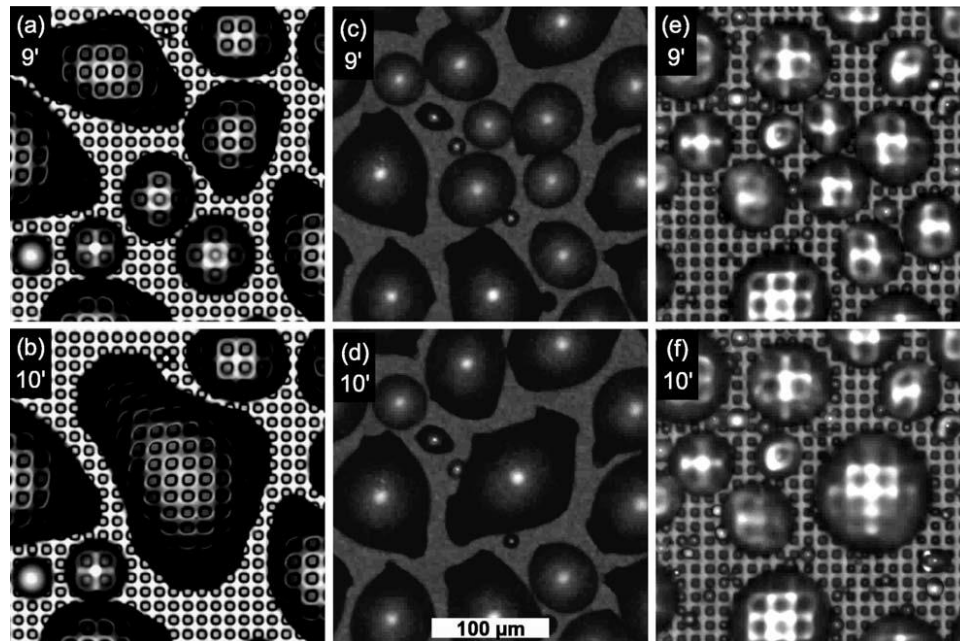


Figure 1.3: (a-b) One-tier with only micropillars, (c-d) one tier surface with only nanopillars, (e-f) two-tier surface with micro and nano pillars. Images were taken 9 (a, c, e) and 10 (b, d, f) minutes after condensation began [8].

Droplets on both of the single-tier surfaces appear to have penetrated the surface cavities meaning that they are in a Wenzel state. This is evident because the droplets on

these two surfaces have irregular shapes which indicate higher contact angle hysteresis, which is a characteristic of the Wenzel state. Droplets on the two-tier surface, however, have a very regular circular cross-section indicating that they have relatively low contact angle hysteresis and are in a Cassie-Baxter state. It is shown through analysis of the contact angles, solid contact fractions and roughness ratios, that Wenzel states on the one tier surfaces and Cassie-Baxter states on the two-tier surface are the thermodynamically stable states for the surfaces on which they were observed.

Another factor that affects droplet mobility was also examined in this study: the effect of a surface coating on the two-tier super hydrophobic surface. Two surface coatings, parylene (polymer coating) and hexadecanethiol (SAM), were applied, one on each of two similar surfaces. The parylene coated surface had relatively low droplet mobility compared to the hexadecanethiol coated surface and the hexadecanethiol coated surface retained its superhydrophobicity after condensation while the parylene coated surface did not [8]. It was also noted that single tiered nano-textured surfaces coated with the hexadecanethiol SAM also displayed superhydrophobicity before and after condensation. Figure 1.4 shows an example of the high droplet mobility on a hexadecanethiol coated two-tier surface, where a relatively large droplet ( $d=120\mu\text{m}$ ) coalesced with another droplet and moved completely out of the camera view in less than a second, leaving dry surface in its previous location.



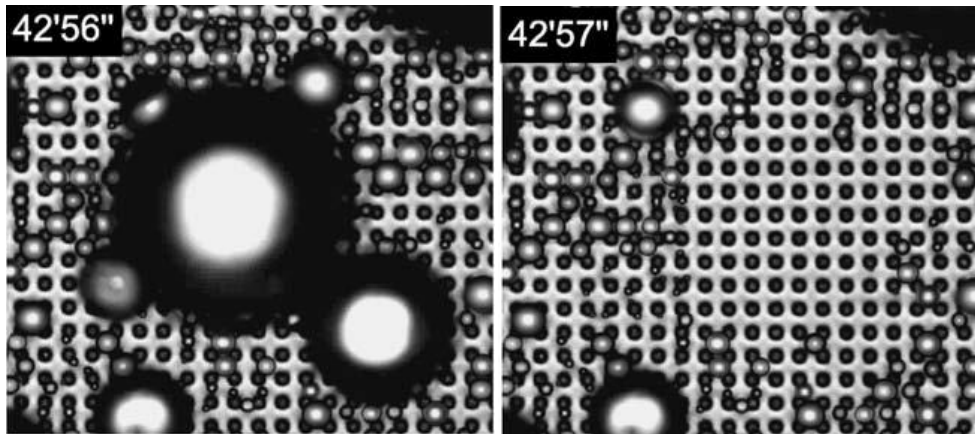


Figure 1.4: Condensation on hexadecanethiol coated two-tier surface, images were captured over the same area. Time of capture is indicated in top left corner [8].

High droplet mobility and the preservation of superhydrophobicity during and after condensation have been shown by others on similar silane coated micro/nano-textured surfaces [35, 36, 38] as well. This indicates that these approaches to optimize condensation show promise for being developed into industrially applicable technologies.

Possibly the most interesting phenomena discussed in subsequent studies on condensation on superhydrophobic two-tiered surfaces was that of a surprising out-of-plane jumping exhibited by coalescing droplets. In the first paper to discuss such a jumping behavior, the surface used was again carbon nanotubes deposited on silicon micropillars and coated with hexadecanethiol. In that study, condensation on hydrophobic and superhydrophobic surfaces was compared. It was observed that in the absence of external forces, condensation on horizontal hydrophobic surfaces progressed through two stages, while on horizontal superhydrophobic surfaces a third stage of condensation was observed [7].

The first stage of condensation is “initial growth without coalescence” [7]. In this stage droplets nucleate and grow on the surface without significant interactions with other

droplets and there is minimal surface coverage [7]. In the second stage of condensation, “immobile coalescence”, sufficient surface coverage was attained for droplets to coalesce; however, the center of mass of the coalescing droplets did not significantly change position after coalescence [7]. The third stage of condensation, “mobile coalescence”, was only observed on the superhydrophobic surface. In this stage once the average droplet diameter reached a threshold value, the coalescence of droplets resulted in the rapid removal of the coalesced droplets from the surface [7]. Figure 1.5 shows these condensation stages on a hydrophobic and super hydrophobic surface. Notice that on the smooth hydrophobic surface the droplet size reaches a much larger diameter because there is no removal of condensate from the substrate. Figure 1.6 shows images of a jumping droplet.

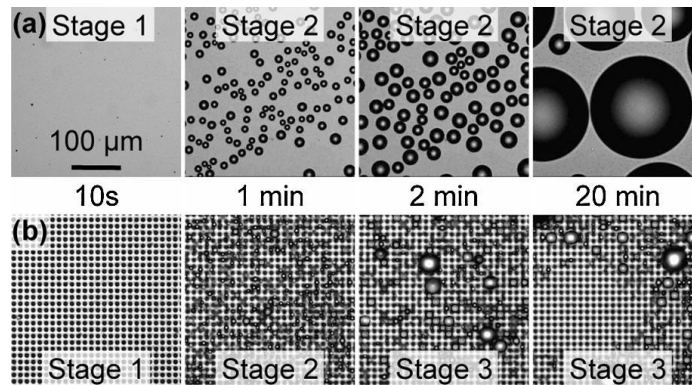


Figure 1.5: Dropwise condensation on (a) a smooth hydrophobic surface and (b) a two-tier superhydrophobic surface [7].

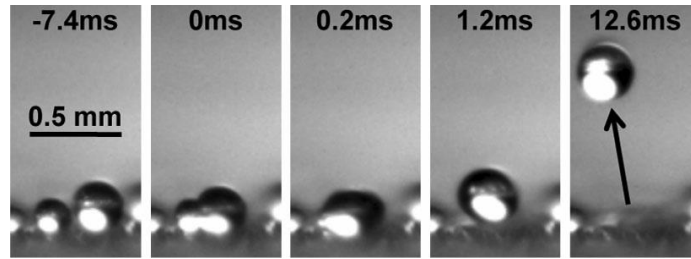


Figure 1.6: Side view of two droplets coalescing and then jumping off of the surface. Notice that the horizontal momentum of the droplets is conserved [7].

As can be seen in Figure 1.7, the surface coverage by condensate is not dramatically lower on the superhydrophobic surface as compared to the hydrophobic surface even though the average droplet size on the superhydrophobic surface is much smaller than that on the hydrophobic surface after about two minutes of condensation [7]. This is because new nucleation occurs on the superhydrophobic surface after droplets remove themselves [7]. Since the superhydrophobic surface promotes a cycle of droplet growth and self-removal it also provides much more efficient heat removal than the hydrophobic surface because heat transfer rates increase as droplet diameter decreases even on surfaces with the same surface coverage [7].

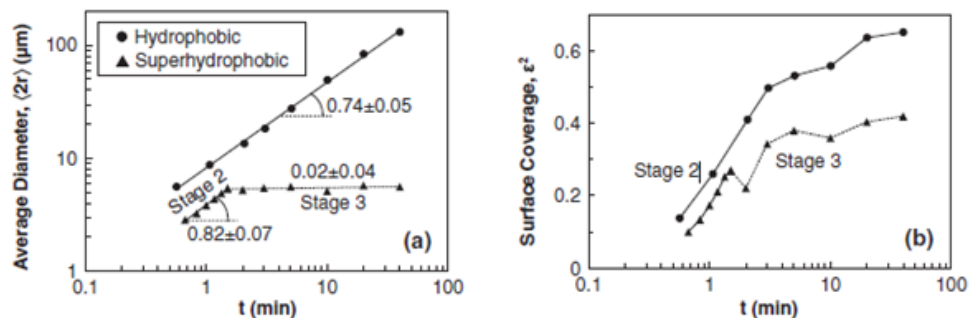


Figure 1.7: (a) Average drop diameter. (b) Surface coverage, which reached a plateau for both surfaces but fluctuated because of the small field of view [7].

A similar jumping droplet phenomenon is also observed in coalescing droplets on a Leidenfrost surface [7]. On a hot surface at the Leidenfrost temperature, droplets float on a vapor layer. When two Leidenfrost droplets coalesce the diameter of the resulting droplet quickly grows to be larger than the diameter of either of the original droplets [7]. At the instant this happens the center of mass is still at the same elevation relative to the surface and the vapor layer under the droplet is compressed by the rapid growth of the resultant droplet [7]. The compressed vapor layer exerts a vertical force that causes the coalesced Leidenfrost droplet to jump off of the surface [7]. It was suspected by the authors of [7] that condensate droplets on a textured superhydrophobic surface jump when they coalesce for the same reason: a vertical force exerted by the compressed vapor layer upon droplet coalescence.

In order for condensation systems relying on jumping drops to be feasible for industrial applications, a surface with characteristics that promote the jumping phenomenon while being easier/less expensive to manufacture and able to accommodate arbitrary shapes must be developed. Subsequent research at MIT revealed such a surface while experimentally achieving a 25% higher overall heat flux and a 30% higher condensation heat transfer coefficient compared to conventional dropwise condensing copper surfaces at low super saturations [4]. The surface studied was silanized copper oxide (CuO). The study proposes CuO as an ideal surface for jumping dropwise condensation because it is relatively easy to manufacture, has a relatively low parasitic conduction thermal conductivity, and forms nanostructures that minimize individual droplet thermal resistance and allow for high nucleation site density. Copper oxide surfaces are also attractive because they can be formed on large and/or arbitrary surfaces

without the need for expensive equipment or processes. A comparison of condensation on various copper tubes with different surface treatments is shown in Figure 1.8.

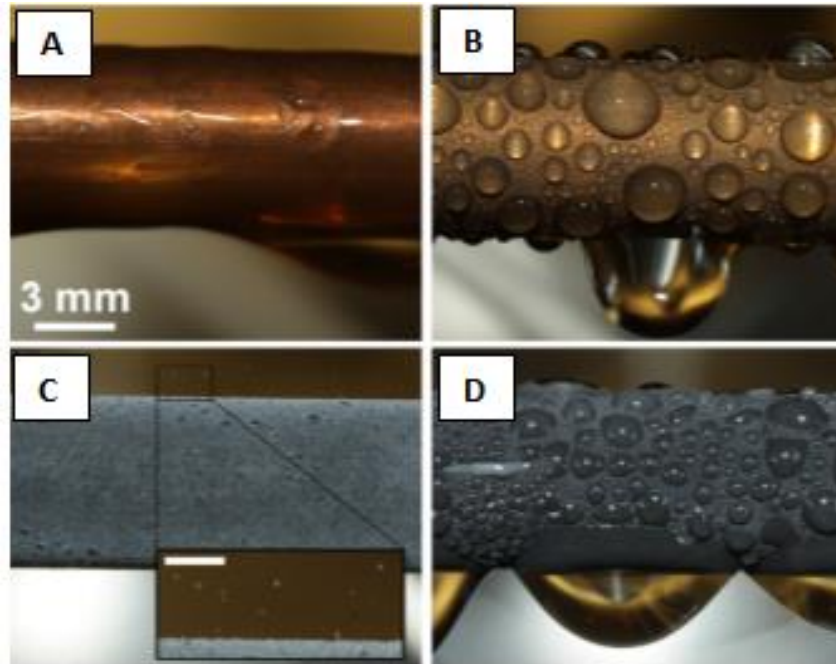


Figure 1.8: (a) Filmwise condensation on a smooth hydrophilic copper tube, (b) dropwise condensation on a silane coated smooth copper tube, (c) jumping-drop superhydrophobic condensation on a nanostructured copper oxide tube with inset of magnified view of droplet jumping, (d) flooded condensation on a nanostructured CuO tube [4].

The overall heat transfer coefficient of the jumping drop condensation on the CuO surface is roughly 30% higher than the overall heat transfer coefficient reported for the dropwise condensation on the smooth copper tube, it is also about 85% higher than the overall heat transfer coefficient reported for the filmwise condensation on the smooth hydrophilic copper tube. This is a drastic improvement over what is the most commonly employed mode of condensation in industrial applications. It is also interesting to note that while the overall heat transfer coefficient for the flooded condensation on the CuO

surface is worse than that of the dropwise condensation on the silane coated smooth copper, it is not as bad as the overall heat transfer coefficient for the filmwise condensation on the smooth hydrophilic copper surface. Clearly the rate of phase change heat transfer is directly correlated to droplet mobility.

The preceding discussion only addresses a sampling of condensation enhancement research involving the use of hierarchical micro/nano scale condensing surfaces. Surface energy is an important consideration because it leads to macroscopic phenomena, such as hydrophobicity and hydrophilicity. The hydrophobicity of a surface can be directly related to the interfacial surface energies using Young's equation [41]:

$$\gamma_l \cos \theta = \gamma_s - \gamma_{sl} \quad (1.1)$$

where  $\theta$  is the contact angle of the fluid on the surface,  $\gamma_l$  is the liquid surface tension,  $\gamma_s$  is the solid surface energy, and  $\gamma_{sl}$  is the interfacial energy between the solid and liquid.  $\gamma_{sl}$  is defined as the energy required to separate two surfaces (one solid and one liquid). Another key factor influencing hydrophobicity is surface roughness. Superhydrophobic surfaces combine appropriately roughened surfaces with low surface energy materials such as fluorinated compounds to drive interfacial phenomena. It is a relatively new research thrust but it shows great promise for future technological advancements and industrial application. The main issue to be addressed before textured condensing surface will be commonly used is identifying materials and manufacturing processes that can be scaled to inexpensively create durable superhydrophobic surfaces that lend themselves to be applied to the type of geometry used on condensing equipment.

### 1.1.2 Surfaces Designed to Promote Droplet and Condensate Fluid Motion

While there are many surfaces that have been designed to promote fluid motion some of which were mentioned in an earlier section [11, 12], the discussion in this section will be limited to surfaces that promote motion in deposited droplets and condensate.

As stated above, dropwise condensation has the potential to have heat transfer coefficients an order of magnitude larger than filmwise condensation. This increase in heat transfer coefficient is due to the cycle of sweeping and renewal of the condenser surface caused by moving droplets that occurs on many dropwise condensing surfaces [42]. In other words, without droplet mobility hydrophobic and superhydrophobic surfaces will not exhibit increased heat transfer coefficients and conversely surfaces that can promote condensate motion may be able to generate high heat transfer coefficients without superhydrophobic properties.

Some recent studies have explored the effects of a wettability gradient on condensate dynamics and report some interesting findings. Tokunaga et al. created a linear wettability gradient on a silicon substrate by applying CYTOP, which is an amorphous fluoropolymer hydrophobic coating, in the pattern shown in Figure 1.9 [34].

Using this horizontally oriented patterned surface with  $W=50\mu\text{m}$  and  $L=20\text{mm}$ , a  $10\mu\text{l}$  droplet was slowly placed on the hydrophobic end of the surface [34]. Due to a force imbalance caused by the difference in contact angle from the front to the rear of the droplet, the droplet moves from the hydrophobic end to the hydrophilic end of the surface without any external forces [34]. Images of this movement are shown in Figure 1.10.

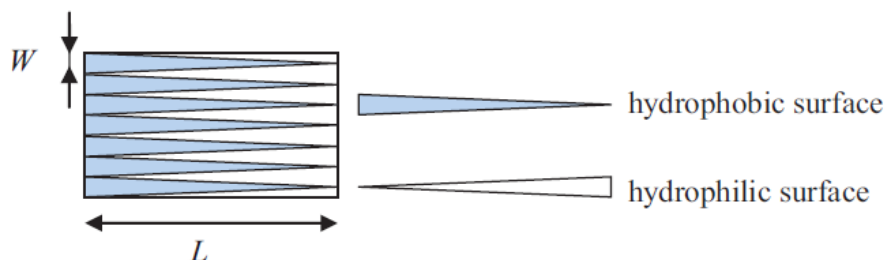


Figure 1.9: Schematic of wettability gradient used by Tokunaga et al. [34].

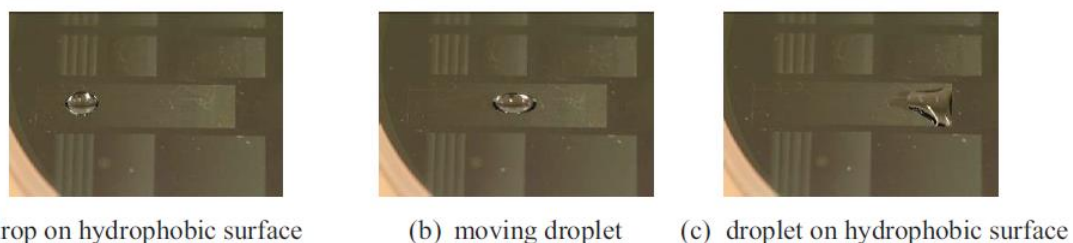


Figure 1.10: As seen in [34] moving water droplet on wettability gradient.

Ghosh et al. [39] also employed a wedge shaped wettability pattern to promote motion in a deposited droplet. These wedges were single hydrophilic wedge shaped tracks surrounded by a superhydrophobic field. The hydrophilic wedge was uncoated mirror polished aluminum while the superhydrophobic background was coated with a fluoroacrylic copolymer dispersion (PMC by DuPont) and  $\text{TiO}_2$  nanoparticles. When a droplet was deposited on the narrow end of the track it was quickly drawn to the wide end of the track by capillary forces. Images depicting this motion are given in Figure 1.11.

In [43] a surface wettability gradient created by exposing a polished silicon wafer to a diffusion of decyltrichlorosilane vapor was shown to be capable of forcing small droplets (radius < 1.5mm) deposited on the more hydrophobic end of this surface run up a



15° incline at speeds of 1 to 2 mm/s. Clearly surface wettability gradients show great promise as solid state fluid pumps. Images captured of this behavior are shown in Figure

1.12

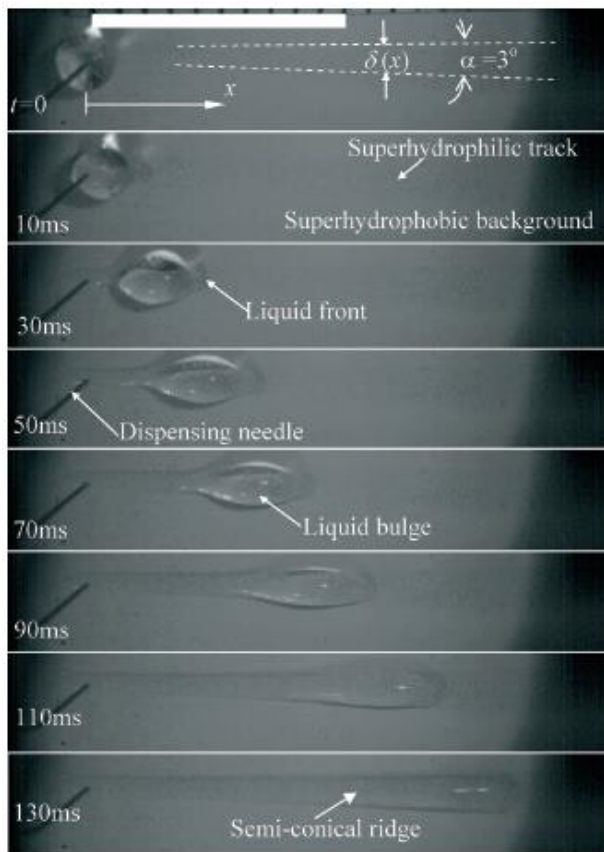


Figure 1.11: Image from [39] of deposited water droplet moving on single wedge shaped hydrophilic track surrounded by superhydrophobic field.

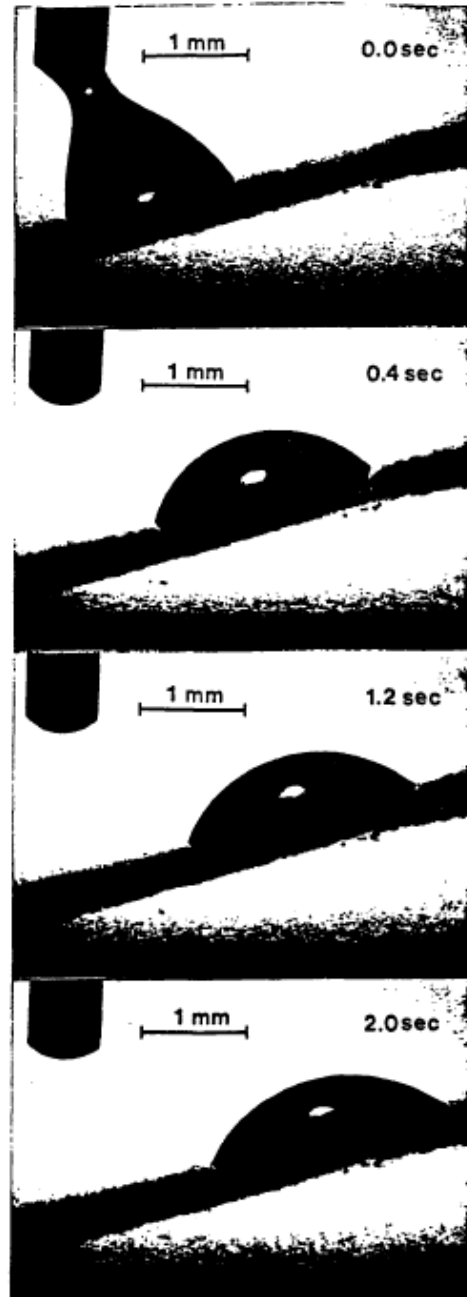


Figure 1.12: As shown in [43], a deposited water droplet travels up a 15° incline due to surface wettability gradient.

Macner et al. show a similar droplet motion on a radial wettability gradient during condensation experiments on surfaces with very moderate contact angles ranging from  $64^\circ$  (totally hydrophilic areas) to  $103^\circ$  (totally hydrophobic areas) [44]. The number of droplets and droplet size distribution during a condensation process on the surface with a radial wettability gradient and a uniform surface was compared. The results show that except for the initial stages of condensation the uniform surface tended to have larger droplets than the surface with the radial wettability gradient. Figure 1.13 shows the results of the comparison.

The stages of condensation as observed in these experiments are: I. Droplet generation, the primary condensation activity is nucleation of new droplets, II. Coalescence, the beginning of this stage occurs when there are more coalescence events than nucleation events, III. Bimodal, coalescence and nucleation are competing condensation activities. The difference between stage IIa and IIb is primarily the difference in droplet size distributions but stage IIb is also characterized by coalescence occurring over larger distances [44].

Any practical process using condensation will be characterized by stage III condensation except for during initial start-up. During stage III condensation the surface with the radial wettability gradient exhibited the largest difference in droplet size distribution compared to the uniform surface with the gradient surface showing a strong tendency to have smaller droplets. On superhydrophobic surfaces very small droplets are responsible for most of the heat transfer [45], and since the surface with a radial wettability gradient self clears and allows “fresh” surface for nucleate condensation, it

has the potential to perform much like a superhydrophobic surface that relies on gravity to remove larger droplets.

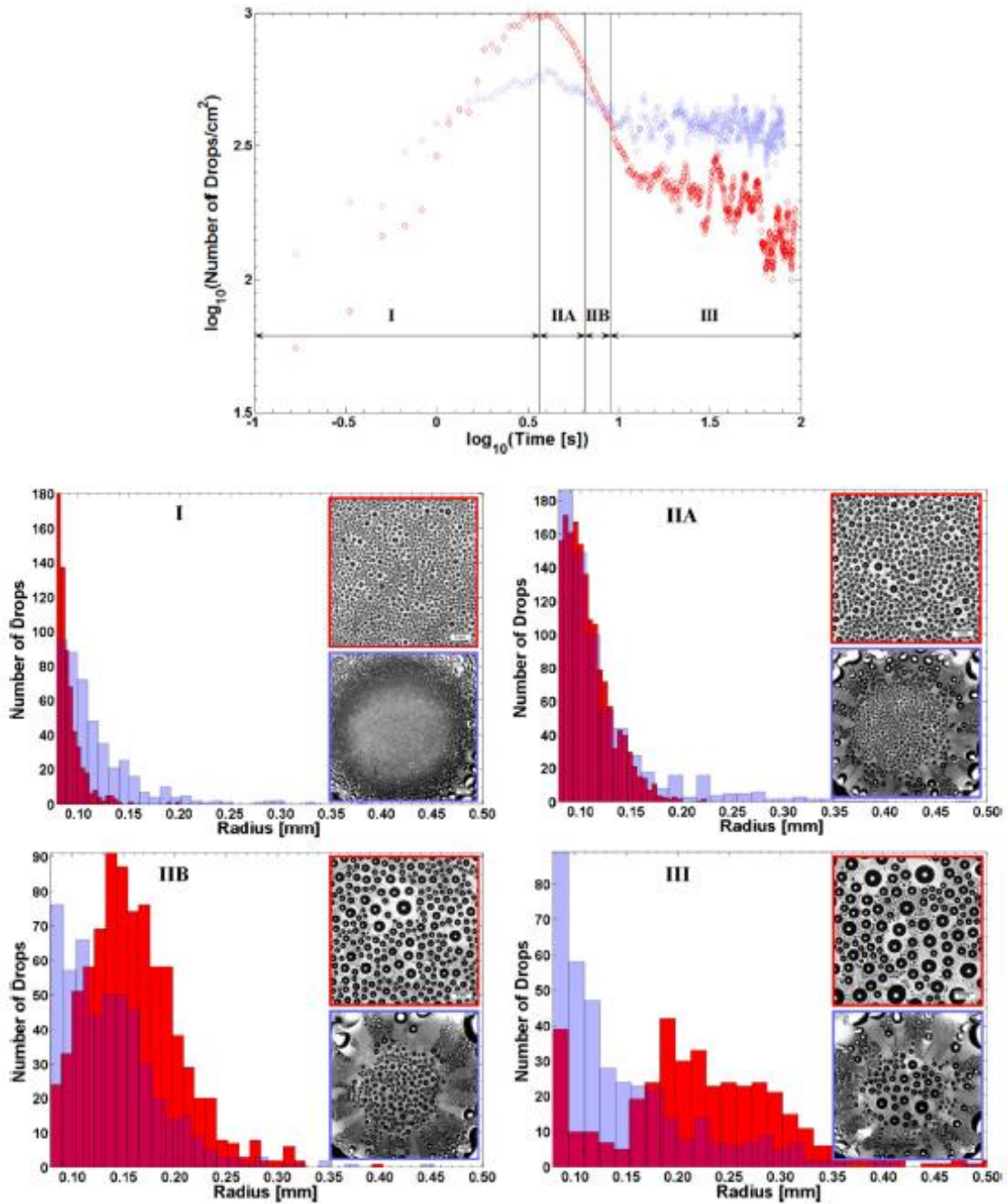


Figure 1.13: Top: Number of droplets vs. time for each type of surface. Below: Images of each surface and histogram of droplet size during each stage of condensation. Red=Uniform surface. Blue=Gradient surface [44].

A quantification of the condensation heat transfer improvements afforded by surfaces with a radial wettability gradient was reported in [46]. In this study it was reported that heat transfer coefficients could be up to seven times greater on silane coated copper surfaces with radial wettability gradients compared to uniformly coated surfaces at low subcoolings [46].

A very recent study reported using wettability patterning in the form of alternating roughened ( $\theta_a = 138^\circ$ ,  $\theta_r = 73^\circ$ ), and smooth ( $\theta_a = 125^\circ$ ,  $\theta_r = 52^\circ$ ) SAM coated stripes to promote increased removal rates of droplets from horizontal copper condenser tubes [47, 48] as shown in Figure 1.14. Several configurations of patterned tubes were tested and compared against totally roughened and totally smooth tubes as well as filmwise condensing tubes. It was found that the highest heat transfer coefficients were measured on the patterned tube with hydrophobic stripes that were twice as wide as the less hydrophobic stripes, 0.6mm and 0.3mm respectively. This surface configuration produced heat transfer coefficients 1.8 and 4.8 times greater than the fully dropwise condensing and fully filmwise condensing surfaces respectively [47]. This increase in heat transfer coefficient is the result of this surface configuration producing the higher droplet departure frequencies for all temperature differences tested than any other surface configuration [48]. The simplicity and effectiveness of this approach are very appealing and show potential for future adoption by industry if this type of surface can be proven to provide adequate durability and longevity.

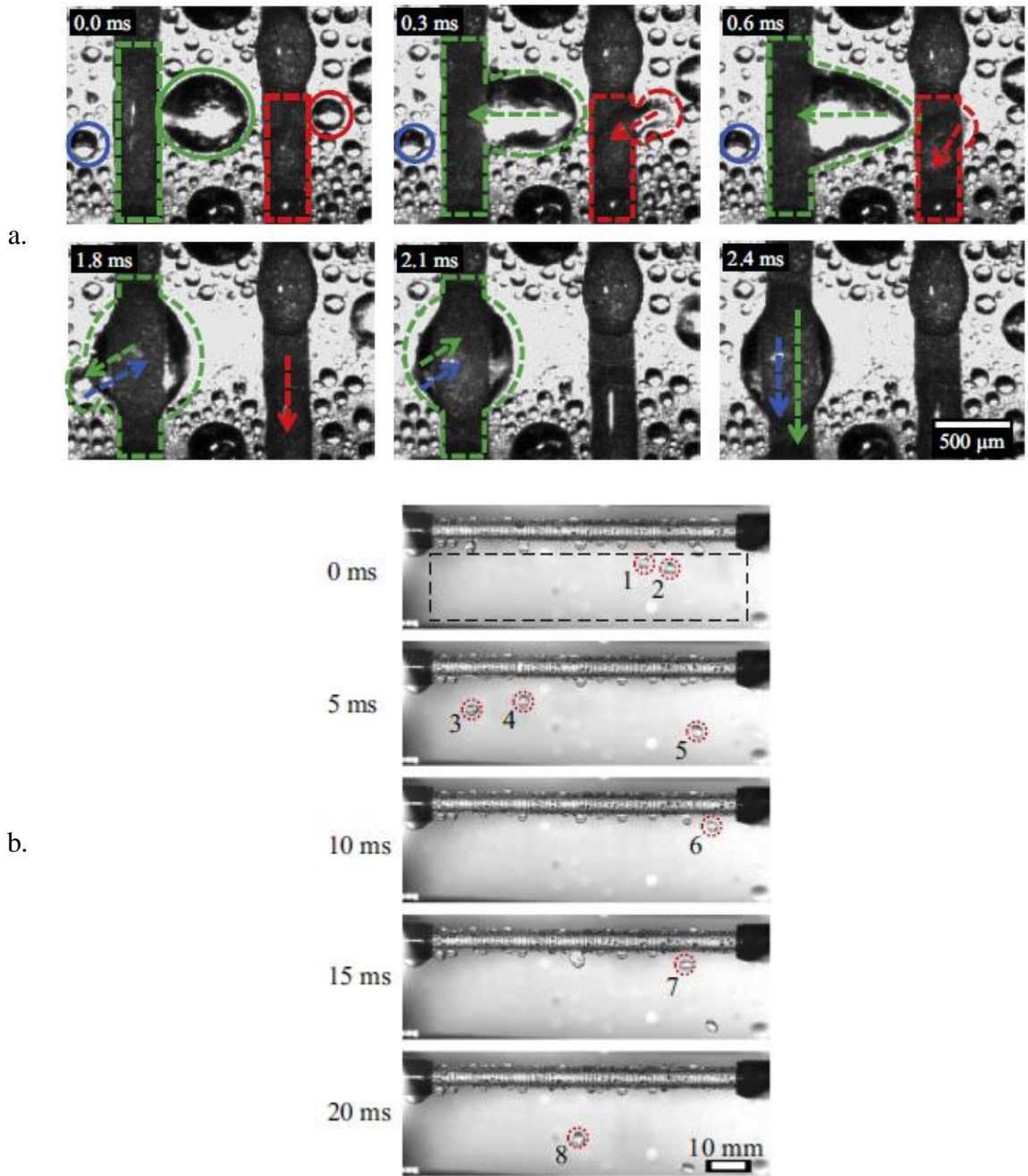


Figure 1.14: a. Droplets on hydrophobic regions migrate to less hydrophobic regions (darker stripes) drain downward [47]. b. Droplets are removed from condenser tube [48].

Recently surfaces have been developed to increase the rate of condensate removal by taking advantage of the jumping droplet phenomenon presented in the previous section. Recent work modeling this jumping phenomenon gives better insight on the actual mechanism of coalescence induced jumping than provided by [7]. In this work it is shown that that identical droplets as small as tens of nano-meters on superhydrophobic surfaces can exhibit jumping behavior [49]. In this study the diameter of droplets modeled was 36 nm. The fluid examined was Argon, therefore, a 36 nm diameter droplet only contains about 1,000,000 atoms. Continuum level modeling and the associated assumptions (like the no slip condition) were deemed inappropriate for this work so molecular dynamics simulation was used instead. A spherically shaped droplet of liquid argon on a superhydrophobic gold surface, surrounded by cubic cell of argon vapor was modeled. This model was then duplicated in the x direction as shown in Figure 1.15 [49].

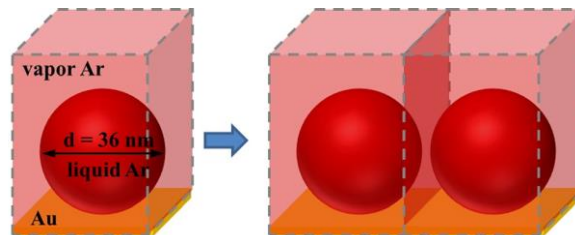


Figure 1.15: Diagram of identical droplet model generation from [49].

The mechanism of coalescence induced jumping behavior is described using five stages. Images of the droplets in each of these stages as well as plots of velocity, pressure and temperature can be found in Figure 1.16. Stage I: The two identical droplets are given equal and opposite x-direction velocities to cause them to move towards each other. Stage II: The droplets touch and start to coalesce. A bridge between the droplets

forms and rapidly expands. Stage III: The bridge impacts the surface and the droplet is accelerated away from the surface due to the increased pressure caused by the impact. Stage IV: The droplet is still in contact with the surface but has begun to detach as it moves away. This causes a decrease in velocity. Stage V: The droplet moves upward in the vapor space with a velocity of 2.3 m/s at the moment it leaves the surface. Deceleration in this stage is caused by Stokes drag.

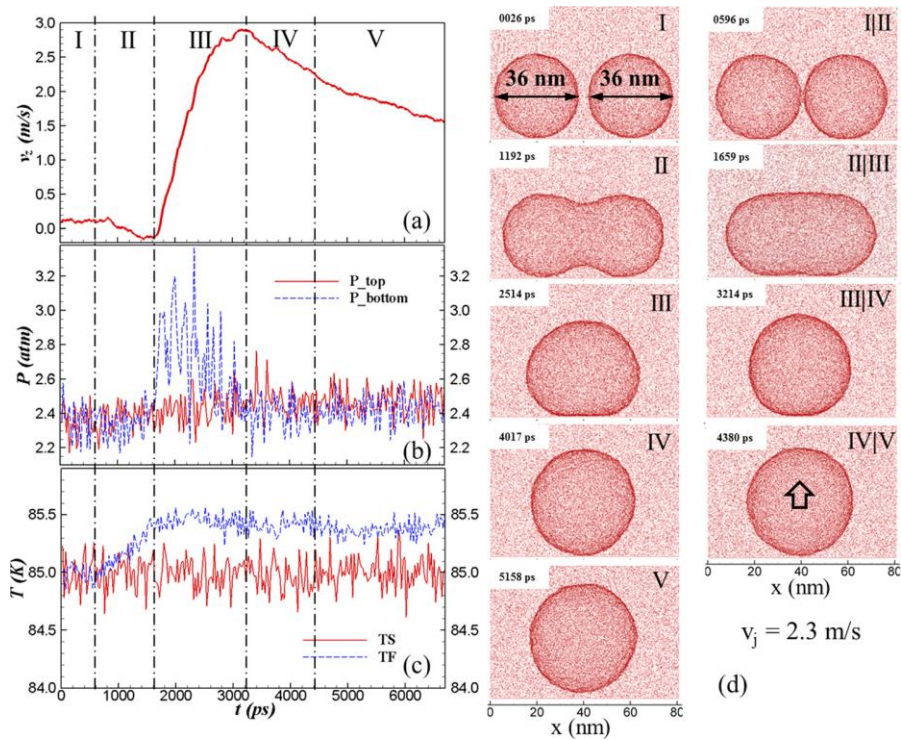


Figure 1.16: (a) Vertical jumping velocity vs. Time. (b) Pressure vs. Time. (pressure of the top and bottom of the droplet) (c) Temperature vs. Time (temperature of surface and droplet fluid) (d) Images of droplet at each stage of jumping (stage transitions are in the second column) [49].

Additional simulations were performed varying the initial x-direction velocity and droplet diameter (22.7 nm to 53.3 nm). It was concluded that the magnitude of the x-direction velocity had negligible effect on the resulting jumping velocity. Also all droplet sizes modeled were only able to convert about 1.3% of the available surface energy into kinetic energy for jumping [49].

Another study has shown that under certain conditions droplets on fibers can exhibit jumping behavior at surface energy to kinetic energy conversion rates approaching 40% [33]. In this study the droplets form on a cooled Teflon coated copper wire with a radius of 40  $\mu\text{m}$  ( $\theta_a=121^\circ\pm 3^\circ$ ;  $\theta_r=108^\circ\pm 3^\circ$ ). Jumping occurs when two droplets at the same axial location on a fiber with radii eight or more times larger than the fiber radius coalesce. The jumping is a two-step process. First, the coalescing droplets are accelerated orthogonally to the fiber due to the fiber's interference with the coalescence process until the resulting droplet has moved almost entirely to one side of the fiber. Second, the coalesced droplet moves radially away from the fiber while the droplet's inertia competes against adhesion forces until the droplet eventually breaks away from the fiber [33]. Figure 1.17 shows images of this process.

Numerical simulations of droplet coalescence on a fiber as well as simulations of droplets of a similar size coalescing on a flat surface with the same contact angle as the fiber revealed that for the conditions given above (droplets are at the same axial location on the fiber and  $r_{\text{droplet}} \geq 8r_{\text{fiber}}$ ) the coalescence event causes the droplet to jump from the fiber but not from the flat surface. This is due to the higher surface energy to kinetic energy conversion rate of the fiber compared to a flat surface. The higher conversion rate (nearly 40% for large  $r_{\text{droplet}}/r_{\text{fiber}}$ ) is due to the geometry of the fiber which reduces



liquid-solid contact area and interferes with coalescence events earlier in their process [33].

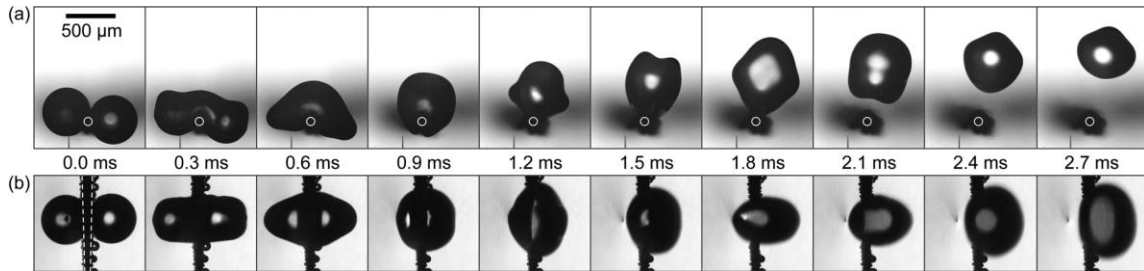


Figure 1.17: Time stepped images of coalescing droplets jumping from a Teflon coated copper wire. (a) end view, approximate fiber location is marked with white circle (b) side view [33].

This type of surface interference with coalescence events was utilized to cause jumping droplets to sweep a flat textured superhydrophobic surface in [37]. This promises to increase the thermal performance benefit provided as the jumping droplet leaves the surface because more area is cleared by a jumping event that in other studies to date. The substrate employed in this study featured silicon micropillars coated with aluminum nanostructures and hexadecanethiol to provide two-tier roughness and hydrophobicity ( $\theta_a=161^\circ\pm 3^\circ$ ;  $\theta_r=135^\circ\pm 3^\circ$ ). The micro pillars were  $20\ \mu\text{m} \times 20\ \mu\text{m}$  square pillars,  $10\ \mu\text{m}$  tall with  $20\ \mu\text{m}$  edge-to-edge spacing [37].

During open air experiments (water vapor from ambient air is condensed) droplets formed within the surface microstructure and when the droplet diameters became comparable to the pillar spacing, coalescing droplets spontaneously departed from the surface. However, because the droplets had formed within the microstructure the departure velocity was nearly parallel to the surface with a small vertical velocity that

allowed the droplet to rise over neighboring pillars; this is illustrated in Figure 1.18. This horizontal velocity caused the jumping droplet to contact and coalesce with several other droplets as it moves, clearing a much larger area than that occupied by the two original coalescing droplets, as can be seen in Figure 1.19 [37].

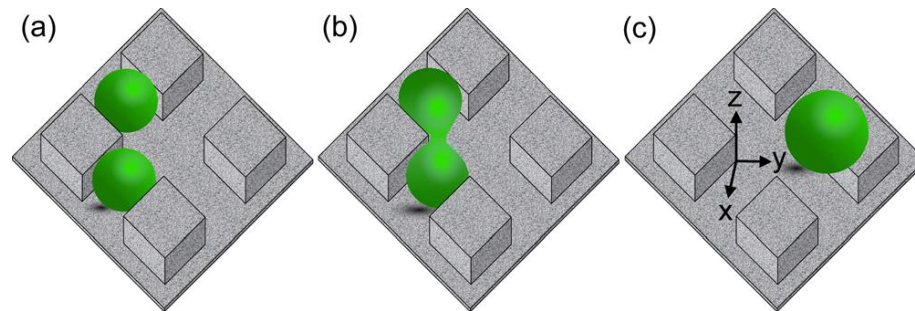


Figure 1.18: Schematic of droplet removal with relatively large horizontal velocity. (a) two droplets grow within the microstructure. (b) the droplets have grown large enough to coalesce around a corner. (c) coalesced droplet expands against the pillar and bottom substrate and jumps in a direction almost orthogonal to the pillar. The small vertical velocity is due to the bottom substrate [37].

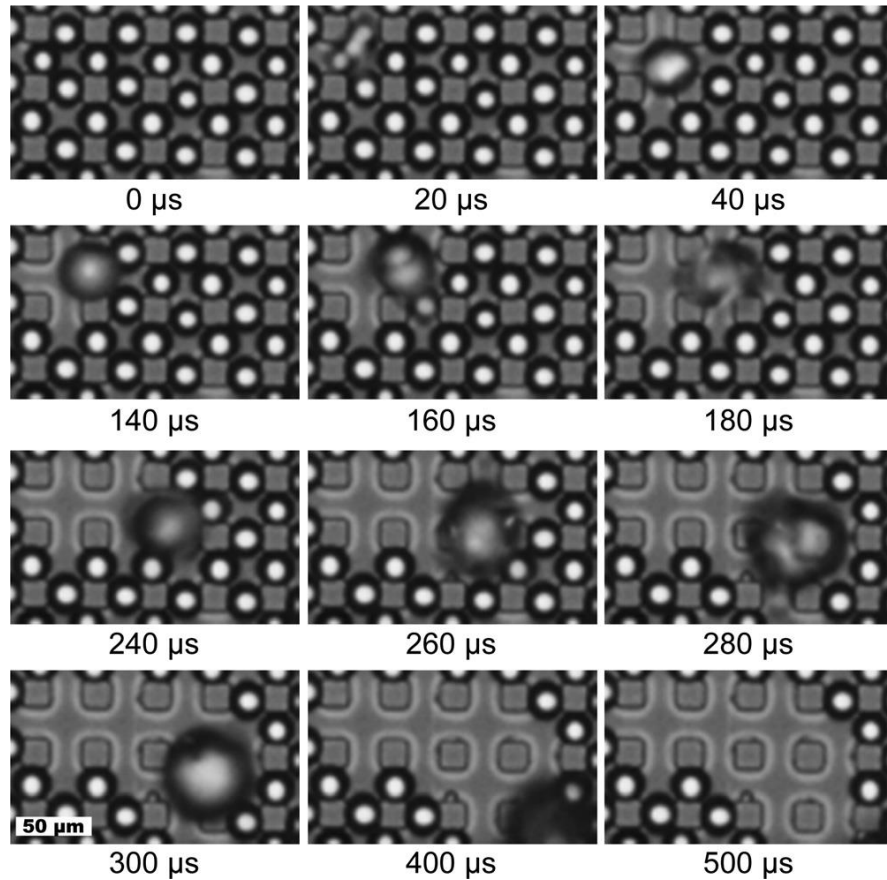


Figure 1.19: Nearly horizontally jumping droplets from the top row sweep the surface removing a total of 15 droplets [37].

The use of asymmetric ratcheted surfaces like those used in this study as a means of promoting fluid motion during condensation is rare. At present the author is only aware of two other studies that report the use of such a surface to promote directional condensate motion. One was conducted by our project partners at the University of California, Davis [13] and the other was conducted by researchers in China observing condensate dynamics on *Morpho Deidamia* butterfly wings that exhibit two-tiered ratchet like structures formed by a series of overlapping scales [14].

The study conducted by our project partners focused on filmwise condensation of FC-72 on a brass surface featuring a series of  $75^{\circ}$ - $15^{\circ}$ - $90^{\circ}$  triangular asymmetric ratchets

3mm wide with drainage pathways cut perpendicular to the ratchets. The performance of this surface was compared with a control surface consisting of a series of similarly sized 45°-45°-90° triangular symmetric ratchets. Both surfaces had walls attached to the ends of the ratchets that served to prevent condensate from draining from the surface in a direction parallel to the ratchets. Fluid motion on these surfaces was measured by comparing the volumes of fluid collected from the ends of the surfaces in vials installed in the experimental apparatus. It was reported that while fluid drained from both ends of both the asymmetric and symmetric surfaces there was a net mass flux rate for the asymmetric test surfaces that indicates a preferred fluid motion direction toward the shorter, steeper ratchet face. It was noted that no such mass flux rate was observed on the symmetric surface. Additionally the heat transfer coefficient produced by the highest performing asymmetric ratcheted surface was 1.8 times higher than the heat transfer coefficient produced by the symmetric surface [13].

The butterfly wing surface while not technically designed, but rather created or evolved to promote fluid motion during dropwise condensation does show the potential of asymmetric ratchets to be an effective mover of fluid during dropwise condensation. As mentioned above, the surface of *Morpho Deidamia* butterfly wings is characterized by a two-tier asymmetric ratchet structure formed by overlapping scales with widths of ~150 μm and lengths of ~200 μm upon which are ridges that are ~75 nm thick and ~50 nm wide. The roughness created by this structure gives the wings superhydrophobic properties (contact angle=151.3°). It was reported in this study that the degree of tilt required for a water droplet to roll off of this surface was significantly lower when tilted in the radially outward (RO) direction than when tilted in the opposite direction, 5.0° and

18.3° respectively. Additionally, condensate motion in the RO direction upon droplet coalescence was also reported [14]. Images of the butterfly, wing structure and condensate motion are shown in Figure 1.20.

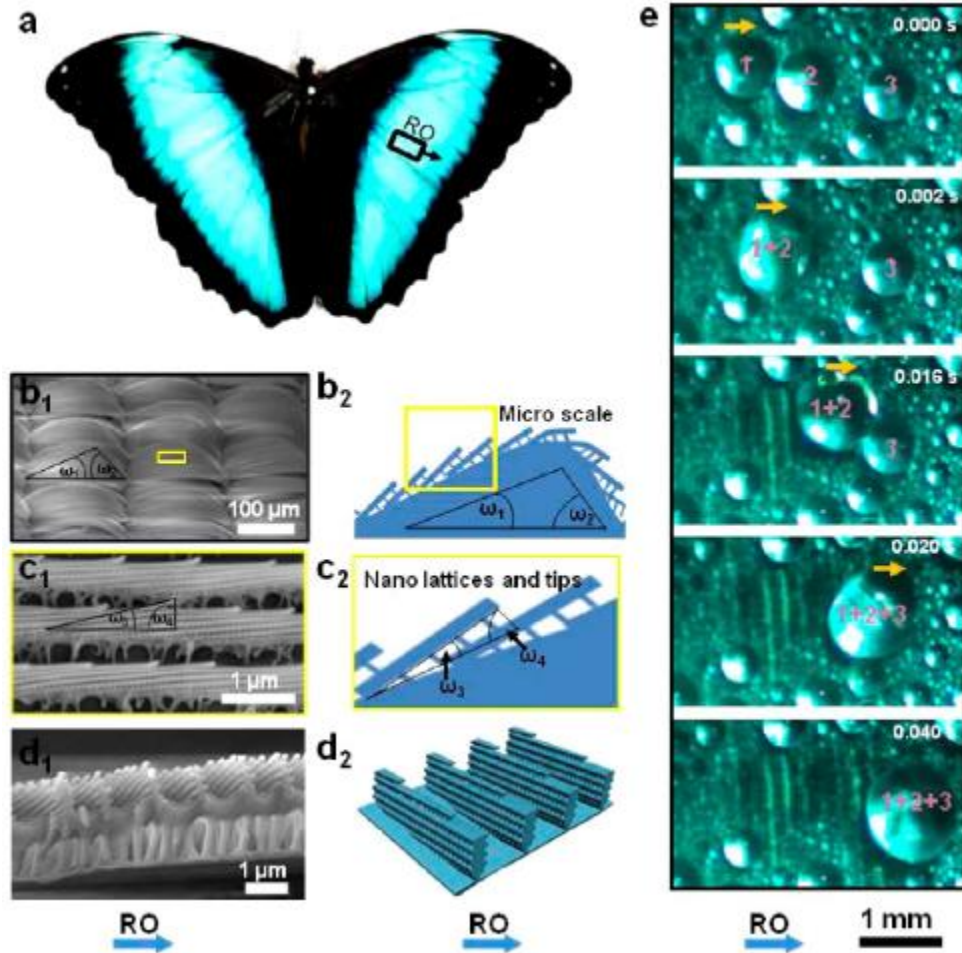


Figure 1.20: From [14], a. Image of *Morpho Deidamia* butterfly with radially outward (RO) direction noted. b<sub>1</sub>. ESEM image of overlapped scales. b<sub>2</sub>. Illustration of two-tiered asymmetric ratchet structure. c<sub>1</sub>. Higher magnification ESEM image of nano-ridges. c<sub>2</sub>. Illustration of nano-ridge structure. d<sub>1</sub>. Cross section ESEM image of nano-ridges. d<sub>2</sub>. Illustration nano-ridge cross section. e. Images of directional motion of coalescing condensate drops on butterfly wings.

## 1.2 Summary and Objectives

As previously stated droplet motion is essential in order to realize the potential heat transfer rate increases afforded by dropwise condensation. The aforementioned studies provide several examples of methods that have been shown to be effective promoters of dropwise condensation and/or directional droplet and condensate motion. The work presented in this dissertation seeks to expand on this area of research by observing the condensate dynamics and effects on heat transfer of both nano-structured superhydrophobic coating with improved durability and scalable application techniques, as well as hydrophobic and hydrophilic grayscale lithography fabricated micro-ratcheted silicon surfaces designed to promote directional droplet and condensate motion.

The key objectives of this study include:

- Development of a durable and scalable nano-textured superhydrophobic coating suitable for common condenser tube materials.
- Fabrication of asymmetric ratchet microstructures on silicon substrates in various sizes ratchet profiles and surface wettability conditions.
- Measurement of the effect the above surface modifications have on condensation heat transfer, droplet mobility and condensate dynamics.

## Chapter 2

### Fabrication of Test Surfaces and Experimental Facility

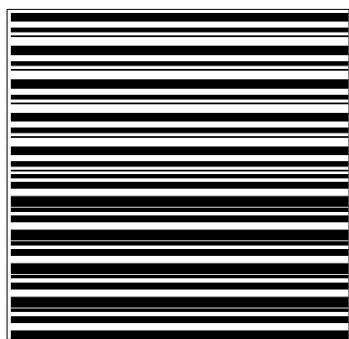
Much of the equipment and all the test surfaces used in this study were custom designed and fabricated in house. This chapter details the fabrication and characterization of these surfaces and provides a thorough description of the design, construction and assembly of the equipment used for experiments. The procedure used for performing experiments is provided in this chapter as well.

#### **2.1 Test Surface Fabrication**

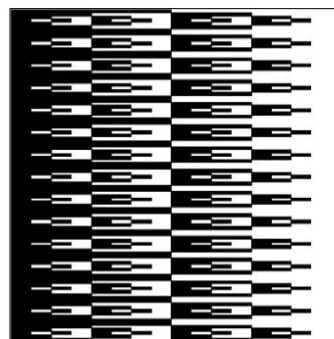
Several types of test surfaces were prepared for this study. Preliminary tests were performed on flat silicon surfaces with patterned wettability. Hemi-cylindrical surfaces, constructed from several condenser tube samples of various materials employed in power generation condensers were used to test the durability and effectiveness of a superhydrophobic surface treatment currently used to protect electronic devices on geometry and materials more commonly used in industrial applications. And asymmetric saw-toothed ratcheted silicon surfaces in several configurations were developed to test the ability of a condenser surface with this type of topography to promote condensate motion in a preferred direction as surfaces with asymmetric ratcheted topography have been shown by others to be effective at promoting directional fluid motion in Marangoni convection [10], Leidenfrost droplets [11] and pool boiling [12].

### 2.1.1 Flat Silicon Surfaces

The first set of test surfaces made for this study were flat silicon surfaces with patterned wettability. The wettability patterning was accomplished by selectively applying a non-wetting or hydrophobic coating over the more wettable or hydrophilic substrate surface. The patterns were designed to manipulate condensate droplet growth and promote droplet motion through force imbalances created by surface tension differences around the contact line of the droplet on the surface. The first two surface patterns were called the “1-D” and “2-D” patterns. They were named such because the 1-D pattern only varies in one dimension and the 2-D pattern varies in two dimensions. Their layout is shown below in Figure 2.1. These patterns both featured an uneven distribution of hydrophilic and hydrophobic space (white =non-wetting, black=wetting). It was hypothesized that droplets forming on the surface would have a tendency to grow or move towards the side of the surface with more wetting area. No motion or preferential growth direction was observed



1-D Pattern



2-D Pattern

Figure 2.1: Layout of 1-D and 2-D flat silicon test surface wettability patterning used for preliminary testing. (white =non-wetting, black=wetting)



however, droplets that formed on these surfaces did exhibit very distorted shapes (discussed in more detail in Appendix B) due to contact line pinning at the boundaries between the coated (non-wetting) and uncoated (wetting) portions of the surface.

Another set of flat silicon test surfaces were created to take advantage of the distorted shapes that the droplets on these surfaces demonstrated. Larger 25mm square surfaces were made for use in this study and smaller 10mm square surfaces were made for use by project partners at the University of California, Davis. Most of this set of surfaces featured a central hydrophobic island with eight hydrophobic spokes extending from the island toward the periphery of the surface in a radial pattern. Five configurations of this pattern along with a pattern consisting of an array of smaller radial patterns were created and tested. A non-radial pattern composed of alternating wedges of hydrophilic and hydrophobic area was also created and tested. Layout schematics of these surfaces are shown in Figure 2.2.

The five configurations of the base radial pattern varied in central island size and radial spoke thickness while keeping the overall surface area 70% hydrophilic, 30% hydrophobic. These patterns were designed to encourage droplets on the surface to grow preferentially toward the edges of the surfaces by being pinned by the hydrophobic island and spokes from growing toward the center of the surface. It was hoped that this type of growth would eventually lead to the droplets removing themselves from the surface and thereby boosting heat transfer rates.

The pattern featuring an array of smaller radial patterns was developed by repeating a smaller version of one of the patterns described in the previous paragraph eight times in the same amount of area and adding an internal border of the hydrophobic coating. This surface layout was created to examine the effects of a radial type pattern on smaller droplets closer to the edge of the surface. It was hoped that this surface would exhibit more frequent removal of smaller droplets near the edges of the surface.



6mm Square Island



7mm Square Island



8mm Square Island



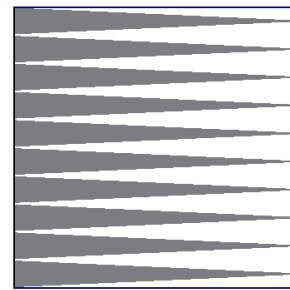
9mm Square Island



10mm Square Island



Array of Radial with Internal Border



Alternating Wedges

Figure 2.2: Layout of surface wettability patterning for second set of flat silicon test surfaces. (white = hydrophobic, gray= hydrophilic)

The wedge pattern consisted of 20 alternating hydrophilic hydrophobic  $5.15^\circ$  wedges and like the 1-D and 2-D surfaces was characterized by an uneven distribution of hydrophilic and hydrophobic area. This surface differs from the 1-D and 2-D surfaces in that a droplet growing on a surface with this pattern does not have to cross the boundaries of hydrophilic and hydrophobic areas to grow toward the hydrophilic side of the surface.

The aim of tests on these surfaces was to determine whether the distorted shape of the droplet could be used to promote growth in a preferred and predicted direction or to create an internal pressure difference (due to differing radii from one end of a drop to the other) sufficient to cause droplet motion. While, these surfaces also proved effective at manipulating the shape of a droplet as it grew, there was little evidence that they reliably promoted fluid motion or increased condensation performance. Since these surfaces didn't exhibit much interesting behavior and they were not of foremost interest to project sponsors or my research very little further testing on these surfaces was performed. Details on the tests that were performed can be found in Appendix B. These surfaces did however, provide good practice in standard lithography processes and using the experimental facility and may be of interest to future studies, as modifying the patterns used may bring more dramatic results, therefore a description of the methods used to fabricate them is provided below.

The substrates used were  $500\mu\text{m}$  thick 100mm single side polished p-type {100} silicon wafers. These wafers were placed in an atmospheric oxidizing oven at  $1200^\circ\text{C}$  for four hours to grow a layer of silicon oxide. This layer of silicon oxide is necessary as it provides the wafer with a uniform hydrophilic surface. AZ 5214-IR photoresist was spin applied to the polished side of the wafer at approximately 2000 rpm leaving a photoresist

thickness of roughly 2 microns. The wafer was then placed on a hot plate at 100°C for 60 seconds to soft bake (harden) the photoresist. After loading the wafer and mask containing the desired surface patterning into a mask aligner, the photoresist on the wafer was exposed to UV light, softening the photoresist under the clear portions of the mask where the less wetting coating was desired. Immersing the wafer in a 1:1 solution of AZ Developer and deionized water for 60 seconds while agitating the solution by gently moving the wafer up and down and side to side removed the softened portions of photoresist. The wafer was then thoroughly rinsed with deionized water and blow dried with compressed air.

The desired hydrophobic surface coating was a PTFE like substance called Perfluorocyclobutane ( $C_4F_8$ ) which was vapor deposited in a Deep Reactive Ion Etching (DRIE) machine. Once the wafer was loaded into the machine's vacuum chamber the pressure was pumped down to 20 mTorr and 84 Sccm of  $C_4F_8$  was allowed to flow into the chamber for two minutes, depositing the coating on the entire wafer. After removing the wafer from the DRIE machine, it was bathed in AZ 400T stripper which removed all of the remaining photoresist and the  $C_4F_8$  that had been applied on top of it, leaving the  $C_4F_8$  coating only in the areas where the photoresist was removed during the exposing and developing steps. The wafer was again thoroughly rinsed in deionized water and blow dried with compressed air before dicing into 25mm (all but wedged pattern) and 10mm (wedged pattern only) square dies around the desired coating patterns. Images of the completed test surfaces can be found in Figure 2.3.

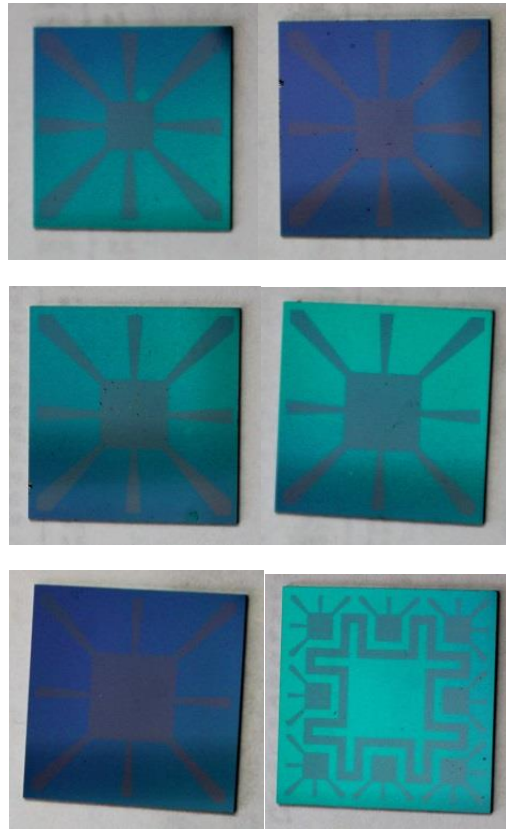


Figure 2.3: Full set of 25mm radial patterned biphilic test sections. The blue/green portions are hydrophilic silicon dioxide the dull gray portions are hydrophobic polymer.

The contact angle of the hydrophilic and hydrophobic portions of the surfaces was determined by depositing a small drop in a wetting area and another in a non-wetting area and taking still images of the drops that were then measured using National Instruments Vision Assistant software. The contact angle of deionized water on the hydrophilic areas was approximately  $70^\circ$  and the contact angle of deionized water on the hydrophobic areas was approximately  $110^\circ$ . Contact angle measurement images are given in Figure 2.4.

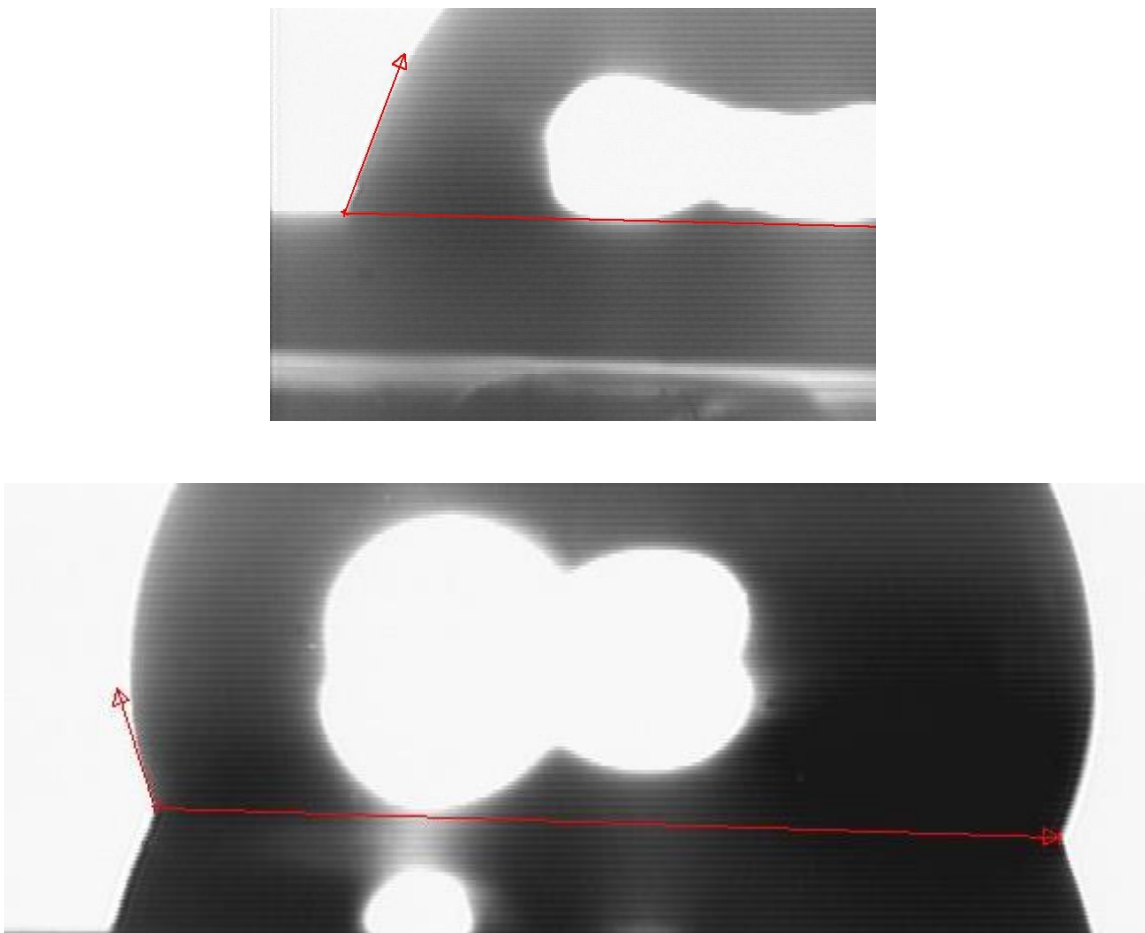


Figure 2.4: Images used for contact angle measurement on flat silicon test surfaces with measurement marks shown. Above: droplet on hydrophilic areas. Below: Droplet on hydrophobic areas.

### **2.1.2 Hemi-cylindrical Condenser Tube Test Surfaces**

Hemi-cylindrical test surfaces were prepared using Southern Company-provided one-inch-diameter condenser tube samples in the following materials: Titanium, Admiralty brass, SEA-CURE and Cupronickel. Flat and hemi-cylindrical control surfaces were machined from 304 stainless steel stock. These surfaces were then coated with customized superhydrophobic films through a modified vapor deposition process. The fabrication of the substrates as well as coating development and application is described below.

#### **2.1.2.1 Hemi-cylindrical Surface Substrate Fabrication**

To produce solid test surfaces, capable of conducting heat, the following fabrication sequence was followed. Aluminum support mandrels were fabricated to match the inner diameter for each tube sample. These were pressed into the tube samples to support them radially and axially to allow the tubes to be clamped and machined like solid round rods. The tube and mandrel assemblies were then machined into one-inch long half cylinders, resulting in a 25mm x 25mm base area matching the cooled surface footprint in the experimental facility (described in section 2.2). The remaining mandrel material was then removed. Lead was cast directly into each half tube section. After cooling, the lead casting and tube section were separated and then permanently joined using silver based thermal interface material and epoxy. Additional flat and half round control surfaces were produced using 304 stainless steel stock machined to the desired dimensions.

After fabrication was completed, surface treatments were applied in an RPX-540 Vapor Deposition System. The system deposits customized nano-composite structures using a hybrid VPD/ALD (vapor phase deposition/atomic layer deposition) process. Up to five precursors can be sequentially applied to create a variety of specialty films for each specific application. All the precursors are heated to create a reservoir of chemical vapor and their introductory timing, dose, and order is controlled by a LabVIEW-based software system with automatic process operation.

A typical coating process is as follows. Incremental layers of Al<sub>2</sub>O<sub>3</sub> nanoparticles are accumulated by repeating VPD cycles, followed by a 600-cycle pyridine-catalyzed silica protection film and a final perfluorinated silane finish layer for superhydrophobicity (contact angle greater than 150°).

#### **2.1.2.2 Superhydrophobic Coatings for Hemi-Cylindrical Test Surfaces**

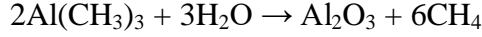
Several coating methods have been studied in recent years. Technologies like CVD (Chemical Vapor Deposition) and ALD (Atomic Layer Deposition) enable nanoparticle film deposition with good uniformity and precise control. Primary scientific merits include the improvement of the process efficiency while maintaining the coating quality. A recent improvement on the CVD process includes introducing varying functional end-group terminated silanes to increase the reactivity of the CVD precursors. A modified VPD (Vapor Phase Deposition) apparatus has the ability to produce aluminum oxide nanoparticles from a gas phase reaction which can then be anchored and coated by the SiO<sub>2</sub> and hydrophobic layers. Superhydrophobic coatings have the potential to revolutionize the condensation process. Since different application environments



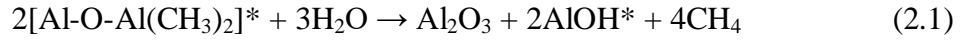
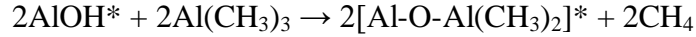
emphasize corresponding film properties, VPD coated substrates are designed for durability, water-resistance performance, electrical properties, thermal properties and other properties based on process requirements.

Two different coatings were produced for condensation and durability evaluation, both were based on a superhydrophobic coating, called Repellix, developed for silicon substrates and currently used to inhibit wetting on microprocessors in portable electronic devices. Repellix is a nanoparticle coating based on a VPD process which uses sub-atmospheric pressure gas phase flow-through the reactor. This coating scheme is highly suited for large batch processes and can be easily scaled. The unique nanostructure of the film is created using a cross between ALD-based surface limited reactions and CVD-based condensation process conditions in which super-saturated vapor conditions are created directly over the targeted coating surface. During the process, a metal organic precursor is oxidized in such a way that the required film roughness and aerial coverage for superhydrophobicity is obtained. Subsequently, the nanoparticles are immobilized into a silica-based matrix to improve the film's durability. It was observed that the use of alternating between deposition/immobilization and adhesion steps similar to conventional ALD resulted in films with better uniformity and durability compared with non-layered deposited films. The final step in the process sequence employed is a surface modification treatment with a perfluorinated agent to create a surface with low energy state over entire film.

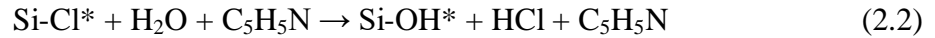
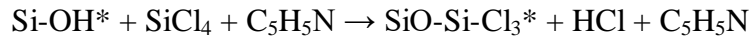
The base nanostructure of alumina is formed by the following oxidation reactions (asterisk indicates surface-bound species):



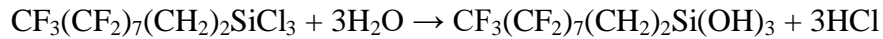
or by



Since the mechanical durability of this nanoscale topography is a major challenge, a pyridine catalyzed process is introduced to strengthen the film and increase its durability:



Finally a perfluorinated agent, Phobix, is applied to increase the surface superhydrophobicity:



While Repellix displays adequate durability on the silicon substrates for which it was developed, when applied to metallic substrates it is very fragile and can be removed from the surface with a very light wipe with a fingertip. The two coatings developed from Repellix for condensation and durability evaluation are modifications to the original

Repellix formulation (detailed in Table 2.1) targeting two potential weaknesses of the Repellix coating on metallic substrates.

The first modification targeted the potentially weak initial bonding between metal and alumina nanoparticles possibly due to low density of hydroxyl group on metal surface. To correct this, a thin layer of silica was added before the alumina layer, which increases the hydroxyl group density and results in stronger surface bonding between nanoparticles. This formulation is called modified Repellix and formulation details can be found in Table 2.2.

The second modification to Repellix is called Repellix 2.0 and was developed to increase the durability of the coating nanostructure by enhancing the robustness of the silica layers. This formulation replaces the Linkerrix+Pyridine reaction with an HMDSO (hexamethyldisiloxane)+O<sub>2</sub> plasma to deposit a thin oxide, which results in much thicker deposited silica layers making the nanostructure more durable. Details for this formulation can be found in Table 2.3.

The contact angles on modified Repellix and Repellix 2.0 coated surfaces are 120° and 151° respectively. More discussion on this topic including images can be found in section 3.1.

Schematics of the coating layers for Repellix, Modified Repellix and Repellix 2.0 are provided in Figure 2.5 and an image of all the hemi-cylindrical test surfaces made is provided in Figure 2.6.

Table 2.1: Repellix process parameters

Deposited Film (Each Cycle)	Chemical partial pressure used for reactions (mTorr)					Typical Reaction Time (secs)	Number of Cycles
	TMA	Zorrix	Linkerrix	Pyridine	Phobix		
Rough Al <sub>2</sub> O <sub>3</sub>	300-400	200-300				30	4
Catalyzed Silica		200	200	100		10	600
Hydrophobic SAM		1000			250	300	2

Table 2.2: Modified repellix process parameters

Deposited Film (Each Cycle)	Chemical partial pressure used for reactions (mTorr)					Typical Reaction Time (secs)	Number of Cycles
	TMA	Zorrix	Linkerrix	Pyridine	Phobix		
Catalyzed Silica		200	200	100		10	50
Rough Al <sub>2</sub> O <sub>3</sub>	300-400	200-300				30	4
Catalyzed Silica		200	200	100		10	600
Hydrophobic SAM		1000			250	300	2

Table 2.3: Repellix 2.0 process parameters

Deposited Film (Each Cycle)	Chemical partial pressure used for reactions (mTorr)				
	TMA	Zorrix	O <sub>2</sub>	HMDSO	Phobix
Rough Al <sub>2</sub> O <sub>3</sub>	300-400	200-300			
Plasma Enhanced Silica			40	160	
Hydrophobic SAM		1000			250

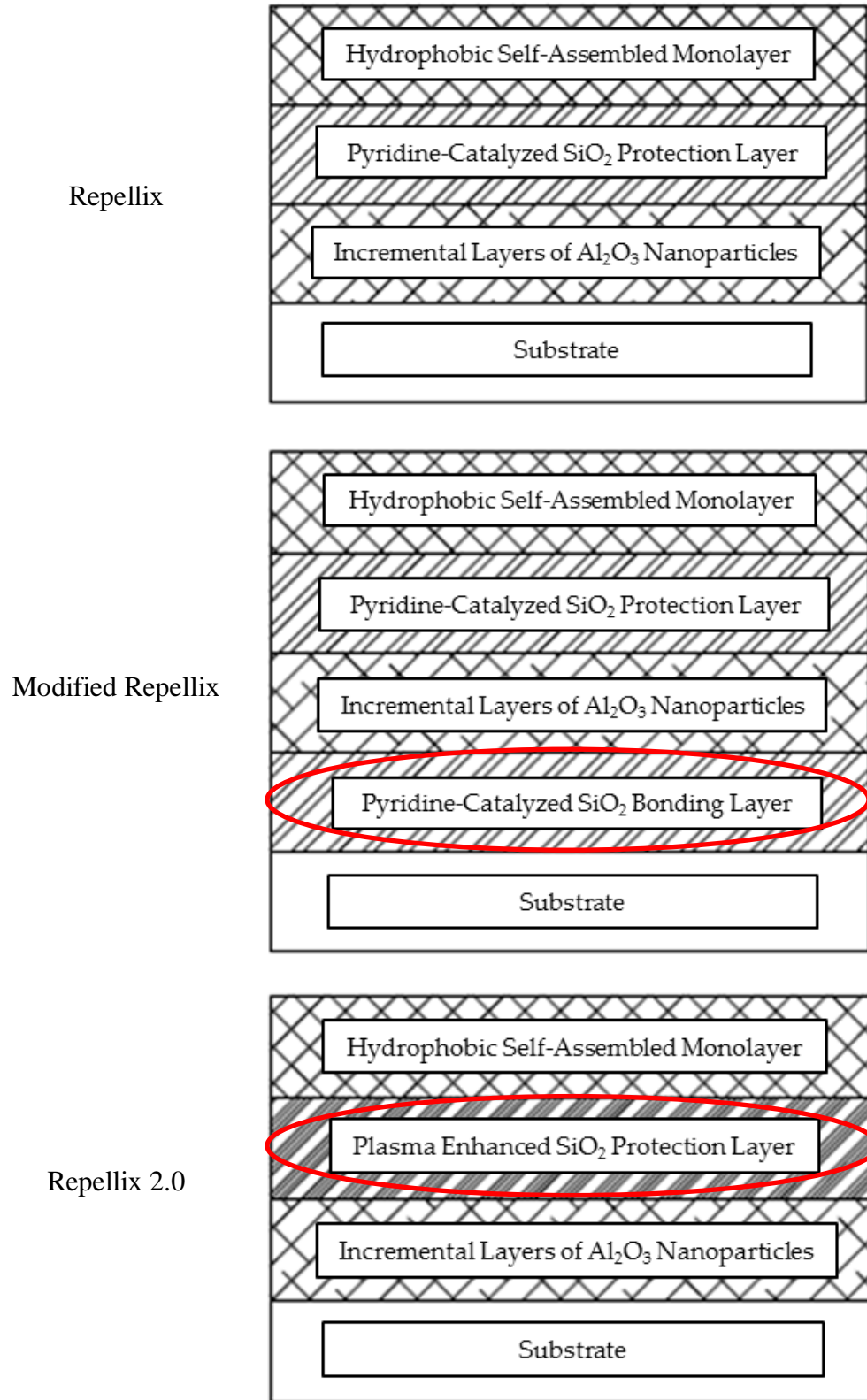


Figure 2.5: Schematics of coating layers for hemi-cylindrical test surfaces with modifications from original Repellix formula circled in red.

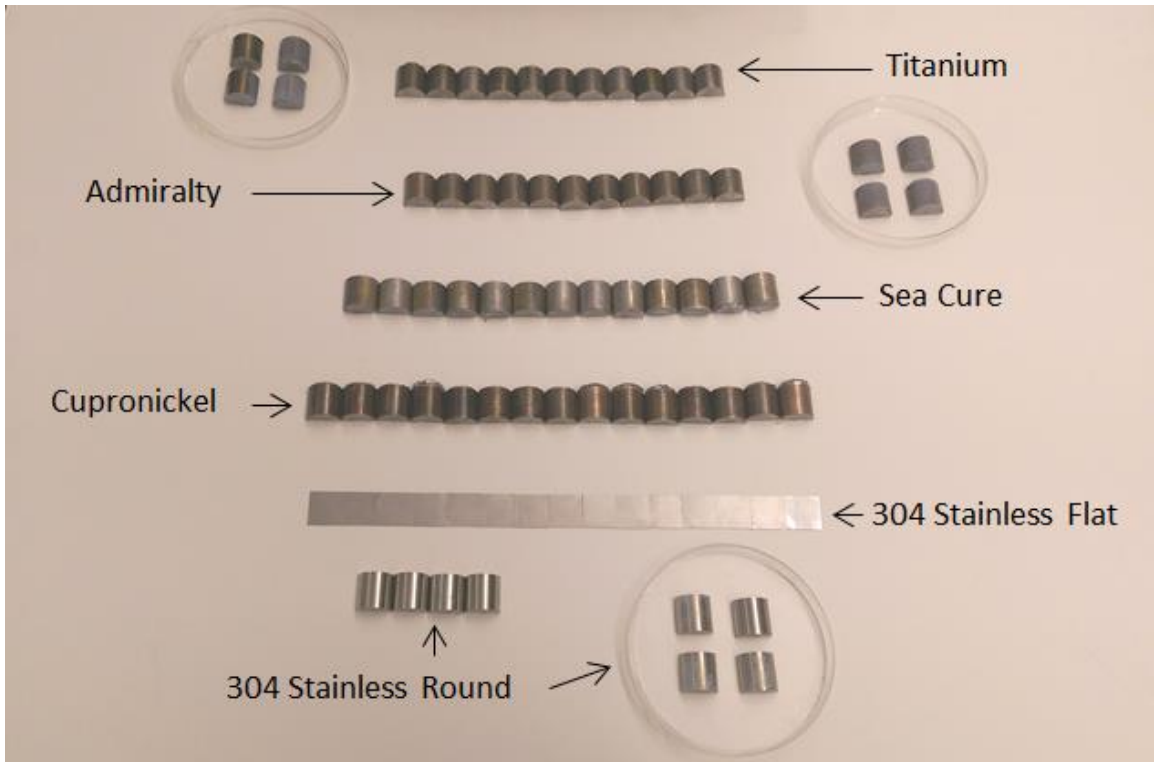


Figure 2.6: Complete set of all hemi-cylindrical condenser tube test surfaces and solid stainless steel control surfaces.

### 2.1.3 Asymmetric Saw-Toothed Ratcheted Silicon Surfaces

Several configurations of asymmetric saw-toothed ratcheted silicon test surfaces were fabricated for this study and for use by project partners at University of California, Davis. These configurations featured three different pitches or ratchet widths—100 $\mu\text{m}$ , 250 $\mu\text{m}$  and 500 $\mu\text{m}$ —three ratchet angles—approximately 30°-60°-90°, 18°-44°-118° and 9°-26°-145°—and three surface wettability conditions—hydrophilic, hydrophobic and biphilic. The ratchet features were formed on 500 $\mu\text{m}$  thick 100mm single side polished p-type {100} silicon wafers using grayscale lithography and Deep Reactive Ion Etching (DRIE) as in [15]. An additional 500 $\mu\text{m}$  thick 100mm single side polished p-type {100} silicon wafer was bonded to the back of the wafer containing the ratchets due to concerns for the fragility of the wafers after the etching process.

Grayscale lithography is a process in which photoresist on a wafer is selectively exposed and developed to give it a gradient thickness by using a grayscale optical mask that has patterns ranging from completely transparent to completely opaque. Exposing photoresist to UV light through such a mask causes the light to penetrate the photoresist to differing depths corresponding to the amount of light allowed to pass through the mask at any given location on the wafer (fully opaque portions have no light penetration, fully transparent portions receive the maximum light penetration). These differences in light penetration during exposure create differences in photoresist thickness after developing [50-52].

A company named Jenoptic performed the photoresist application and grayscale exposure and developing for the wafers used to fabricate the ratchet test surfaces used in

this study. The photoresist used was AZ4330. The layout provided to them detailing our requirements and Jenoptic's documents providing measurements on the final photoresist thickness profile are given in Appendix C and D respectively.

As can be seen in the photoresist thickness measurement documents provided by Jenoptic, after exposing and developing the photoresist no silicon was exposed at the ratchet valleys. In order to insure that etching would start evenly across the surfaces during DRIE, the wafers were processed through an oxygen plasma de-scum sequence in which the photoresist on a wafer is more or less uniformly reduced in thickness until silicon is exposed at all ratchet valleys. This is a lengthy process as it requires frequent process stops to check for photoresist presence at ratchet valleys after every few minutes of de-scum.

Once silicon is exposed at the valleys of all the ratchets on a wafer, the wafer is then ready for DRIE. DRIE processes are a cycle of two alternating steps, etching and passivation. During an etching step  $O_2$  and  $SF_6$  gasses flow over the wafer in a vacuum chamber etching both photoresist and silicon. Adjusting the ratio of these gasses changes the etch selectivity (rate of silicon etch to photoresist etch) of the process. During a passivation step the wafer is exposed to  $C_4F_8$  gas which deposits a PTFE like protective coating on the side walls of the freshly etched surface to prevent undercutting during the next etching step.

All DRIE was performed using an STS ICP etcher. While the first wafer was being etched it broke inside the machine because it was too thin at the ratchet valleys to support its own weight. All subsequent wafers were bonded to a second 500 $\mu$ m thick



100mm single side polished p-type {100} silicon wafer using a 20 $\mu$ m thick, silver impregnated thermally conductive film called WaferGrip made by Dynatex before etching. The bonding is a simple process—first the bonding surfaces are thoroughly cleaned and dried, then the film is sandwiched between the wafers and they are heated for 30 seconds on a hot plate at 100°C which softens the film and causes it to adhere to both wafers.

All wafers with 30°-60°-90° triangle ratchet profiles were etched using the same DRIE process. The duration of the process was different for each ratchet pitch as it was adjusted based on the required depth of the ratchets. Wafers with the shallower ratchet profiles were produced from 250 $\mu$ m ratchet pitch wafers by adjusting the etch selectivity. The etch parameters for these processes are given in Table 2.4. Figure 2.7 is an illustration of some of the geometric parameters presented in Table 2.4.

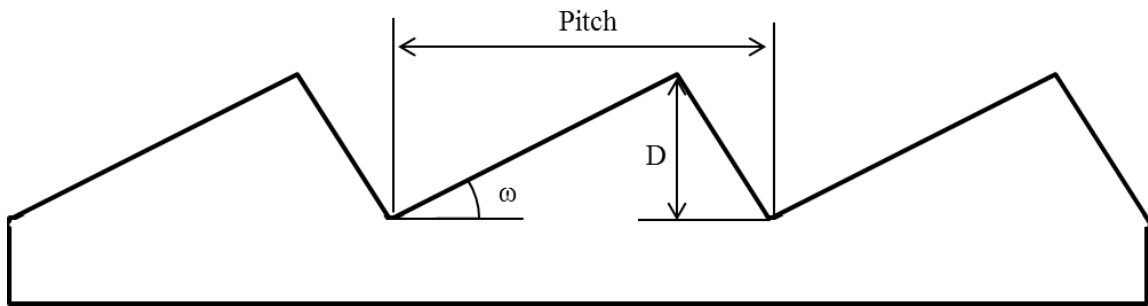


Figure 2.7: Illustration of some geometric parameters presented in Table 2.4

Table 2.4: DRIE process parameters and resulting geometric parameters					
Etching Gas Flow Rate O <sub>2</sub> /SF <sub>6</sub> (SCCM)	Etch/ Passivation Step Duration (s)	Angle $\omega$ (deg)	Depth D ( $\mu$ m)		
			100 $\mu$ m pitch	250 $\mu$ m pitch	500 $\mu$ m pitch
53/100	13/3	30	37	101	212
80/100	13/3	18	N/A	62	N/A
100/100	13/3	9	N/A	30	N/A

Since the pitch (or width) of the ratchets was set by the photoresist patterning, the only measurement that was needed to confirm that the ratchets had reached the desired profile was the depth. This was obtained using a microscope to measure the difference in height between the valleys and crests of the ratchets on a wafer. After the ratchet profiles were formed, the wafers were diced into 25mm square and 5mm by 10mm test surfaces. The smaller surfaces were for use by our project partners at U.C. Davis. The 25mm square surfaces feature a 20mm by 25mm ratcheted area and two 2.5mm by 25mm strips of flat un-etched area running parallel to the ratchets on two sides of the surface as shown by the drawing in Figure 2.8.

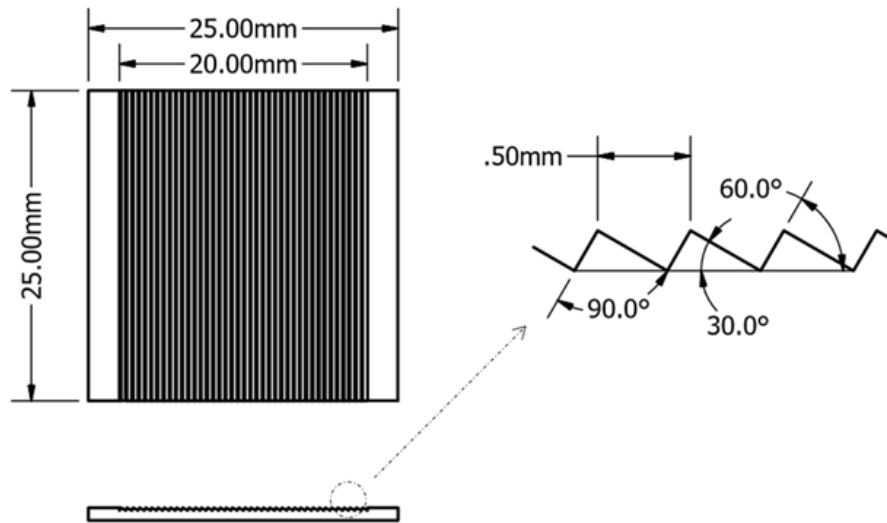


Figure 2.8: Illustration of 25mm square asymmetric ratchet test surface. 500  $\mu$ m pitch shown.

After dicing, several units of each ratchet surface type were fully coated with Rust-Oleum's® NeverWet multi-surface liquid repelling treatment, which is a two part hydrophobic coating that was chosen for its availability, low cost and good performance. This coating imparts a small scale rough texture to the smooth silicon and produced a static contact angle in deionized water of approximately  $140^\circ$  on these silicon surfaces (the static contact angle of deionized water on uncoated silicon surfaces was measured to be approximately  $70^\circ$ ). Some of the  $500\mu\text{m}$  ratchet pitch test surfaces were coated by spraying the surface at a  $45^\circ$  angle which allowed the long slopes of the ratchet to shield the short slopes from the coating as shown in Figure 2.9. This creates a biphilic surface that has hydrophobic properties on the long ratchet slopes and hydrophilic properties on the short slopes.

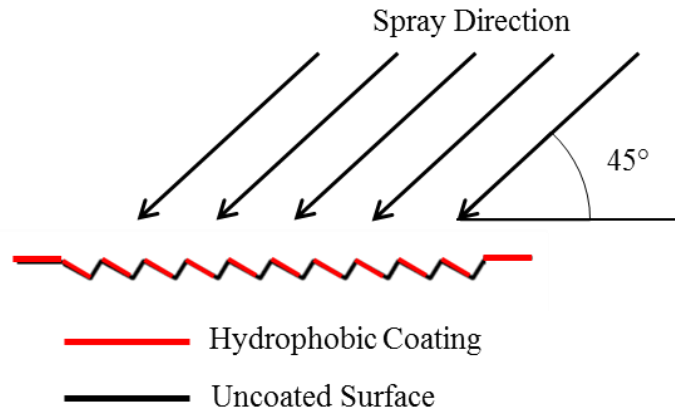


Figure 2.9: Schematic of biphilic asymmetric ratchet test surface coating application.

The fabrication steps for these asymmetric saw-toothed ratcheted silicon surfaces are depicted in Figure 2.10. Images of wafers at several process stages are shown in Figure 2.11. A side view of a fully processed  $500\mu\text{m}$  pitch ratchet test surface is shown in Figure 2.12.

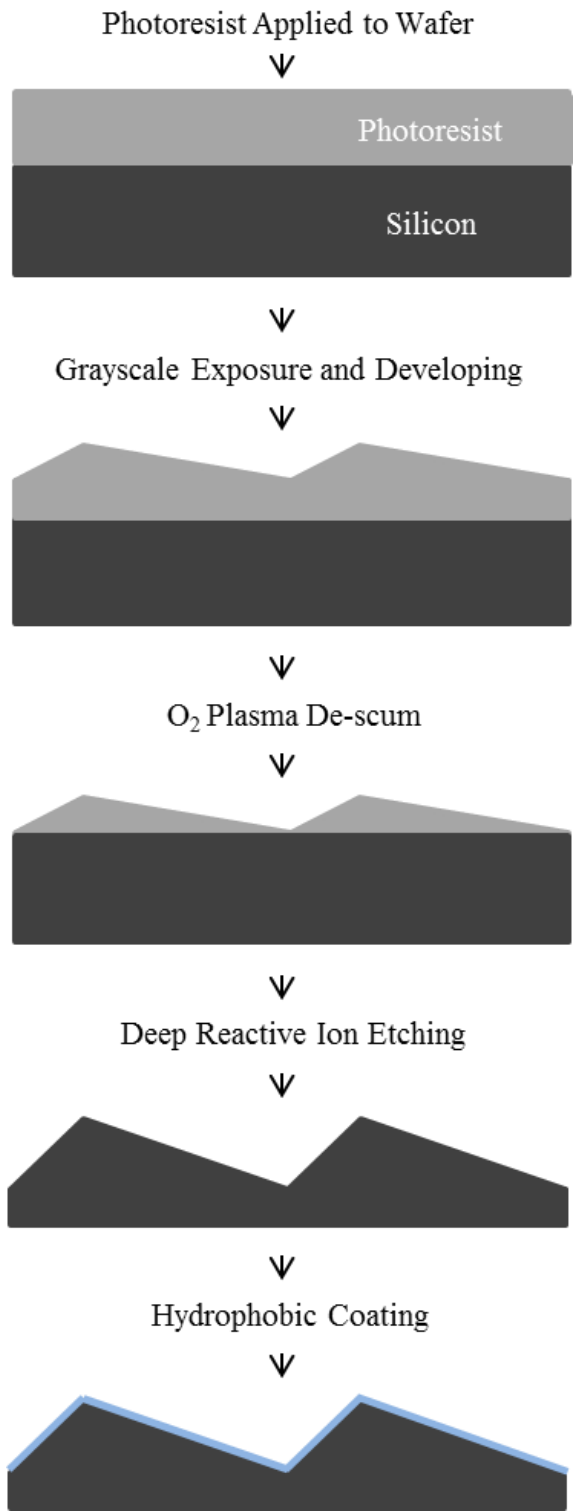
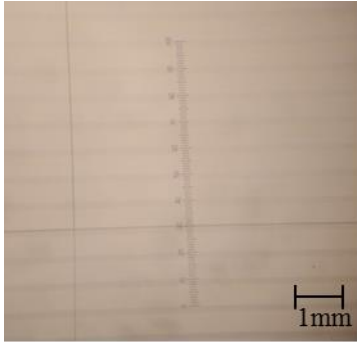


Figure 2.10: Illustration of fabrication steps required to form asymmetric ratchets in silicon.



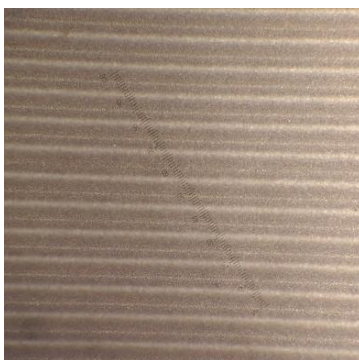
Wafer before processing. Gray scale photoresist patterning is apparent. The darker horizontal bands are the short side of the ratchet and the lighter horizontal bands are the long side of the ratchet. The sharp black lines are the boundary of individual projections of the 5mmx5mm pattern tile used in the photoresist developing process. They are only a remnant of the previous process and disappear during plasma de-scum.



Edges of a patterned portion of a wafer during plasma de-scum. As the photoresist gets thinner the non-uniformity in photoresist thickness refracts light like a prism creating the colors shown. The end of a ratchet trough highlighted in the red box shows where bare silicon has started to show through the photoresist. More processing is required to expose bare silicon uniformly across the length of all of the troughs on the wafer.



Patterned section of a wafer after all stage one processing is complete. The colored bands are where photoresist remains on the wafer and refracts light. The white bands are bare silicon. Now that silicon is exposed uniformly across the patterned section this wafer is ready for stage two processing: Deep Reactive-ion Etching (DRIE)



Wafer after DRIE. The brighter bands are the ratchet valleys and the wider gray bands are the ratchets themselves. The gray bands consist of a darker and a lighter portion; these are the two slopes of the ratchet. The darker and thinner portion is the steep and short slope. The lighter and wider portion is the shallow and long slope.

Figure 2.11: Microscopic images of wafer at several stages of processing. Top to bottom: Fresh grayscale photoresist before de-scum, During de-scum, De-scum completed, DRIE completed.

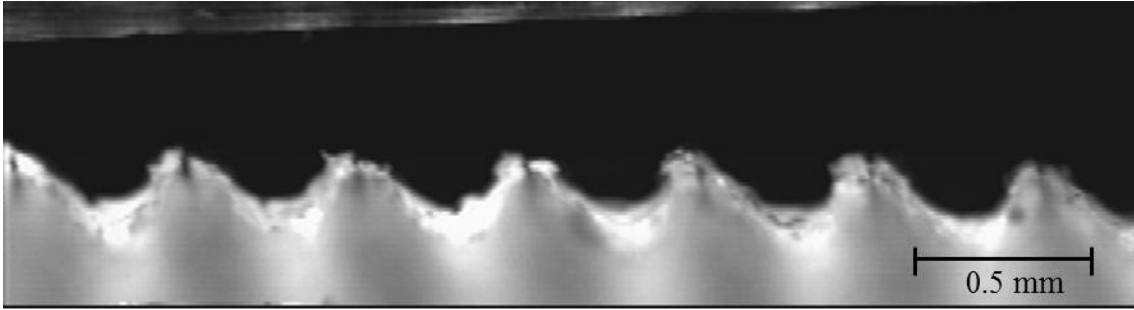


Figure 2.12: Side view of a fully processed 500µm pitch ratchet test surface. Camera is focused on far edge of the surface so the profile can be seen. Some upset or raised material (burr) from the dicing operation can also be seen between the ratchets.

Flat silicon control surfaces were also created for this study by simply dicing extra wafers to the correct size and applying the NeverWet coating to some. An image of the contact angle measurement on this type of surfaces is given in Figure 2.13.



Figure 2.13: Image used for contact angle measurement on NeverWet coated silicon test surfaces with measurement marks shown.

## 2.2 Experimental Facility

All condensation experiments were performed in a custom designed and fabricated condensation chamber. This chamber provides a controlled atmosphere for observing condensation phase change. This, along with a boiler (to supply vapor), a vacuum pump (to remove non-condensable gasses before experiments), and data acquisition system constitutes the main components of the experimental facility.

Other notable features of the original experimental facility include:

(Note: A few alterations were made to this facility as the project matured. These will be described in subsequent paragraphs.)

- A thermoelectric cooler is used to remove heat from the condensation chamber through the heat flux sensor/measurement head and promote condensation on the test section. The cooler is matched with an aluminum heat sink and an electronic fan to increase its performance and life.

- ITO (Indium Tin Oxide) heated windows are used to maintain a clear view of the test section as they are fully transparent non-condensing surfaces. Another benefit to using heated windows is that the power to the windows can be controlled and they can be used to help maintain the temperature in the condensing chamber. The windows are 6in. x 6in. and are placed perpendicular to each other on three sides. These windows not only allow video to be captured from the top and sides simultaneously with multiple cameras but also allow flexibility in lighting configurations. The test section can be lighted from a

window perpendicular to the camera view or even from the same window that the camera is using because of the window's large size.

- The Optical Prism allows a camera mounted horizontally to capture video through the condensation chamber's top window. This allows for quick transitions from a side view to a top view using one camera.

- A pneumatic vibration isolating system is employed to reduce the effect of building vibrations on the formation and movement of condensate. The system consists of four Newport SLM-1A vibration isolating feet each rated for 100lb.

- All vapor tubes are heated to prevent condensation inside the tubes which insures that high quality vapor is delivered to the condensation chamber.

- Heat flux meter/ measurement head is used to gather heat flux and surface temperature data. Length meters are attached near the test section, oriented such that one can be clearly viewed from each window to facilitate size measurements while processing captured video.

- Thermocouples and a pressure transducer are used to gather temperature and pressure data from the boiler and condensation chamber.

After gaining some familiarity with the project, three notable improvements to the experimental facility were implemented. The first was a new boiling chamber. The boiling enclosure adapted from a previous boiling project developed a leak from one of its windows so a new boiling chamber without windows, ports for measurement equipment or a removable lid was fabricated. The new boiling chamber consists of a 12



inch section of 4 inch diameter stainless steel pipe with two threaded end caps. Since there are far fewer connection points than before, and all interfaces are threaded, arresting leaks was a very quick process and the experimental facility holds vacuum much better than it did before.

The second notable improvement was switching from thermoelectric cooling to chilled water cooling. The thermoelectric cooler previously used only produced very modest heat fluxes. In an attempt to expedite condensation activity, a more aggressive water cooling system was installed. A custom cold plate was designed to fasten to the bottom of the measurement head where the thermoelectric cooler was previously affixed. Chilled water is pumped through the cold plate to extract heat from the condensation chamber through the measurement head. This new system can produce heat fluxes that are more than ten times greater than the previous system.

The third and final experimental facility improvement was the addition of a small surface mount thermistor that attaches to the test surfaces to directly measure the surface temperature during experiments. The probe can be seen in the lower left corners of most of the test surface images in later chapters and appendices. Incorporating surface temperature measurement capability into the data acquisition system enabled the evaluation of the thermal resistance between the top-most thermocouple in the measurement head and the top of the test section. This, in turn, enabled the calculation of the surface temperature during the experiment.

All condensation experiment data presented in later chapters of this work was gathered using the improved system. A diagram of the experimental facility is shown in Figure 2.14.

The condensation chamber is fabricated from aluminum plate and features three orthogonally oriented indium tin oxide heated windows (Seaclear Ind. 6 x 6 x 3/8 electrically heated window) that allow visualization of condensate activity, and a measurement head that gathers the data used to calculate heat flux (see subsection below). A pressure transducer (Omegadyne model no. PX319-050A5V) and thermocouple are used to gather environmental data in the condensation chamber and a surface mount thermistor (Omega OL-729) is used to measure the surface temperature of the test surface.

Vapor is produced in a boiler constructed of stainless steel pipe and two endcaps with cartridge heaters inserted from one end. The steam flows into the condensation chamber through a braided stainless steel tube that is wrapped with a rope heater (Briskheat model HSTAT101006) to prevent condensation inside the tube.

A vacuum pump (Welch-Ilmvac Dryfast Ultra 2042) is used to remove noncondensable gases from the condensation chamber and boiler before each experiment. A soft bladder holds the fluid to be used while evacuation takes place.

Heat is extracted through the measurement head to promote condensation on the test surface by a chiller (Neslab Endocal refrigerated circulating bath RTE-4).

Video data of condensate activity is captured using a high speed camera (Phantom v310 or Kodak Motioncorder model 1000) which takes top-view images through an optical prism (Thorlabs PS913-N-BK7 uncoated right angle prism 60mm).

The condensation chamber and other equipment are mounted onto a structure originally built by Thiagarajan [15] for use on a NASA Zero-g flight for microgravity experiments. This structure is constructed from 1 inch square aluminum t-slotted extrusions and was retrofitted with pneumatic vibration isolating feet (Newport SLM-1A) to reduce the effect of equipment and building vibrations on condensate dynamics. The sturdy construction of the structure allowed the entire experimental facility to be tilted during experiments designed to assess the effects of tilt on condensate behavior. Images of the experimental facility fully assembled and installed into this structure are provided in Figure 2.15.

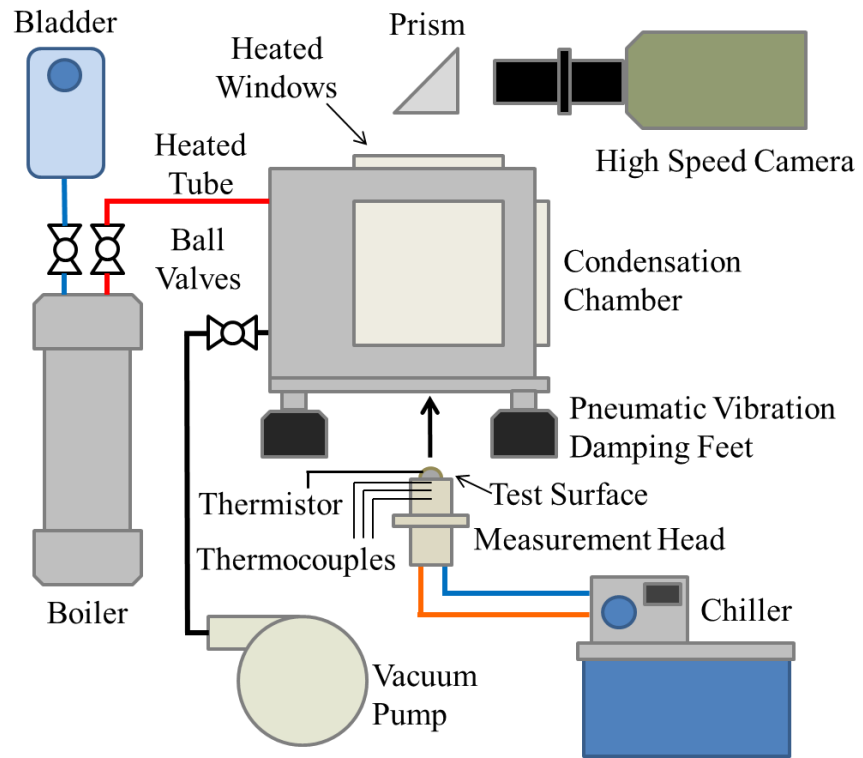


Figure 2.14: Diagram of experimental facility components.

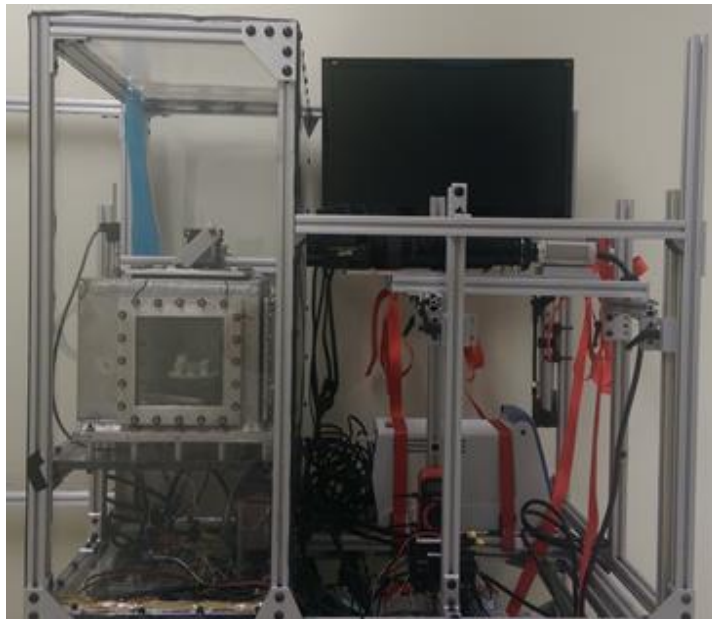
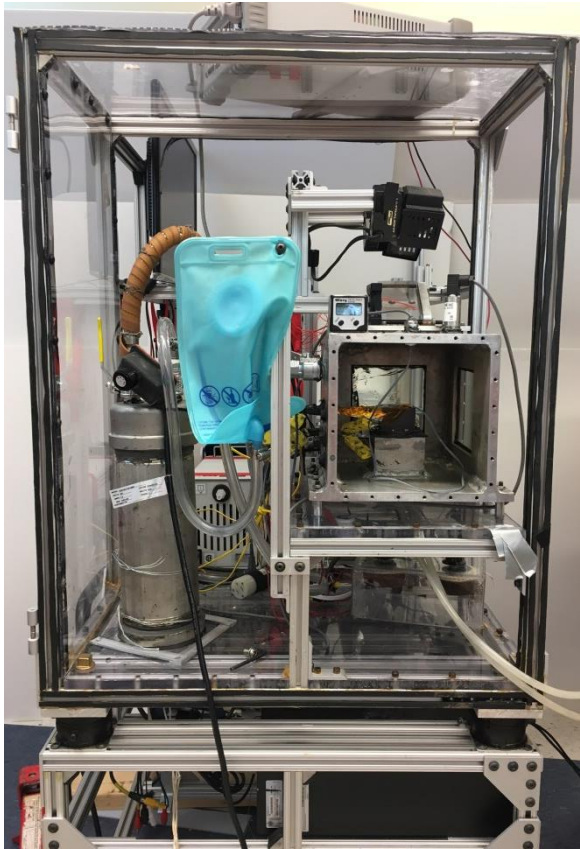


Figure 2.15: Top: Side view of experimental equipment in aluminum structure. Bottom: Front view of experimental equipment in aluminum structure.

### 2.2.1 Measurement Head

The measurement head is an insulated aluminum (previously copper, see below) conductor with a series of thermocouples embedded into a portion with a constant cross section that allows the measurement of a temperature gradient that can be used to calculate heat flux and surface temperature. The end of the metal conductor that extends outside of the condensation chamber is cooled. This extracts heat from the opposite end of the conductor, lowering the surface temperature and promoting condensation inside the vapor-filled condensation chamber. The data collected from the series of thermocouples is used to deduce the heat flux, extrapolate test surface temperatures and calculate heat transfer coefficients.

The previous thermoelectric cooled measurement head had two flaws that were corrected in the current unit. The first was the thermoelectric cooler itself. It provided very moderate heat fluxes at the operating parameters allowed by the condensation system therefore condensation activity was very slow. To increase condensation rates thermoelectric cooling was replaced by a conventional chilled water cooling system that consists of a custom-designed and fabricated cold plate and a Neslab Endocal refrigerated circulating bath (model RTE-4).

The second flaw addressed in the design of the current measurement head was the very small temperature differences measured by neighboring thermocouples in the previous measurement head. This problem was addressed using two strategies; larger distances between thermocouples and a lower conductivity metal core. The previous measurement head core was fabricated from 99.99% pure copper ( $k \approx 400$  W/mK) and the

thermocouples were placed 5mm apart. The current measurement head uses an aluminum core ( $k \approx 170 \text{ W/mK}$ ) with 10mm thermocouple spacing. The new design had provided much larger temperature differences between neighboring thermocouples and therefore more confidence in the collected data. Figure 2.16 shows images of both the current and previous measurement head as well as dimensions of the current measurement head.

The new heat flux sensor also uses a different type of PTFE insulation that is easier to machine, stiffer and allows for the use of O-ring seals, which are the preferred seal for vacuum environments. Photographs of the current measurement head, including the aluminum core before insertion are provided in Figure 2.17.

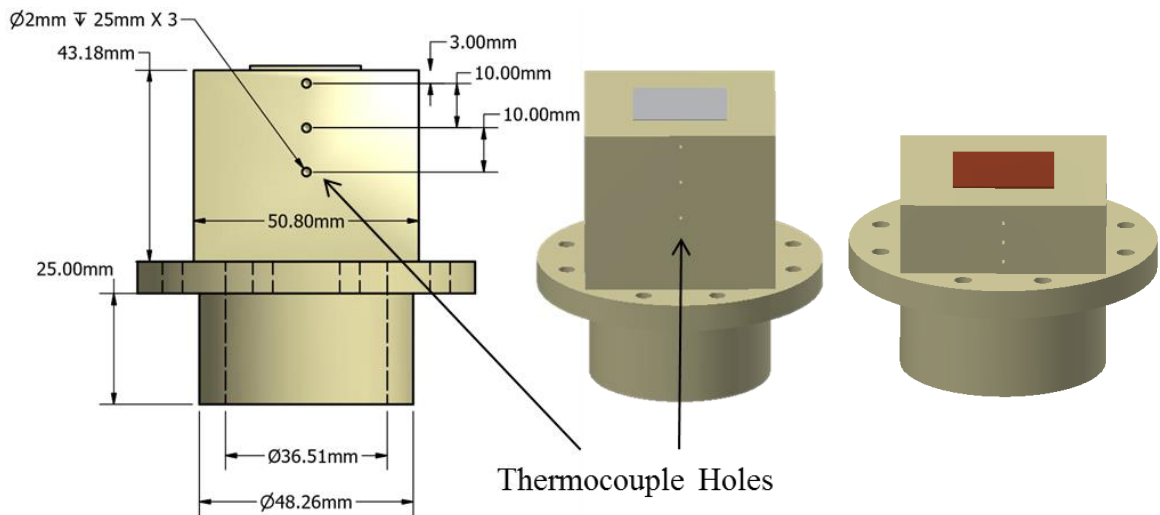


Figure 2.16: CAD images of measurement head. Left: Current longer, aluminum measurement head design. Notice the difference in the distance between thermocouple holes. Right: Previous copper measurement head design.

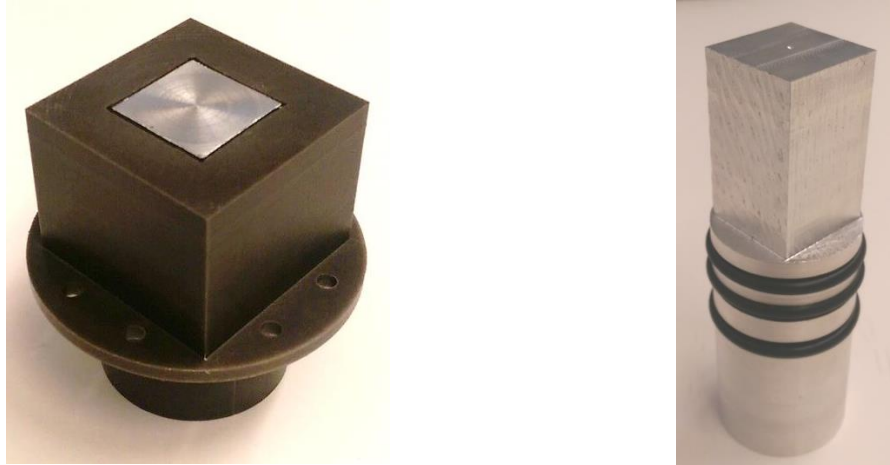


Figure 2.17: Images of current aluminum core measurement head. Left: Current longer, aluminum measurement head with new type of Delrin filled PTFE insulation. Right: Measurement head core before insertion. Three o-rings are used to provide a good vacuum seal.

## 2.2.2 Heat Flux, Surface Temperature, and Heat Transfer Coefficient

### Measurements

Heat flux is calculated using a built-in-function of LabVIEW. The temperatures measured by the thermocouples in the measurement head, along with their distances from the top of the measurement head are fed into the built-in function which uses least-squares to fit a second order polynomial to the measurements for each data collection iteration during an experiment. These polynomial fits give an equation for the temperature distribution in the measurement head's aluminum block. The equations are used to calculate the heat flux (and temperature) at the top of the aluminum block ( $x=0$ ) by taking the derivative of the equation and applying Fourier's Law as shown below:

General equation for temperature distribution:

$$T = Ax^2 + Bx + C \quad T(0) = C \quad (2.4)$$



$$\frac{dT}{dx} = 2Ax + B \quad \frac{dT}{dx}(0) = B \quad (2.5)$$

Fourier's Law:

$$q = -k \frac{dT}{dx} \quad q(0) = -kB \quad (2.6)$$

where  $k$  is the thermal conductivity of the aluminum block

In order to calculate the heat transfer coefficient, the surface temperature must first be calculated. This is done by assuming 1-D steady state conduction through the thermal grease and test surface and calculating the thermal resistance. Thermal resistance values are impossible to calculate without knowing the thickness of the material imposing the resistance. Because there are no reliable method of measuring the thickness of the thermal grease between the test surface and the measurement head, a surface mount thermistor was used to measure the surface temperature under controlled conditions to determine the average thermal resistance of the thermal grease and test surfaces. The calculations are performed as follows:

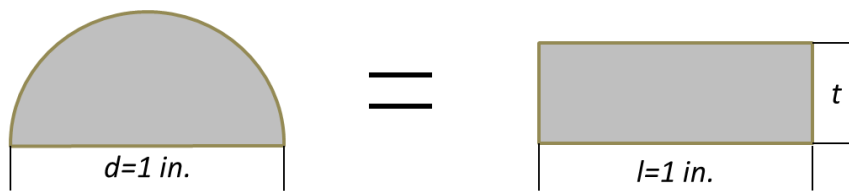
$$\Delta T = (T_{Test} - T_{AL}) = q \times R \quad (2.7)$$

$$T_{Test} = q \times R + T_{AL} \quad (2.8)$$

where  $T_{Test}$  is the temperature of the test surface,  $T_{AL}$  is the temperature of the aluminum block at  $x=0$  (the parameter  $C$ , from the fitted polynomial equation),  $q$  is the heat flux calculated above and  $R$  is the thermal resistance.

For the half-cylinder test sections the surface temperature actually varies with the distance from the surface to the top of the measurement head. An average resistance value was calculated by using a quasi-average surface temperature. This temperature was measured by placing the thermistor on a specific height on the curved surface that was determined to be where the local surface temperature would equal the quasi-average surface temperature. This height chosen was the average thickness of the half-round test surfaces or 0.39". A jig was made to hold the thermistor at this height on the half round test surfaces during experimental runs. Figure 2.18 shows how this value was determined.

The reason the thermistor values aren't used to calculate heat transfer coefficients is that during an experiment when the condensation chamber is filled with hot vapor the thermistor outputs a temperature somewhere between the test surface temperature and the vapor temperature.



$$A = \frac{\pi r^2}{2} = \frac{\pi 0.5 \text{ in.}^2}{2} = 0.3927 \text{ in.}^2$$

$$t = \frac{A}{l} = \frac{0.3927 \text{ in.}^2}{1 \text{ in}} = 0.3927 \text{ in.}$$

Where A is the cross section area and t is the average thickness.

Figure 2.18: Half-cylinder average thickness determination for placement of surface mount thermistor.

Once the heat flux and the surface temperature are calculated, the heat transfer coefficient is calculated using Newton's Law of cooling as shown:

Newton's Law of Cooling:

$$q = h A (T_{Chamber} - T_{Test}) \quad (2.9)$$

$$h = \frac{q}{A (T_{Chamber} - T_{Test})} \quad (2.10)$$

where  $q$  is the same heat flux as above,  $h$  is the heat transfer coefficient,  $A$  is the area of the test section,  $T_{chamber}$  is the measured chamber temperature and  $T_{Test}$  is the same as above.

### **2.2.3 Adiabatic Growth/Deposited Drop Experiment Equipment**

A small and simple test fixture was made for depositing drops and observing their behavior on ratchet test surfaces. This fixture consists of a support stand, rod clamp, test tube clamp, leveling plate and small gage insulin syringe. The syringe is held in place by the stand and clamps over a test surface resting on the leveling plate. The leveling plate has a screw at each of its four corners that can be adjusted to achieve a perfectly level surface. Leveling was performed by using a standard bullseye level. The white background was installed to aid video capture.

This fixture allowed deionized water to be deposited onto the test surface in a controlled manner without movement or misalignment that could be induced by manual droplet deposition. An image of this fixture is provided in Figure 2.19.

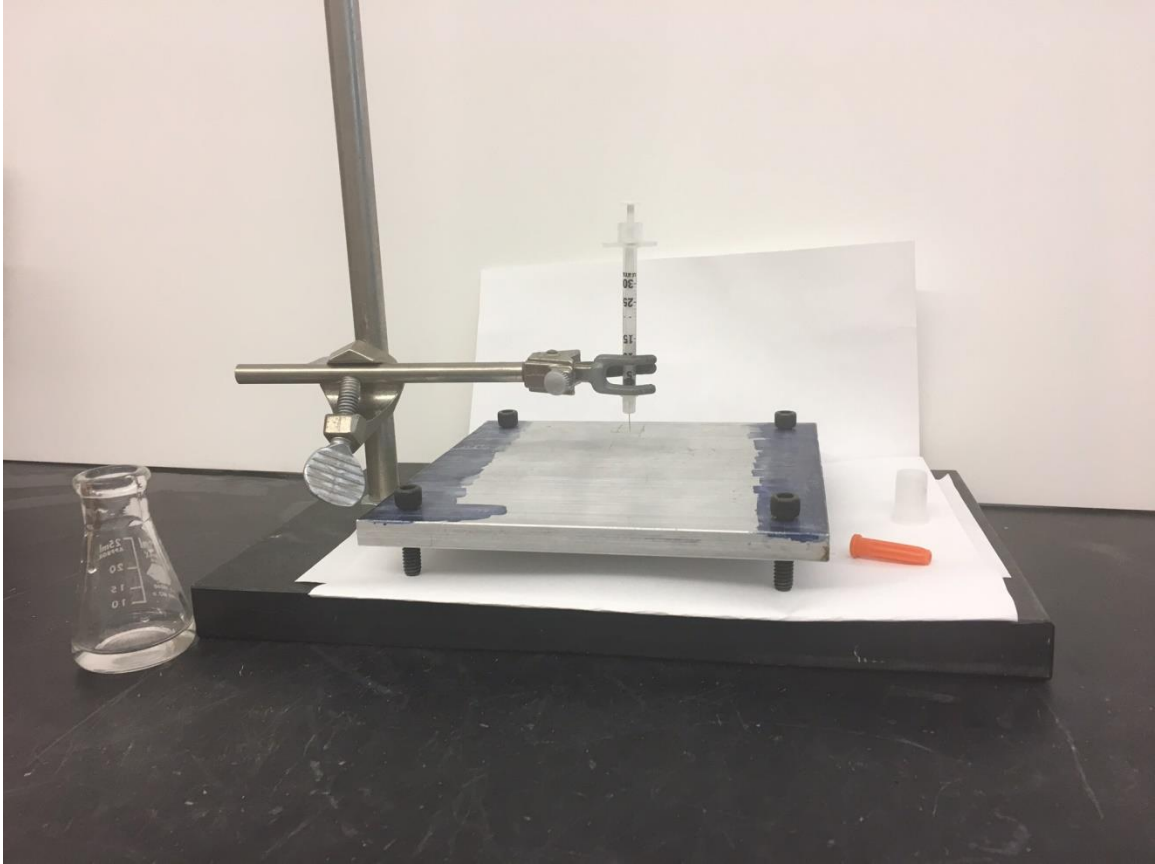


Figure 2.19: Deposited drop experiment fixture.

### 2.3 Experimental Procedure

The experimental procedure is as follows:

1. Experimental equipment is inspected for readiness. Wires are visually checked for proper connection, tubes are checked for leaks, and vibration isolating feet are pumped up to proper height. Newport instructions note that all vibration isolating feet used in a system must be inflated such that all feet are the same height when under load. This means that if there is an uneven weight distribution some feet may require more pressure to reach the desired height.

2. The appropriate test surface is attached to the measurement head using Dow Corning TC-5622 thermal grease and the surface mount thermistor is attached to the test surface using Omegatherm 201 thermal paste. The condensation and boiling chambers are sealed. The valve between the chambers is left open.
3. The condensation chamber is checked to insure that it is level and then the entire structure is tilted to the desired degree for the experiment about to be performed using a scissor jack under one of the bottom rails.
4. After insuring the ball valve between the bladder and boiling chamber is closed. The appropriate amount of deionized water (1000 ml.) or FC-72 (500ml.) is poured into the external bladder connected to the boiling chamber. Excess air in the line between the boiling chamber and the bladder and in the bladder itself is removed before the bladder is sealed.
5. The camera and lighting are checked for correct alignment. Labview and Movavi video capture software are initialized and given the correct file name and directory for the current experiment.
6. The chiller and heated windows are turned on. The boiling and condensation chambers are evacuated to 0.6 psi., and then the valve between the two chambers is closed.
7. The valve between the boiling chamber and bladder is opened, drawing the fluid into the boiling chamber and then closed again.
8. The boiling chamber's heaters are turned on.

9. After a prescribed amount of time (5 min. for most experiments) chilled water from the refrigerated circulating bath is allowed to flow through the measurement head and the data acquisition and high speed camera recording are started using LabView and Movavi video respectively. The virtual instrument used to collect experiment data is called condensation.vi.
10. The valve between the boiling chamber and condensation chamber is then opened allowing vapor to enter the condensation chamber.
11. All systems are stopped after 10 to 20 minutes depending on the experiment.
12. The boiling and condensation chambers are then opened, drained, cleaned and dried with compressed air in preparation for the next experiment.

The above procedure was designed to accomplish two main goals, to catch any equipment issues before experiments were run and to insure consistent operation and therefore consistent experimental conditions and data capture regardless of who was running the experiment. This procedure in checklist form was posted near the experimental facility.

## **2.4 Summary**

A detailed description of all experimental equipment and materials used in this study was provided in this chapter. Many configurations of three main types of test surfaces (flat silicon surfaces, hemi-cylindrical condenser tube surfaces, and asymmetric saw-toothed ratcheted silicon surfaces) were fabricated. Surface fabrication and characterization descriptions and specifications were provided in great detail in section

2.1. The design, configuration and specifications of the experimental facility, including custom designed and off-the-shelf components were described in section 2.4. This section also includes additional detail on instrumentation and data reduction. In section 2.3 the experimental procedure used for all condensation experiments performed during this study was provided.

## Chapter 3

### Hemi-Cylindrical Surface Experiments

The surfaces testing discussed in this chapter include experiments on hemi-cylindrical test surfaces fabricated from several common condenser tube materials used in power generation system condensers, namely Titanium, Admiralty brass, Cupronickel, and Sea Cure stainless steel. Flat and hemi-cylindrical surfaces machined from 304 stainless steel stock were tested as well. Units of each type of these surfaces were treated with hydrophobic and superhydrophobic coatings to compare condensate behavior and heat transfer rates against that on uncoated surfaces. The coatings used on these surfaces was adapted from a nano-scale, vapor phase deposited superhydrophobic coating comprised of several layers of rough alumina nano-particles and catalyzed silica with a finishing layer of perfluorinated silane called Repellix that is currently used to protect electronic devices. This type of surface treatment was selected for this study because it shows promising durability performance potential while maintaining sufficient non-wetting characteristics and can be applied to condenser tubes in-situ through vapor deposition processes all of which are desirable characteristics for coatings intended to be applied to condenser tubes in industrial applications.

Since Repellix was originally developed for the silicon surfaces in electronic devices and does not have sufficient durability when applied to metallic surfaces, two coatings, each based on Repellix with one modification intended to correct a possible



weakness in the original formulation were developed for this study. The first is called Modified Repellix which featured an additional initial layer of silica to the metallic substrate before the Repellix coating was applied to improve the bonding of the coating to the surface. The second is called Repellix 2.0 which employs an enhanced protection layer to increase the coating's durability. More details on the formulation of these coatings can be found in chapter 2.

### **3.1 Durability Testing**

Water erosion durability tests were performed on both modified Repellix and Repellix 2.0 coated flat 304 stainless steel test surfaces using the same methods as [53]. In these tests tap water flowing at six liters per minute through a 3 mm diameter nozzle impinged the surface which was held in place by a simple fixture constructed from two plastic protractors a plastic ruler and several binder clips, 30 cm below the nozzle and tilted 45 degrees from the flow direction. The flow rate of the water was determined by measuring the time it took to fill a two liter beaker. An image of the fixture used is provided in Figure 3.1.

Images of droplets deposited on the surfaces were taken before the tests and periodically during testing to measure contact angle degradation. These images are shown in Figure 3.2. The surfaces were dried with compressed air before droplets were deposited and contact angle measurements were taken using National Instruments Vision Assistant software. Testing was stopped when the surface was no longer hydrophobic, meaning the contact angle had dropped to 90° or below.

Both modified Repellix and Repellix 2.0 displayed dramatic durability improvements over the original Repellix formulation on metallic substrates which was not included in the water erosion tests because the coating was so fragile it did not withstand handling on most test surfaces. Modified Repellix coated surfaces initially display a contact angle of approximately  $120^\circ$  which degraded to about  $93^\circ$  after 2.5 hours of water erosion and then further degraded to  $70^\circ$  after another half hour of erosion (3 hours total). Repellix 2.0 coated surfaces start with a contact angle of  $151^\circ$  which classifies this coating, in new condition, as superhydrophobic [6]. Additionally Repellix 2.0 was able to withstand water erosion for approximately three times as long compared to modified Repellix before the contact angle degraded to  $90^\circ$  (8 hours versus 2.5 for modified Repellix). For comparison, the original Repellix coating applied to a silicon substrate creates an initial contact angle for water of  $148^\circ$  and degrades to  $90^\circ$  after 7.5 hours of similar water erosion testing. Figure 3.3 shows a plot of contact angle degradation for the two coatings tested and Table 3.1 contains the contact angle values for each plot point in Figure 3.3.

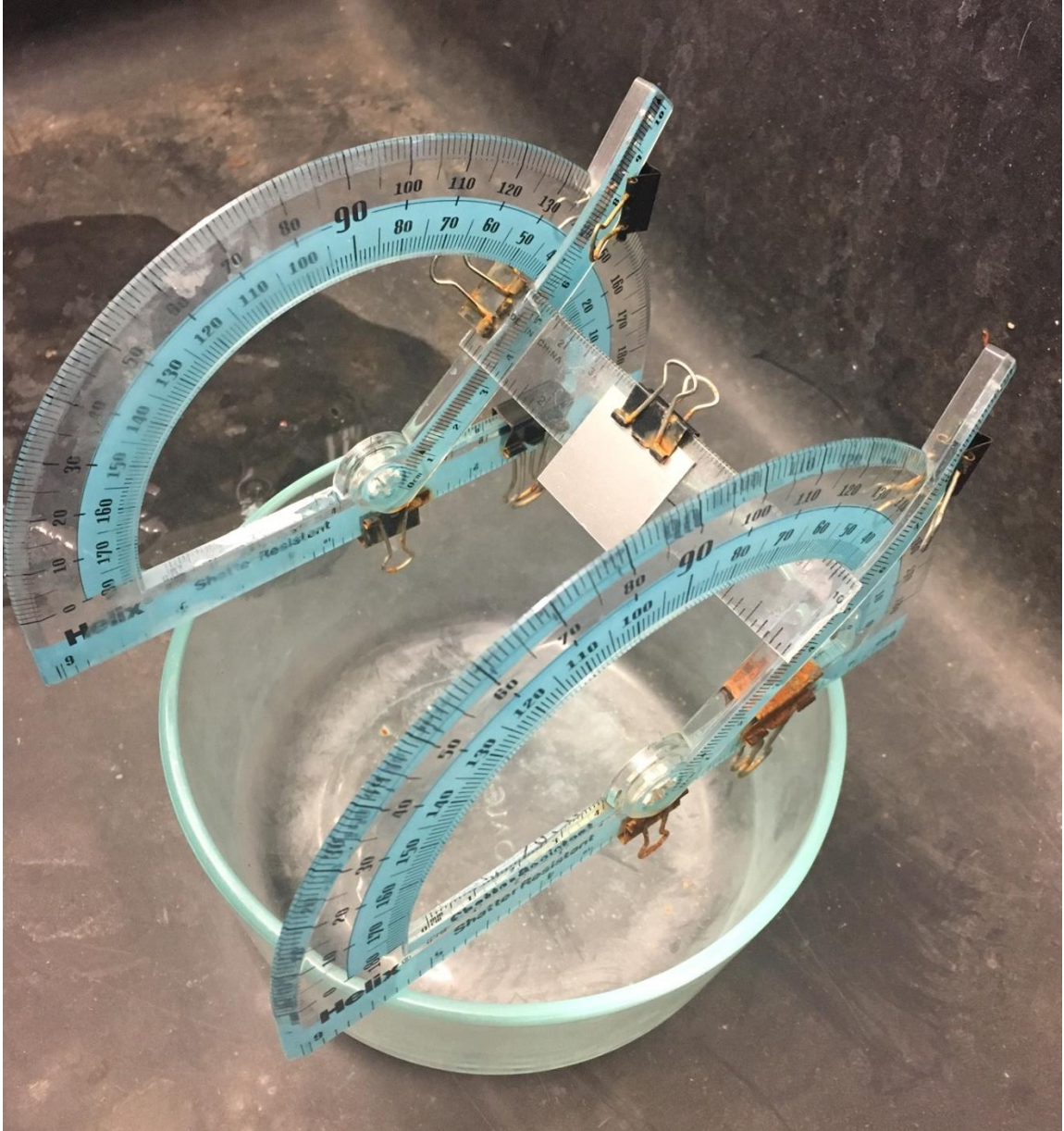


Figure 3.1: Jig used for holding flat 304 stainless steel surfaces coated with modified Repellix and Repellix 2.0 at 45° under the water stream during coating durability testing.

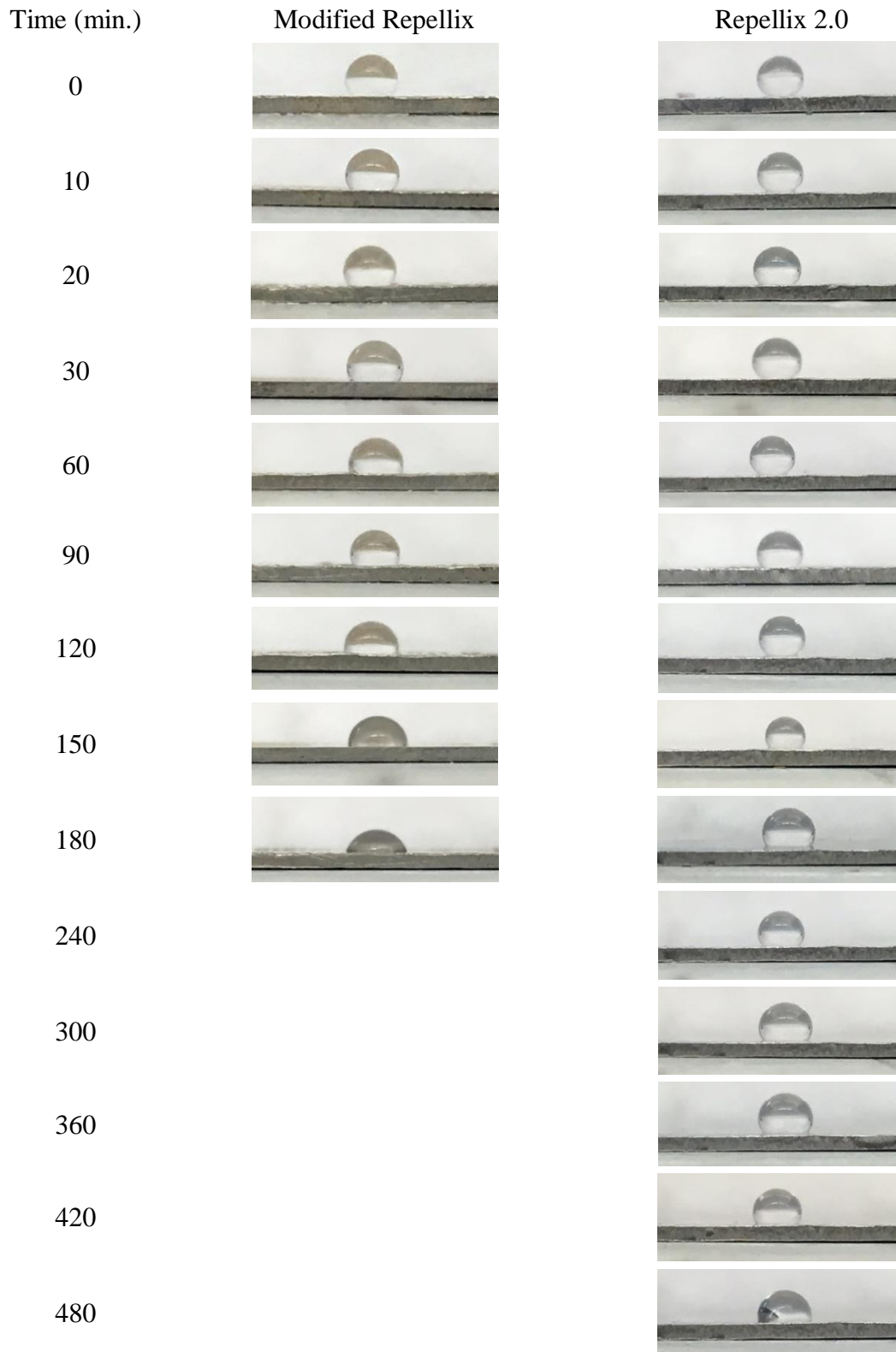


Figure 3.2: Contact angle images and values for flat 304 stainless steel surfaces coated with modified Repellix and Repellix 2.0 during coating durability testing.

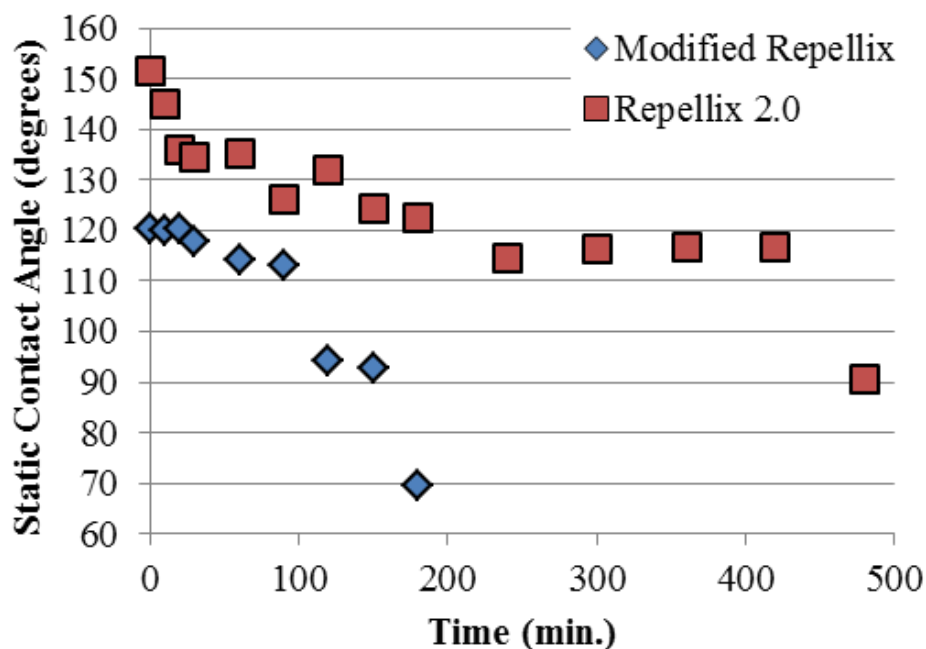


Figure 3.3: Plot of contact angle degradation for flat 304 stainless steel surfaces coated with modified Repellix and Repellix 2.0 during coating durability testing.

Table 3.1: Contact angle values corresponding to plot points in Figure 3.3

Time (min.)	Contact Angle (deg.)	
	Modified Repellix	Repellix 2.0
0	120.26	151.4
10	119.87	145.1
20	120.38	135.84
30	117.76	134.52
60	114.25	135.32
90	112.96	126.2
120	94.12	132.05
150	92.64	124.21
180	69.6	122.62
240		114.6
300		116.22
360		116.76
420		116.73
480		90.68

## **3.2 Results and Discussion**

Condensation experiments were performed on bare, modified Repellix coated and Repellix 2.0 coated hemi-cylindrical condenser tube material surfaces and 304 stainless control surfaces. The fluid used was deionized water. Each surface configuration was tested three times to insure performance repeatability.

### **3.2.1 Condensate Morphology**

As expected, the Repellix coatings greatly decreased the wettability of the test surfaces to which they were applied. As shown in Figure 3.4, the bare surfaces exhibited condensate films or large irregularly shaped droplets, while the Repellix coated surfaces were covered with smaller, more spherical droplets.

The spherical shape indicates that they have relatively low contact angle hysteresis and are in a Cassie-Baxter state. Repellix 2.0 coated surfaces tended to have a smaller droplet size and more regular spherical droplet perimeters than the surfaces coated with the original Repellix recipe. As seen in Figure 3.4, the bare flat 304 stainless steel surfaces also produced discrete round droplets meaning that the surface had a lower wettability than bare surfaces of different materials. This is because of the fine surface finish on the material used to fabricate these surfaces. The application of Repellix coatings did still reduce wettability on the flat 304 stainless surfaces. For the same conditions, high droplet densities (number of droplets per unit area) indicate a more hydrophobic or less wettable surface. Since all flat 304 stainless steel test surfaces have the same surface area, the number of droplets present after 5, 10 and 15 minutes of condensation activity were compared. The comparison chart in Figure 3.5 clearly shows

that the Repellix 2.0 coated surface produced the largest number of droplets and is therefore the most hydrophobic of the three surface conditions.

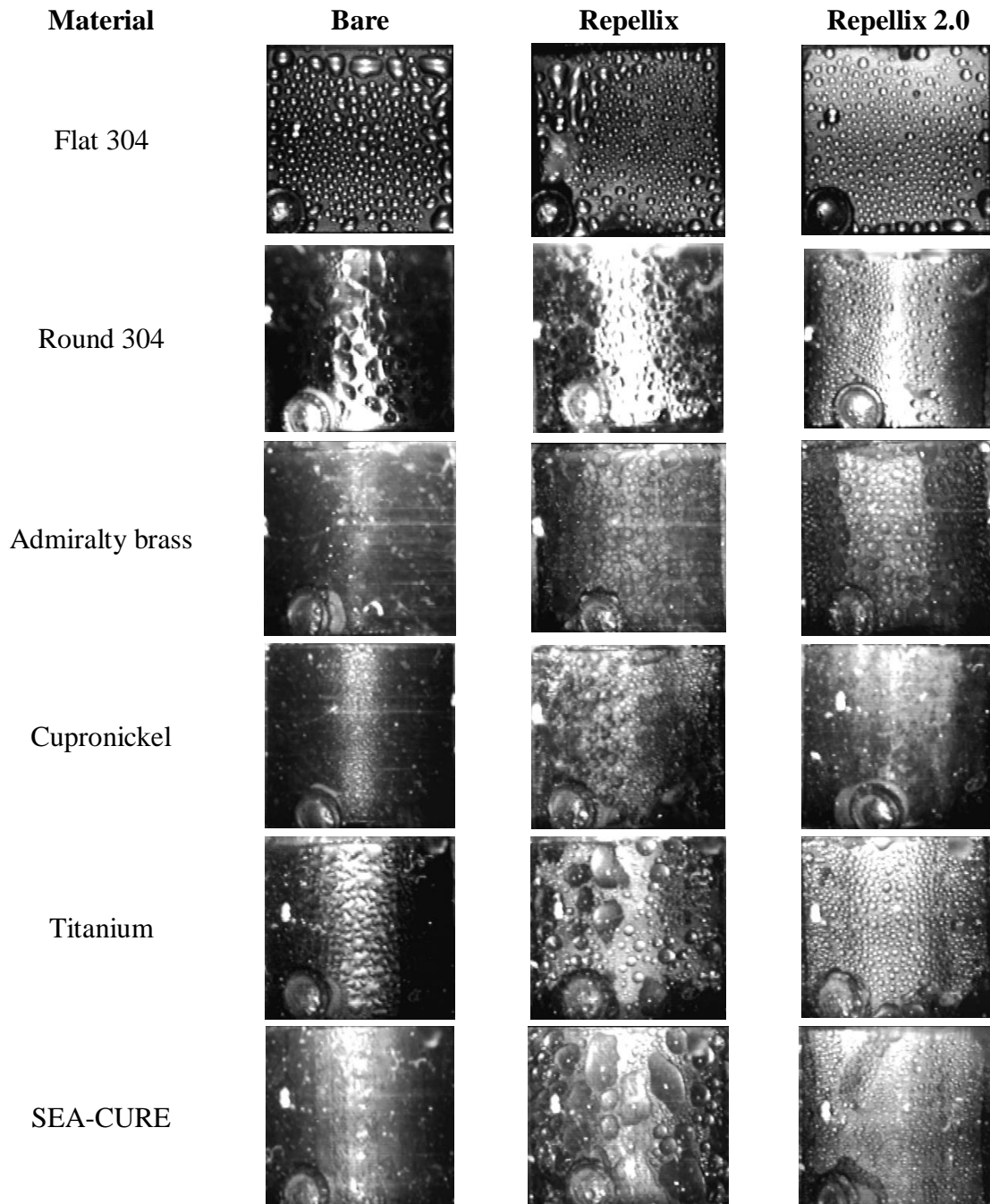


Figure 3.4: Comparison images of bare surfaces and both coatings on each material. All images were taken after 10 minutes of condensation activity.

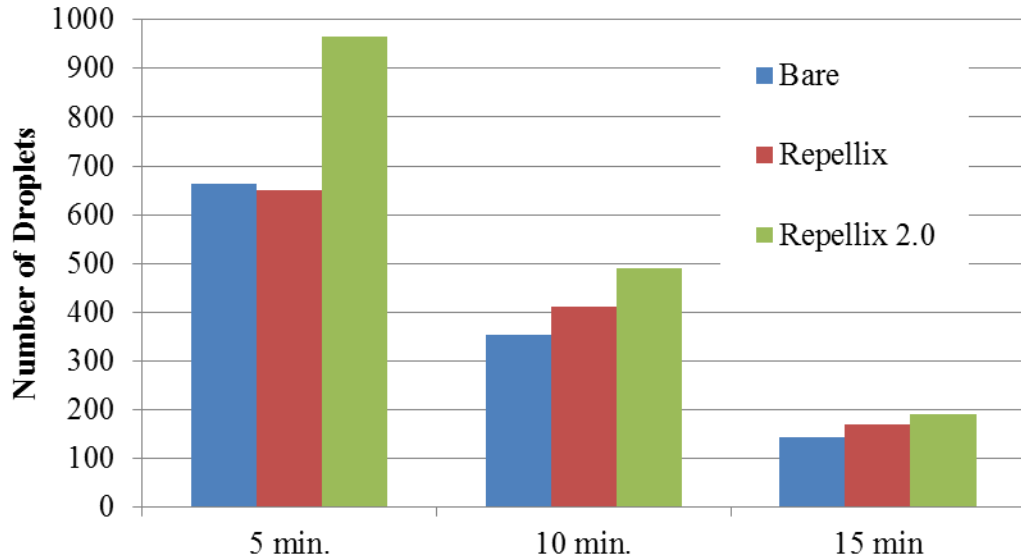


Figure 3.5: Comparison of droplets present on flat 304 stainless steel surfaces after various amounts of condensation activity.

### 3.2.2 Heat Transfer Performance

It stands to reason to expect that the surfaces coated with the most hydrophobic coating (Repellix 2.0) would exhibit better heat transfer performance than the bare or even original Repellix coated surfaces because hydrophobic condensing surfaces promote dropwise condensation which can be a 10 times more effective heat transfer mechanism than filmwise condensation. However, for every half cylinder test specimen material except titanium, the Repellix 2.0 coated specimens produced the lowest heat transfer coefficients and the bare surfaces produced the highest heat transfer coefficients for a given material. A sample set of plots is given in Figures 3.6 and 3.7. The full set can be found in Appendix G.



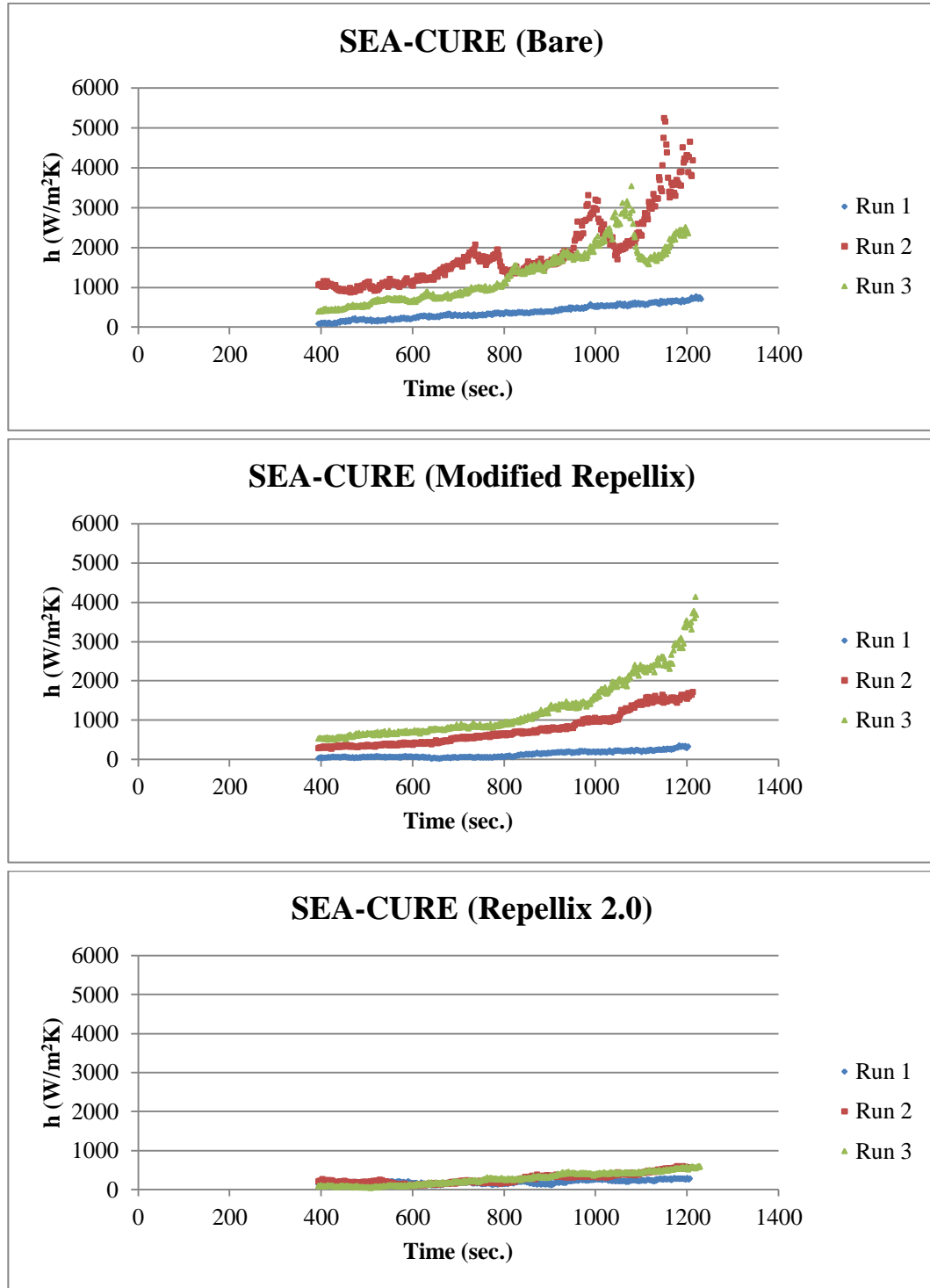


Figure 3.6: Heat transfer coefficient as a function of time for SEA-CURE test surfaces for all three surface conditions. Notice that the highest heat transfer coefficients for SEA-CURE were achieved with the bare surfaces and the lowest were achieved with the Repellix 2.0 surfaces. This trend was also true for the Admiralty brass and cupronickel surfaces. Data before 400s is not shown due to interference and therefore unreliable values caused by initial transients.

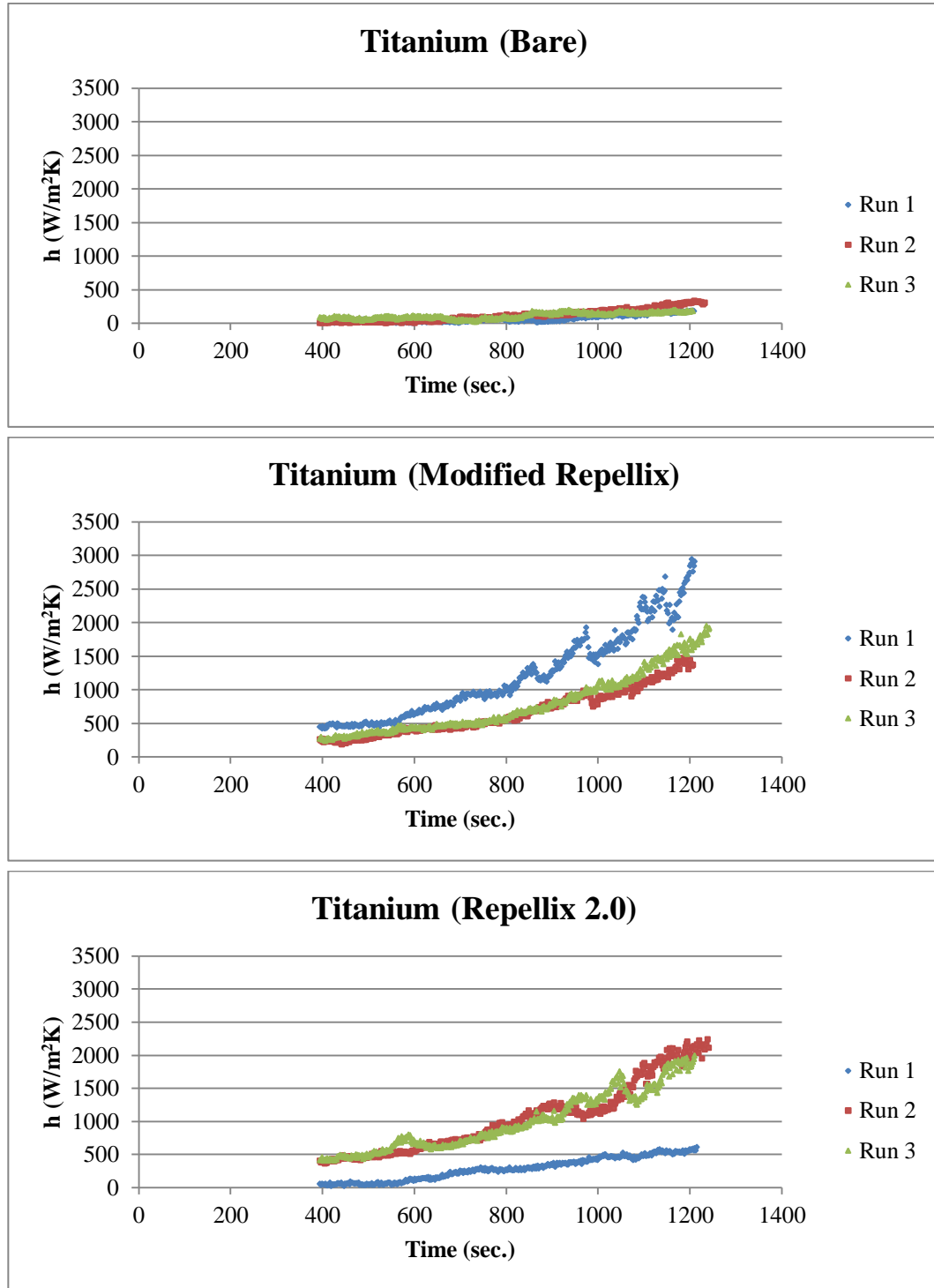


Figure 3.7: Heat transfer coefficient as function of time for titanium test surfaces for all three surface conditions. Notice that the highest heat transfer coefficients for titanium were achieved with the Repellix 2.0 coated surfaces and the lowest were achieved with the bare surfaces. This is opposite to the trend observed on the other three tube material test surfaces. Data before 400s is not shown due to interference and therefore unreliable values caused by initial transients.

To make sense of this somewhat surprising result, it must be understood that in order to realize the heat transfer performance improvements that are possible for dropwise condensing systems, the drops must move and sweep other drops off of the surface creating freshly cleared areas on the condensing surface. If the droplets are stationary, they create a local thermal resistance that can be larger than that of a film because drops on a hydrophobic surface tend to have heights greater than the thickness of a film on a corresponding hydrophilic surface under the same conditions.

Figure 3.8 shows a comparison chart of the average number of roll off events for each Repellix 2.0 coated tube material. A roll-off event was defined as any instance where a droplet was removed from the surface by gravity. Often these droplets will remove other droplets in their path on their way off of the surface. The information shown reveals that the titanium was the only material to have a heat transfer improvement with the Repellix 2.0 coating since it had a large number of roll-off events. SEA-CURE had the next highest number of events and also has the second highest heat transfer coefficient values for the Repellix 2.0 coated surfaces. The trend also holds for the Repellix 2.0 coated Admiralty brass and Cupronickel surfaces.

As stated earlier, these roll off events drive the increased heat transfer coefficient values that can be achieved in dropwise condensation. The heat transfer on the cleared surface left behind by an event is uninhibited by any additional thermal resistance imposed by condensate films or stationary drops. Without roll-off events, superhydrophobic dropwise condensing surfaces do not offer improved heat transfer performance. Figure 3.9 illustrates the heat transfer performance gains achieved by the Repellix 2.0 coated Titanium surfaces which produced a high number of roll-off events.

It is anticipated the normal operating environment of a power-plant condenser with flowing condensing steam will inherently provide plenty of impetus for droplet mobility.

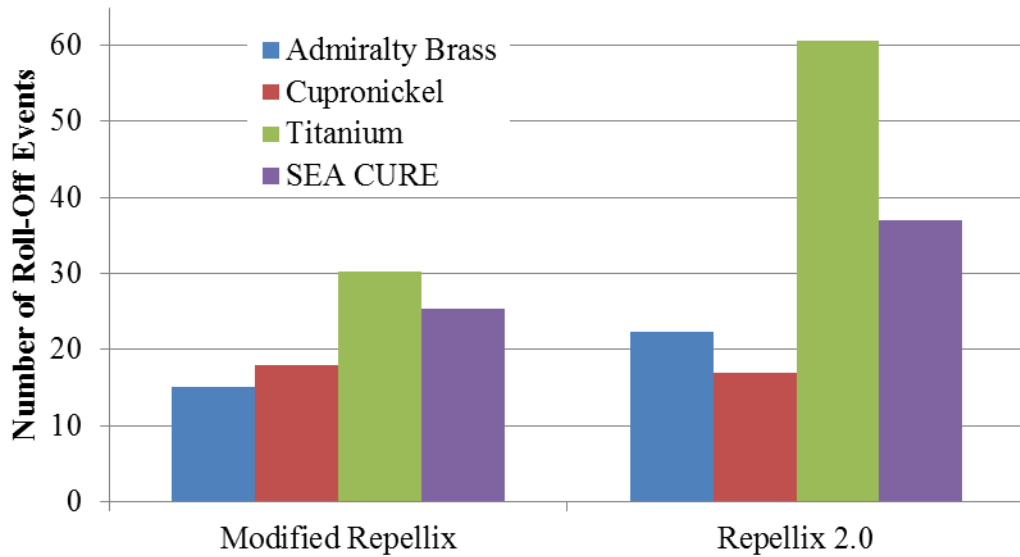


Figure 3.8: Average number of roll-off events for each Modified Repellix and Repellix 2.0 coated tube material.

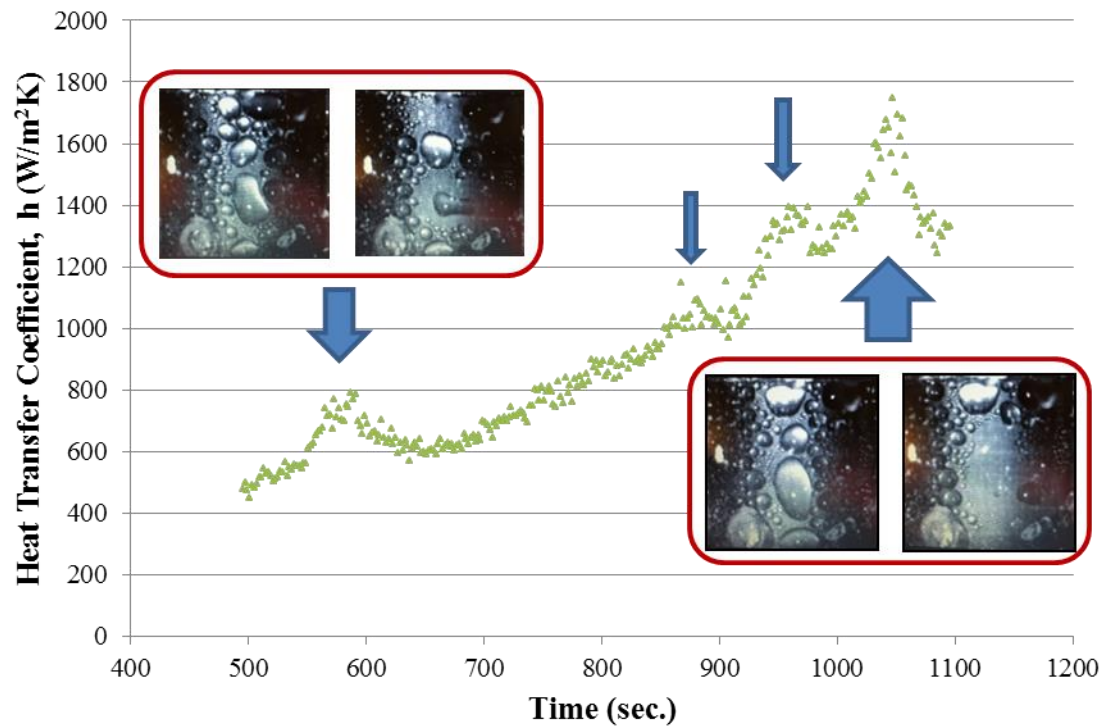


Figure 3.9: Plot highlighting roll-off events and corresponding heat transfer coefficient spikes. Arrows indicate heat transfer coefficient spike after a roll-off event. Two insets show the surface before and after a roll off event corresponding to a spike in heat transfer coefficient.

## Chapter 4

### Asymmetric Saw-Toothed Ratchet Surface Experiments

As documented earlier in Chapter 1, several previous studies have shown that surfaces with asymmetric ratchet topographies can be effective at promoting directional fluid motion [10-12]. Jo [10] used a heated asymmetric saw tooth surface that promotes single phase fluid motion by augmenting Marangoni convection. Linke et al. [11] demonstrated R-134a droplets moving in a consistent direction at velocities as high as 5 cm/s on an asymmetric ratcheted surface that was heated above the Leidenfrost point. More recently Thiagarajan et al. [12] employed a surface that utilized reentrant cavities to promote boiling activity and a series of asymmetrical ratchets that impose a force imbalance on bubbles on the surface during nucleate boiling. This force imbalance gives the bubbles a lateral velocity component as they depart their nucleation site, which in turn causes the liquid in the vicinity of the bubble to move in the same direction. The successful promotion of fluid motion in a preferred direction by the ratcheted surfaces in these studies led the use of asymmetric saw-toothed ratchet surfaces in this condensation study.

Much effort has been put into creating superhydrophobic surfaces to promote dropwise condensation which can boost condensation heat transfer coefficients; however as was seen in Chapter 3, dropwise condensation without droplet mobility can actually hinder heat transfer rates. Therefore a surface that promotes condensate motion in a

preferred direction through surface structure and wettability modifications has the potential to achieve increased heat transfer coefficients without the complicated and often delicate treatments required for superhydrophobicity. Furthermore, if a condensing surface that promotes condensate motion in a preferred direction were coupled with the boiling surface described above, a pump-less self-regulating phase change cooling system could possibly be developed.

The surfaces used for the experimentation discussed in this chapter were all fabricated from silicon wafers as discussed in Chapter 2. Except for the flat control surfaces, these surfaces feature asymmetric saw-toothed ratchet topographies in three different ratchet pitches—100 $\mu\text{m}$ , 250  $\mu\text{m}$ , and 500  $\mu\text{m}$ —and three triangular ratchet profiles—nominally 30°-60°-90°, 18°-44°-118° and 9°-26°-145°. Figure 2.7 and Table 2.4 contain additional detail on the ratchet pitches and profiles.

Units of these surfaces were made with three different surface wettability conditions. Uncoated surfaces were hydrophilic and featured a static contact angle in deionized water of 70°. NeverWet coated surfaces were hydrophobic and featured a static contact angle in deionized water of approximately 140°. A third surface wettability condition was created by selectively coating only the longer shallow ratchet slopes on a surface by using them to shield the neighboring slope while spraying the NeverWet coating (see Figure 2.9). Since these surfaces feature both hydrophobic and hydrophilic portions they are called biphilic surfaces.

Testing on these surfaces included adiabatic deposited drop experiments aimed at better understanding the fluid/surface interactions and condensation experiments aimed at

assessing the performance of this type of surface in a variety of conditions as a condenser surface.

#### **4.1 Adiabatic Deposited Drop Mobility Experiments**

Adiabatic deposited droplet tests were performed on hydrophobic ratcheted silicon surfaces using the equipment described in section 2.2.3. During the adiabatic experiments on these surfaces, it was observed that as fluid was added to the droplet through a small gauge syringe, the droplet grew preferentially toward the short, steep,  $60^\circ$  slope of the ratchet as shown in the diagram in Figure 4.1, while the opposite edge of the droplet remained pinned at the crest of the ratchet that it was originally placed upon.

The preferential growth toward the short, steep  $60^\circ$  slope of the ratchet is due to internal pressure differences caused by the asymmetric surface texture which creates droplet radius differences between the pinned and ascending sides of the droplet. When a droplet grows in this manner it goes through five stages of growth each time it fills a new ratchet. In stage one, the droplet is in an approximately equilibrium state. The pinned and ascending edges are both resting on the crest of a ratchet and there is very little difference in pinned versus ascending radii. As more fluid is injected into the droplet in stage 2, both edges are still pinned at ratchet crests and both radii begin to grow. The ascending radius grows larger than the pinned radius creating a pressure difference inside the droplet. Stage 3 occurs at the moment the ascending edge breaks away from the ratchet crest and starts to travel down the long face of the ratchet. The largest difference in pinned versus ascending radii and therefore the largest pressure difference is achieved in stage 3. During stage 4 the ascending edge travels down the long face of the ratchet to



restore equilibrium to the droplet. The difference in radii and pressure decay as equilibrium is achieved. At the end of the ascending edge's travel down the long face of the ratchet the droplet comes in contact with the short face of the neighboring ratchet because the contact angle is greater than  $90^\circ$  therefore the body of the droplet contacts the neighboring ratchet face before the contact line reaches the ratchet trough. Once the droplet contacts the ratchet face it immediately adjusts, placing the ascending edge on the crest of this new ratchet. Once on the crest, the droplet can fully return to equilibrium marking stage 5 (which is the same as stage 1 except the droplet is now one ratchet pitch wider). Images of the pinned and ascending edges of a droplet during these 5 stages of growth are provided in Figure 4.2.

This behavior was observed on both the  $250\mu\text{m}$  and  $500\mu\text{m}$  pitch surfaces however  $100\mu\text{m}$  pitch surfaces exhibited less repeatable behavior. It is believed that the smaller ratchets may only produce this behavior for smaller droplets and that slight misalignment of the syringe can provide a lateral momentum to the fluid entering the droplet that can counteract the pressure difference created by the asymmetric ratchet structure.

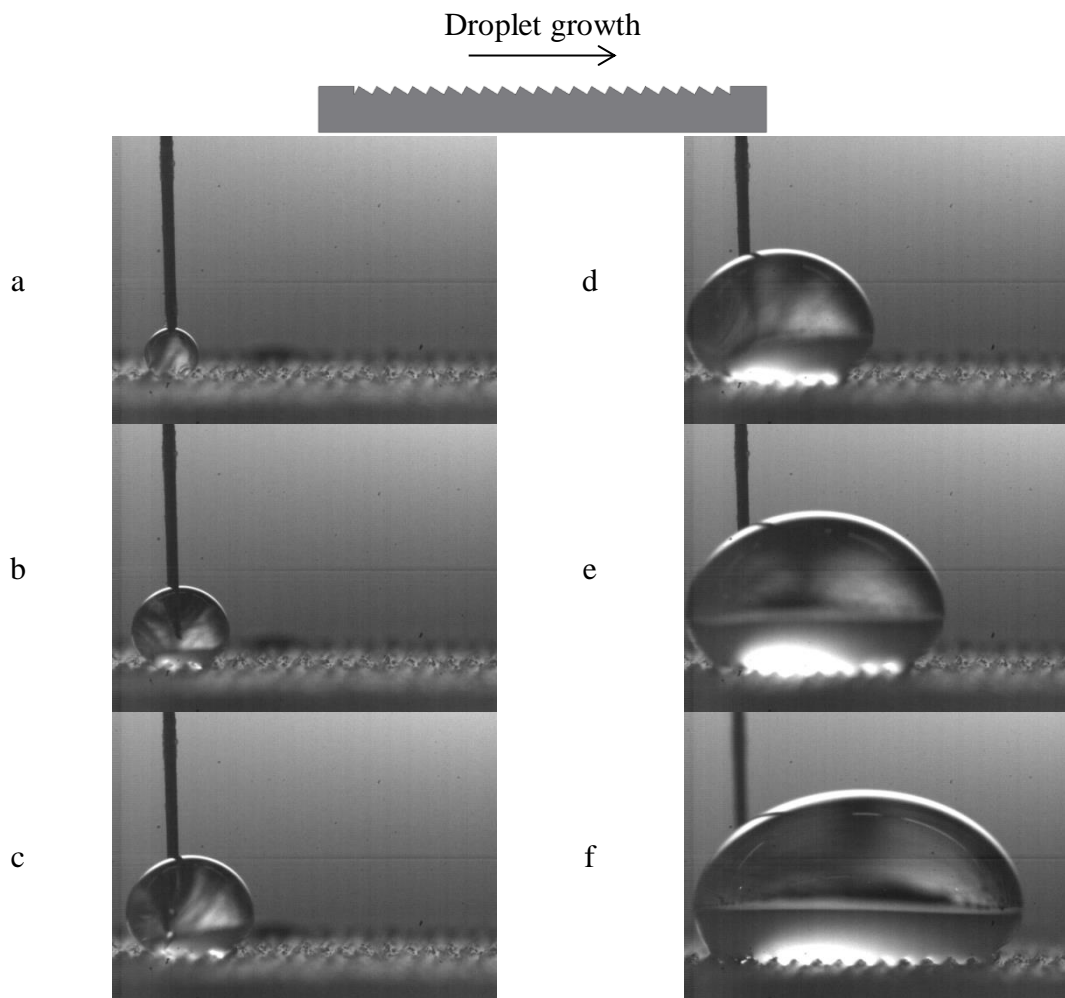


Figure 4.1: Images of deposited water drop growing on 500 $\mu$ m pitch hydrophobic ratcheted surface.

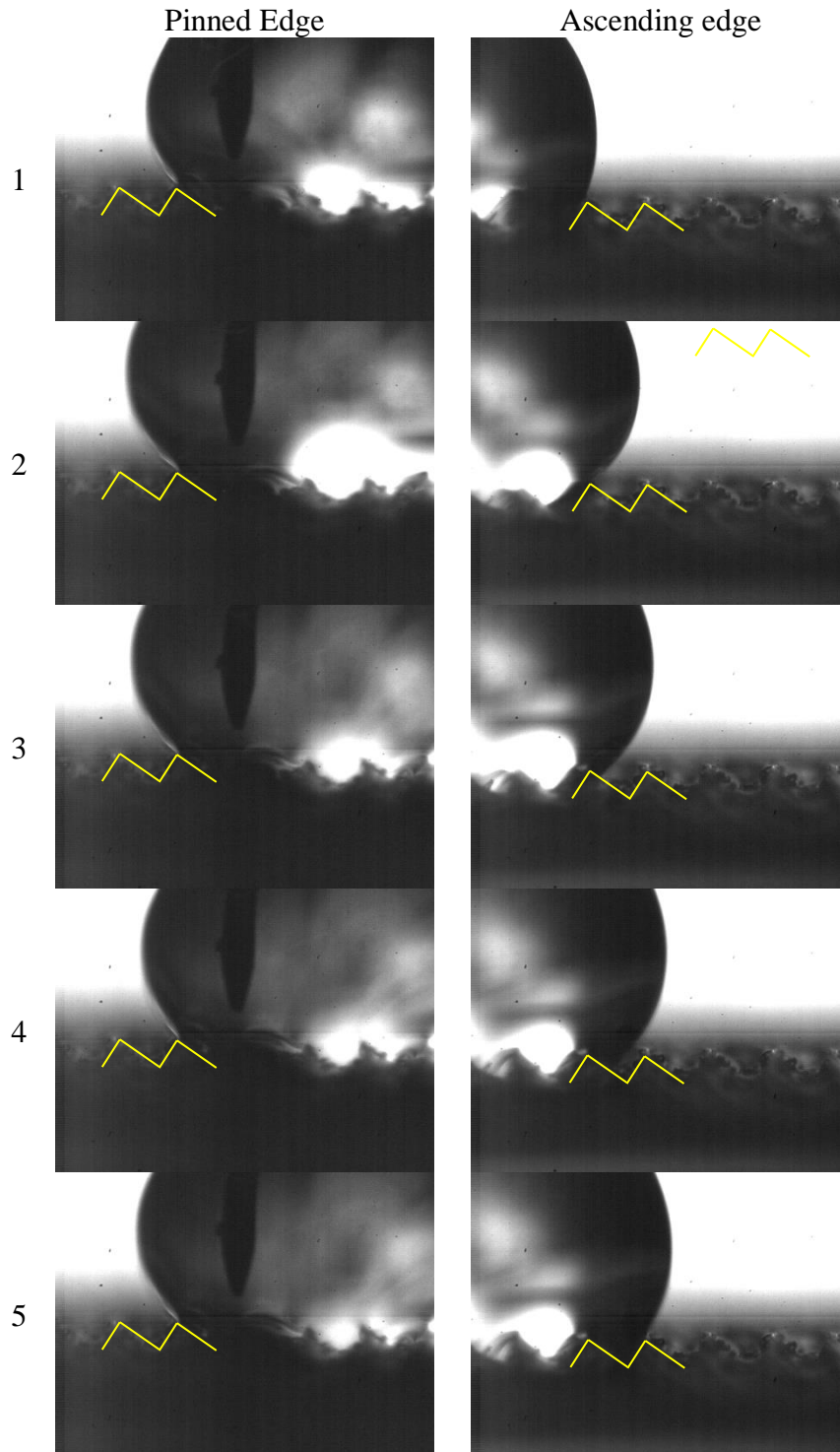


Figure 4.2: Images taken at each stage of droplet growth on ratcheted surface. Notice that the image for stage 3 was taken just after the ascending edge broke over the crest. The image for stage 4 clearly shows the contact line is on the long face of the ratchet and that the body of the droplet will contact the adjacent ratchet face before the contact line reaches the trough.

### 4.1.1 Directional Droplet Growth Internal Pressure and Force Calculation

The force and internal pressures driving this motion can be calculated using equations 4.1 and 4.3, respectively and plots of the values of these calculations for one growth cycle are given in Figures 4.3 and 4.4, respectively. As shown in [14] and [54] the force that drives this motion can be calculated using the following equation:

$$F = w \cdot \sigma (\cos \theta_p - \cos \theta_a) \quad (4.1)$$

Where  $F$  is the force in Newtons,  $w$  is the width of the droplet in meters,  $\sigma$  is the surface tension in N/m,  $\theta_p$  is the contact angle on the pinned side of the drop and  $\theta_a$  is the contact angle on the ascending side of the drop. The droplet width and contact angles along with the droplet radius on both the pinned and ascending edges were measured from high speed images taken during the experiments using National Instruments Vision Assistant Software. The actual images used for measurements for one growth cycle are shown in Figure 4.5.

The radii measured were used to calculate the internal pressure of the droplet during directional growth using the Young-Laplace equation:

$$\Delta P = \frac{2\sigma}{r} \rightarrow \Delta P_p = \frac{2\sigma}{r_p}, \quad \Delta P_a = \frac{2\sigma}{r_a} \quad (4.2)$$

Where  $P$  is pressure in Pascals, and  $r$  is the drop radius in meters. Because the external pressure is the same for both edges of the droplet, the difference of  $\Delta P_p$  and  $\Delta P_a$  gives the driving pressure difference inside of the droplet:

$$\Delta P_p - \Delta P_a = \Delta P_{internal} \quad (4.3)$$

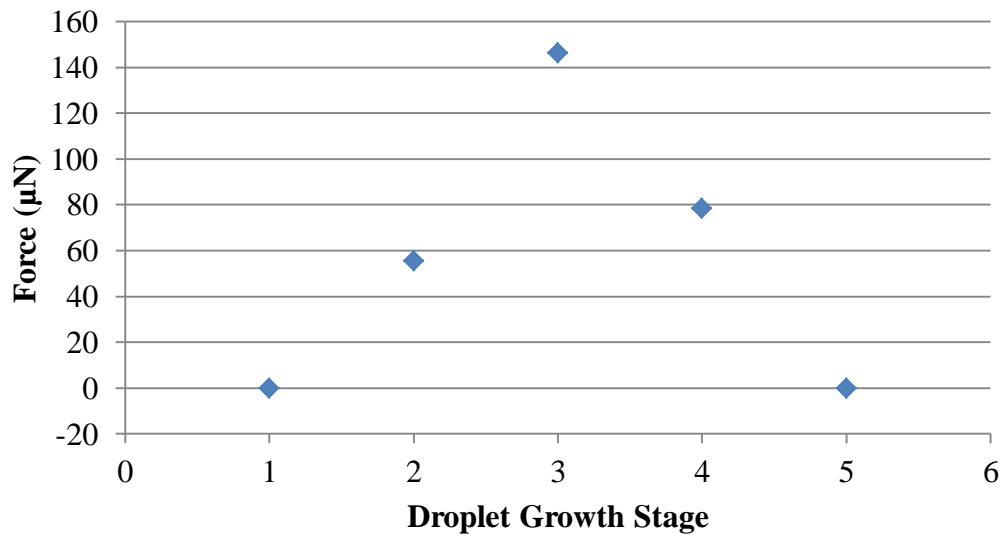


Figure 4.3: Directional growth driving force calculated from equation 4.1 for one growth cycle on 500μm pitch hydrophobic ratcheted surface.

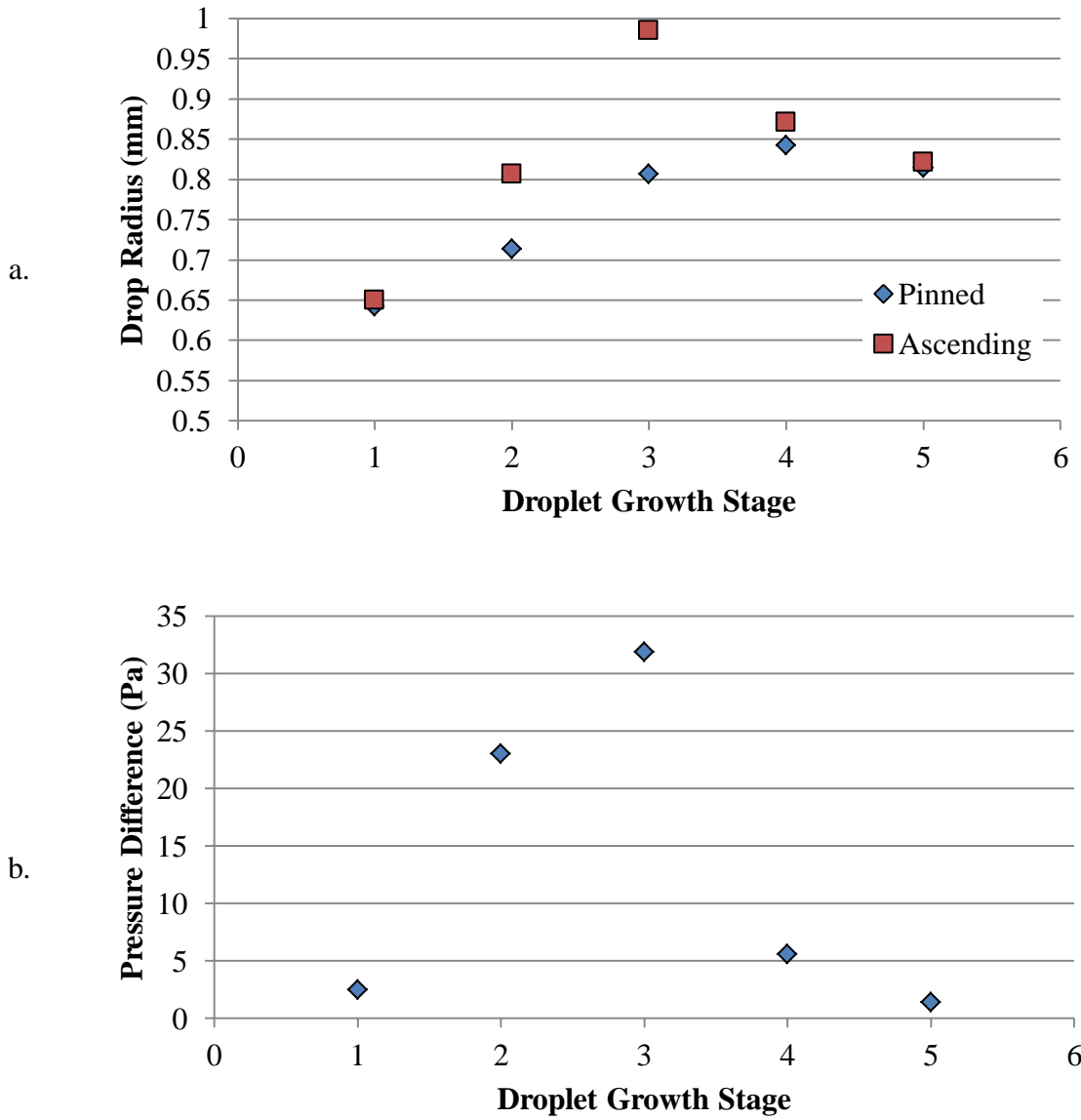
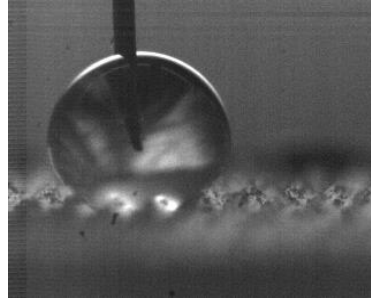
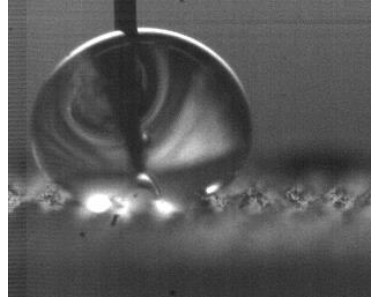


Figure 4.4: a. Pinned and ascending drop radius data at each growth stage. b. Internal pressure difference calculated from equation 4.3 at each growth stage on 500 $\mu$ m pitch hydrophobic ratcheted surface.

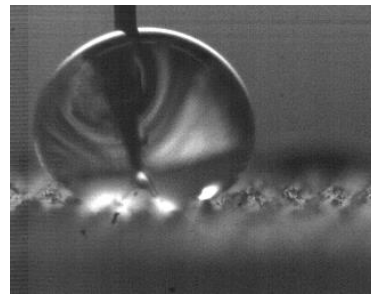
1



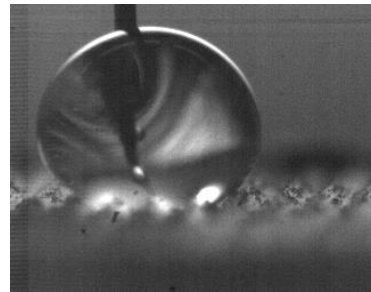
2



3



4



5

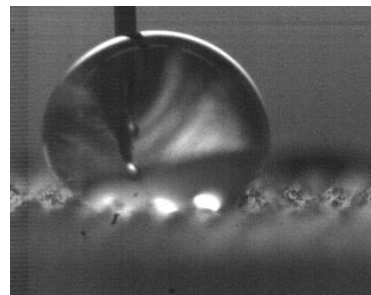


Figure 4.5: Images used for measurements needed for force and internal pressure calculation for one growth cycle on 500 $\mu\text{m}$  pitch hydrophobic ratcheted surface.

The above analysis was continued on the 500  $\mu\text{m}$  ratchet surface to track the force and pressure differences in a droplet as it grew over several ratchets. Force data can be found in Figure 4.6, ascending and pinned radii data are shown in Figure 4.7 and the internal pressure differences calculated from the droplet radii are given in Figure 4.8. As expected, as the droplet grows a larger force is required to advance the ascending edge from one ratchet to the next. Interestingly this force is achieved with increasingly smaller ascending and pinned radii differences and therefore smaller pressure differences. This implies that there is a maximum droplet size that will exhibit directional growth on this surface. This may be why the 100 $\mu\text{m}$  ratchet surfaces exhibited less repeatable behavior; the droplets deposited were just too large for the surface texturing to affect growth stages in the manner larger ratchets affected similarly sized droplets.



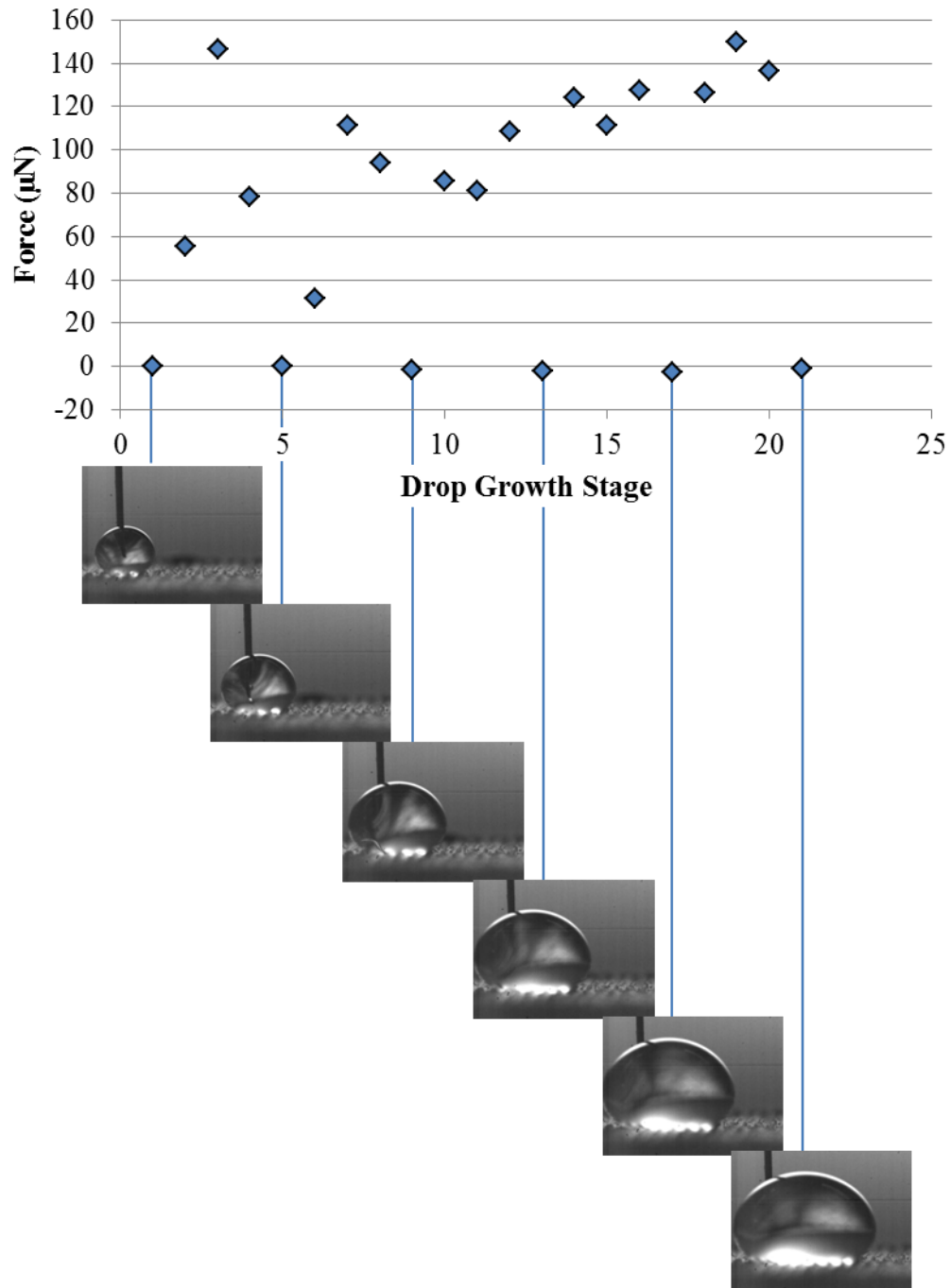


Figure 4.6: Force values calculated from equation 4.1 for deposited droplet on 500μm pitch hydrophobic ratcheted surface growing in preferred direction over several ratchets. Images at stage 1 for each ratchet are given.

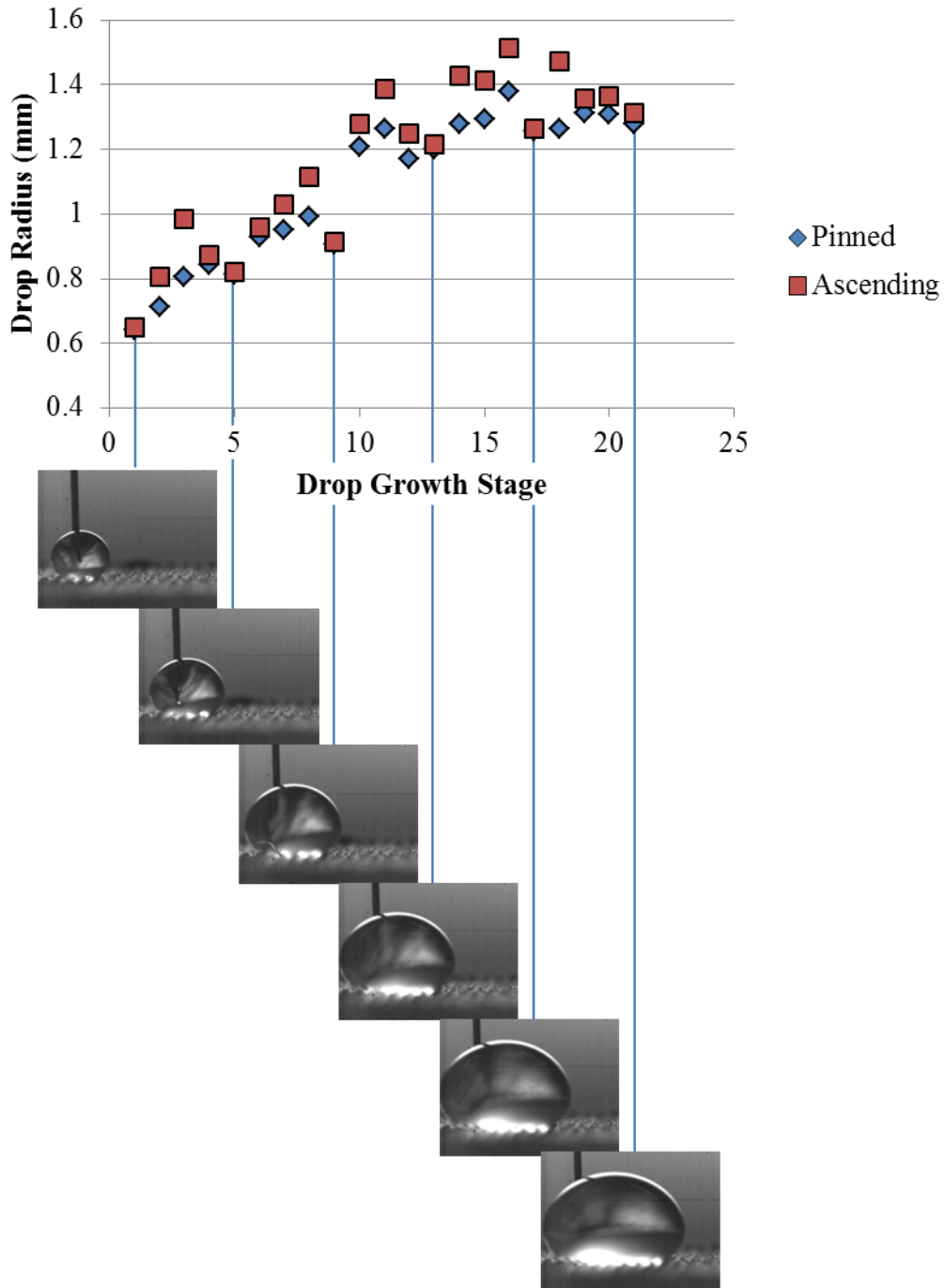


Figure 4.7: Pinned and ascending radii data for deposited droplet on 500 $\mu$ m pitch hydrophobic ratcheted surface growing in preferred direction over several ratchets. Images at stage 1 for each ratchet are given.

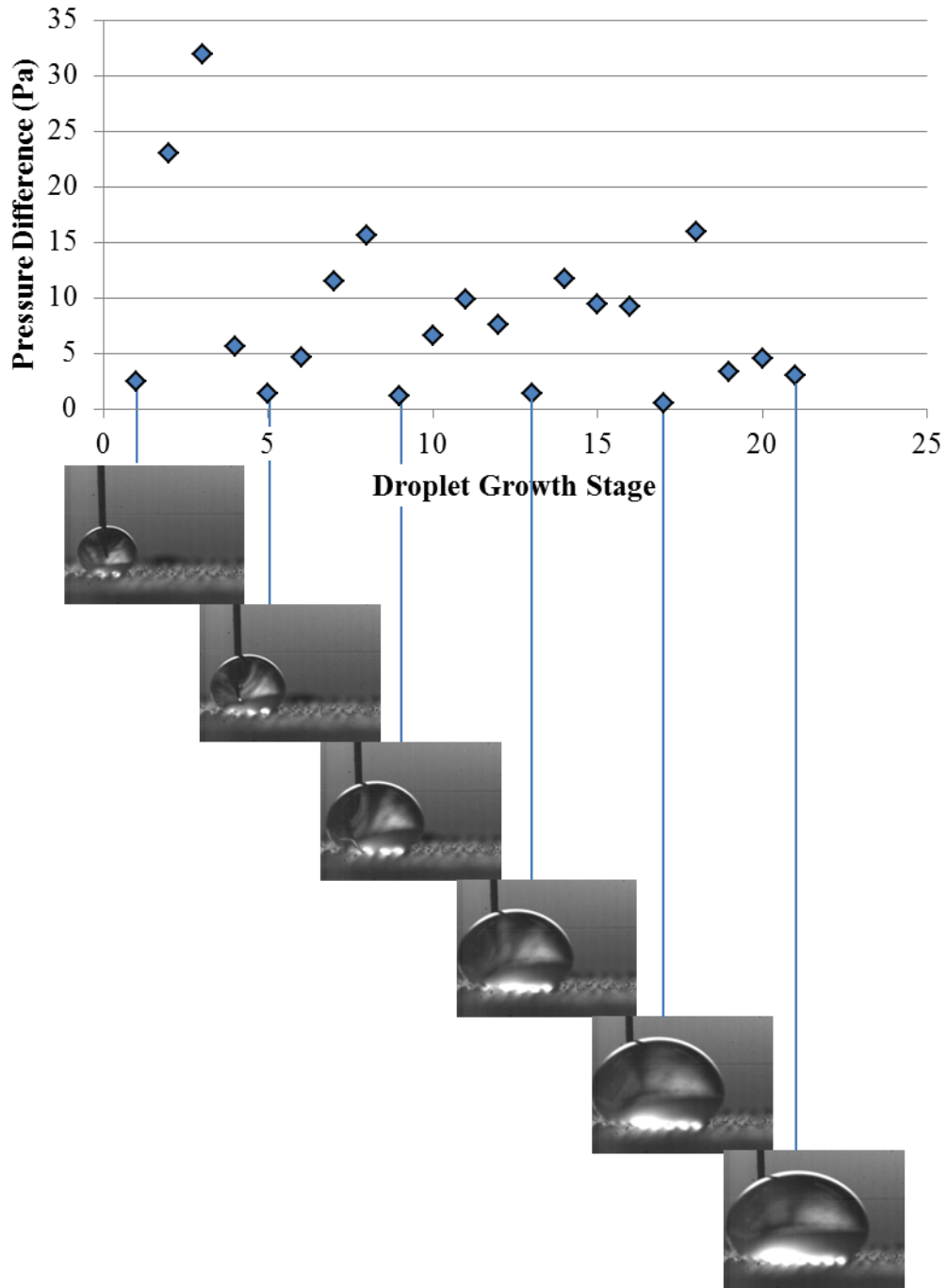


Figure 4.8: Internal pressure difference values calculate from equation 4.3 for deposited droplet on 500 $\mu$ m pitch hydrophobic ratcheted surface growing in preferred direction over several ratchets. Images at stage 1 for each ratchet are given.

## **4.2 Condensation Experiments**

Two working fluids were used during condensation tests, deionized water and FC-72. FC-72 was tested because it is a dielectric fluid with a low boiling point commonly used in boiling studies on phase change thermal management systems for electronic devices. However, FC-72 proved to be very difficult to work with as it condenses very quickly (experiments using FC-72 lasted only a number of seconds) due to its low surface tension and boiling point therefore the bulk of the experimentation was done using deionized water. Two pressure conditions—high, transient and low, quasi-steady—and several surface tilt angles were tested using deionized water. The results of condensation experiments on many combinations of these variables and surface configurations are discussed below.

### **4.2.1 Uncontrolled Pressure Rise Experiments**

The heaters in the boiling chamber were set to full power for the entire duration of the experiments discussed in this section. This led to a pressure rise of around 70 kPa (10 psi) over the course of a 20 minute experiment (average length of water experiments). The experiments consisted of FC-72 condensation on hydrophilic ratcheted (100  $\mu\text{m}$ , 250  $\mu\text{m}$  and 500  $\mu\text{m}$  pitches) and flat surfaces and deionized water condensation on hydrophobic ratcheted (100  $\mu\text{m}$ , 250  $\mu\text{m}$  and 500  $\mu\text{m}$  pitches) and flat surfaces. The boiler was charged with 1 liter of fluid for water experiments and 0.5 liters of fluid for the FC-72 experiments.

#### 4.2.1.1 FC-72 Condensation on Hydrophilic Surfaces

Figure 4.9 shows a pair of images of FC-72 condensing on a hydrophilic test surface with 500 $\mu\text{m}$  ratchet pitch (yellow outlines in first image show flat portions of the surface and the surface mount thermistor). This combination of working fluid and surface wettability produces very uniform condensation activity. A film of condensate quickly forms and continues to grow in thickness. Approximately five seconds after condensation begins, the surface structure is completely filled with liquid. The clarity of FC-72 and the uniformity of the film make the presence of a condensate film difficult to discern in still images, however subtle evidence exists and is marked with red arrows in the figure; arrows 1 and 2 point to light reflecting on the surface of the film, arrow 3 points to the film's shadow (notice the curved line).

No condensate motion was observed during any of the experiments performed on hydrophilic test surfaces with FC-72 as the working fluid. Although it seems that at least the largest ratchets did have a measurable effect on the heat transfer coefficient as evidenced by the plot provided in Figure 4.10. The 500  $\mu\text{m}$  pitch ratcheted surface clearly produced the highest heat transfer coefficients so some degree of condensate mobility may have been achieved for this surface, causing the average condensate film thickness to be lower than that for a flat surface. The Gregorig effect (where condensate films on wavy surfaces are thinner on the peak region than the valley regions due to internal pressure differences that cause condensate to flow from the peaks to the valleys) [42] or gravity or a combination of the two would cause the condensate film thickness to be lower at the crests of the ratchets thereby creating regions of low thermal resistance that would boost heat transfer rates. The surfaces with smaller ratchets may not have

realized the same performance increases as the 500  $\mu\text{m}$  pitch ratcheted surface because they become fully flooded with condensate more quickly due to the smaller volume of condensate required to fill the surface structure and once a surface is fully flooded the surface topography no longer asserts much influence on condensate dynamics.

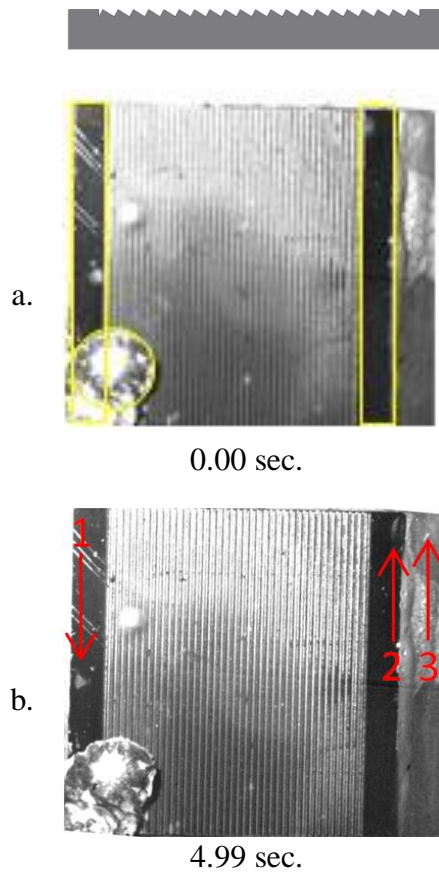


Figure 4.9: Images of FC-72 condensation on a 500 $\mu\text{m}$  pitch ratcheted hydrophilic test surface. The diagram above the images shows the orientation of the ratchets. a. Surface just before condensation begins. b. Surface after flooding with condensate.

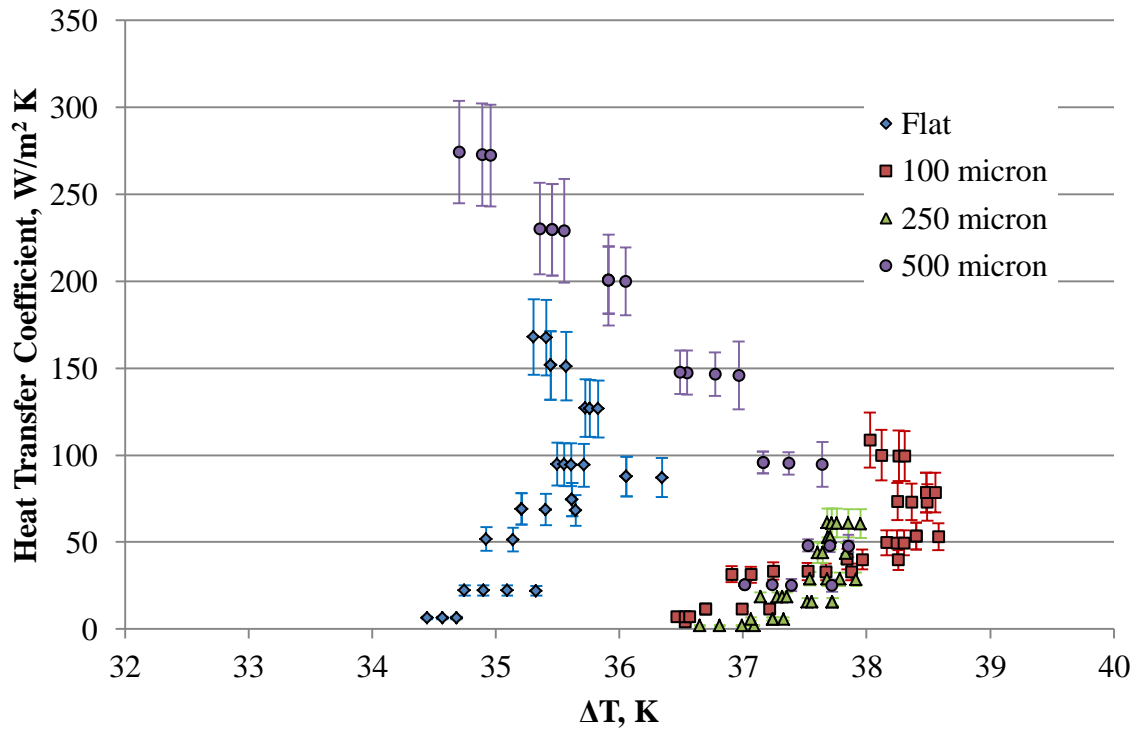


Figure 4.10: Condensation heat transfer coefficient as a function of  $\Delta T$  for FC-72 on hydrophilic surfaces.

Since FC-72 is a highly wetting fluid and filmwise condensation is already a well understood phenomenon, no condensate film mobility was observable during experiments, and the experiments were very short and difficult to control, attention was turned to deionized water condensation on hydrophobic surfaces for the remainder of this study.

Note: Calculation details for the error bars shown on Figure 4.10 and subsequent comparison plots are provided in Appendix H.

#### 4.2.1.2 Deionized Water Condensation on Hydrophobic Surfaces

During deionized water condensation on hydrophobic ratcheted surface experiments frequent instances of self-propelled condensate motion perpendicular to the series of ratchets on the test surface were observed on all hydrophobic ratcheted test surfaces. A series of images of deionized water vapor condensing on a hydrophobic test section with 500 $\mu$ m ratchet pitch is shown in Figure 4.11 (yellow outlines in first image show flat portions of the surface and the surface mount thermistor). This series of images was chosen to show a representative instance of condensate motion. The hydrophobic ratchets on these surfaces tend to force the water droplets into an elongated shape in the ratchet troughs. When condensate moves on the ratcheted portion of the test surface it starts with a larger droplet that has formed in a ratchet that has grown to reach the crest of the ratchet. This droplet then spills over the 30° slope and coalesces with the condensate occupying the adjacent ratchet. To verify that this behavior is caused by the surface topography and not by gravitational forces acting on an un-level test surface, additional experimental runs were performed with the test surface rotated 180°. These runs verified that water condensate droplets on these hydrophobic ratcheted surfaces do in fact prefer to climb the 30° slope of the ratchets when growing and then coalescing with other condensate.



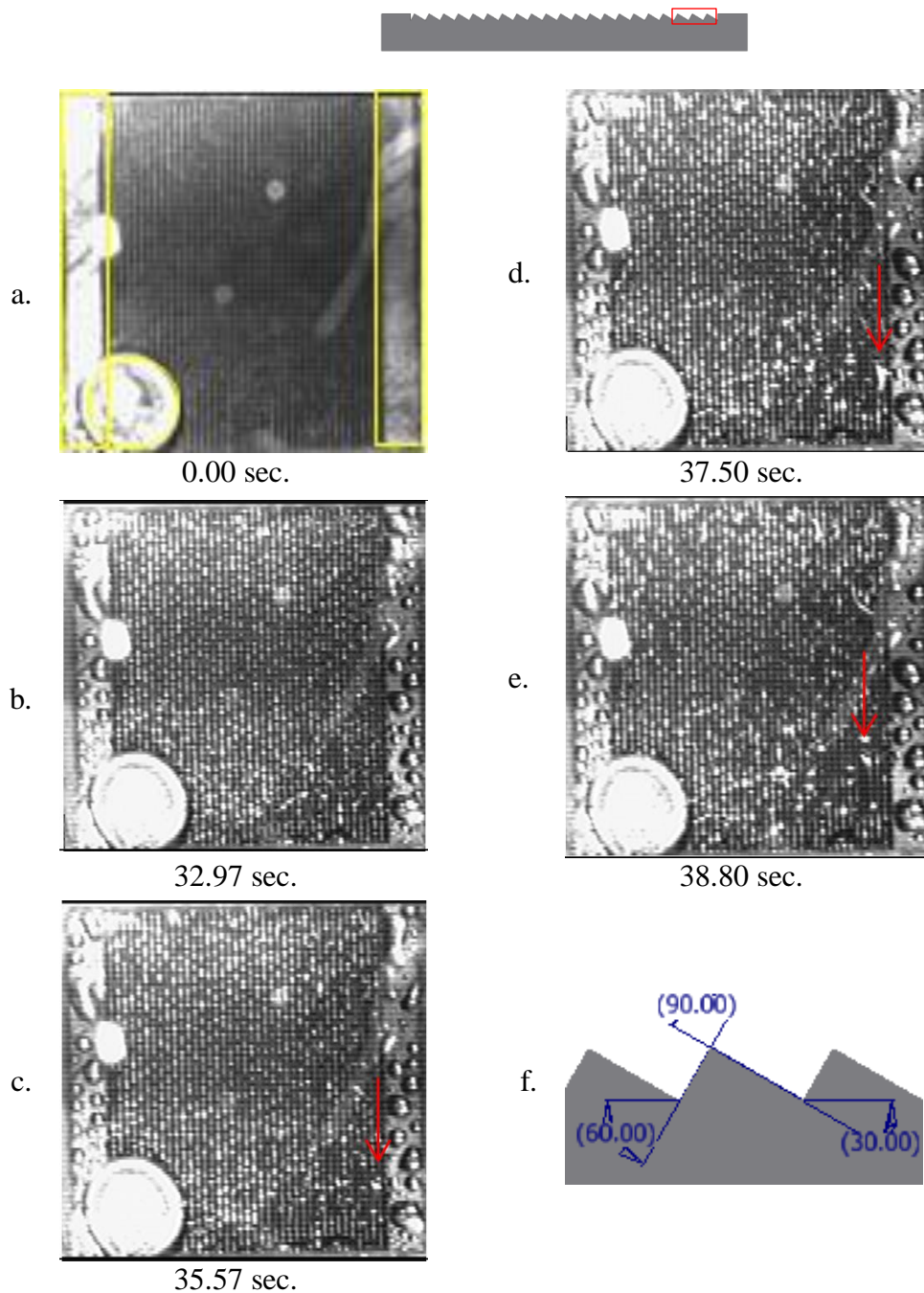


Figure 4.11: Images of condensation on a 500 $\mu\text{m}$  pitch ratcheted hydrophobic test surface. The diagram above the images shows the orientation of the ratchets. a. Surface just before condensation begins. b. several large droplets populate the flat, un-ratcheted, sections of the test section and elongated droplets occupy most of the area in the valleys between ratchet peaks. c. A large droplet has formed on the ratcheted portion of the surface rather than on the flats (second ratchet from the right). d. The droplet coalesces with other smaller droplets becoming almost large enough to spill over the ratchet crest. e. The fluid has spilled over the ratchet crest and coalesced with the droplets filling the neighboring ratchet (third ratchet from the right). Images were taken at a rate of 30 frames per second. f. Detail view with dimensions of CAD model of ratchets.

This activity was observed mostly early in an experiment when the average droplet diameter was relatively small. Although, condensate motion in a preferred direction was exhibited on these surfaces there was no self-clearing of the surface during the experiments and condensate droplets continued to grow until the surfaces eventually became flooded with condensate. Complete flooding of the surface generally occurred after 20 minutes of condensation activity.

An interesting trend between ratchet size and condensation heat transfer coefficients of deionized water vapor on hydrophobic test surfaces is shown by the plot in Figure 4.12. Surfaces with smaller ratchets tended to produce higher heat transfer coefficients than surfaces with larger ratchets for a given surface  $\Delta T$ . It is believed that the improved heat transfer coefficients measured on surfaces with smaller ratchets compared to surfaces with larger ratchets could be caused by condensate droplets moving more readily over smaller ratchets because the droplet grows to a large enough size to reach the crest of the ratchet more quickly and is therefore able to coalesce with droplets occupying neighboring ratchets sooner. This produces more motion events in a given amount of time. And just as on a vertical dropwise condensing surface, each motion event leaves a small area of bare surface where the moving droplet previously resided [42]. Very small droplets, which impose a much smaller thermal resistance than the large droplet previously occupying the space, then form on the bare area, creating an area of high heat transfer each time a droplet moves [55].

The largest separation of heat transfer coefficients between the surfaces tested occurs at lower temperature differences which in turn occurred earlier during experiments when condensate motion was more frequent. This separation closes completely at the

higher temperature differences that were produced near the end of experiments when the test surfaces were nearly entirely covered with very large condensate drops.

The pressure rise that characterizes these experiments was constant and linear and is represented in the plot inset on Figure 4.12.

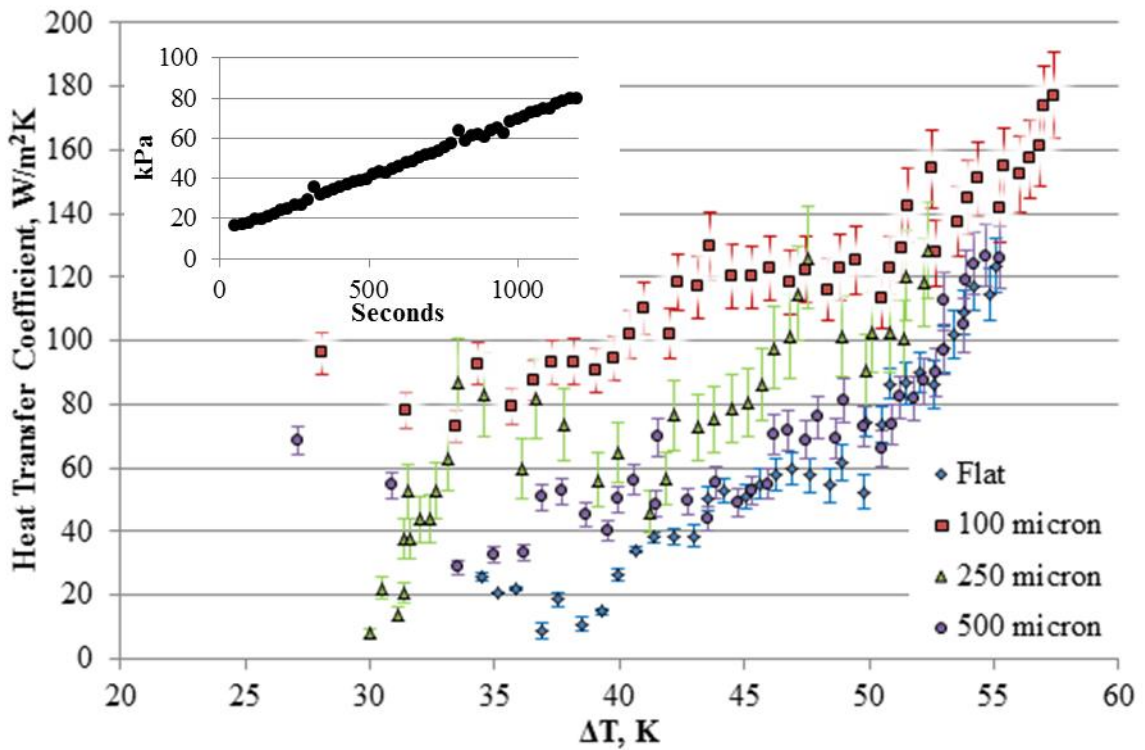


Figure 4.12: Condensation heat transfer coefficient as a function of  $\Delta T$  for deionized water on hydrophobic surfaces. Inset plot shows representative pressure rise for these experiments.

#### 4.2.2 Controlled Pressure Rise Experiments

In this group of experiments the heaters were modulated allowing only a 17 kPa (2.4 psi) pressure rise over the course of a 10 minute experiment. All experiments employed deionized water as the working fluid which was condensed on 100  $\mu\text{m}$ , 250  $\mu\text{m}$ , and 500  $\mu\text{m}$  pitch 30°-60°-90° asymmetric triangular profile hydrophobic ratcheted surfaces, 250  $\mu\text{m}$  pitch 18°-44°-118° and 9°-26°-145° asymmetric triangular profile hydrophobic ratcheted surfaces, 500  $\mu\text{m}$  pitch 30°-60°-90° asymmetric triangular profile biphilic ratcheted surfaces and hydrophobic flat control surfaces. Experiments were performed to measure the effect of surface tilt on condensate dynamics and condensation heat transfer rates. The orientations tested were 0° (horizontal), 1° left and right, 5° left and right, and 10° left and right (not all surfaces were tested at all orientations). As before, the boiler was charged with one liter of deionized water before each experiment.

The test surfaces were freshly coated and regularly stripped and recoated during experimentation to maintain consistent surface characteristics as contamination of these freshly coated surfaces with the thermal grease used to attach the surfaces to the measurement head would degrade the hydrophobic properties of the coating.

The results gathered from the horizontal orientation tests were unexpected and frankly somewhat disappointing. It was expected that the fresh hydrophobic coating on the ratcheted surfaces would improve droplet mobility and thereby the heat transfer coefficients however in reality the opposite occurred. No significant droplet mobility was observed on ratcheted surfaces; in fact the ratchets may have hindered droplet mobility as coalescence events tended to happen along the ratchets rather than across

them. This led to the heat transfer coefficients for all ratcheted surfaces being lower than those measured on the flat control surface as shown in Figure 4.13. (Data presented in the following comparison plots are the average of all test runs performed on a certain surface type at the parameters noted. The downward trend in heat transfer coefficients with increasing  $\Delta T$ —opposite from data presented in previous section—apparent in Figure 4.13 is due to the boiler heater modulation.)

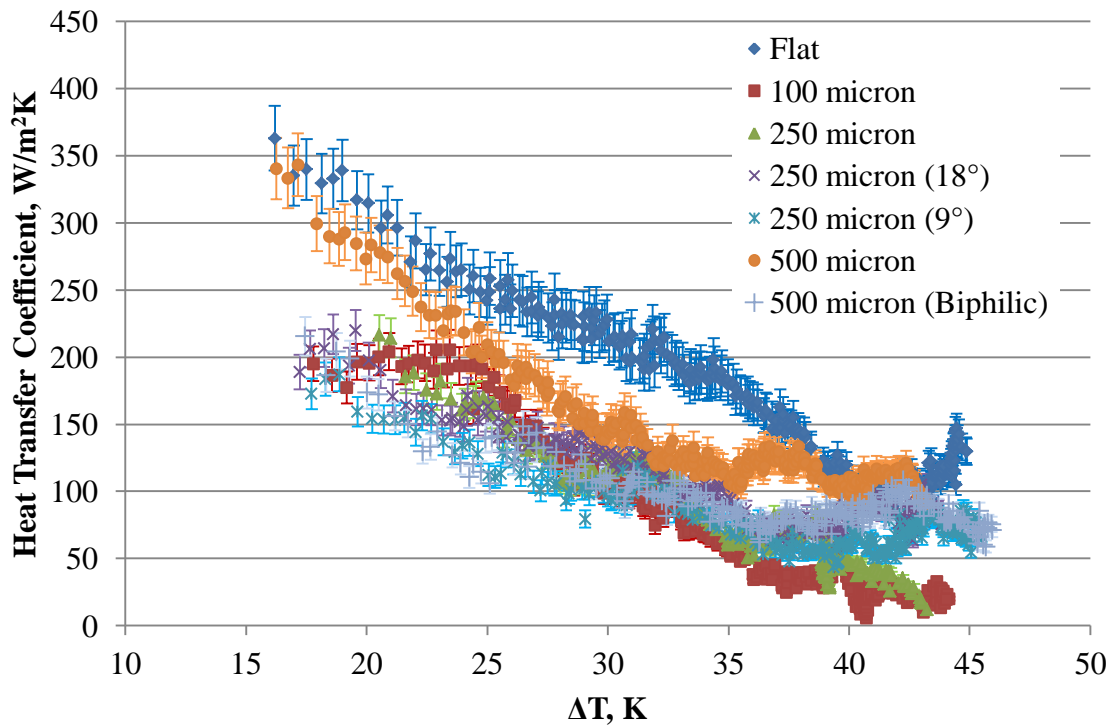


Figure 4.13: Plot of heat transfer coefficients as a function of  $\Delta T$  on horizontally oriented test surfaces for all surface configurations.

Additionally there was no real distinction in performance between ratchet surfaces other than the hydrophobic 500  $\mu\text{m}$  ratcheted surface exhibiting slightly higher values of

heat transfer coefficient than the surfaces with other ratchet sizes, ratchet profiles and wettability.

Since very little across-ratchet droplet mobility was present in these tests, roll-off angle tests were performed on all surfaces. In these tests, one surface at a time was placed on a tilt table such that the axis of tilt was parallel to the ratchets and leveled. Then a droplet was placed in the middle of the test surface using a small gauge syringe and the surface was tilted until the droplet rolled off across the ratchets. Tilt angle readings were taken using a digital angle meter with  $0.1^\circ$  resolution. Two droplet volumes were tested and surfaces were tilted in both left and right directions as shown in Figure 4.14. Each test was performed several times and the results were averaged. The data gathered from this testing is given in Table 4.1. An image of the two sizes of droplets tested is shown in Figure 4.15.

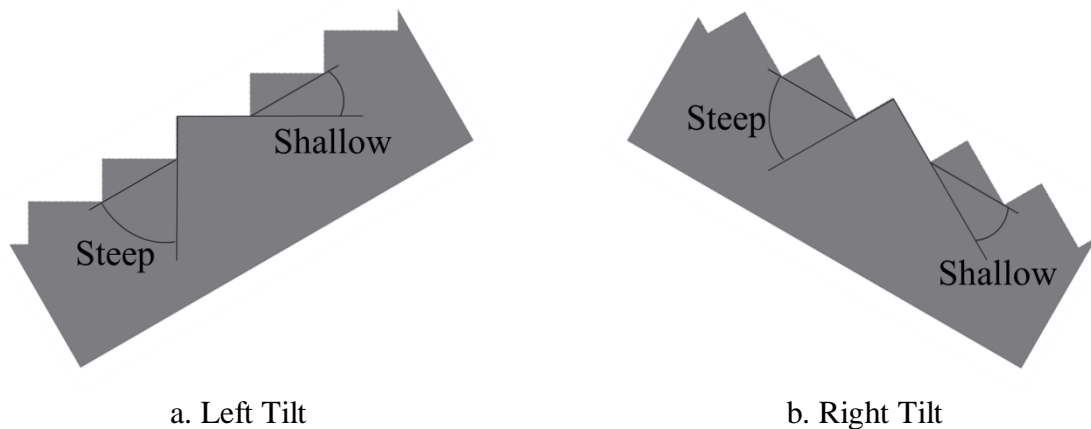


Figure 4.14: Illustration of tilt direction and ratchet orientation for roll-off angle tests. a. (left tilt) Long, shallow slope of ratchet is up. b. (right tilt) Short, steep slope of ratchet is up.

Table 4.1: Average roll-off angle

Surface	0.01cc		0.05cc	
	Left	Right	Left	Right
Flat	0.73°	0.7°	0.4°	0.4°
100 μm	1.23°	1.43°	0.26°	0.3°
250 μm	1.2°	1.26°	0.33°	0.36°
500 μm	0.63°	1.83°	0.1°	0.25°
250 μm (9°)	0.93°	1.03°	0.26°	0.33°
250 μm (18°)	0.8°	0.87°	0.2°	0.26°
500 μm Biphilic	6.63°	9.7°	1.33°	2°



Figure 4.15: Image of 0.01cc and 0.05cc droplet on 500 μm ratcheted hydrophobic test surface

A few key observations can be made from these data: 1. Droplets roll off of these surfaces at relatively low angles indicating a high degree of mobility that wasn't seen in the horizontal surface condensation experiments, and 2. Slightly less tilt is required for droplets to roll off when tilted to the left on ratcheted surfaces, this is most prominent on

the 500 $\mu\text{m}$  surfaces. One will also notice that the larger droplets required less tilt to roll off of the surface than the smaller droplets; this is to be expected, as explained in [54] heavier droplets overcome retention forces on a tilted surface more readily than lighter droplets.

Additional condensation experiments were performed at 1°, 5°, and 10° left and right tilts for many of the surfaces to determine if slightly changing the orientation of these surfaces could promote more droplet mobility and higher heat transfer coefficients and to determine if there was a direction of tilt that did so more than the other. Again the results were not what were expected. For most surfaces tilt had little effect on the heat transfer coefficient. The 100  $\mu\text{m}$  and 250  $\mu\text{m}$  ratcheted surfaces did show a slight increase in heat transfer coefficients during the tilted condensation experiments however as can be seen in Figure 4.17 all tilt angles, left and right performed about the same. The surfaces that did show a substantial heat transfer coefficient increase associated with a specific tilt angle and direction were the shallow ratchet test surfaces comparison plots of these surface's heat transfer coefficients in several configurations are given in Figure 4.16. These surfaces both performed significantly better when tilted 10° to the left. One of these surfaces has a long ratchet slope angle of 9° and the other has a long ratchet slope of 18° as opposed to 30° for the rest of the ratchet surfaces meaning that when tilted 10° to the left, the long ratchet slopes on these surfaces were very close to horizontal. Condensate was removed from these surfaces during the experiments however it was in the form of large sheets of condensation that didn't entirely leave the surface rather than discrete droplets, an example of this is shown in Figure 4.18.



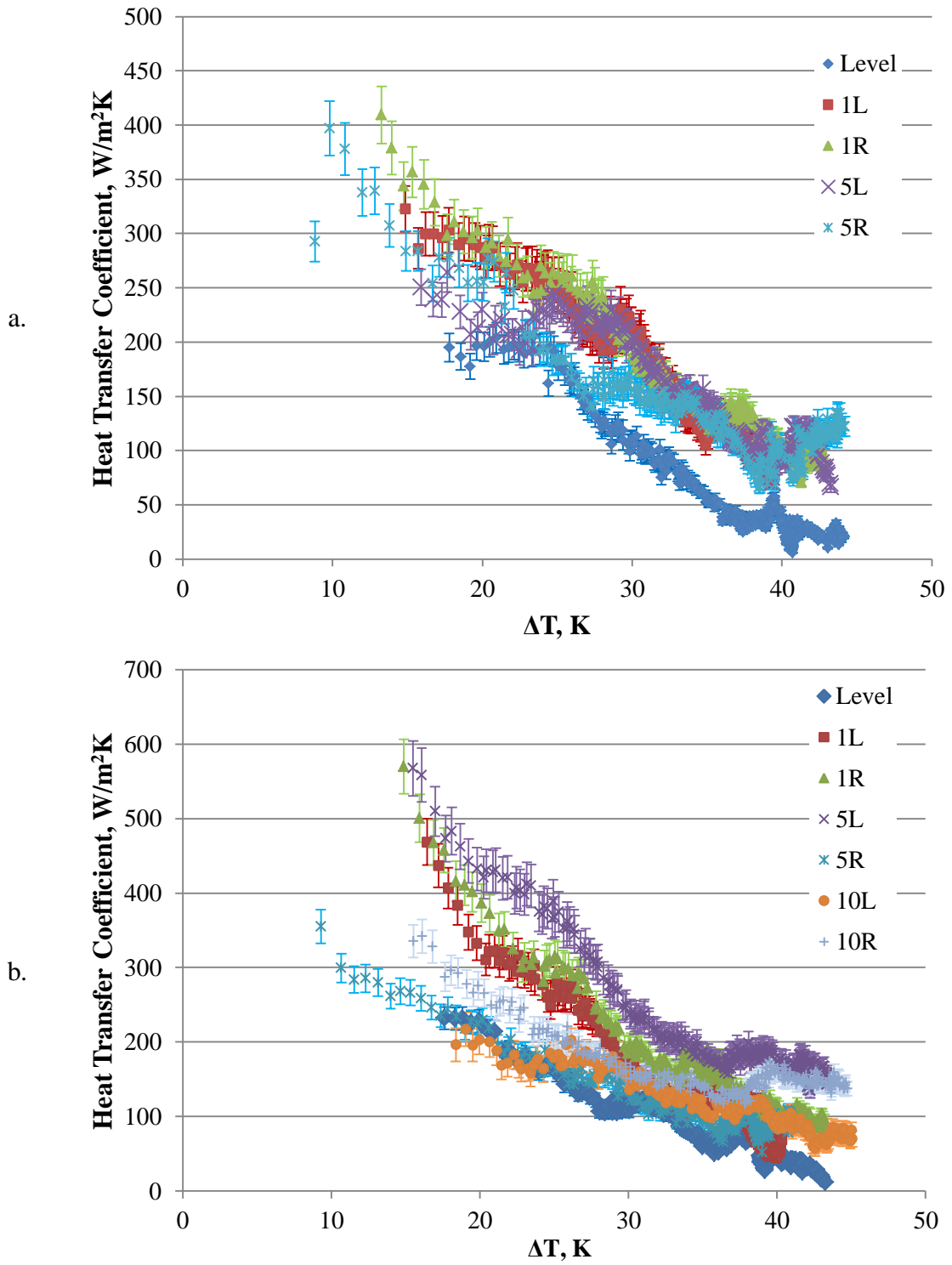


Figure 4.16: Heat transfer coefficient as a function of  $\Delta T$  for all tilt configurations tested on a. 100  $\mu\text{m}$  hydrophobic ratcheted surfaces and b. 250  $\mu\text{m}$  hydrophobic ratcheted surfaces.

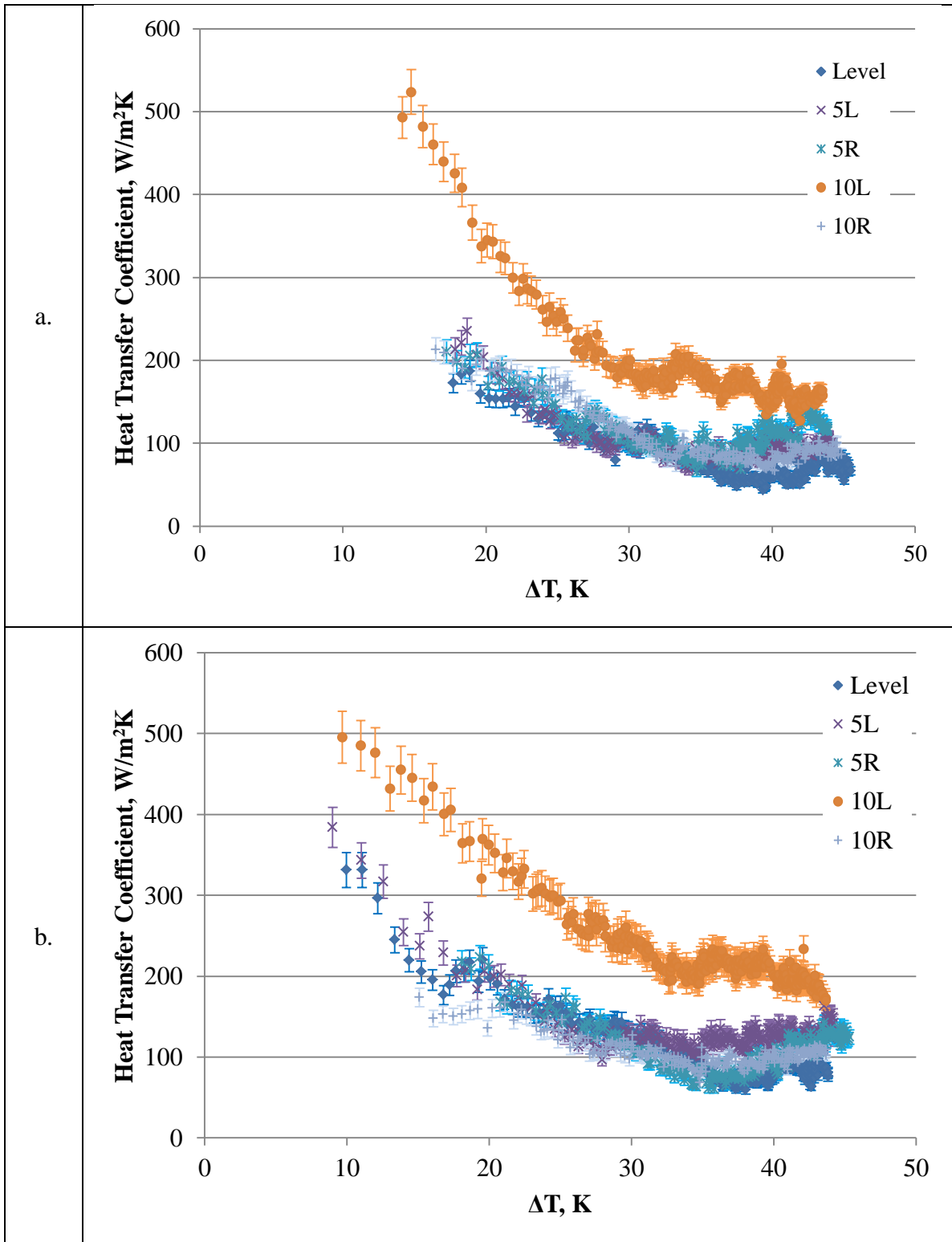


Figure 4.17: Heat transfer coefficient as a function of  $\Delta T$  for all tilt configurations tested on a. 250  $\mu\text{m}$  9° hydrophobic ratcheted surfaces and b. 250  $\mu\text{m}$  18° hydrophobic ratcheted surfaces.

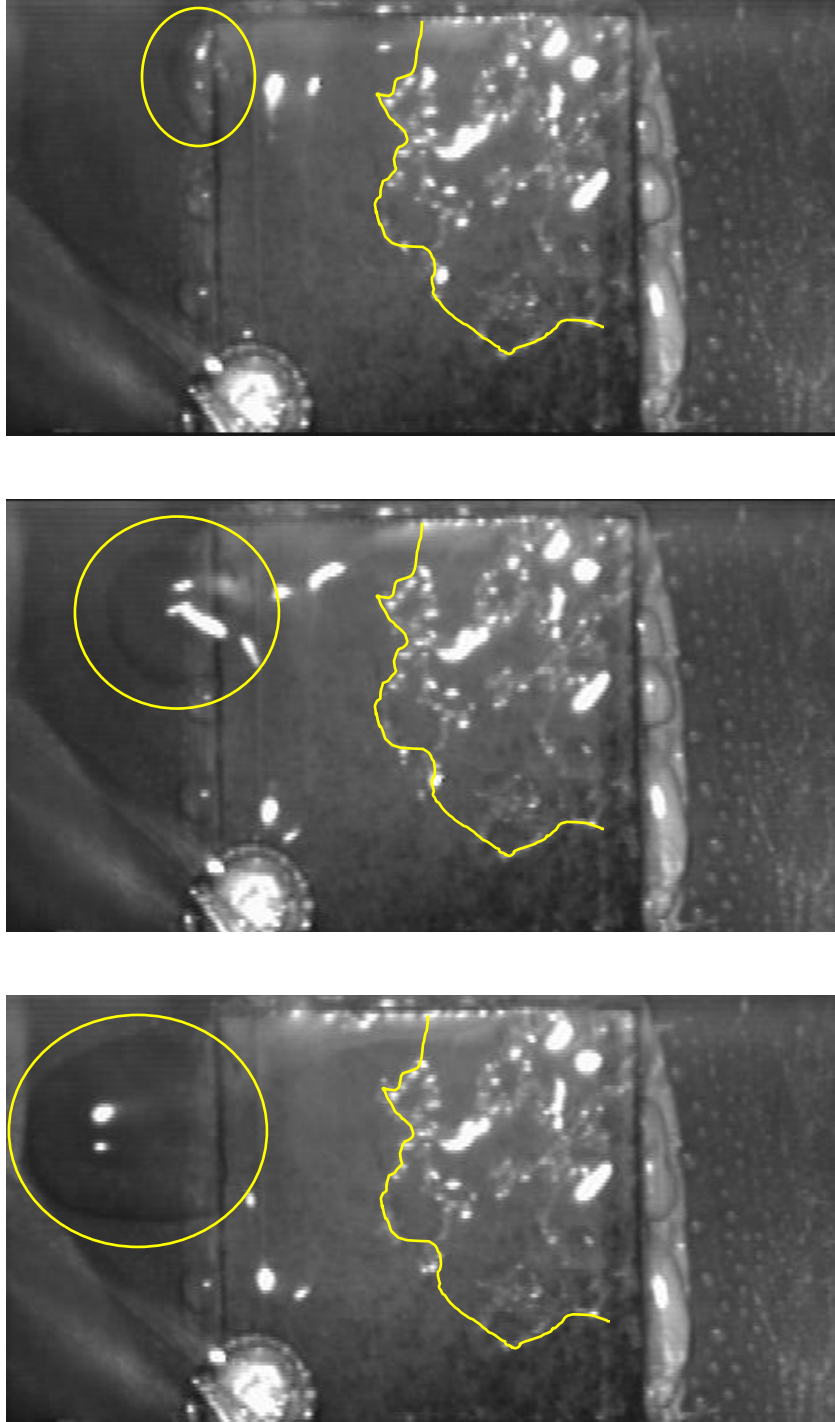


Figure 4.18: Images of condensate removal from 250  $\mu\text{m}$   $18^\circ$  hydrophobic ratcheted surface notice that the area where the condensate draining occurred remained wet after drainage. Contact line (marked in yellow) doesn't move even after large amount of condensate (yellow ovals) leaves the test surface.

Since tilting the test surfaces during condensation experiments, even to degrees much larger than that required to cause a deposited droplet to roll off of the surface still didn't produce a dramatic increase in condensate mobility even on the flat control surface it is clear that the hydrophobic surface coating was inhibiting droplet motion. Since the NeverWet coating applies a microstructure to the surface, droplets can exist on the surface in one of two states; the Cassie-Baxter state and the Wenzel state. As discussed in Chapter 1, a droplet in the Cassie-Baxter state sits on top of the surface microstructure and therefore actually has very little contact with the surface which allows droplets in this state to be highly mobile. In the Wenzel state, a droplet fills the surface microstructure and is consequently held in place by the microstructure. It appears that deposited droplets on these surfaces existed in the Cassie-Baxter state and condensate existed in the Wenzel state. This is supported by images taken during condensation experiments where coalescing droplets do not return to a spherical shape after coalescence and instead feature an irregular perimeter as shown in Figure 4.19 (compare to Figure 1.3 for examples of Wenzel and Cassie-Baxter droplets). Droplets in the Wenzel state are very detrimental to condensation heat transfer as droplets on a hydrophobic surface tend to be taller than the thickness of a condensate film and if these droplets can't move and drain from the surface they impose a larger thermal resistance a condensate film would.

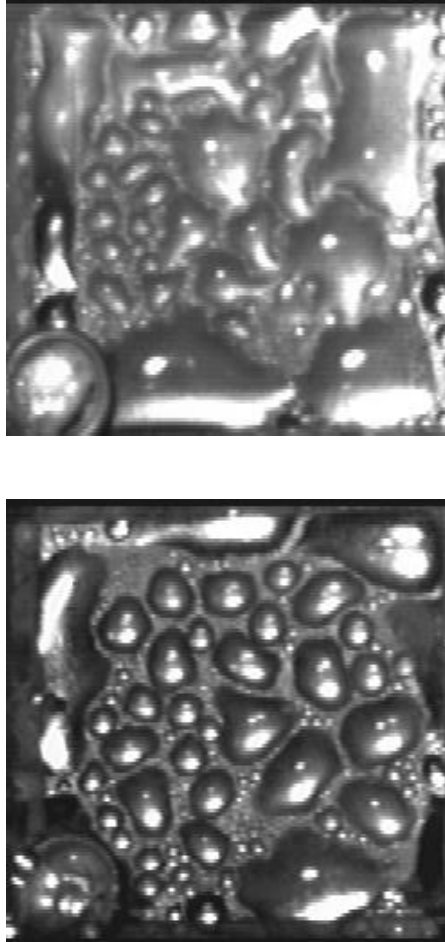


Figure 4.19: Images of condensate drops on 250  $\mu\text{m}$  hydrophobic ratcheted surface tilted 5 degrees to the right (above) and flat hydrophobic control surface tilted 5 degrees to the left. Irregular droplet perimeters indicate Wenzel state as discussed in [8].

### **4.3 Dropwise Condensation Heat Transfer Coefficient Model**

Even though dropwise condensation is the preferred mode of condensation and there has been significant recent interest in developing durable superhydrophobic surfaces capable of maintaining this mode of condensation for extended periods, there are surprisingly few models for predicting the heat transfer coefficient during dropwise condensation. The most commonly used model was proposed by Rose and his coworkers

[56, 57]. In this model the heat flux through a single drop and into the condenser surface is calculated by:

$$q_d = \frac{(\Delta T_t - 2\sigma v_l T_{sat}/rh_{lv})}{\left(\frac{K_1 r}{k_l} + \frac{K_2 v_v T_{sat}}{h_{lv}^2} \left(\frac{\hat{\sigma} + 1}{\hat{\sigma} - 1}\right) \sqrt{\frac{RT_{sat}}{2\pi}}\right)} \quad (4.4)$$

Where  $\Delta T_t$  is the difference between the surface temperature and the saturation temperature,  $r$  is the drop radius,  $R$  is the specific gas constant (461.5 J/kgK for water vapor), and  $\hat{\sigma}$  is the accommodation coefficient (taken as 0.03 for condensation of water).  $\sigma$ ,  $v_l$ ,  $v_v$ ,  $h_{lv}$ ,  $k_l$  and  $T_{sat}$  are the fluid properties surface tension, liquid specific volume, vapor specific volume, latent heat of vaporization, liquid thermal conductivity and saturation temperature respectively.  $K_1$  and  $K_2$  are constants [56].

To calculate the heat flux for the entire surface, first the drop size distribution must be known. The drop size distribution is represented as a cumulative distribution function having the form of:

$$f(r) = 1 - \left(\frac{r}{r_{max}}\right)^n \quad (4.5)$$

This function defines the fraction of the surface covered by drops with a radius between  $r$  and that of the largest drop present on the surface,  $r_{max}$ . To prepare for integration a related distribution function  $G(r)$  is defined such that  $G(r)dr$  is equal to the fraction of the surface covered by drops with a radius between  $r$  and  $r + dr$ :

$$G(r) = -\frac{df}{dr} = \frac{nr^{n-1}}{r_{max}^n} \quad (4.6)$$

The heat flux for the entire surface is calculated by multiplying Equation 4.4 and the drop size distribution, equation 4.6, and then integrating from the smallest drop radius to the largest:

$$q'' = \int_{r_{min}}^{r_{max}} q_d G(r) dr \quad (4.7)$$

Where  $r_{max}$  and  $r_{min}$  are the maximum and minimum drop radii present on the surface.

Using Newton's law of cooling the heat transfer coefficient is defined as:

$$h = \frac{q''}{\Delta T} = \frac{1}{\Delta T_t} \int_{r_{min}}^{r_{max}} q_d G(r) dr \quad (4.8)$$

Substituting for  $q_d$  and  $A(r)$  yields an equation for the dropwise condensation heat transfer coefficient:

$$h_{dc} = \left( \frac{n}{r_{max}^n \Delta T_t} \right) \int_{r_{min}}^{r_{max}} \frac{(\Delta T_t - 2\sigma v_l T_{sat} / r h_{lv})}{\left( \frac{K_l r}{k_l} + \frac{K_2 v_v T_{sat}}{h_{lv}^2} \left( \frac{\hat{\sigma} + 1}{\hat{\sigma} - 1} \right) \sqrt{\frac{RT_{sat}}{2\pi}} \right)} r^{n-1} dr \quad (4.9)$$

The constants  $K_1$ ,  $K_2$  and  $n$  have proposed best fit values for steam of  $K_1 = 2/3$ ,  $K_2 = 1/2$ , and  $n = 1/3$  [56, 57].

In order to properly use equation 4.9 the maximum and minimum drop radii on the surface at any instant the heat transfer coefficient would be calculated must be known. The maximum drop radius is usually easy to measure from images as was done for the calculations in this study using National Instruments Vision Assistant software. To measure the maximum drop radius an image taken from the video data at the appropriate time was opened in the NI Vision assistant software. The perimeters of several of the largest droplets were traced to calculate the area inside the perimeter to identify the largest droplet. Since some of these large drops are the product of recent coalescence events they may have a slight oval shape, therefore the equivalent radius of the largest droplet is calculated using the equation for the area of a circle and solving for  $r$ . All measurements up to this point are measured in units of pixels; to convert to millimeters first the width of the 25mm test surface is measured in pixels to obtain a conversion factor. Figure 4.20 contains screen capture images of large droplets on a flat test surface after their perimeters have been traced using the Vision Assistant Software.

The smallest drops on a surface (often  $<10\mu\text{m}$ ) are usually too small to be seen without a microscope which means that direct measurement of the smallest drop radius present on a surface is at least impractical if not impossible. There have been many studies focused on determining accurate drop size distributions on condenser surfaces [57-62] however currently there are no accurate methods for determining the radius of the smallest drop present on a textured hydrophobic condenser surface such as those used in



this study and the hierarchical micro-nano textured superhydrophobic surfaces developed for other studies [4, 7, 8].

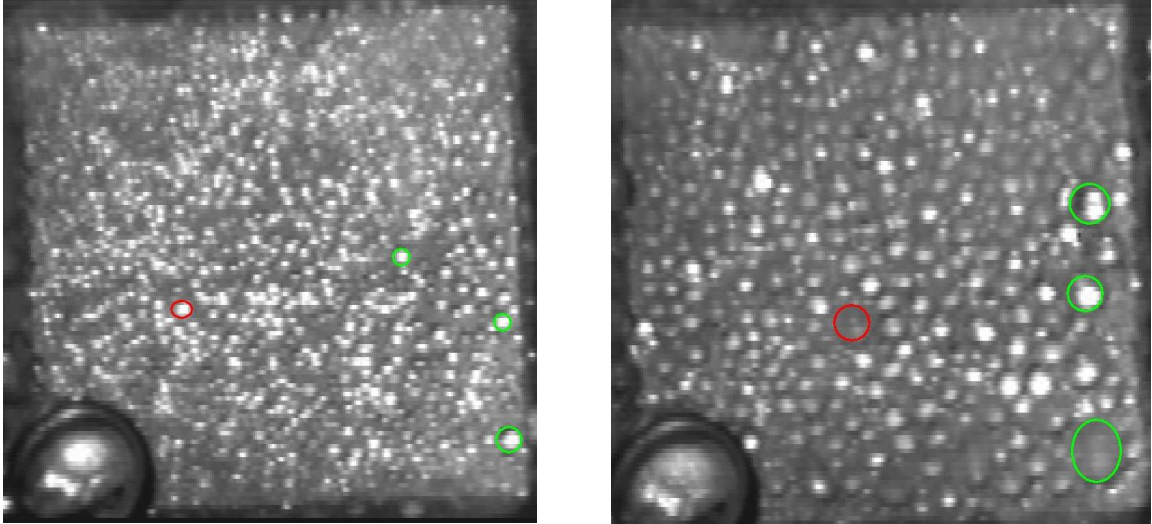


Figure 4.20: Images of maximum droplet radius measurement on flat test surface for two data points; 2 minutes elapsed time (left) and 6 minutes elapsed time (right)

For very small drops there must be a temperature difference between the drop and the saturation temperature for the droplet to exist [42], this temperature difference can be calculated using equation 4.10 as found in [63]:

$$\Delta T_e = \frac{2v_l\sigma T_w}{h_{lv}r} \quad (4.10)$$

This equation can be rearranged to calculate the smallest thermodynamically stable droplet radius, or equilibrium radius  $r_e$ , for a certain saturation pressure, subcooling and fluid. Since the condenser surface is the location that provides the maximum subcooling  $\Delta T_e$  is replaced with  $T_{\text{sat}} - T_w$  yielding equation 4.11.

$$r_e = \frac{2v_l\sigma T_w}{h_{lv}(T_{sat} - T_w)} \quad (4.11)$$

This equation has been used with good results to calculate the minimum drop radius for metallic condenser surfaces with a mirror polish [57, 59, 63, 64] but underestimates the minimum drop radius on the NeverWet coated silicon surfaces used in this study. Figure 4.21 shows a plot of heat transfer coefficient data collected overlaid with heat transfer coefficients calculated using Equation 4.9 and choosing values  $r_{min}$  that fit the data for water condensation on a flat, level hydrophobic silicon test surface experiment. The values of  $r_e$  calculated,  $r_{min}$  used and  $r_{max}$  measured are provided in Table 4.2.

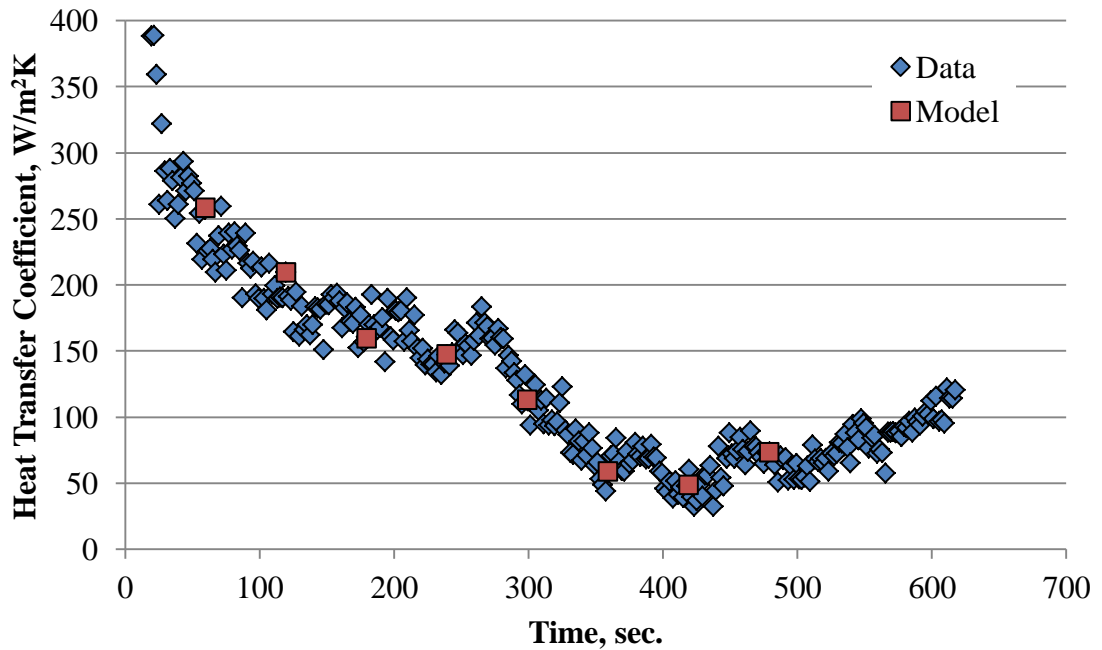


Figure 4.21: Heat transfer coefficient as function of time (collected data and model) for flat level hydrophobic silicon surface.

Table 4.2:  $r_e$ ,  $r_{min}$ , and  $r_{max}$  values for flat level hydrophobic silicon surface

Time (sec.)	$r_e$ (m)	$r_{min}$ (m)	$r_{max}$ (m)
59.93	4.57E-10	9.54E-06	3.74E-04
119.86	3.81E-10	9.76E-06	6.60E-04
179.8	3.74E-10	1.11E-05	7.79E-04
239.73	3.43E-10	1.14E-05	8.93E-04
299.7	3.47E-10	1.33E-05	9.27E-04
359.63	3.30E-10	1.82E-05	0.0014
419.56	3.17E-10	2.01E-05	0.0015
479.5	3.11E-10	1.54E-05	0.0017

As can be seen from the values in Table 4.2 the values used for  $r_{min}$  are significantly larger than the equilibrium radius calculated. This indicates that the texturing on the test surfaces may affect the size of the smallest possible drop on the surface. This exercise was also performed for data gathered from experiments on 100  $\mu\text{m}$ , 250  $\mu\text{m}$ , and 500  $\mu\text{m}$  pitch 30°-60°-90° asymmetric triangular profile hydrophobic ratcheted surfaces. Figures 4.22 through 4.24 contain plots of heat transfer coefficient data collected overlaid with heat transfer coefficients calculated using Equation 4.9 and choosing values  $r_{min}$  to fit the data for these surfaces. Tables 4.3 through 4.5 contain the values of  $r_e$  calculated,  $r_{min}$  used and  $r_{max}$  measured for these surfaces.

After comparing the selected  $r_{min}$  versus  $r_e$  values it was clear that the surface micro texturing did not affect the shift required to fit calculated heat transfer coefficients to the data. This makes sense as the ratchet features are much larger than the calculated minimum drop radii.

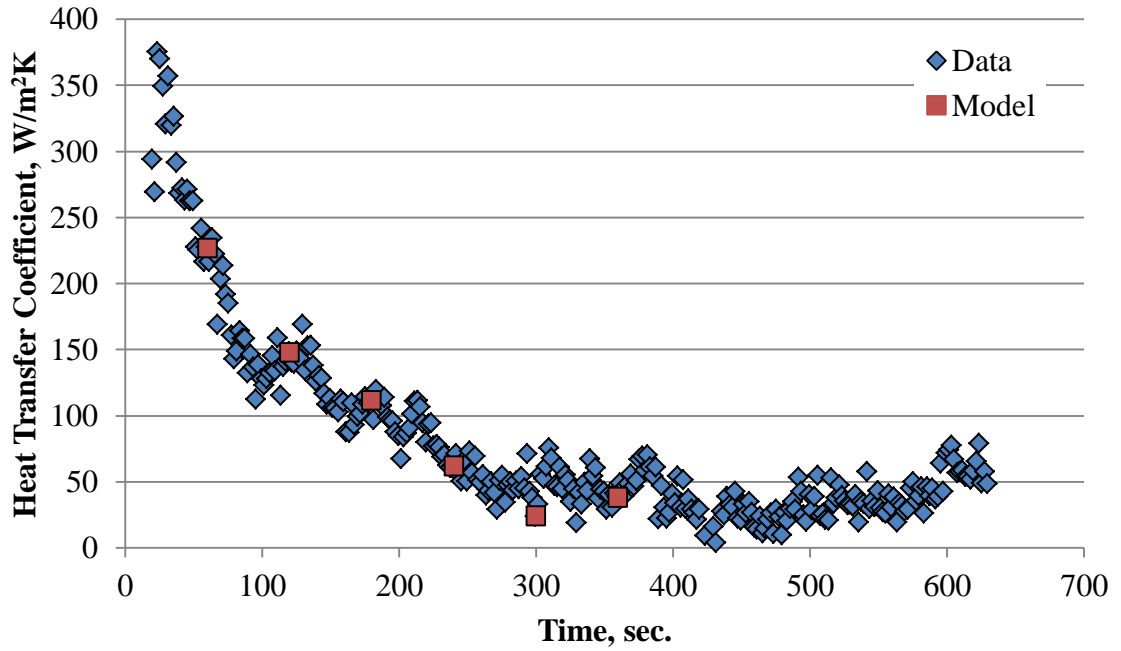


Figure 4.22: Heat transfer coefficient as function of time (collected data and model) for level 100µm ratchet pitch hydrophobic silicon surface.

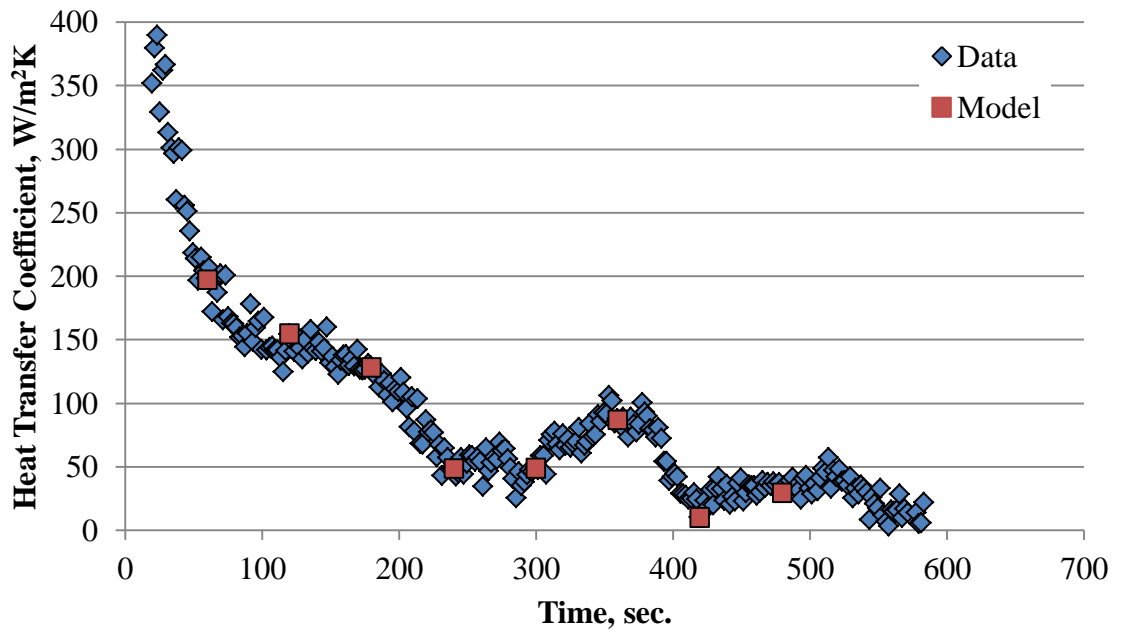


Figure 4.23: Heat transfer coefficient as function of time (collected data and model) for level 250µm ratchet pitch hydrophobic silicon surface.

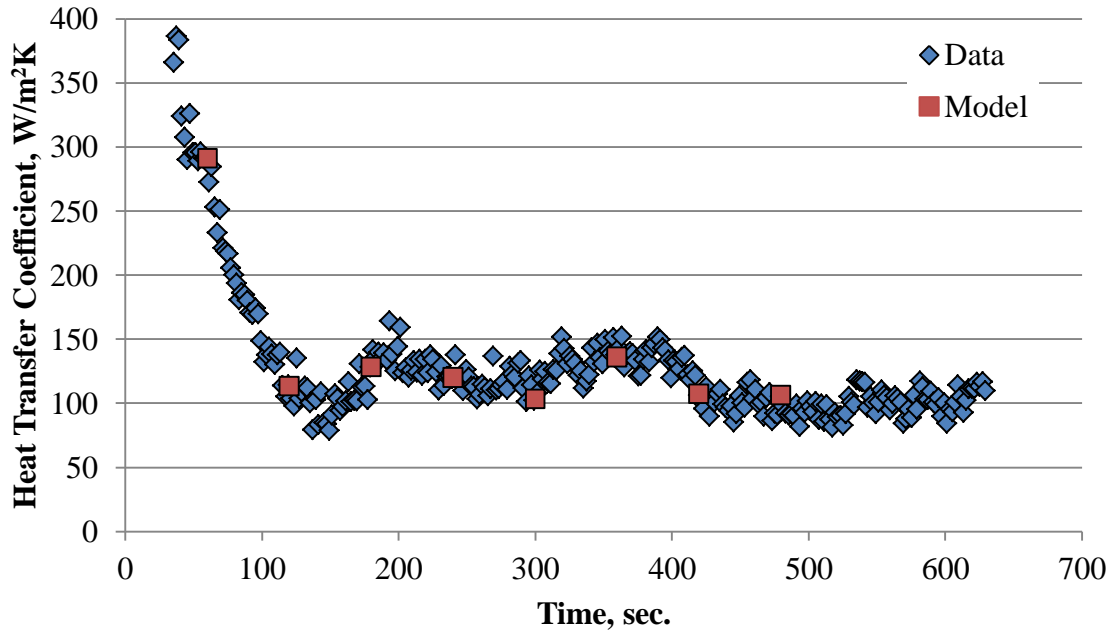


Figure 4.24: Heat transfer coefficient as function of time (collected data and model) for level 500µm ratchet pitch hydrophobic silicon surface.

Table 4.3:  $r_e$ ,  $r_{min}$ , and  $r_{max}$  values for level 100µm ratcheted hydrophobic silicon surface

Time (sec.)	$r_e$ (m)	$r_{min}$ (m)	$r_{max}$ (m)
59.93	5.27E-10	1.06E-05	3.10E-04
119.86	3.79E-10	1.08E-05	1.10E-03
179.8	3.63E-10	1.21E-05	1.50E-03
239.73	3.37E-10	1.57E-05	2.40E-03
299.7	3.30E-10	2.49E-05	4.00E-03
359.63	3.06E-10	1.85E-05	0.0046

Table 4.4:  $r_e$ ,  $r_{min}$ , and  $r_{max}$  values for level 250 $\mu$ m ratcheted hydrophobic silicon surface

Time (sec.)	$r_e$ (m)	$r_{min}$ (m)	$r_{max}$ (m)
59.93	4.47E-10	1.20E-05	2.66E-04
119.86	3.72E-10	1.28E-05	4.21E-04
179.8	3.21E-10	1.32E-05	6.78E-04
239.73	3.21E-10	2.16E-05	1.00E-03
299.7	3.11E-10	2.11E-05	1.10E-03
359.63	3.14E-10	1.46E-05	1.30E-03
419.56	2.88E-10	4.85E-05	2.00E-03
479.5	3.00E-10	2.43E-05	2.60E-03

Table 4.5:  $r_e$ ,  $r_{min}$ , and  $r_{max}$  values for 500 $\mu$ m ratcheted hydrophobic silicon surface

Time (sec.)	$r_e$ (m)	$r_{min}$ (m)	$r_{max}$ (m)
59.93	5.07E-10	8.57E-06	4.44E-04
119.86	3.91E-10	1.38E-05	7.16E-04
179.8	3.64E-10	1.24E-05	8.62E-04
239.73	3.71E-10	1.18E-05	1.30E-03
299.7	3.46E-10	1.28E-05	1.40E-03
359.63	3.51E-10	1.06E-05	0.0016
419.56	3.32E-10	1.16E-05	0.0021
479.5	3.24E-10	1.15E-05	0.0024

Figure 4.25 provides a plot of  $r_{min}$  as a function of  $r_e$  for all surfaces considered in this analysis (hydrophobic flat and hydrophobic 100 $\mu$ m, 250  $\mu$ m, and 500  $\mu$ m ratcheted surfaces). A linear fit trendline was generated from this plot and used in conjunction with equation 4.11 to predict  $r_{min}$  values rather than selecting them to fit the data to recalculate heat transfer coefficients for the data points modeled earlier. Plots of these modified

model calculated values along with the data and model calculations shown above are presented in Figures 4.26 through 4.29.

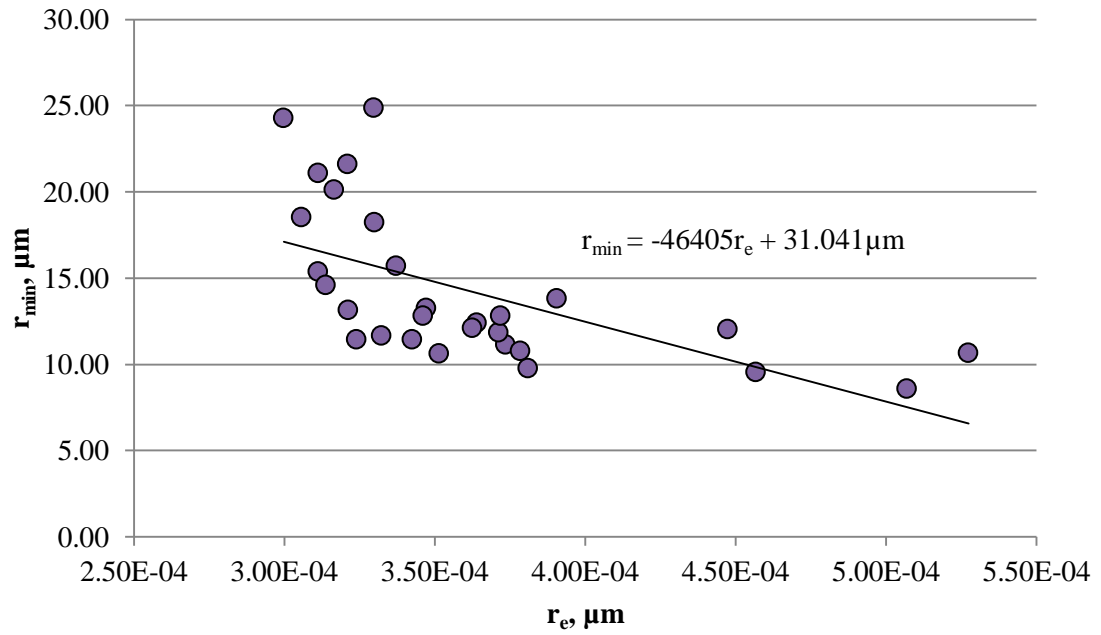


Figure 4.25:  $r_{min}$  as a function of  $r_e$  with trendline for data points on all surfaces considered in this analysis.

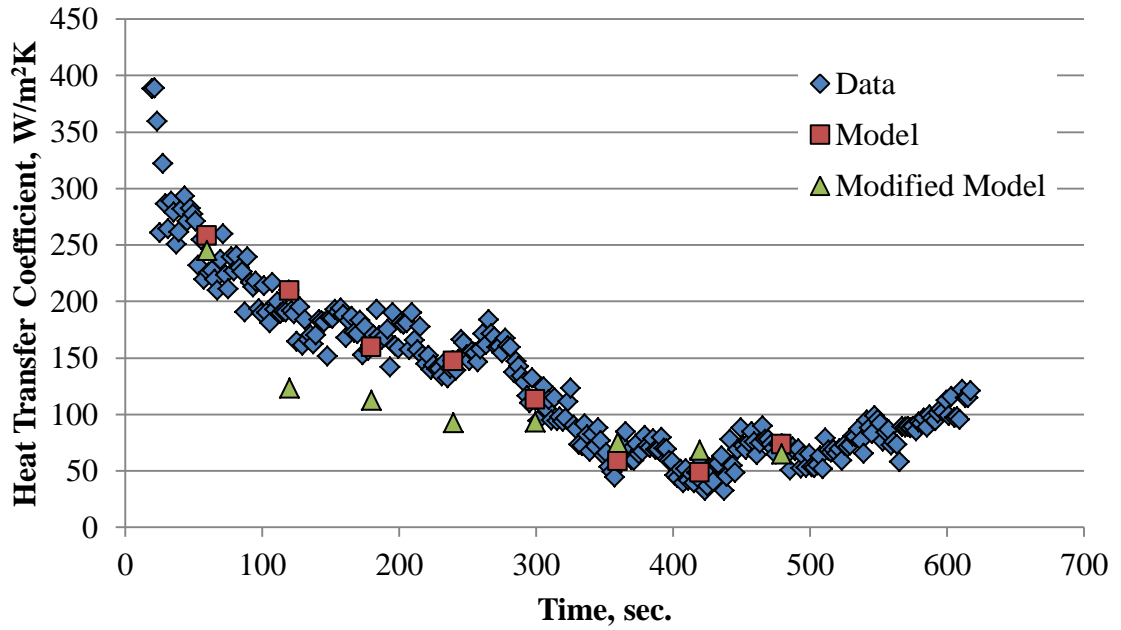


Figure 4.26: Heat transfer coefficient as function of time (collected data, model, and modified model) for flat level hydrophobic silicon surface.

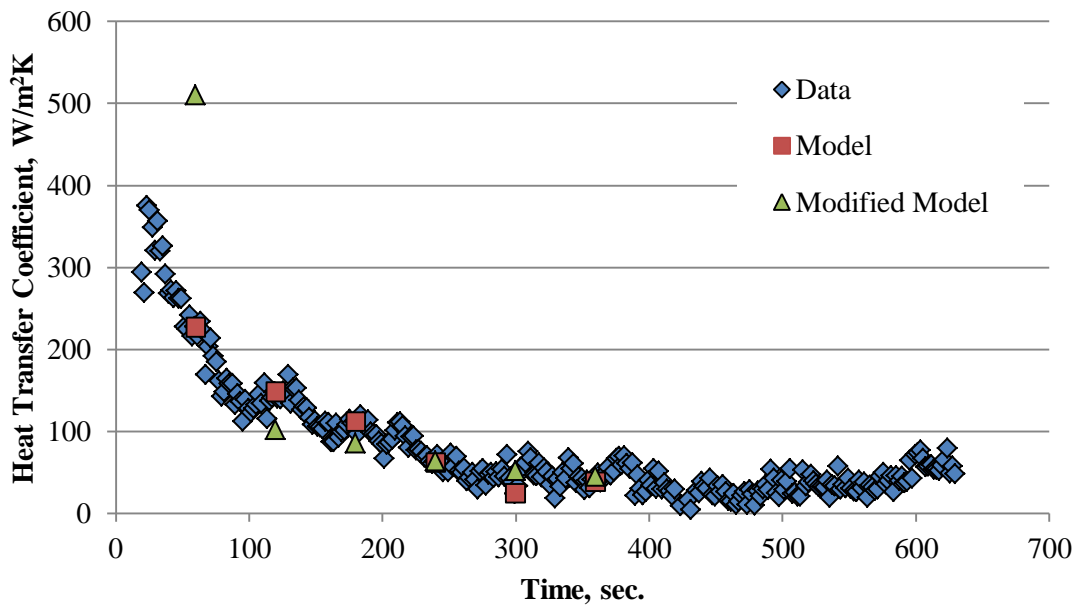


Figure 4.27: Heat transfer coefficient as function of time (collected data, model, and modified model) for level 100  $\mu\text{m}$  ratchet pitch hydrophobic silicon surface.



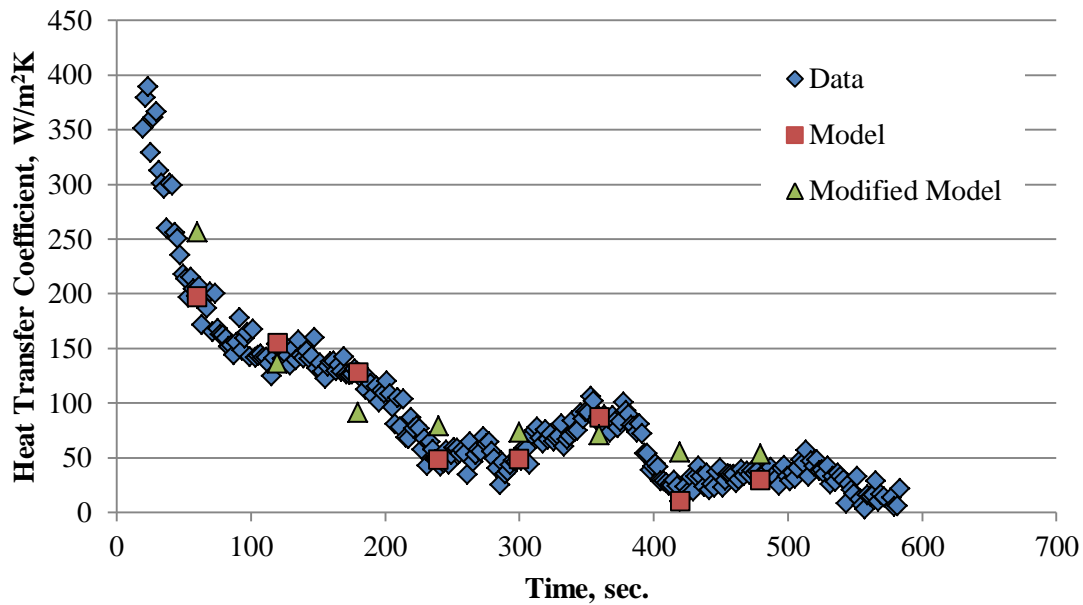


Figure 4.28: Heat transfer coefficient as function of time (collected data, model, and modified model) for level 250  $\mu\text{m}$  ratchet pitch hydrophobic silicon surface.

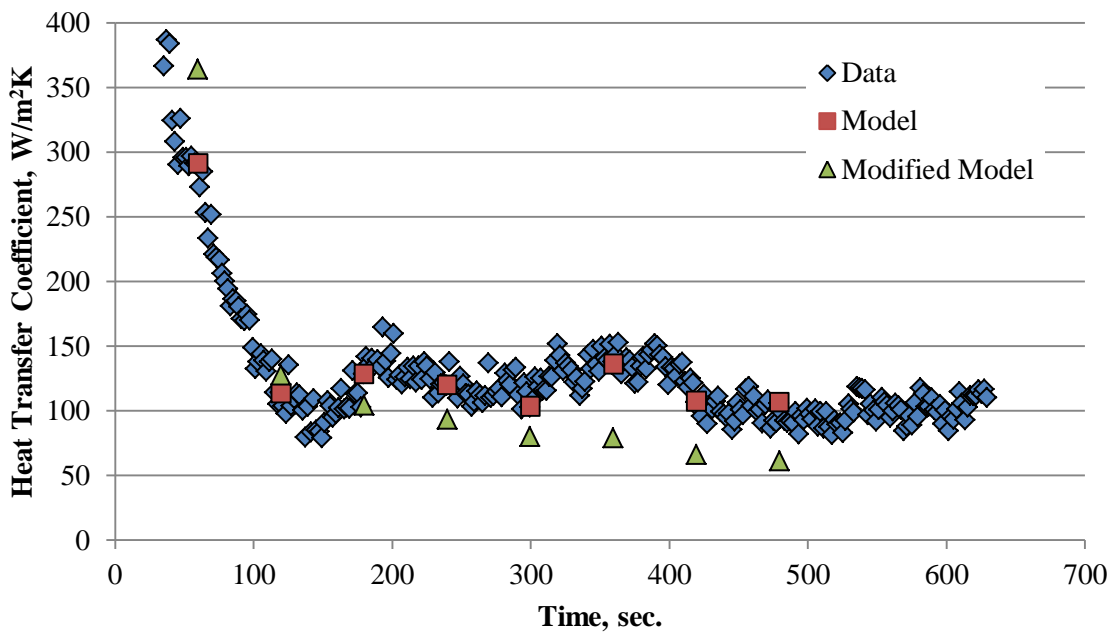


Figure 4.29: Heat transfer coefficient as function of time (collected data, model, and modified model) for level 500  $\mu\text{m}$  ratchet pitch hydrophobic silicon surface.

As seen from these plots the modified minimum drop radius calculation, while by no means perfect, does provide a decent prediction of the heat transfer coefficient on these surfaces. It is believed that the surface texturing imparted by the NeverWet coating is the cause of the larger minimum drop radii hypothesized to exist on these surfaces. Since control over the spacing of the micro and perhaps nano-particles that compose the coating is not possible, the surface texture features that are created during spray deposition and curing may form so closely together that embryonic droplets that form on these features may immediately coalesce with others prohibiting the stable formation of droplets with radii approaching the minimum thermodynamically stable drop size.

The obvious semi-empiricism used to predict  $r_{min}$  values by scaling  $r_e$  values in this proposed model could be improved by relating the minimum droplet radius shift to physical properties of the condenser surfaces. However accurate SEM (Scanning Electron Microscope) imaging of the NeverWet coating was impossible since it is a non-metallic coating and would require a 20-30 nm thick layer of gold deposited on the surface for the SEM to produce images which may obscure some of the smaller features. Rust-Oleum was contacted to request information about the particle size and surface texture of NeverWet however no response was received. In light of these limitations the above analysis represents the best prediction method available to the author for predicting heat transfer coefficients on the NeverWet coated silicon surfaces studied in this work.

## Chapter 5

### Conclusions and Recommendations

Two methods for increasing droplet mobility and thereby condensation heat transfer coefficients consisting of combinations of surface structure and wettability modifications were studied in this work. First, customized nano-composite superhydrophobic coatings with increased durability were successfully developed and applied to test surfaces fabricated from four of the most common power generation plant condenser tube materials—Admiralty brass, cupronickel, titanium and Sea-Cure stainless steel. These coatings were adapted for use on metallic substrates from an existing superhydrophobic coating called Repellix, originally designed for use on silicon surfaces. And second, several configurations of silicon surfaces featuring arrays of asymmetric saw-toothed ratchet structures similar to those shown in other studies to be effective at promoting directional fluid motion [10-14], were fabricated using grayscale lithography. Some of these surfaces were left bare and were therefore hydrophilic; these bare surfaces were paired with a highly wetting dielectric fluid (FC-72) for condensation experiments. The rest of the silicon ratchet surfaces were coated with Rust-Oleum's NeverWet multi-surface liquid repelling treatment and paired with deionized water for condensation experiments.

The following conclusions are drawn from experimentation performed to measure the effect of the above methods on droplet mobility and condensation heat transfer coefficients:

### **5.1 Custom Nano-composite Hydrophobic Coatings on Hemi-cylindrical Condenser Tube Test Surfaces**

- The vapor deposition process used to apply Repellix family surface treatments is very scalable and is able to be adapted to treat condenser tubes in-situ reducing the cost and labor required to implement this type of coating in power plant condensers. Applying the surface treatment in-situ eliminates the possibility of damage to the coating during tube handling and installation.
- Both methods used to increase the durability of Repellix family surface treatments on metallic substrates (Modified Repellix-addition of silica base layer. Repellix 2.0-use of plasma-enhanced protection layers) were shown to be effective. The results of water erosion tests show that Repellix 2.0 was significantly more hydrophobic (initial static contact angle measurements were in the superhydrophobic range) and more durable than Modified Repellix.
- For all coated test surfaces except for titanium surfaces (which produced the most droplet mobility), droplet mobility during condensation experiments was less than expected and led to reduced heat transfer coefficients as the stationary droplets had higher thicknesses than liquid films due to the increased contact angle (the greater thickness of these stationary drops imposes a larger thermal resistance than the thinner liquid films). This lack of droplet mobility would likely be remedied by the environment inside of a power generation plant condenser were

vapor flow and turbine vibrations would increase droplet removal rates however it would be of interest to further study the chemical interactions of the coating on the titanium surfaces that led to their increased droplet mobility (64% more roll-off events than the next most active surface) in the controlled experiment environment employed in this study.

## **5.2 Asymmetric Saw-toothed Ratchet Silicon Surfaces**

- Deposited drops on hydrophobic asymmetric ratcheted surfaces were observed to grow in a preferred direction (toward the short, steep ratchet slopes) when fluid was added to the drop through a small gauge syringe. The internal pressures and surface tension forces that cause this directional growth were calculated.
- Data collected showing heat transfer coefficients up to 57% higher than on flat surfaces for 500 $\mu$ m hydrophilic ratcheted surfaces condensing FC-72 vapor suggests that there is some condensate motion promoted by the larger hydrophilic ratchet structures, however no visual confirmation of fluid motion was observed.
- Droplet motion in a preferred direction was observed on hydrophobic ratcheted surfaces during coalescence of two droplets in neighboring ratchet valleys when the droplets were roughly the width of the ratchets on which they formed. During coalescence of these droplets one droplet would be pulled over the long shallow ratchet slope joining the other droplet in the neighboring ratchet forming a new larger droplet. This motion was only observed during early stages of condensation when droplet sizes were relatively small. Heat transfer coefficient

data suggests that smaller ratchets more readily produced this motion and therefore produced higher heat transfer coefficients than larger ratchets.

- Comparing roll-off angle data with observations of condensate behavior on tilted surfaces indicates that condensate can grow within the NeverWet coating structure producing droplets in the Wenzel state. The reduced mobility of Wenzel state droplets is detrimental to condensation heat transfer coefficients. At extreme tilt angles, surfaces with shallow ratchet profiles did have condensate removed from the surface producing increased heat transfer coefficients.
- A model for predicting heat transfer coefficients on NeverWet coated surfaces where the surface texturing may affect the minimum condensate drop size on the surface is proposed.

### **5.3 Recommendations for Future Work**

- Since both modifications made to the original Repellix surface treatment produced coatings with increased durability when applied to metallic surfaces one more coating, a Repellix 3.0 perhaps, could be developed and tested for durability that incorporates both modifications.
- Actual condenser tubes with coolant fluid flowing through them, instead of solid test surfaces fabricated from condenser tubes could be tested in a simulated power generation plant condenser environment to determine how Repellix family surface treatments perform in a more realistic environment with steam flow and machinery vibrations.

- As seen in Figures 3.6 and 3.7 there was a significant amount of run to run variation for the experiments performed on coated and uncoated hemi-cylindrical condenser tube test surfaces. This may be caused by insufficient surface drying between experiments. Another study [9] mentioned maintaining very low pressures for a period of time before starting an experiment as a means of insuring a dry surface. While a vacuum pump was used to remove noncondensable gasses from the condensation chamber prior to running experiments in this work, it was incapable of reaching the low pressures achieved in [9]. Perhaps a more powerful vacuum system is necessary for fully drying nano-textured surfaces.
- Other hydrophobic coating types, perhaps a SAM or thin polymer coatings, which do not impart any surface texture, should be tested on ratcheted surfaces to further study the effect this type of surface structure can have on condensate droplets. Textureless hydrophobic coatings don't produce the incredibly high droplet mobility observed on Cassie-Baxter state droplets but they also don't produce immobile Wenzel state droplets seen in some of the experiments in this study.
- Ratcheted test surfaces with drainage pathways or other features intended to remove larger condensate droplets could be fabricated and tested to study and discover methods of reducing the average drop size on the surface and thereby allowing the directional droplet motion observed under certain conditions on these surfaces to continue for longer periods of time.
- A previous study performed at Auburn University showed that liquid can be moved in a preferred direction by boiling activity on a ratcheted surface with reentrant cavities. Pairing this kind of surface with a ratcheted condenser surface

that also produces directional fluid motion seems like a worthy exercise since successful operation of such a system could lead to the development of a passive, self-regulating pumpless phase change thermal management loop.



## References

- [1] Anand, S., Paxson, A. T., Dhiman, R., Smith, J. D., & Varanasi, K. K. (2012). Enhanced condensation on lubricant-impregnated nanotextured surfaces. *ACS nano*, 6(11), 10122-10129.
- [2] <https://arpa-e.energy.gov/?q=news-item/arpa-e-arid-program-advances-technologies-reduce-water-usage-power-plants>
- [3] Enright, R., Miljkovic, N., Al-Obeidi, A., Thompson, C. V., & Wang, E. N. (2012). Condensation on superhydrophobic surfaces: the role of local energy barriers and structure length scale. *Langmuir*, 28(40), 14424-14432.
- [4] Miljkovic, N., Enright, R., Nam, Y., Lopez, K., Dou, N., Sack, J., & Wang, E. N. (2012). Jumping-droplet-enhanced condensation on scalable superhydrophobic nanostructured surfaces. *Nano letters*, 13(1), 179-187.
- [5] Lin, S., Sefiane, K., & Christy, J. R. E. (2002). Prospects of confined flow boiling in thermal management of microsystems. *Applied Thermal Engineering*, 22(7), 825-837.
- [6] Verho, T., Bower, C., Andrew, P., Franssila, S., Ikkala, O., & Ras, R. H. (2011). Mechanically durable superhydrophobic surfaces. *Advanced Materials*, 23(5), 673-678.
- [7] Boreyko, J. B., & Chen, C. H. (2009). Self-propelled dropwise condensate on superhydrophobic surfaces. *Physical review letters*, 103(18), 184501.
- [8] Chen, C. H., Cai, Q., Tsai, C., Chen, C. L., Xiong, G., Yu, Y., & Ren, Z. (2007). Dropwise condensation on superhydrophobic surfaces with two-tier roughness. *Applied Physics Letters*, 90(17), 173108.
- [9] Varanasi, K. K., Hsu, M., Bhate, N., Yang, W., & Deng, T. (2009). Spatial control in the heterogeneous nucleation of water. *Applied Physics Letters*, 95(9), 094101.
- [10] Jo, M. C. (2008). *Thermally Actuated Pumping of a Single-Phase Fluid Using Surface Asymmetry* (Master's Thesis, Oregon State University).
- [11] Linke, H., Alemán, B. J., Melling, L. D., Taormina, M. J., Francis, M. J., Dow-Hygelund, C. C., ... & Stout, A. (2006). Self-propelled Leidenfrost droplets. *Physical review letters*, 96(15), 154502.

- [12] Thiagarajan, N., Kapsenberg, F., Narayanan, V., Bhavnani, S. H., & Ellis, C. (2011). On the lateral motion of bubbles generated from re-entrant cavities located on asymmetrically structured surfaces. *ASME Paper No. IPACK2011-52056*.
- [13] Natesh, S., Truong, E., Narayanan, V., & Bhavnani, S. H. (2017). Directional passive condensate film drainage on a horizontal surface with periodic asymmetrical structures. *Journal of Heat Transfer*.
- [14] Liu, C., Ju, J., Zheng, Y., & Jiang, L. (2014). Asymmetric ratchet effect for directional transport of fog drops on static and dynamic butterfly wings. *ACS nano*, 8(2), 1321-1329.
- [15] Thiagarajan, N. (2013). *Investigation of Thermally-Actuated Pumping During Pool Boiling of a Dielectric Liquid on an Asymmetric Microstructured Silicon Heat Sink* (Doctoral Dissertation, Auburn University).
- [16] Ulman, A. (1996). Formation and structure of self-assembled monolayers. *Chemical reviews*, 96(4), 1533-1554.
- [17] Depew, C. A., & Reisbig, R. L. (1964). Vapor condensation on a horizontal tube using teflon to promote dropwise condensation. *Industrial & Engineering Chemistry Process Design and Development*, 3(4), 365-369.
- [18] Manvel, J. T. Jr. (1979). An experimental study of dropwise condensation on horizontal condenser tubes. M.S. Thesis, Naval Postgraduate School, Monterey, CA.
- [19] Parylene Coating Promotes Dropwise Condensation on Condenser Tubes, *Chemical Engineering News Archive*, Vol. 43, No. 42, p. 45, 1965.
- [20] Haraguchi, T., Shimada, R., Kumagai, S., & Takeyama, T. (1991). The effect of polyvinylidene chloride coating thickness on promotion of dropwise steam condensation. *International journal of heat and mass transfer*, 34(12), 3047-3054.
- [21] Paxson, A. T., Yagüe, J. L., Gleason, K. K., & Varanasi, K. K. (2014). Stable dropwise condensation for enhancing heat transfer via the initiated chemical vapor deposition (iCVD) of grafted polymer films. *Advanced Materials*, 26(3), 418-423.
- [22] Wilkins, D. G., Bromley, L. A., & Read, S. M. (1973). Dropwise and filmwise condensation of water vapor on gold. *AIChE Journal*, 19(1), 119-123.
- [23] Erb, R. A., & Thelen, E. (1966). Dropwise condensation characteristics of permanent hydrophobic systems. U.S. Government Printing Office, Washington, DC.
- [24] Erb, R. A. (1973). Dropwise condensation on gold. *Gold Bulletin*, 6(1), 2-6.

- [25] Woodruff, D. W., & Westwater, J. W. (1979). Steam condensation on electroplated gold: Effect of plating thickness. *International Journal of Heat and Mass Transfer*, 22(4), 629-632.
- [26] Smith, T. (1980). The hydrophilic nature of a clean gold surface. *Journal of Colloid and Interface Science*, 75(1), 51-55.
- [27] Schrader, M. E. (1970). Ultrahigh-vacuum techniques in the measurement of contact angles. II. Water on gold. *The journal of physical chemistry*, 74(11), 2313-2317.
- [28] Marto, P. J., Looney, D. J., Rose, J. W., & Wanniarachchi, A. S. (1986). Evaluation of organic coatings for the promotion of dropwise condensation of steam. *International journal of heat and mass transfer*, 29(8), 1109-1117.
- [29] Gupta, M., Kapur, V., Pinkerton, N. M., & Gleason, K. K. (2008). Initiated chemical vapor deposition (iCVD) of conformal polymeric nanocoatings for the surface modification of high-aspect-ratio pores. *Chemistry of Materials*, 20(4), 1646-1651.
- [30] Enright, R., Miljkovic, N., Alvarado, J. L., Kim, K., & Rose, J. W. (2014). Dropwise condensation on micro- and nanostructured surfaces. *Nanoscale and Microscale Thermophysical Engineering*, 18(3), 223-250.
- [31] Das, A. K., Kilty, H. P., Marto, P. J., Andeen, G. B., Kumar, A. (2000). The use of an organic self-assembled monolayer coating to promote dropwise condensation of steam on horizontal tubes. *Journal of Heat Transfer*, 122(2), 278-286
- [32] Callies, M., & Quéré, D. (2005). On water repellency. *Soft matter*, 1(1), 55-61.
- [33] Zhang, K., Liu, F., Williams, A. J., Qu, X., Feng, J. J., & Chen, C. H. (2015). Self-propelled droplet removal from hydrophobic fiber-based coalescers. *Physical review letters*, 115(7), 074502.
- [34] Tokunaga, A., Mizutani, M., Nagayama, G., & Tsuruta, T. (2014). Condensation Heat Transfer Characteristics on a Micro-Structured Surface with Wettability Gradient. In *is" InternationalHeat Transfer Conf.* (pp. IHTC15-9033).
- [35] Miljkovic, N., Enright, R., & Wang, E. N. (2012). Effect of droplet morphology on growth dynamics and heat transfer during condensation on superhydrophobic nanostructured surfaces. *ACS nano*, 6(2), 1776-1785.
- [36] Chen, X., Wu, J., Ma, R., Hua, M., Koratkar, N., Yao, S., & Wang, Z. (2011). Nanograssed micropyramidal architectures for continuous dropwise condensation. *Advanced functional materials*, 21(24), 4617-4623.

- [37] Qu, X., Boreyko, J. B., Liu, F., Agapov, R. L., Lavrik, N. V., Retterer, S. T., ... & Chen, C. H. (2015). Self-propelled sweeping removal of dropwise condensate. *Applied Physics Letters*, *106*(22), 221601.
- [38] He, M., Zhang, Q., Zeng, X., Cui, D., Chen, J., Li, H., ... & Song, Y. (2013). Hierarchical Porous Surface for Efficiently Controlling Microdroplets' Self-Removal. *Advanced Materials*, *25*(16), 2291-2295.
- [39] Ghosh, A., Ganguly, R., Schutzius, T. M., & Megaridis, C. M. (2014). Wettability patterning for high-rate, pumpless fluid transport on open, non-planar microfluidic platforms. *Lab on a Chip*, *14*(9), 1538-1550.
- [40] [http://soft-matter.seas.harvard.edu/index.php/Pitcher\\_plant\\_inspired\\_non-stick\\_surface](http://soft-matter.seas.harvard.edu/index.php/Pitcher_plant_inspired_non-stick_surface)
- [41] Adamson, A. W., Gast, A. P. (1990). *Physical Chemistry of Surfaces*, 6th ed. New York, NY: Wiley & Sons.
- [42] Carey, V. P. (2008). *Liquid-Vapor Phase-Change Phenomena*, 2nd ed. New York, NY: Taylor & Francis Group.
- [43] Chaudhury, M. K., & Whitesides, G. M. (1992). *How to make water run uphill* (No. TR-48). HARVARD UNIV CAMBRIDGE MA DEPT OF CHEMISTRY.
- [44] Macner, A. M., Daniel, S., & Steen, P. H. (2014). Condensation on surface energy gradient shifts drop size distribution toward small drops. *Langmuir*, *30*(7), 1788-1798.
- [45] Kim, S., & Kim, K. J. (2011). Dropwise condensation modeling suitable for superhydrophobic surfaces. *Journal of heat transfer*, *133*(8), 081502.
- [46] Daniel, S., Chaudhury, M. K., & Chen, J. C. (2001). Fast drop movements resulting from the phase change on a gradient surface. *Science*, *291*(5504), 633-636.
- [47] Alwazzan, M., Egab, K., Peng, B., Khan, J., & Li, C. (2017). Condensation on hybrid-patterned copper tubes (I): Characterization of condensation heat transfer. *International Journal of Heat and Mass Transfer*, *112*, 991-1004.
- [48] Alwazzan, M., Egab, K., Peng, B., & Khan, J. (2017). Condensation on hybrid-patterned copper tubes (II): Visualization study of droplet dynamics. *International Journal of Heat and Mass Transfer*, *112*, 950-958.
- [49] Liang, Z., & Keblinski, P. (2015). Coalescence-induced jumping of nanoscale droplets on super-hydrophobic surfaces. *Applied Physics Letters*, *107*(14), 143105.

- [50] Morgan, B., Waits, C. M., Krizmanic, J., & Ghodssi, R. (2004). Development of a deep silicon phase Fresnel lens using gray-scale lithography and deep reactive ion etching. *Journal of microelectromechanical systems*, 13(1), 113-120.
- [51] Waits, C. M., Modafe, A., & Ghodssi, R. (2002). Investigation of gray-scale technology for large area 3D silicon MEMS structures. *Journal of Micromechanics and Microengineering*, 13(2), 170.
- [52] Waits, C. M., Morgan, B., Kastantin, M., & Ghodssi, R. (2005). Microfabrication of 3D silicon MEMS structures using gray-scale lithography and deep reactive ion etching. *Sensors and Actuators A: Physical*, 119(1), 245-253.
- [53] Zhong, J. (2016). *Nanoparticle Coatings for Surface Morphology Control and Superhydrophobicity* (Doctoral Dissertation, Auburn University).
- [54] Yadav, P. S., Bahadur, P., Tadmor, R., Chaurasia, K., & Leh, A. (2008). Drop retention force as a function of drop size. *Langmuir*, 24(7), 3181-3184.
- [55] Zheng, Y., Chen, C. H., Pearlman, H., Flannery, M., & Bonner, R. (2015). Effect of porous coating on condensation heat transfer. In *9th Boiling and Condensation Conf* (p. 178).
- [56] LeFevre, E. J., & Rose, J. W. (1966, January). A theory of heat transfer by dropwise condensation. In *Chemical Engineering Progress* (Vol. 62, No. 7, p. 86). 345 E 47TH ST, NEW YORK, NY 10017: AMER INST CHEMICAL ENGINEERS.
- [57] Rose, J. W. (1988). Some aspects of condensation heat transfer theory. *International communications in heat and mass transfer*, 15(4), 449-473.
- [58] Rose, J. W., & Glicksman, L. R. (1973). Dropwise condensation—the distribution of drop sizes. *International Journal of Heat and Mass Transfer*, 16(2), 411-425.
- [59] Tanaka, H. (1975). Measurements of drop-size distributions during transient dropwise condensation. *Journal of Heat Transfer*, 97(3), 341-346.
- [60] Wen, H. W., & Jer, R. M. (1976). On the heat transfer in dropwise condensation. *The chemical engineering journal*, 12(3), 225-231.
- [61] Maa, J. R. (1978). Drop size distribution and heat flux of dropwise condensation. *The Chemical Engineering Journal*, 16(3), 171-176.
- [62] Abu-Orabi, M. (1998). Modeling of heat transfer in dropwise condensation. *International journal of heat and mass transfer*, 41(1), 81-87.

- [63] Graham, C., & Griffith, P. (1973). Drop size distributions and heat transfer in dropwise condensation. *International Journal of Heat and Mass Transfer*, 16(2), 337-346.
- [64] Welch, J. F., & Westwater, J. W. (1961) Microscopic study of dropwise condensation. In *International Heat Transfer Conf.* (p.302)

## Appendix A

### Thermophysical Properties of Water and FC-72

Tables containing the thermophysical properties of water and FC-72 at sub-atmospheric pressures are provided in this appendix. Table A.1 contains properties of saturated water. Table A.2 contains properties of saturated FC-72.

Table A.1: Thermophysical properties of saturated water

$T_{sat}$ (K)	303.2	323.2	343.2	363.2	373.15
$P_{sat}$ (kPa)	4.25	12.35	31.20	70.2	101.3
$\rho_l$ (kg/m <sup>3</sup> )	995.6	988.0	977.7	965.3	958.3
$\rho_v$ (kg/m <sup>3</sup> )	0.0387	0.0831	0.1984	0.423	0.597
$h_{lv}$ (kJ/kg)	2429.9	2382.0	2332.9	2282.5	2256.7
$c_{pl}$ (kJ/kgK)	4.18	4.18	4.19	4.21	4.22
$c_{pv}$ (kJ/kgK)	1.92	1.95	1.99	2.04	2.03
$\mu_l$ ( $\mu$ Ns/m <sup>2</sup> )	797.4	546.8	403.9	314.4	277.53
$\mu_v$ ( $\mu$ Ns/m <sup>2</sup> )	10.0	10.6	11.3	11.9	12.55
$k_l$ (mW/mK)	615.5	643.6	663.1	675.3	679.0
$k_v$ (mW/mK)	18.9	20.4	22.1	24.0	25.0
$Pr_l$	5.41	3.55	2.55	1.96	1.72
$Pr_v$	1.02	1.02	1.01	1.01	1.02
$\sigma$ (mN/m)	71.19	67.94	64.48	60.82	58.91



Table A.2: Thermophysical properties of saturated FC-72

$T_{sat}$ (K)	298	306	314	322	329.8
$P_{sat}$ (kPa)	30.1	42.2	57.9	77.7	101.3
$\rho_l$ (kg/m <sup>3</sup> )	1723.1	1691.2	1654.3	1631.4	1619.73
$\rho_v$ (kg/m <sup>3</sup> )	4.22	5.81	7.84	10.37	13.396
$h_{lv}$ (kJ/kg)	104.911	102.426	99.911	97.366	94.734
$c_{pl}$ (kJ/kgK)	1.094	1.094	1.095	1.095	1.097
$\mu_l$ ( $\mu$ Ns/m <sup>2</sup> )					454
$k_l$ (mW/mK)					52.16
$Pr_l$					9.555
$\sigma$ (mN/m)					8.273

## Appendix B

### Flat Silicon Surface Testing

This appendix contains a description of the experiments performed on the flat silicon test surfaces and of the observations made during those experiments. Reasons for not further pursuing testing on this type of surface and a suggested improvement to these surfaces are also presented.

Condensation activity on the flat silicon test surfaces showed some interesting behavior mostly involving distorted droplet shapes due to pinning on the borders between coated (hydrophobic) and uncoated (hydrophilic) portions of the surface. Attempts were made to develop surface wettability patterns that would promote droplet growth or movement in a preferred direction on these surfaces however after two iterations of surfaces and testing little more than distorted droplet shapes were observed so this type of surface treatment was abandoned in order to study more advanced and complex surfaces. The following is a brief description of the observations made during testing on the flat silicon surfaces.

Elongated drops tended to form on the hydrophilic portions of the 1-D and 2-D patterned surfaces because nucleation and growth of water condensate droplets occurs at higher rates on a surface with higher wettability than on a surface with low wettability at the same surface subcooling [9, 46]. Absent of outside influences, water condensate droplets nucleate and grow with a circular perimeter on planar smooth surfaces. However, on a silicon surface with alternating hydrophilic and hydrophobic bands, the higher nucleation and growth rates on the hydrophilic bands leads to circular droplets on those bands growing to the point where the droplet diameter equals the band width much faster than the droplets on the hydrophobic bands on either side. Once this point is reached it was observed that droplets on the 1-D and 2-D patterned surfaces continued to grow preferentially along the hydrophilic band forming elongated droplets rather than continuing to grow with a circular perimeter. This behavior continued until the droplets on the hydrophilic band grow to a sufficient size that when they coalesced with another elongated droplet, the resulting droplet is pulled partially onto the hydrophobic band as

can be seen in Figure B.1. Incremental stages of elongated droplet growth on 2-D patterned surfaces are shown in Figure B.2 and a plot of droplet elongation vs time is provided in Figure B.3.

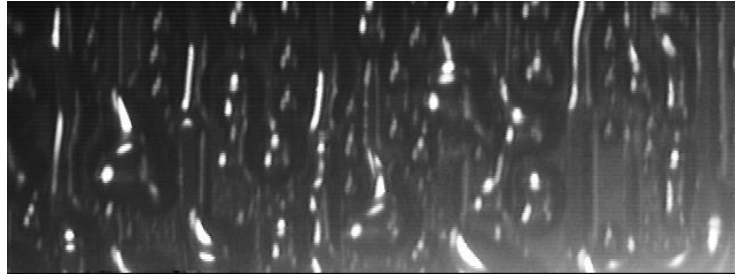


Figure B.1: Droplets on 1-D patterned test surfaces exhibiting both elongated and irregular shapes from pinning and eventual coalescence.

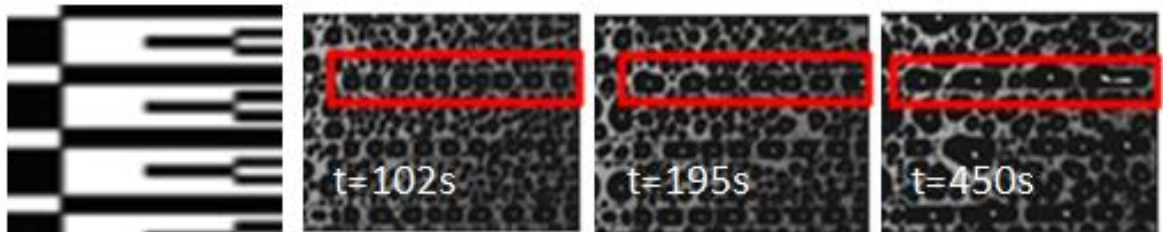


Figure B.2: Droplet growth on 2-D patterned surface. From left to right: 1. Schematic of surface patterning black=hydrophilic, white=hydrophobic. 2. Circular droplets with diameters equal to hydrophobic band width. 3. Droplets on hydrophobic bands beginning to elongate. 4. Elongated bands begin to coalesce with droplets on the hydrophobic bands.

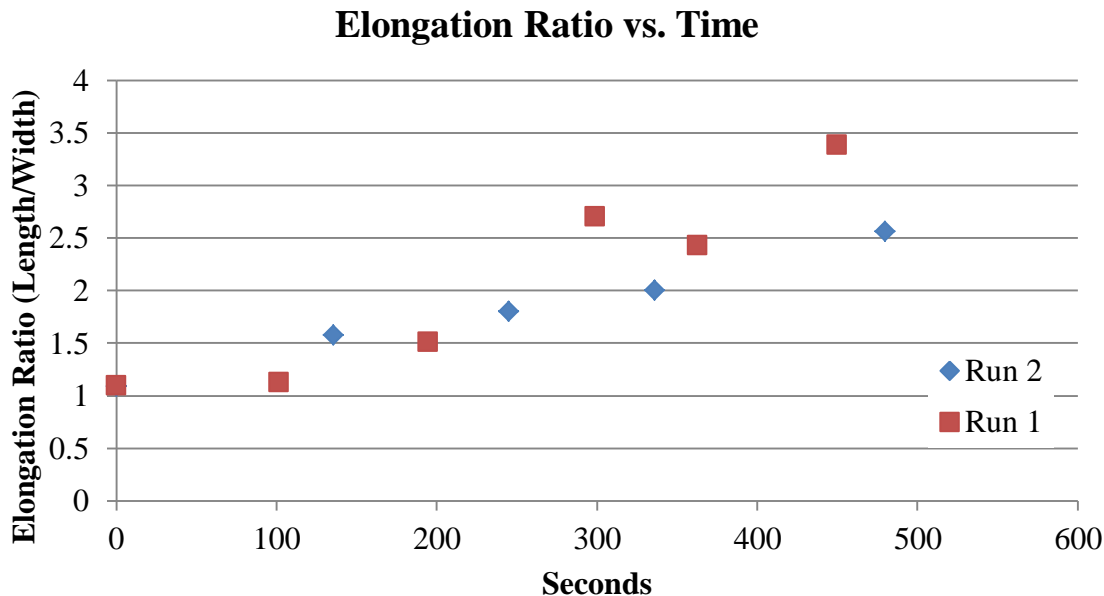


Figure B.3: Plot of elongation ratio as a function of time on two identical 2-D patterned surfaces.

Similar droplet deformation occurred on the radial patterned surfaces. Just as on the surfaces discussed above, higher nucleation and growth rates on the hydrophilic portions of the test surface led to larger droplets on those portions. When the droplets grew large enough to make contact with the boundary of the wetting portion, the perimeter deformed with continuing growth, yielding large non-circular droplets, pinned at the line dividing the wetting and hydrophobic regions. After this, the spoke pattern of these test sections facilitated droplet growth toward the edges of the surface and limited growth toward the center. When a droplet is pinned between the hydrophobic spokes, a smaller radius is forced on the inner side of the droplet compared to the side of the droplet nearer to the periphery of the surface by the “wedge” shape of the hydrophilic region. According to the Young-Laplace equation this creates a higher pressure on the inner side of the droplet compared to the side nearer to the periphery. Therefore, as a droplet continued to grow on the hydrophilic portions it eventually reached the outer

periphery and left the surface, many times gathering other small droplets and even similar sized droplets and carrying them off of the surface as well. This condensate removal behavior is depicted in Figure B.4.

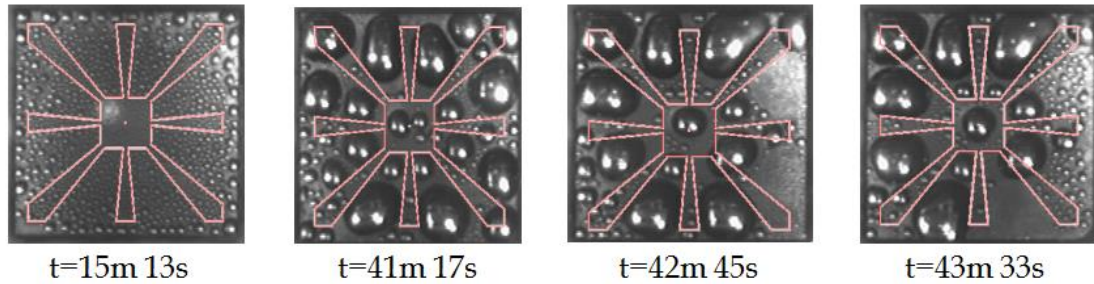


Figure B.4: Images of condensation on 25mm radial patterned test section with 6mm inner non-wetting island. From left to right. 1. Higher nucleation rate on hydrophilic portions begins to be obvious. 2. Borders of large droplets are affected by patterning. 3. Droplets grow to periphery and leave the surface. 4. Another droplet reaches the periphery and leaves while condensate nucleates and repopulates bare surface where previous droplets left.

Droplets on the hydrophilic portions of the wedge patterned surface also displayed shapes that had a smaller radius on one side and a larger radius on the other that resulted in the same type of internal pressure differences mentioned above in droplets on the radial patterned surfaces. There was some small droplet motion observed on this surface that occurred when two droplets on the same wedge coalesced with each other. The droplet on the wide side of the wedge tended to pull the droplet on the narrow side of the wedge toward the wide side. This however usually only occurred for the first instance of coalescence between droplets that had grown and become pinned by the wettability pattern boundaries. Further coalescence of these drops usually occurred across the pattern boundaries and yielded motion in random directions. Images demonstrating the progression of this behavior are shown in Figure B.5.

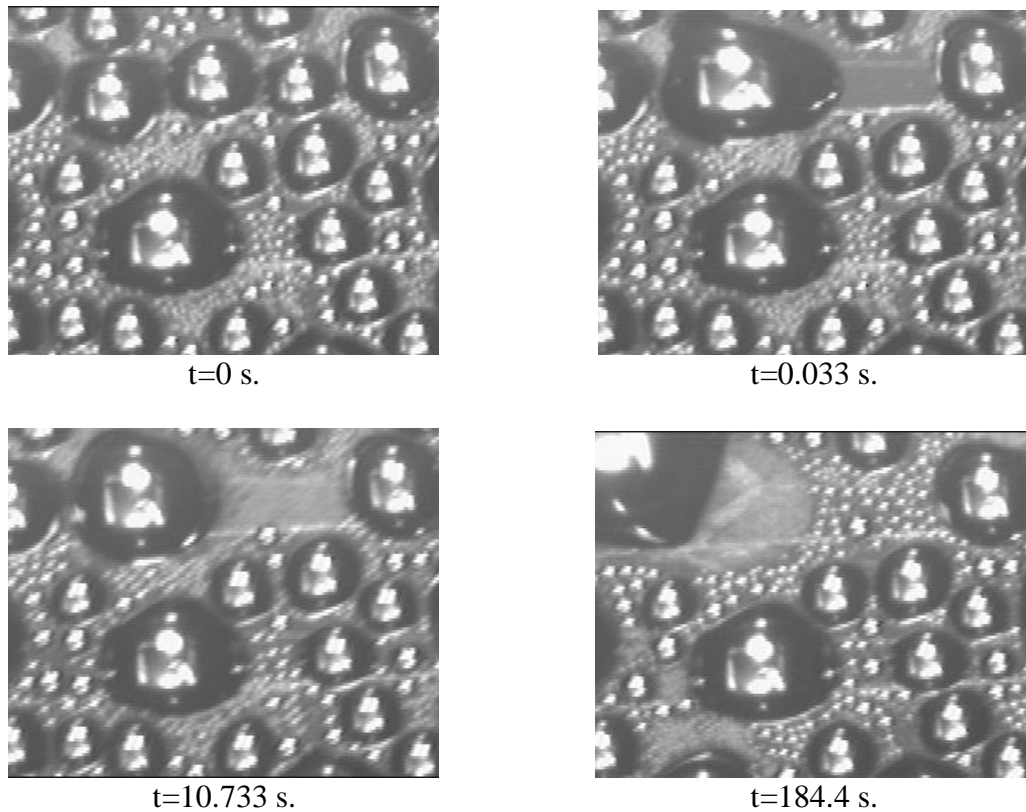


Figure B.5: Droplet coalescence on wedge patterned flat silicon test surface. Top Left: Three droplets sitting on a wetting wedge. Top Right: Droplets coalesce and resulting droplet features larger radius on left side. Bottom Left: Droplet finally achieves circular shape when internal pressures equalize. Bottom Right: Droplet coalesces with others across pattern boundaries.

Disappointingly, droplet removal from the radial surfaces wasn't always the result of the surface patterning manipulating droplet growth. Often droplets would coalesce over the radial spokes creating very large droplets. These large droplets and those roughly the size of those shown leaving the surface in Figure B.4 would on occasion coalesce with droplets that had formed off of the test surface which made it impossible to claim that all of the liquid leaving the surface was due to the surface treatment. This combined with the limited effect on condensate behavior produced by the other flat silicon surfaces is why testing of this type of surface was eventually halted and efforts were focused on the hemi-cylindrical and ratcheted test surfaces.

It is believed that the main problem with the flat silicon surfaces tested was that the wettability pattern features were too large and widely spaced. Therefore, droplets pinned between features tended to be too large and heavy for the modest surface tension forces imposed by the droplet's distorted shape to reliably cause the droplet to move. Other studies examining these types of surfaces were able to demonstrate droplet motion for deposited droplets [34, 39] and during condensation [43, 44, 46] by using very small pattern features and surface wettability gradients.

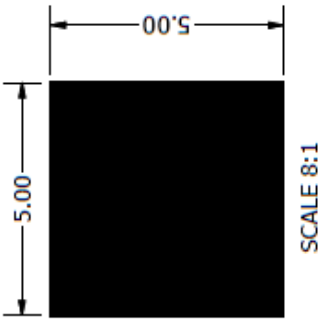
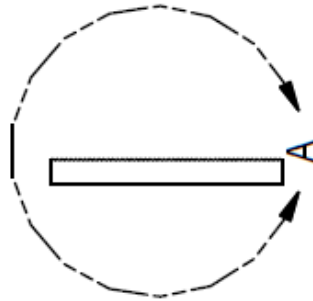


## Appendix C

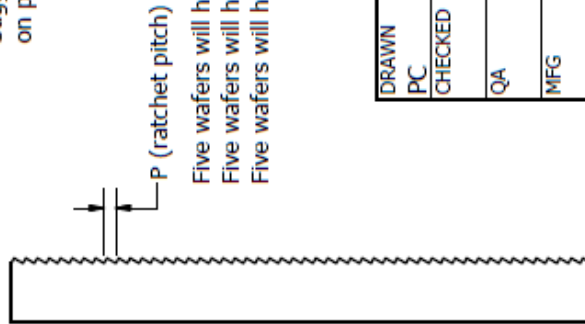
### Grayscale Photoresist Pattern Layout and Requirements

The document containing the requirements given to Jenoptic for grayscale photoresist processing of silicon wafers that would be used to fabricate the asymmetric saw-toothed ratchet test surfaces is provided in this appendix. Jenoptic's grayscale masking and exposure process only allows exposure of a 5mm by 5mm square that is repeated in a grid pattern to cover the desired area. The first page of this document provided a suggested layout for the exposed portions of the wafer. Three four by five grids would provide the 20mm by 25mm ratcheted area for the 25mm square test surfaces used at Auburn and three one by two grids would provide the 5mm by 10mm ratcheted area for the smaller test surfaces used by our partners at U.C. Davis.

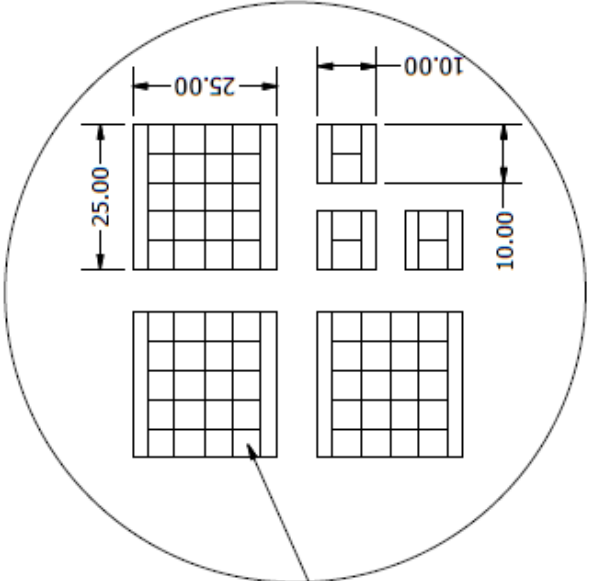
The second page of this document gave details on the desired resulting ratchet profile after DRIE was performed on the wafers provided by Jenoptic. Suggested photoresist ratchet depths were given based on an etch selectivity of 63 as that was the etch selectivity that provided the 30°-60°-90° triangle ratchet profile in [15].



Suggested unit cell size based on previous patterning



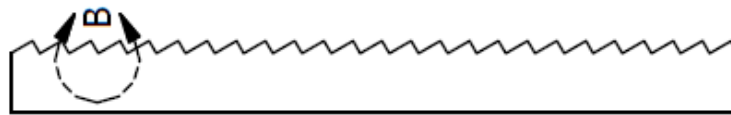
Five wafers will have a pitch of  $P=0.1$  mm.  
 Five wafers will have a pitch of  $P=0.25$  mm  
 Five wafers will have a pitch of  $P=0.5$  mm



NOTE:  
All dimensions are in millimeters

DRAWN	4/20/2014	TITLE		REV	1
PC		Wafer Layout		DWG NO	
CHECKED				Wafer Layout	
QA		SIZE	A	SCALE	
MFG					
APPROVED					
				SHEET 1 OF 2	

DETAIL A  
SCALE 20 : 1



SCALE 5:1

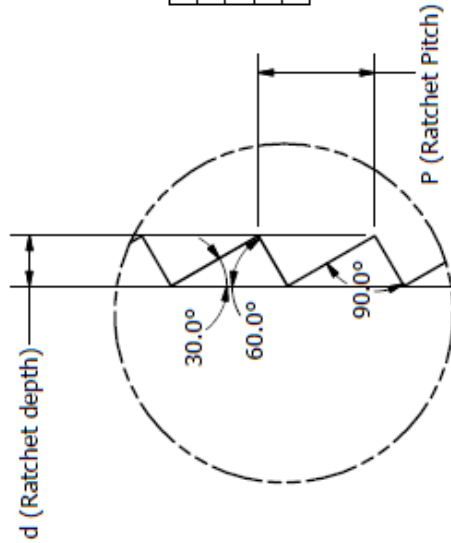


TABLE			
No.	Pitch	d Silicon	d Photoresist
1	100	43.3	0.687
2	250	108.3	1.72
3	500	216.5	3.44

Table dimensions are in micrometers.  
 Resulting ratchets in silicon should be  
 30-60-90 triangular profile.

**DETAIL B**  
**SCALE 20 : 1**

DRAWN	4/20/2014	TITLE	
PC		Wafer Layout	
CHECKED		SIZE	DWG NO
QA		A	Wafer Layout
MFG		SCALE	REV
APPROVED			1
			SHEET 2 OF 2

## Appendix D

### Grayscale Photoresist Profile Measurements

This appendix features figures provided by Jenoptic of the grayscale photoresist profile measurement documentation, verifying that each wafer they processed had met the requirements given to them.

Figures D.1, D.2 and D.3 show the photoresist profile plots provided by Jenoptic for 100 $\mu\text{m}$ , 250  $\mu\text{m}$  and 500  $\mu\text{m}$  ratchet pitch wafers respectively.

Figure D.4 shows the locations at which Jenoptic took photoresist thickness measurements on all wafers.

Tables D.1, D.2 and D.3 provide the photoresist thickness measurements provided by Jenoptic for 100 $\mu\text{m}$ , 250  $\mu\text{m}$  and 500  $\mu\text{m}$  ratchet pitch wafers respectively.

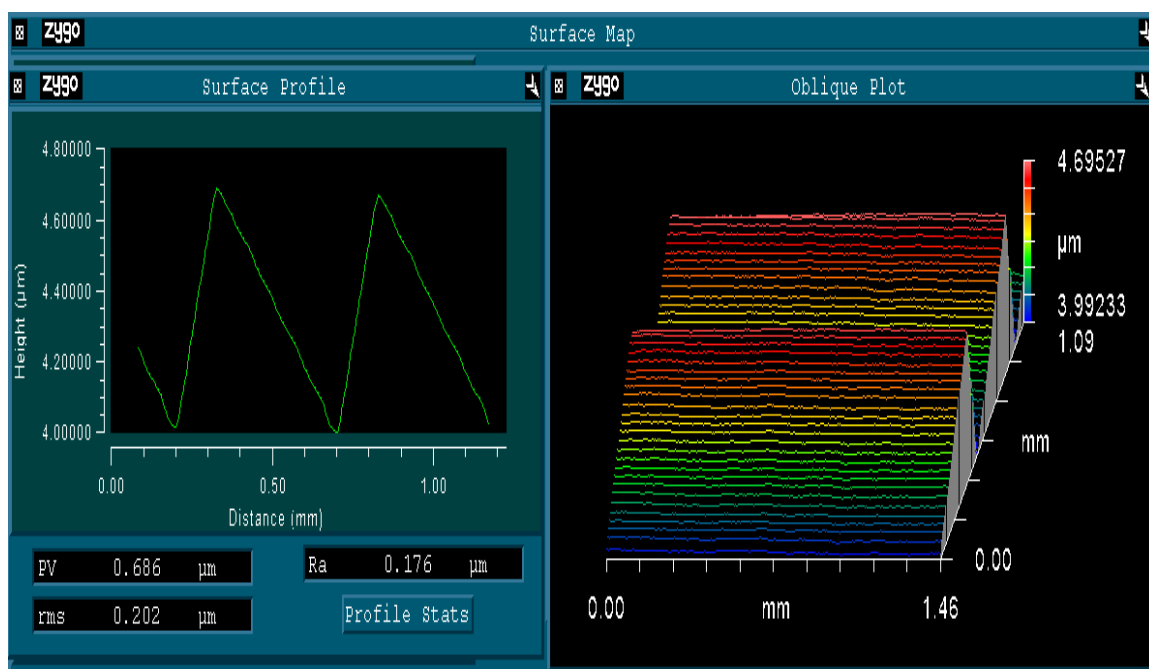


Figure D.1: Grayscale exposed and developed photoresist height profile on 100 $\mu\text{m}$  ratchet pitch wafer

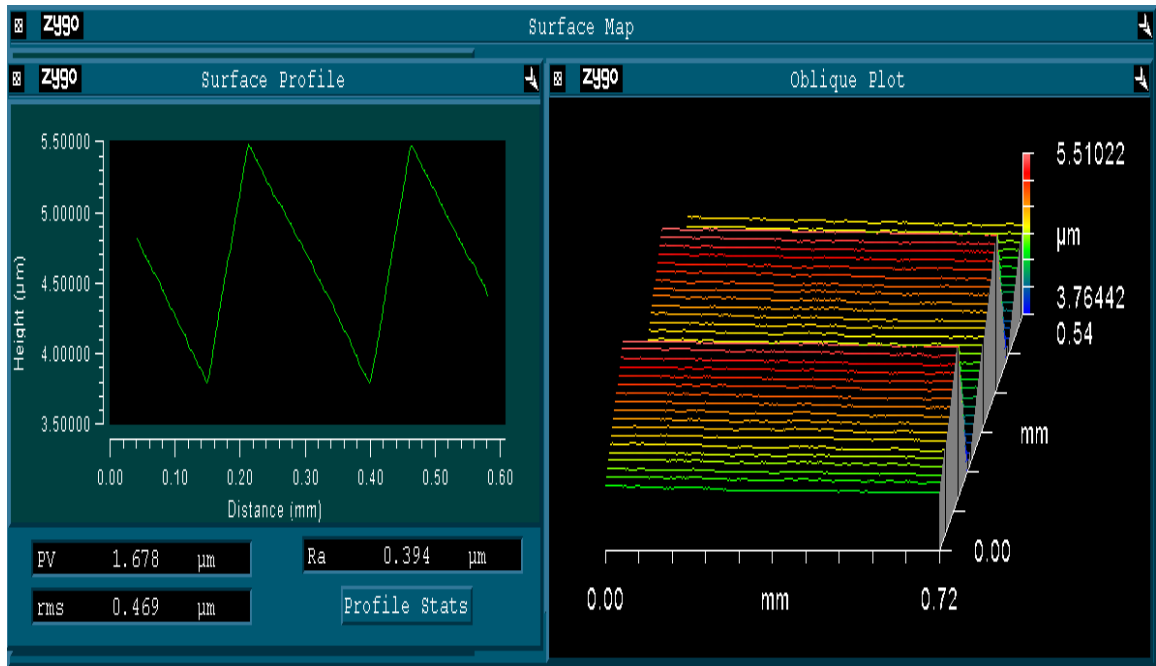


Figure D.2: Grayscale exposed and developed photoresist height profile on 250 $\mu\text{m}$  ratchet pitch wafer

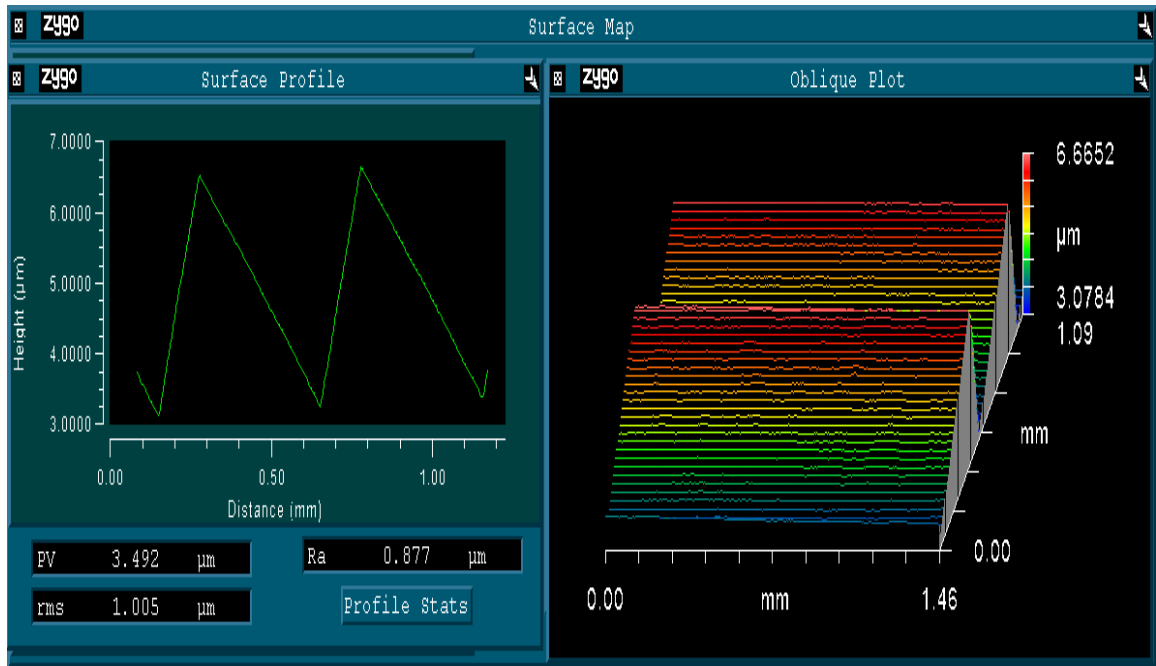


Figure D.3: Grayscale exposed and developed photoresist height profile on 500μm ratchet pitch wafer

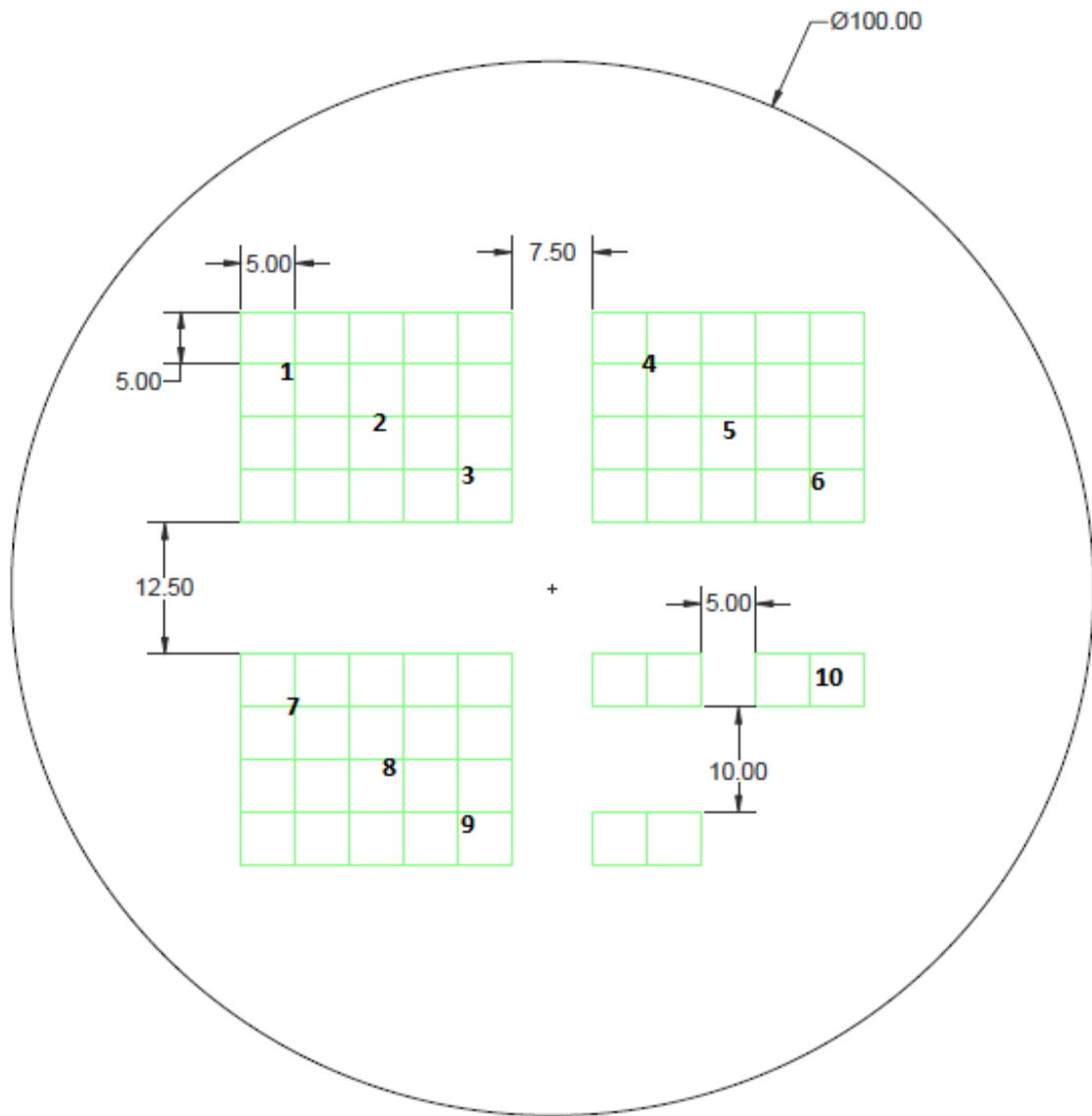


Figure D.4: Layout drawing 5mm square unit cells of grayscale processed photoresist on 100mm wafer with photoresist height measurement locations indicated by numbers 1-10.



Table D.1: Grayscale processed photoresist thickness measurements on 100 $\mu$ m ratchet pitch wafers

Number	1	2	3	4	5	6	
Wafer ID	W1	W2	W3	W4	W5	W6	
Target Pattern Depth ( $\mu$ m)	0.687	0.687	0.687	0.687	0.687	0.687	
Tolerance ( $\mu$ m)	$\pm 10\%$	$\pm 10\%$	$\pm 10\%$	$\pm 10\%$	$\pm 10\%$	$\pm 10\%$	
Range ( $\mu$ m)	0.618 - 0.756	0.618 - 0.756	0.618 - 0.756	0.618 - 0.756	0.618 - 0.756	0.618 - 0.756	
Pre-Processing PR Thickness ( $\mu$ m)	7.43	7.43	7.42	7.37	7.40	7.52	
Observation ( $\mu$ m)	1	0.726	0.647	0.650	0.674	0.622	0.659
	2	0.722	0.630	0.654	0.661	0.613	0.658
	3	0.709	0.622	0.655	0.666	0.599	0.634
	4	0.699	0.632	0.650	0.672	0.597	0.637
	5	0.715	0.634	0.662	0.673	0.623	0.630
	6	0.716	0.620	0.657	0.673	0.623	0.635
	7	0.722	0.633	0.648	0.669	0.578	0.650
	8	0.715	0.657	0.665	0.669	0.563	0.648
	9	0.728	0.670	0.667	0.665	0.552	0.659
	10	0.715	0.635	0.664	0.677	0.586	0.625
Average	0.7167	0.638	0.6572	0.6699	0.5956	0.6435	
Standard Deviation	0.0085	0.0156	0.0069	0.0048	0.0256	0.0128	
Minimum	0.699	0.620	0.648	0.661	0.552	0.625	
Maximum	0.728	0.670	0.667	0.677	0.623	0.659	
Range	0.029	0.05	0.019	0.016	0.071	0.034	

Table D.2: Grayscale processed photoresist thickness measurements on 250 $\mu\text{m}$  ratchet pitch wafers

Number	1	2	3	4	5	6	
Wafer ID	W7	W8	W9	W10	W11	W12	
Target Pattern Depth ( $\mu\text{m}$ )	1.72	1.72	1.72	1.72	1.72	1.72	
Tolerance ( $\mu\text{m}$ )	$\pm 10\%$	$\pm 10\%$	$\pm 10\%$	$\pm 10\%$	$\pm 10\%$	$\pm 10\%$	
Range ( $\mu\text{m}$ )	1.548 – 1.892	1.548 – 1.892	1.548 – 1.892	1.548 – 1.892	1.548 – 1.892	1.548 – 1.892	
Pre-Processing PR Thickness ( $\mu\text{m}$ )	7.98	7.29	8.13	8.01	8.15	7.91	
Observation ( $\mu\text{m}$ )	1	1.726	1.647	1.684	1.622	1.719	1.637
	2	1.68	1.615	1.654	1.617	1.71	1.679
	3	1.71	1.634	1.676	1.588	1.736	1.679
	4	1.679	1.654	1.633	1.65	1.732	1.65
	5	1.711	1.669	1.626	1.614	1.708	1.612
	6	1.726	1.649	1.642	1.606	1.729	1.666
	7	1.718	1.653	1.697	1.658	1.781	1.655
	8	1.703	1.631	1.665	1.655	1.754	1.711
	9	1.698	1.63	1.676	1.672	1.769	1.718
	10	1.723	1.66	1.651	1.624	1.761	1.665
Average	1.7074	1.6442	1.6604	1.6306	1.7399	1.6672	
Standard Deviation	0.0174	0.0163	0.0231	0.0267	0.0252	0.032	
Minimum	1.679	1.615	1.626	1.588	1.708	1.612	
Maximum	1.726	1.669	1.697	1.672	1.781	1.718	
Range	0.047	0.054	0.071	0.084	0.073	0.106	

Table D.3: Grayscale processed photoresist thickness measurements on 500 $\mu\text{m}$  ratchet pitch wafers

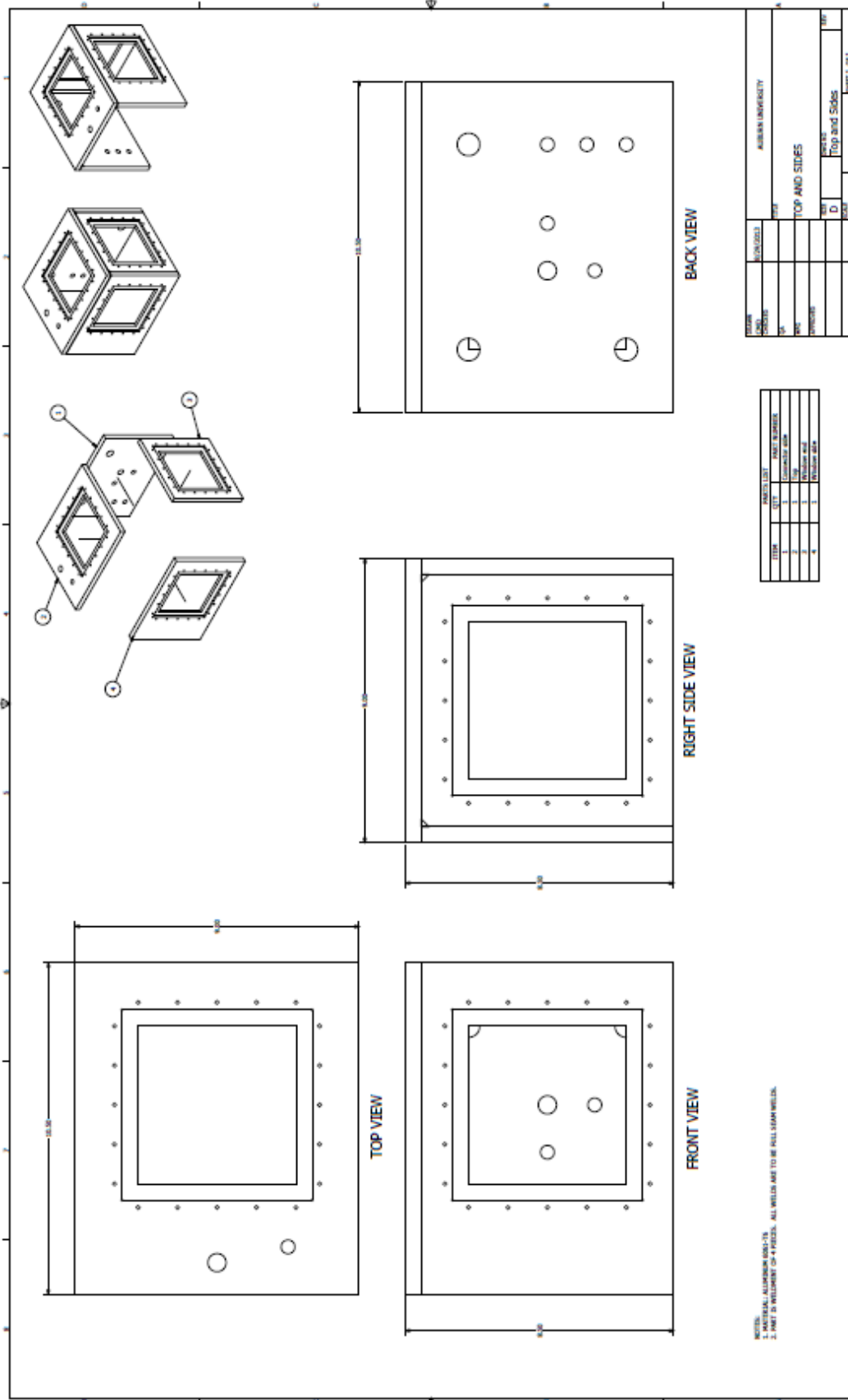
Number	1	2	3	4	5	6	
Wafer ID	W13	W14	W15	W16	W17	W18	
Target Pattern Depth ( $\mu\text{m}$ )	3.44	3.44	3.44	3.44	3.44	3.44	
Tolerance ( $\mu\text{m}$ )	$\pm 10\%$	$\pm 10\%$	$\pm 10\%$	$\pm 10\%$	$\pm 10\%$	$\pm 10\%$	
Range ( $\mu\text{m}$ )	3.096 – 3.784	3.096 – 3.784	3.096 – 3.784	3.096 – 3.784	3.096 – 3.784	3.096 – 3.784	
Pre-Processing PR Thickness ( $\mu\text{m}$ )	13.53	13.55	13.63	13.57	13.67	13.41	
Observation ( $\mu\text{m}$ )	1	3.422	3.32	3.464	3.467	3.327	3.5
	2	3.42	3.456	3.477	3.428	3.353	3.444
	3	3.515	3.431	3.45	3.46	3.322	3.466
	4	3.461	3.483	3.473	3.448	3.33	3.441
	5	3.42	3.416	3.409	3.418	3.339	3.42
	6	3.376	3.435	3.466	3.417	3.373	3.45
	7	3.403	3.469	3.493	3.508	3.348	3.496
	8	3.413	3.417	3.492	3.456	3.339	3.476
	9	3.425	3.361	3.535	3.49	3.376	3.458
	10	3.44	3.415	3.362	3.423	3.348	3.485
Average	3.4295	3.4203	3.4621	3.4515	3.3455	3.4636	
Standard Deviation	0.0373	0.0489	0.0477	0.0311	0.0182	0.0258	
Minimum	3.376	3.32	3.362	3.417	3.322	3.42	
Maximum	3.515	3.483	3.535	3.508	3.376	3.5	
Range	0.139	0.163	0.173	0.091	0.054	0.08	

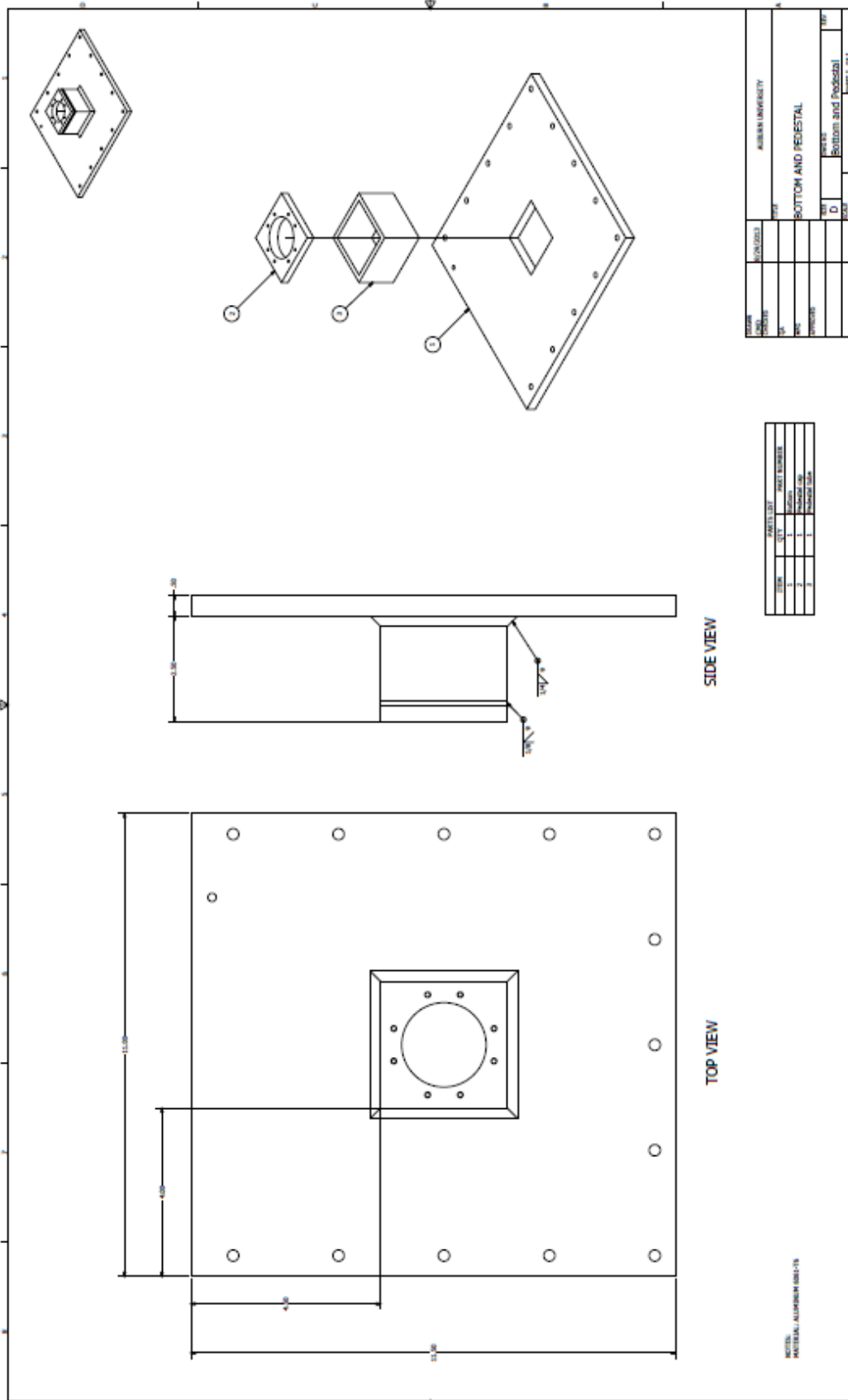
## Appendix E

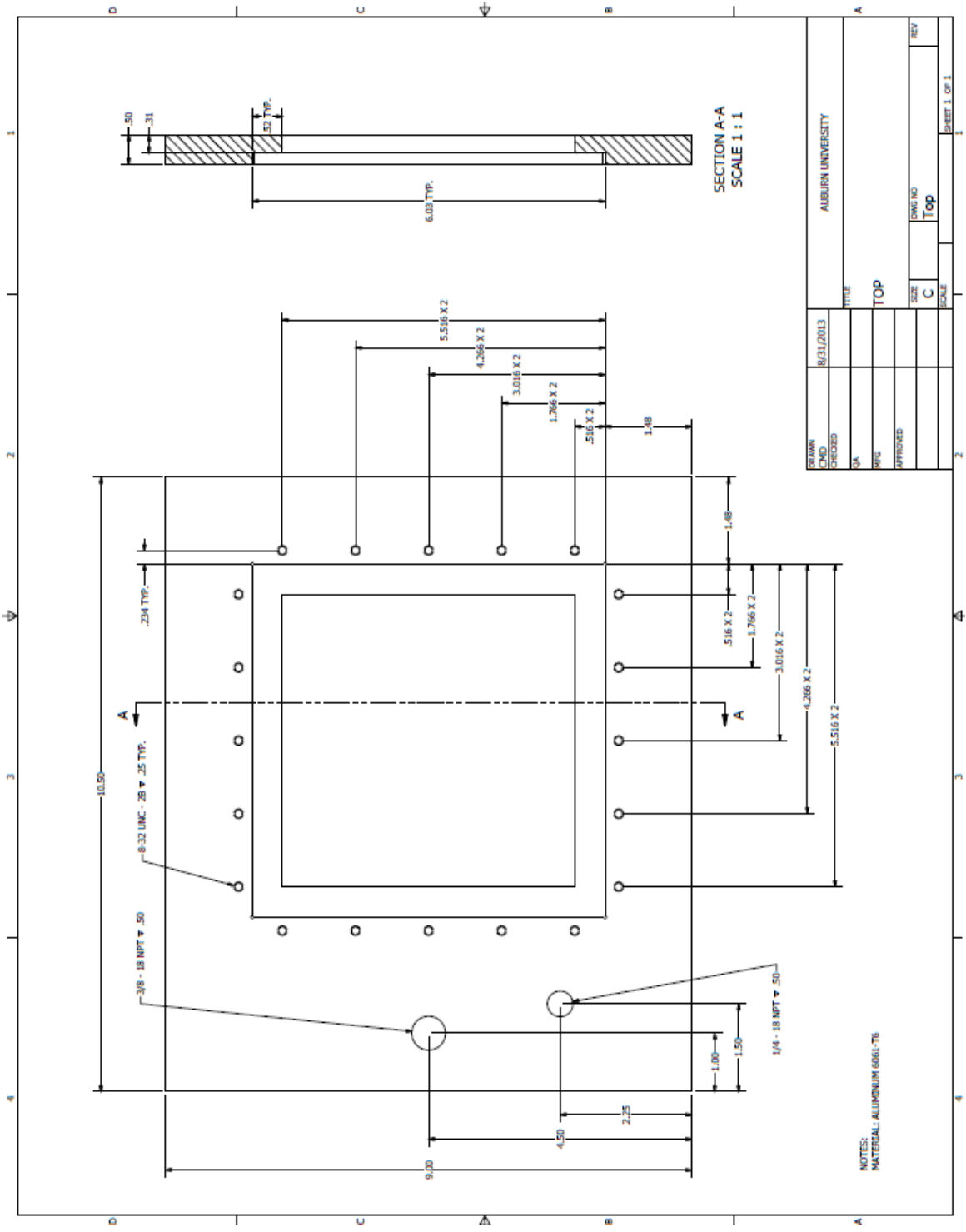
### Design Draft Files for Condensation Chamber and Measurement Head

All drawings used to fabricate the condensation chamber and measurement head including the channel plate made to retrofit the measurement head for water cooling are contained in this appendix.

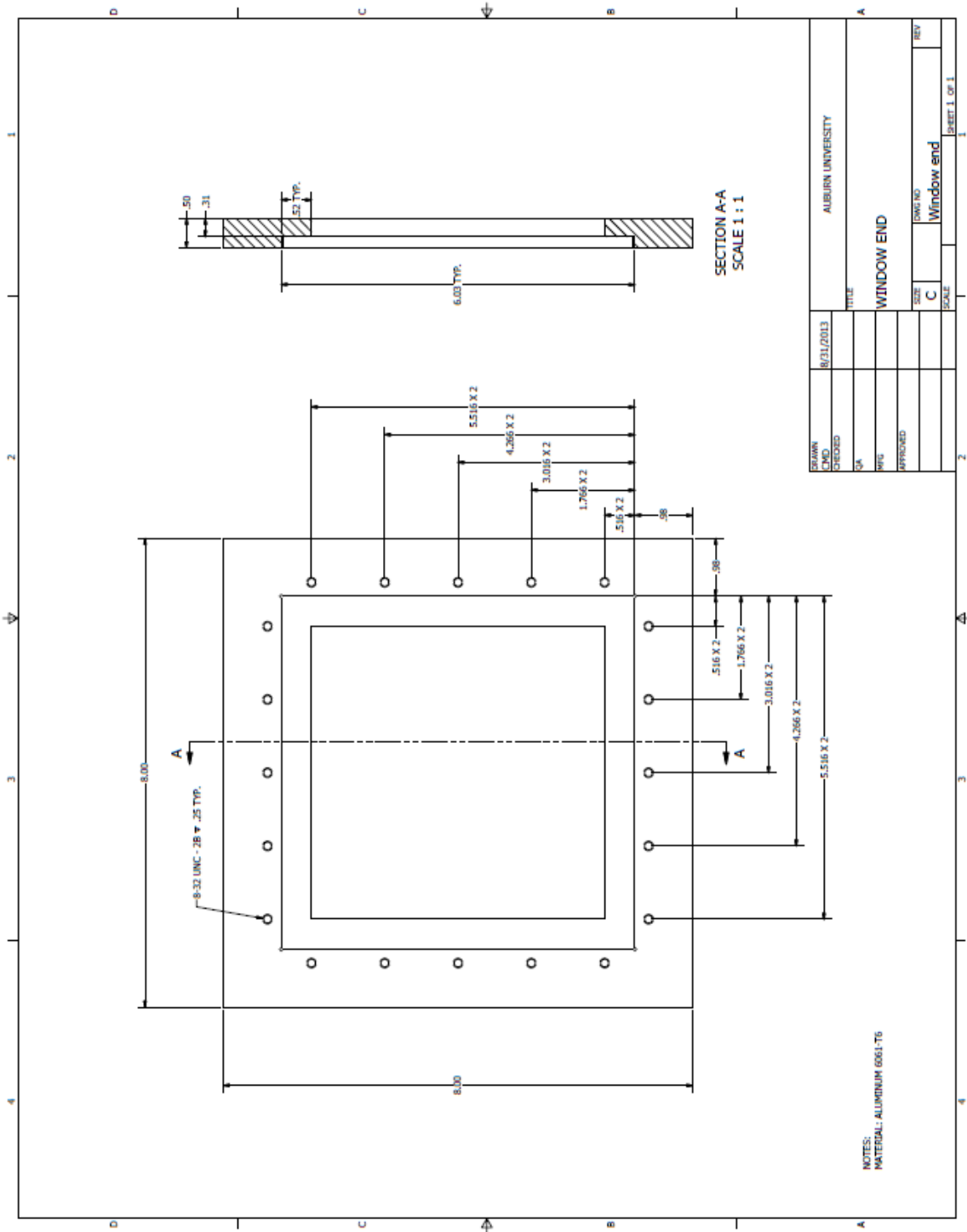






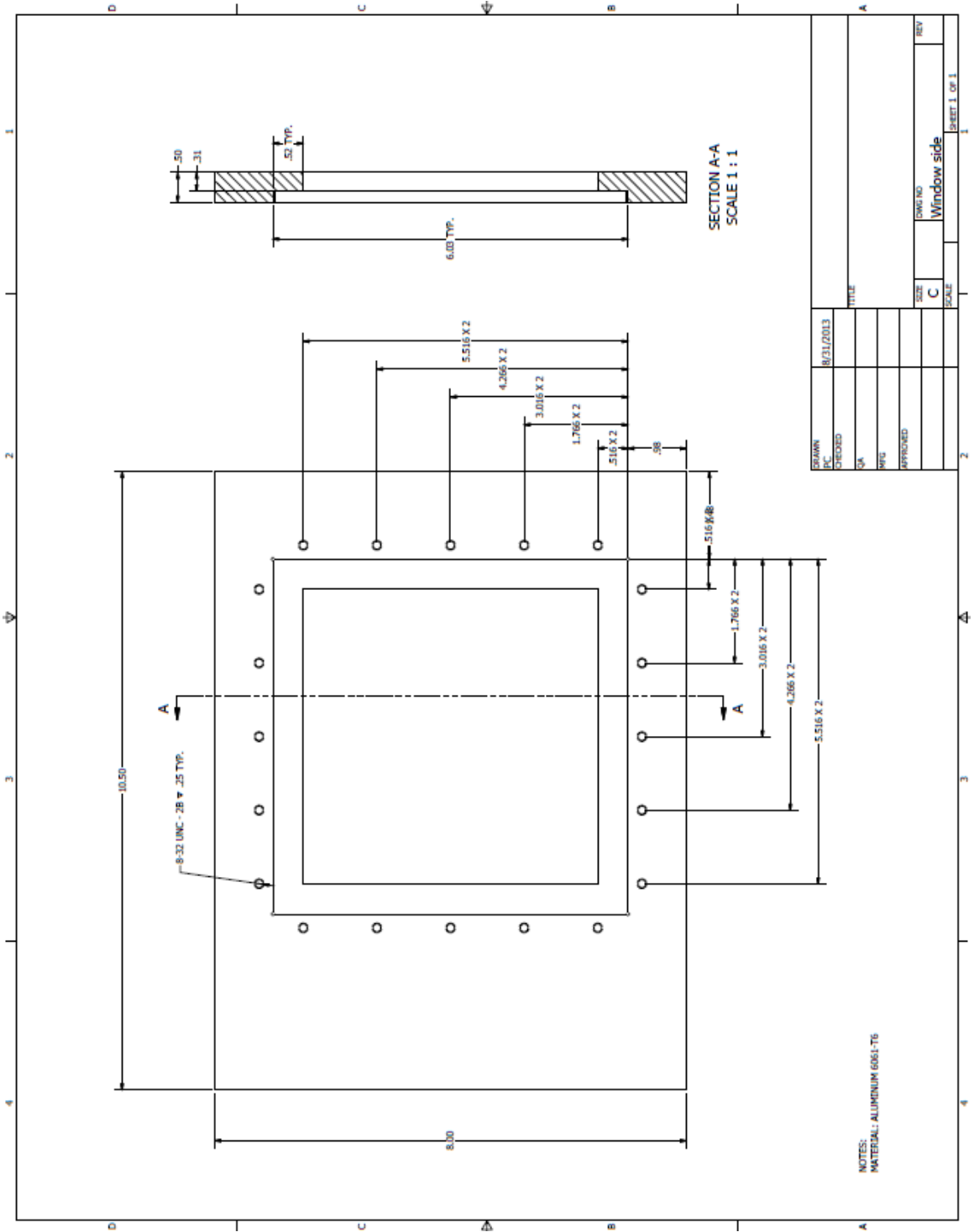


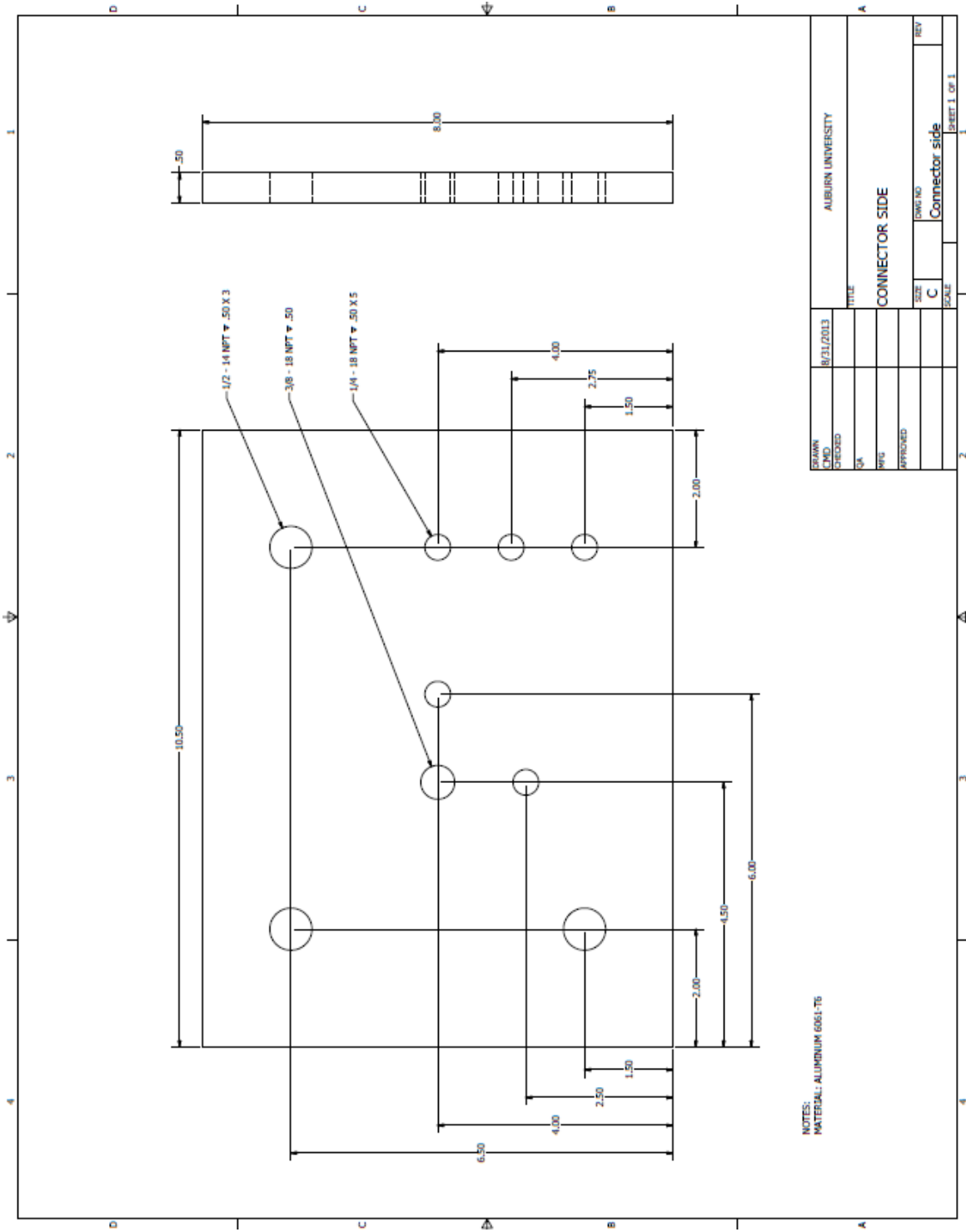


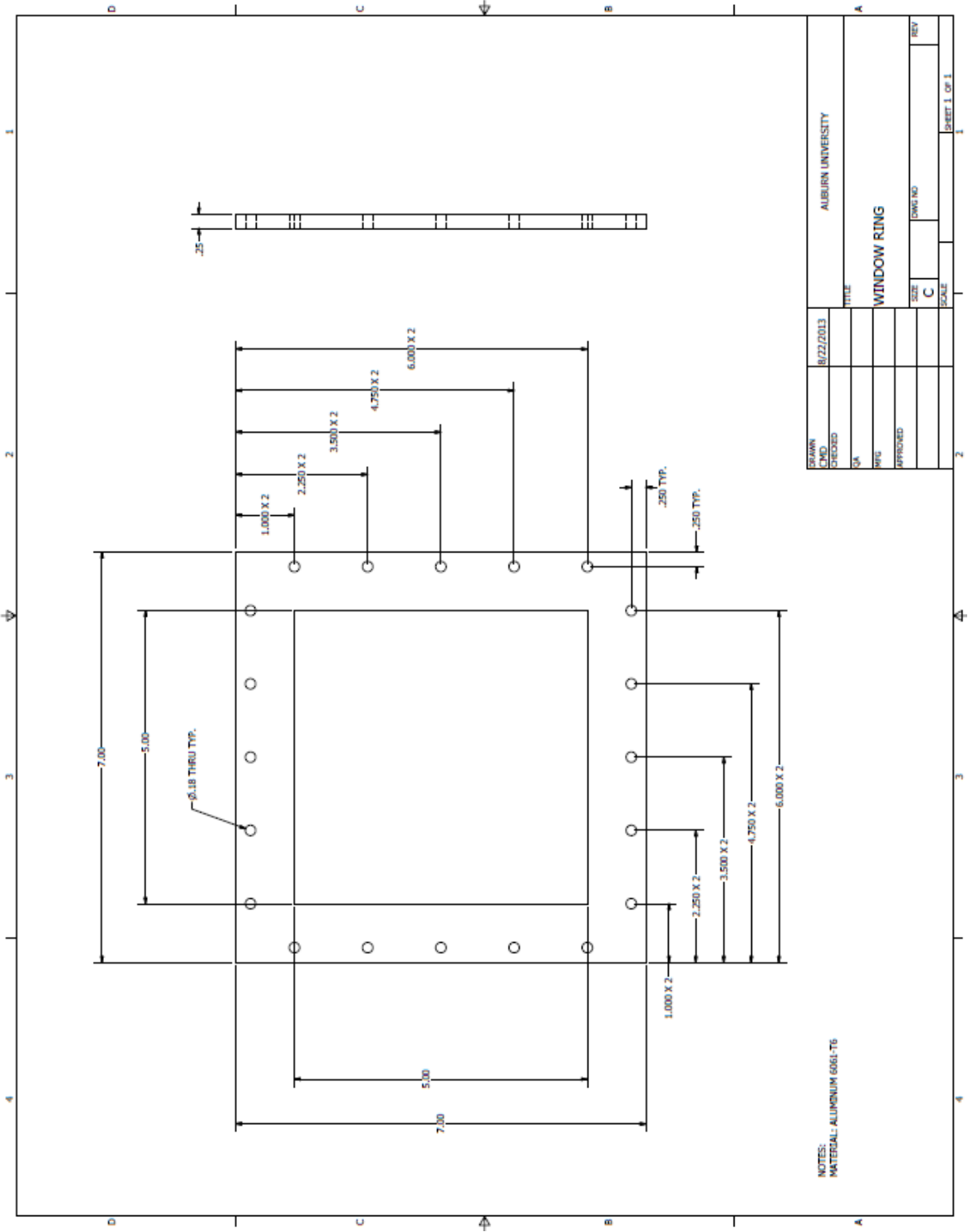


DESIGN	8/31/2013		
CHKD			
ENGR			
APPROVED			
TITLE	ALBURN UNIVERSITY		
SCALE	WINDOW END		
SIZE	C	DWG NO	Window end
REV			

NOTES:  
MATERIAL: ALUMINUM 6061-T6

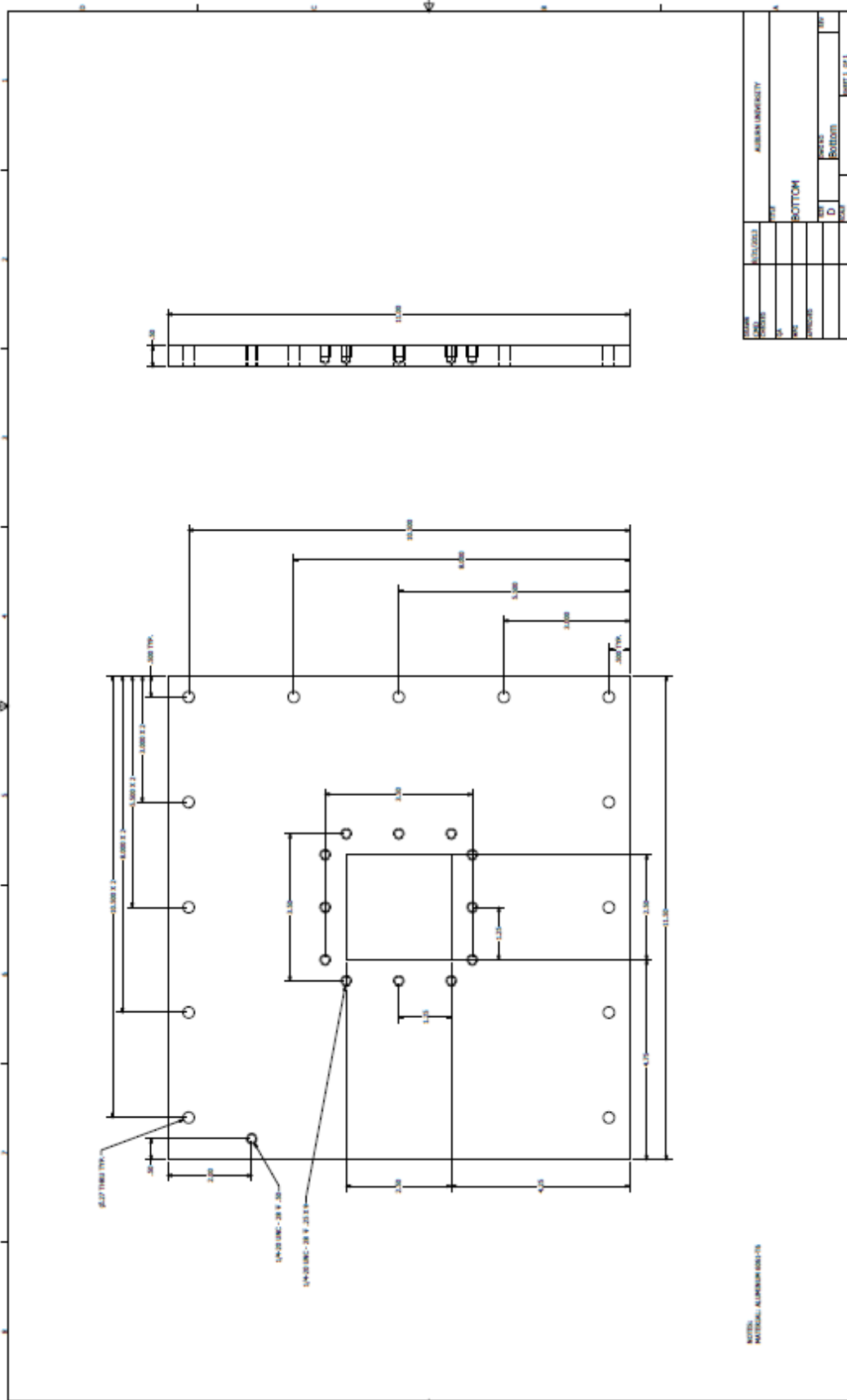


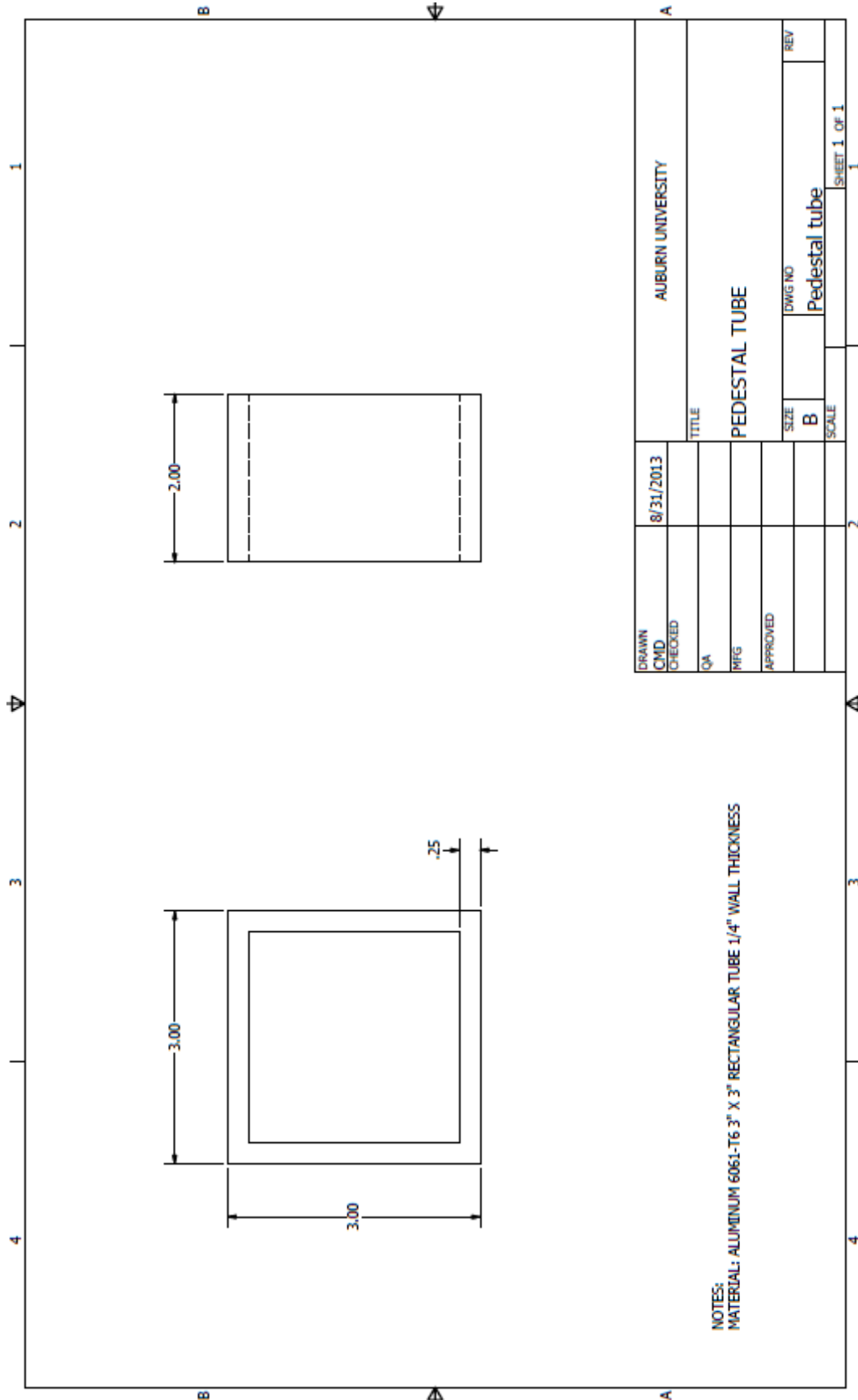




NOTES:  
MATERIAL: ALUMINUM 6061-T6

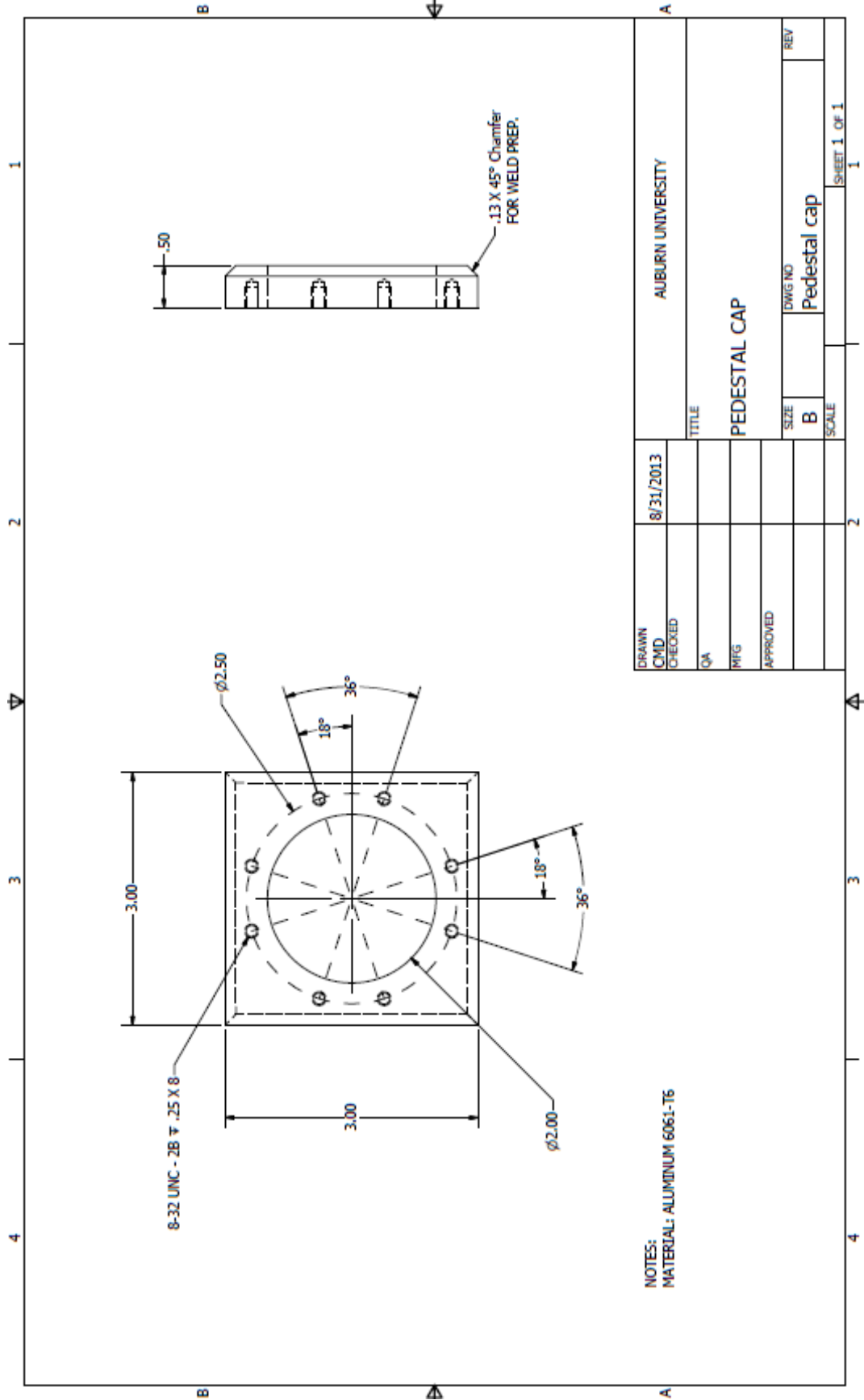
DATE	8/22/2013	SCALE	1
DRAWN	GA	TITLE	WINDOW RING
CHECKED	GA	SIZE	C
APPROVED		DWG NO.	
		REV	
		SHEET 1 OF 1	

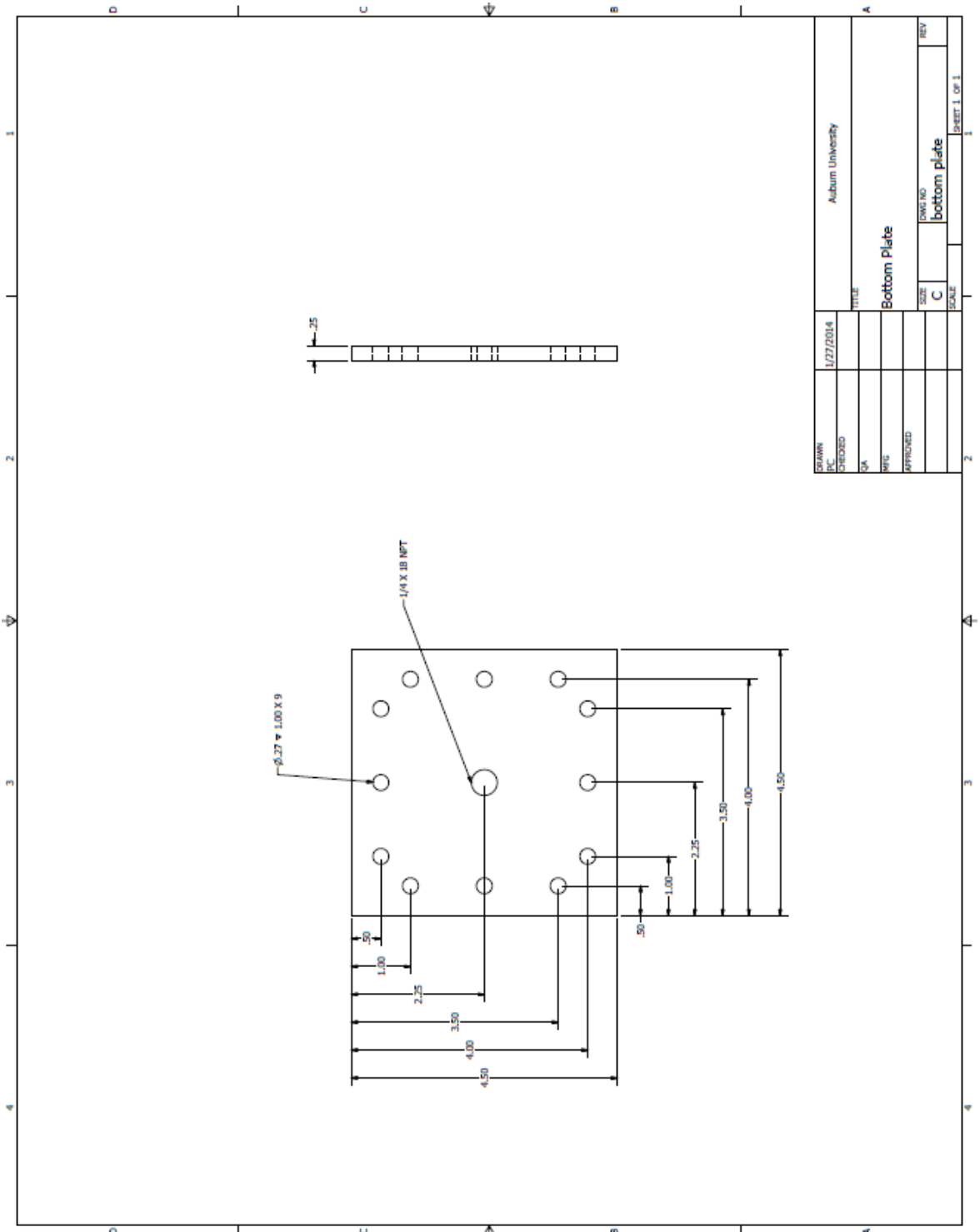




NOTES:  
 MATERIAL: ALUMINUM 6061-T6 3" X 3" RECTANGULAR TUBE 1/4" WALL THICKNESS

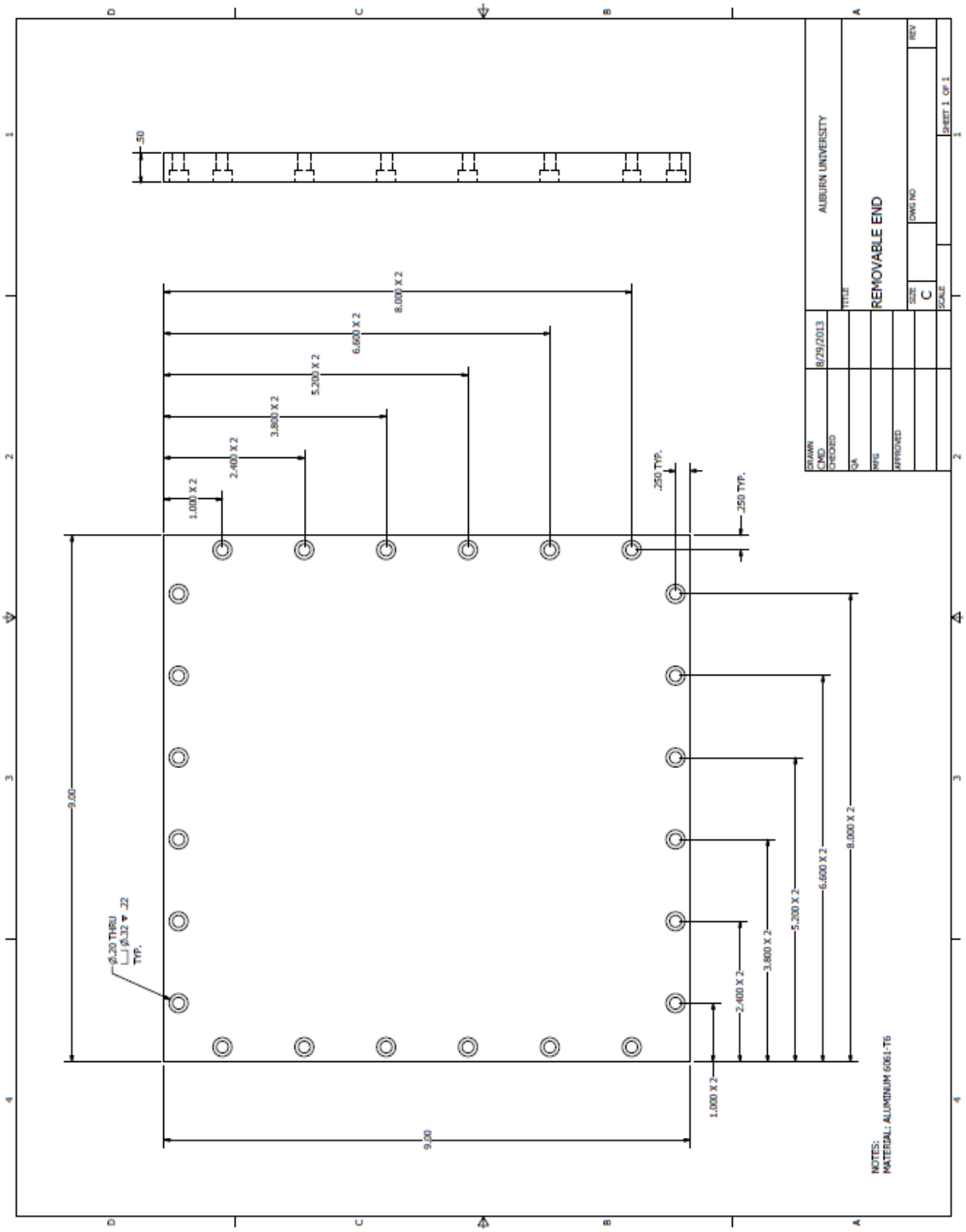
8/31/2013	ALBURN UNIVERSITY	
CMD CHECKED	TITLE	
QA	PEDESTAL TUBE	
MFG	SIZE	DWG NO
APPROVED	B	Pedestal tube
	SCALE	REV
		1
		SHEET 1 OF 1





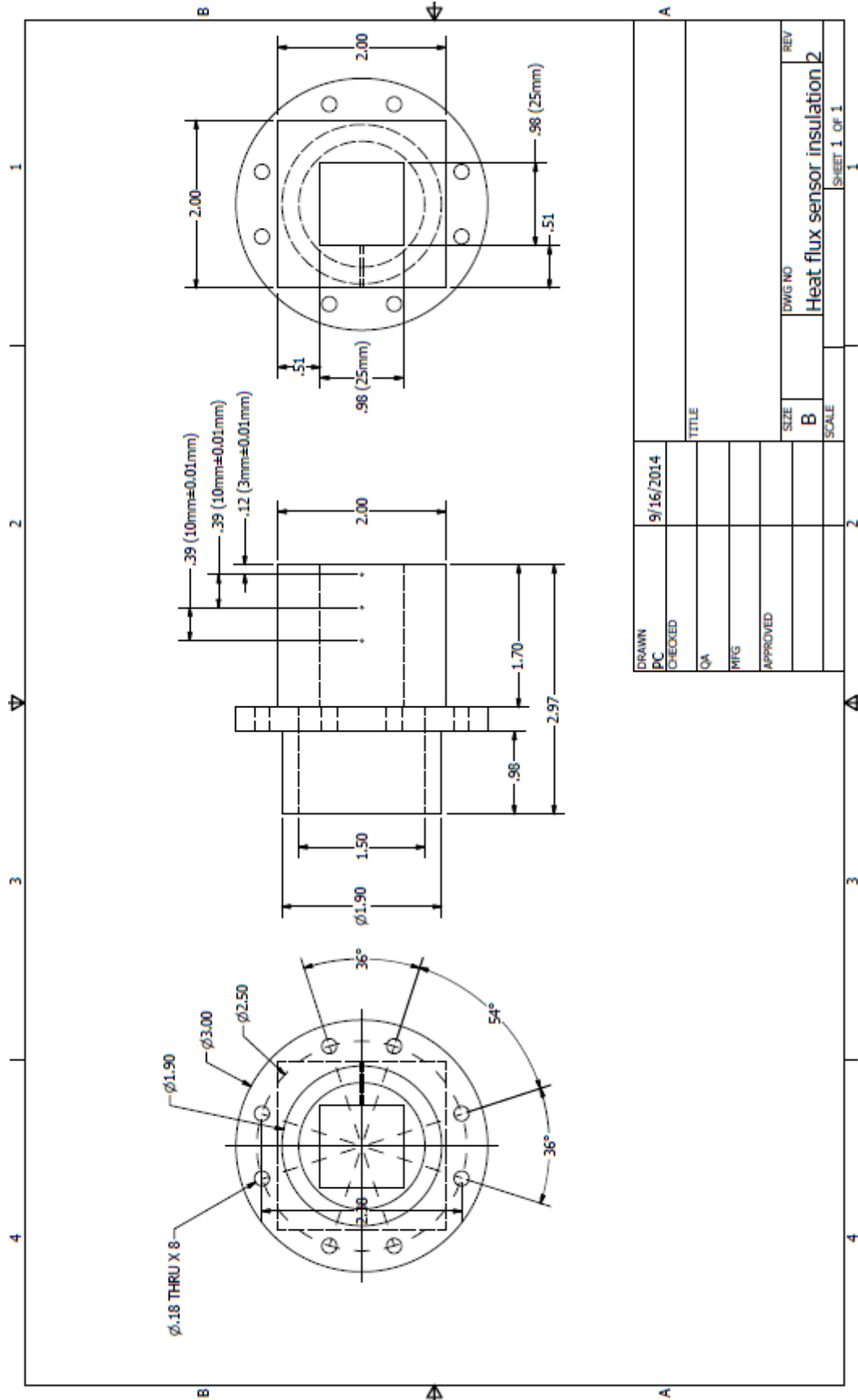
DATE	1/27/2014	SCALE	1
DESIGNED			
CHKD			
APPROVED			
TITLE		A	
Bottom Plate		REF	
SIZE	C	DWG NO	Bottom plate
SCALE		SHEET 1 OF 1	



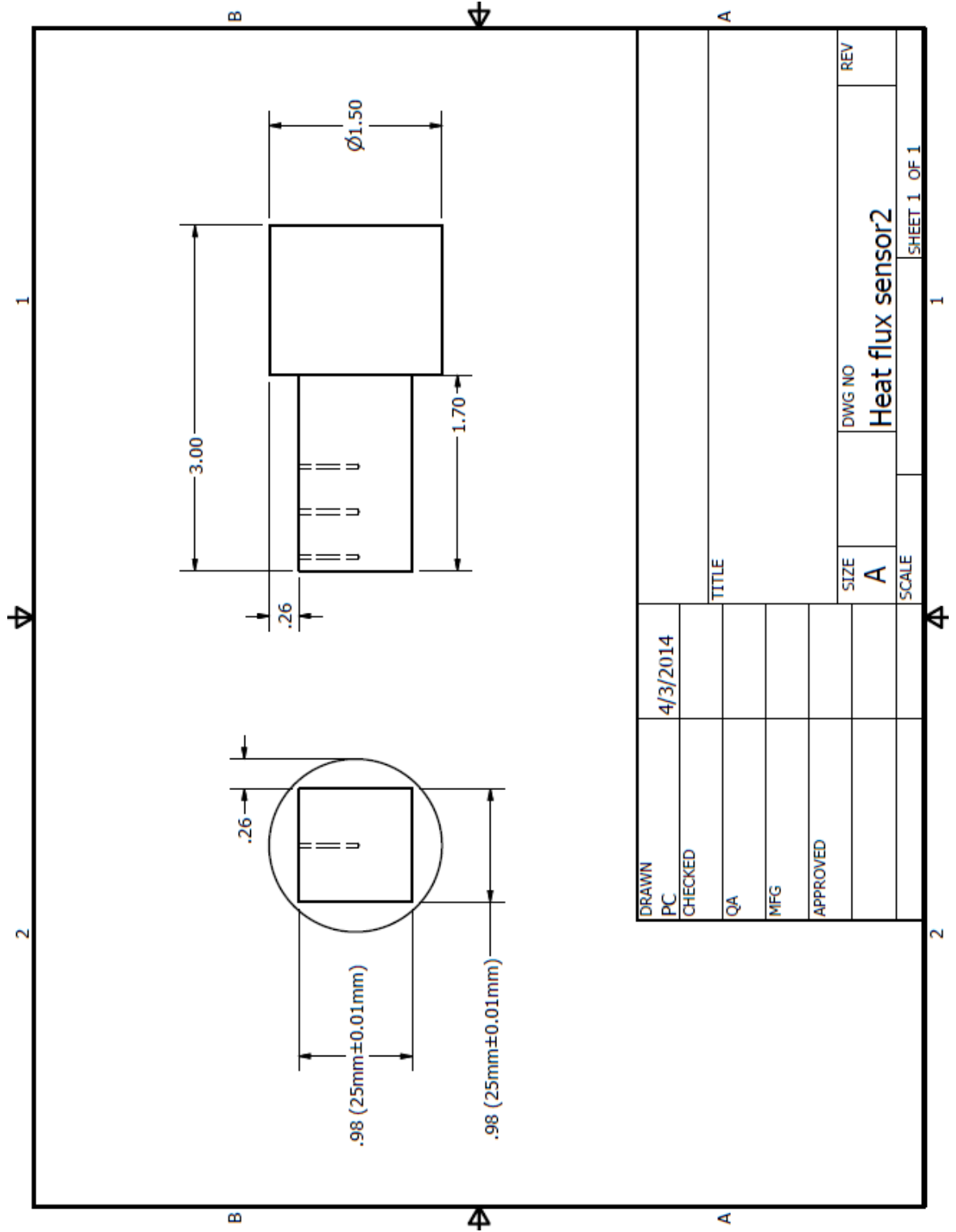


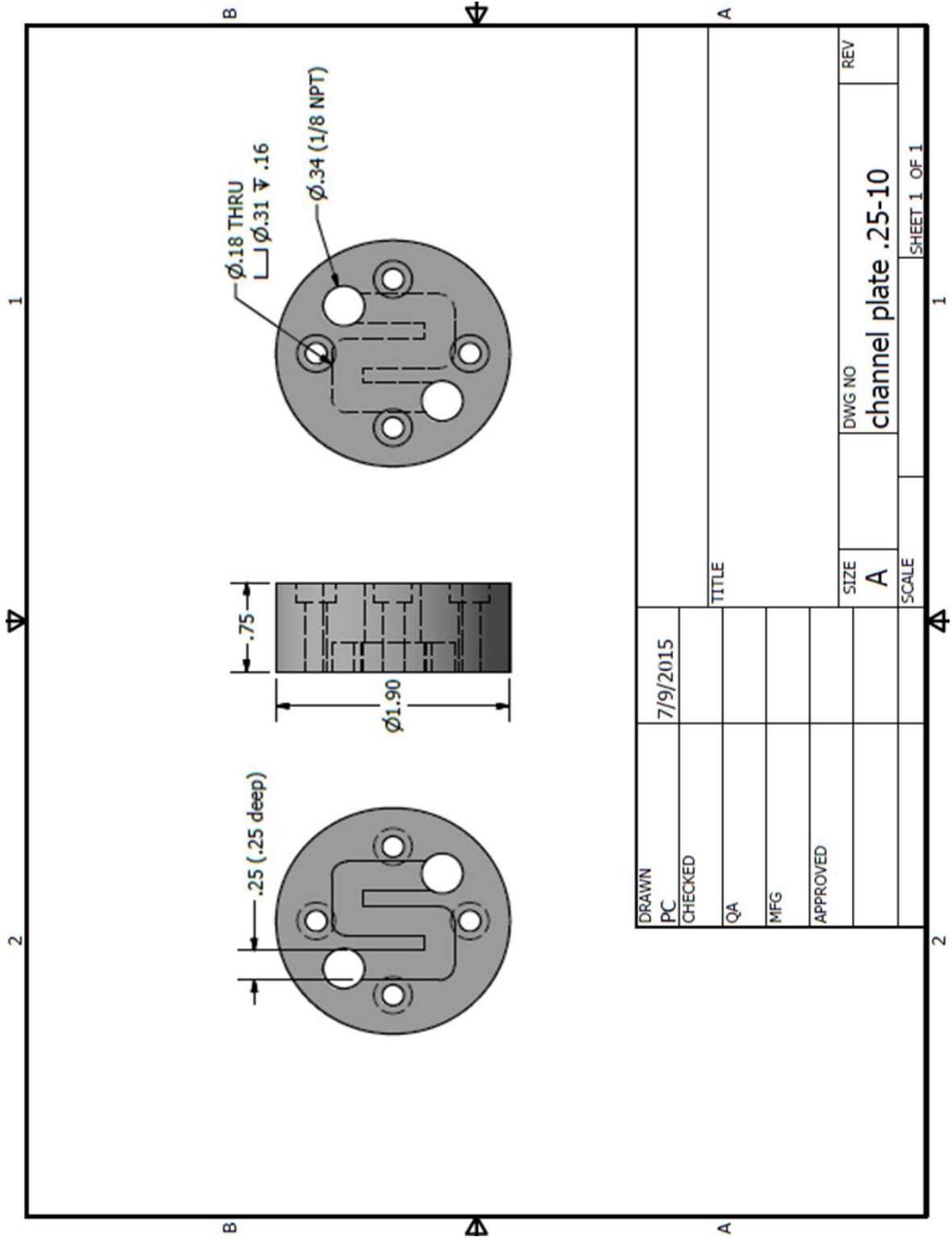
DRAWN		8/29/2013		TITLE	
CHECKED				ALBURN UNIVERSITY	
DESIGNED				REMOVABLE END	
APPROVED				SIZE	
				C	
				SCALE	
				SHEET 1 OF 1	

NOTES:  
MATERIAL: ALUMINUM 6061-T6



DRAWN	9/16/2014	TITLE	SCALE	SHEET 1 OF 1
PC				
CHECKED				
QA				
MFG				
APPROVED				
SIZE	B	DWG NO		REV
Heat flux sensor insulation 2				





## Appendix F

### Adhesives and other Consumables

This appendix contains a list of the adhesives and other consumables used during experiments and to construct the experimental facility or test surfaces. Manufacturer, sources, properties and uses are noted.

## **NeverWet Multi-Surface Liquid Repelling Treatment**

**Manufacturer:** Rust-Oleum

**Description/Properties:** Two-step superhydrophobic surface treatment can be applied to a variety of surfaces to create contact angles in water up to 165°

**Source:** amazon.com

**Use:** Used to treat silicon saw-toothed ratchet and flat control surfaces

**Notes:** Surface must be very clean for best results. Can be removed with acetone.

Fairly robust but contact angle does diminish with use so test surfaces were recoated often. Multiple light coats work best.

## **WaferGrip**

**Manufacturer:** Dynatex International (P/N CWG-4000000-RPA)

**Description/Properties:** 20µm thick silver impregnated thermally conductive, electrically non-conductive film

**Source:** John Tyler ([JT Tyler@dynatex.com](mailto:JT Tyler@dynatex.com))

**Use:** Used to bond reinforcing wafer to silicon ratchet wafers

**Notes:** Must be applied in cleanroom as trapped dust will cause air pockets which will expand while under vacuum during DRIE causing the wafer to crack. Can be removed with StripAid also made by Dynatex. Acetone can be used to remove WaferGrip but is less effective.

### **Silver Conductive Epoxy**

**Manufacturer:** M. G. Chemicals (CAT. NO. 8330S-21G)

**Description/Properties:** Two-part silver impregnated thermally conductive, electrically non-conductive epoxy. Operating temperature range: -40°C to 150°C  
Cure time: 96 hours at 25°C, 60 minutes at 65°C

**Source:** amazon.com, mgchemicals.com

**Use:** Used to bond tube material to lead casting when fabricating hemi-cylindrical condenser tube test surfaces.

**Notes:** Surface must be very clean for best results. Can be removed with acetone.  
Must be stored in refrigerator

### **Arctic Silver 5**

**Manufacturer:** Arctic Silver Inc. (P/N AS5-3.5G)

**Description/Properties:** High-Density Polysynthetic Silver Thermal Compound. 99.9% pure silver. Operating temperature range: -50°C to 130°C. Thermal conductivity: 8.7 W/mK

**Source:** amazon.com, arcticsilver.com

**Use:** Used in conjunction with silver epoxy to bond tube material to lead casting. Arctic Silver 5 is much less expensive and has a higher thermal conductivity so it was used in the center and the edges were adhered with silver epoxy.

**Notes:** Some argue that the manufacturer advertised thermal conductivity is grossly over stated. Some experimental data measures the conductivity to be as low as 0.94 W/mK.

### **High Vacuum Grease**

**Manufacturer:** Dow Corning (P/N 146355D)

**Description/Properties:** Silicone-based compound used as sealant & lubricant for vacuum systems

**Source:** amazon.com, McMaster-Carr, Grainger

**Use:** Used to lubricate metal conducting body with O-rings when inserting into measurement head insulation. Provided added benefit of better vacuum sealing.

**Notes:** Silicone is not compatible with FC-72 so care has to be taken to make sure the external surfaces of the measurement head are clean before use.

### **Colloidal Silver Paste**

**Manufacturer:** PELCO (P/N 16032-20)

**Description/Properties:** Room temperature curing silver paste. High conductivity and high adhesion. 60% silver suspended in lacquer. Max. Temp: 200°C.

**Source:** tedpella.com

**Use:** Used to bond thermocouples into measurement head core.

**Notes:** Very runny, shrinks when drying, quite expensive, much stronger adhesion than thermal grease.



### **Loctite® Plastics Bonding System**

**Manufacturer:** Loctite (Item # 681925)

**Description/Properties:** Two-part cyanoacrylate adhesive that sets in seconds. Activator primes hard-to-bond surfaces such as polypropylene and polyethylene. Resistant to water and most chemicals

**Source:** amazon.com, Home Depot

**Use:** Used to bond measurement head core to Teflon insulation. Applied only to square portion of core. Also applied to thermocouple leads where they exited the measurement head insulation for added security.

**Notes:** Only adhesive found to work reasonable well on Teflon.

### **All-Purpose GRRIP**

**Manufacturer:** Oatey-Hercules (P/N 15520)

**Description/Properties:** All-purpose non-petroleum hydrocarbon based sealant. Operating temperature range: -68°C to 232°C

**Source:** amazon.com

**Use:** Used to seal large threaded connections when Teflon tape is impractical

**Notes:** Works on many materials—all metals, PVC, ABS, CPVC plastics. Does not harden or shrink. Very messy, use only when absolutely required.

### **Ultra Black Maximum Oil Resistance RTV Silicone Gasket Maker**

**Manufacturer:** Permatex (P/N 82180)

**Description/Properties:** Non-corrosive, sensor safe. Operating temperature range: -54°C to 260°C

**Source:** AutoZone, Advance Auto Parts

**Use:** Used to dress rubber gaskets on windows and measurement head.

**Notes:** Works very well. Reduces screw pressure needed for adequate seal.

### **Adhesive Transfer Tape 966**

**Manufacturer:** 3M (P/N 966)

**Description/Properties:** Transparent, double sided, 2 mil (0.05 mm) adhesive transfer tape offers a thin profile combined with high temperature acrylic adhesive for a long-lasting bond. Operating temperature range: -40°C to 232°C

**Source:** RS Huges

**Use:** Used to apply Capton heaters to windows.

**Notes:** Works well at the temperatures experienced by the windows. If it is not applied well bubbles will form when heated. Will not re-stick once removed from the surface.

## **J-B Weld**

**Manufacturer:** J-B Weld

**Description/Properties:** Strong (3960psi.) and versatile two-part epoxy

**Source:** any hardware store

**Use:** Used to repair and seal various items

**Notes:** Works best on a rough, clean surface. Use for any permanent bond.

Never use if disassembly may be required in the future.

## **TC-5022 Thermally Conductive Compound**

**Manufacturer:** Dow Corning (P/N TC-5022)

**Description/Properties:** High-quality thermal grease for medium to high power electronic devices. Thermal conductivity: 4.0 W/mK

**Source:** various online retailers

**Use:** Used for mounting test surfaces to measurement head

**Notes:** Messy to work with and will spoil hydrophobic coatings. If the grease gets on the top side of coated test surfaces the hydrophobic coating must be stripped and re-applied.

### **Omegatherm “201” High Conductivity Paste**

**Manufacturer:** Omega Engineering (OT-201-1/2)

**Description/Properties:** Thermal paste designed for thermal sensors

**Source:** omega.com

**Use:** Used for mounting surface mount thermistor to test surfaces

**Notes:** Use sparingly. Difficult to clean off of coated surfaces.

### **ArctiClean**

**Manufacturer:** Arctic Silver Inc.

**Description/Properties:** Two-step thermal surface cleaner. ArctiClean 1 is non-toxic citrus and soy based solvent that emulsifies thermal greases and pads.

ArctiClean 2 removes residues left by ArctiClean 1.

**Source:** amazon.com, arcticsilver.com

**Use:** Used to clean backs of test surfaces and measurement head mounting surface.

**Notes:** Very effective. Be sure to use ArctiClean when surface or surrounding items would be damaged by acetone.

**Acetone-Methanol-Isopropanol-Distilled Water**

**Manufacturer:** Many

**Description/Properties:** Series of chemicals used to clean silicon wafers and test surfaces.

**Source:** On-Campus chemistry supply

**Use:** Used to clean silicon wafers and test surfaces.

**Notes:** Must use in Acetone-Methanol-Isopropanol-Distilled Water order.

Deionized water can be substituted for distilled water. Will remove hydrophobic coating. Will not leave any residue if dried with compressed air.

## Appendix G

### Heat Transfer Coefficient Plots for Hemi-cylindrical Test Surfaces

Plots of heat transfer coefficient as a function of time for each hemi-cylindrical test surface and 304 stainless steel control surface in all three surface conditions—bare, modified Repellix coated, and Repellix 2.0 coated—are provided in this appendix. The table below indicates the contents of each figure.

Table G.1: List of figures in Appendix G

---

Figure G.1	Comparison of heat transfer coefficient as a function of time on flat 304 stainless steel test surfaces
Figure G.2	Comparison of heat transfer coefficient as a function of time on round 304 stainless steel test surfaces
Figure G.3	Comparison of heat transfer coefficient as a function of time on Admiralty brass test surfaces
Figure G.4	Comparison of heat transfer coefficient as a function of time on cupronickel test surfaces
Figure G.5	Comparison of Heat transfer coefficient as a function of time on titanium test surfaces
Figure G.6	Comparison of Heat transfer coefficient as a function of time on SEA-CURE test surfaces

---

### Heat Transfer Coefficient vs. Time on Flat 304 Stainless Steel Test Surfaces

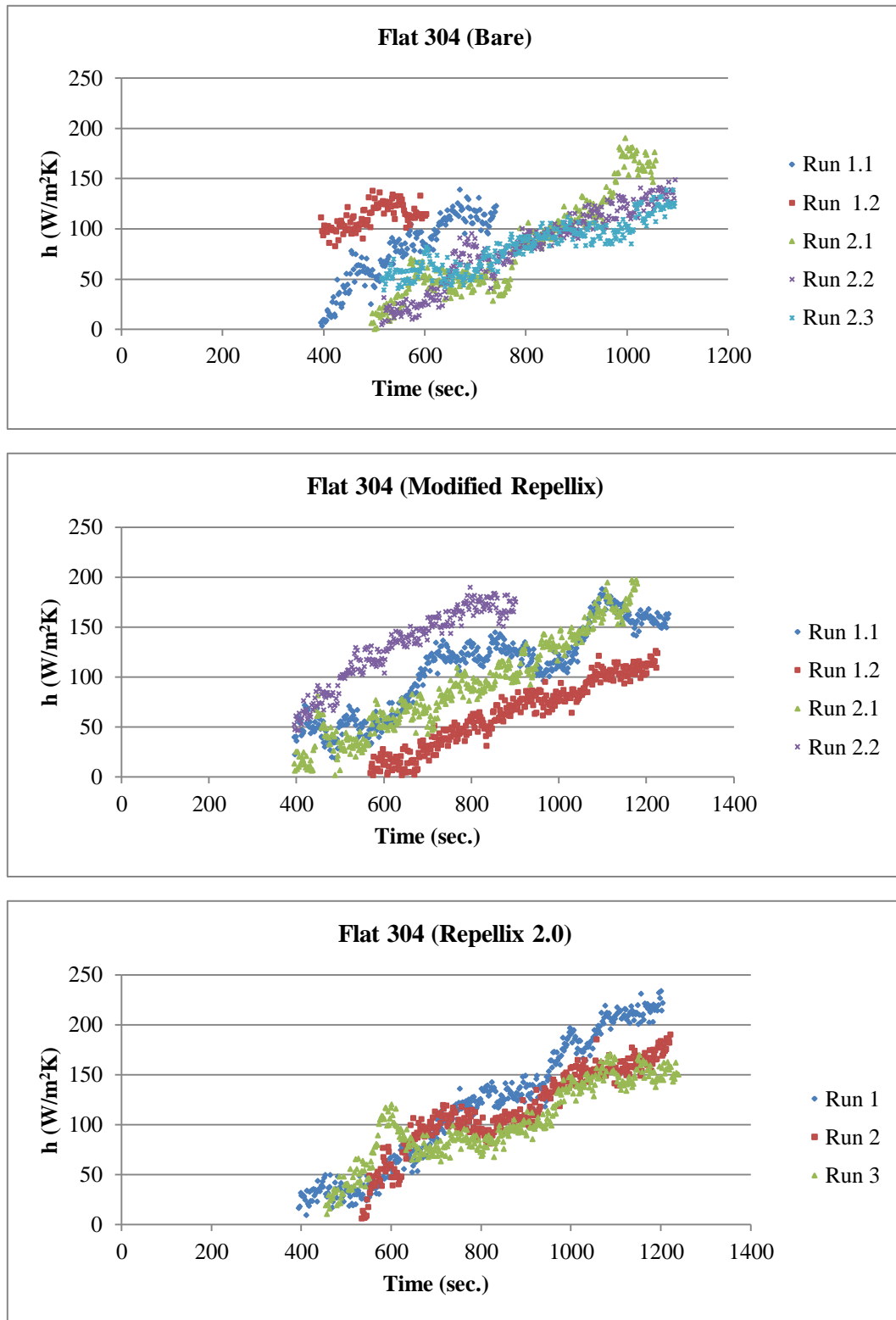


Figure G1: Comparison of heat transfer coefficient as a function of time on flat 304 Stainless Steel test surfaces for bare, Modified Repellix coated, and Repellix 2.0 coated

**Heat Transfer Coefficient vs. Time on Round 304 Stainless Steel Test Surfaces**

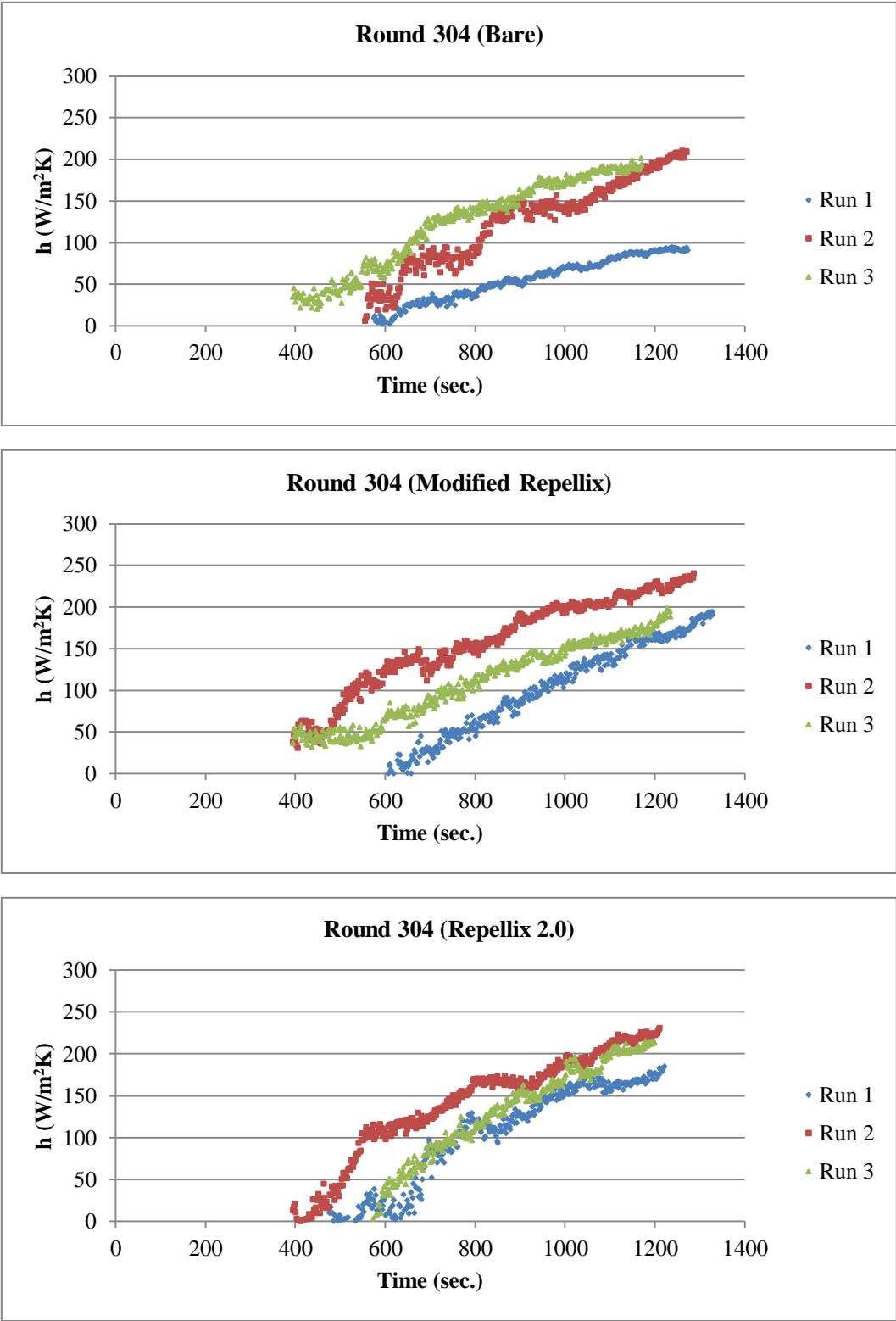


Figure G2: Comparison of Heat transfer coefficient as a function of time on Round 304 Stainless Steel test surfaces for bare, Modified Repellix coated, and Repellix 2.0 coated



### Heat Transfer Coefficient vs. Time on Admiralty Test Surfaces

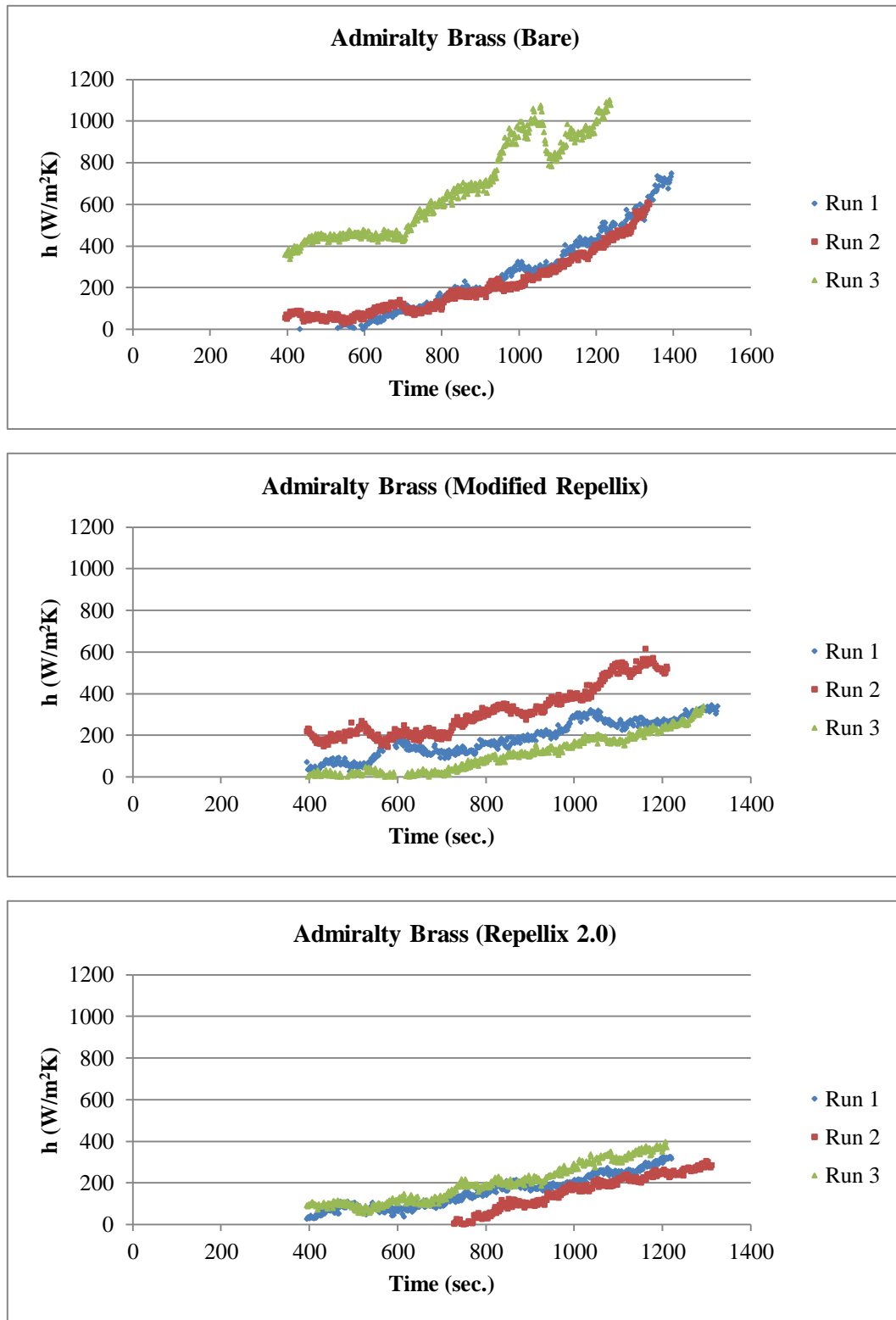


Figure G3: Comparison of Heat transfer coefficient as a function of time on Admiralty brass test surfaces for bare, Modified Repellix coated, and Repellix 2.0 coated

### Heat Transfer Coefficient vs. Time on Cupronickel Test Surfaces

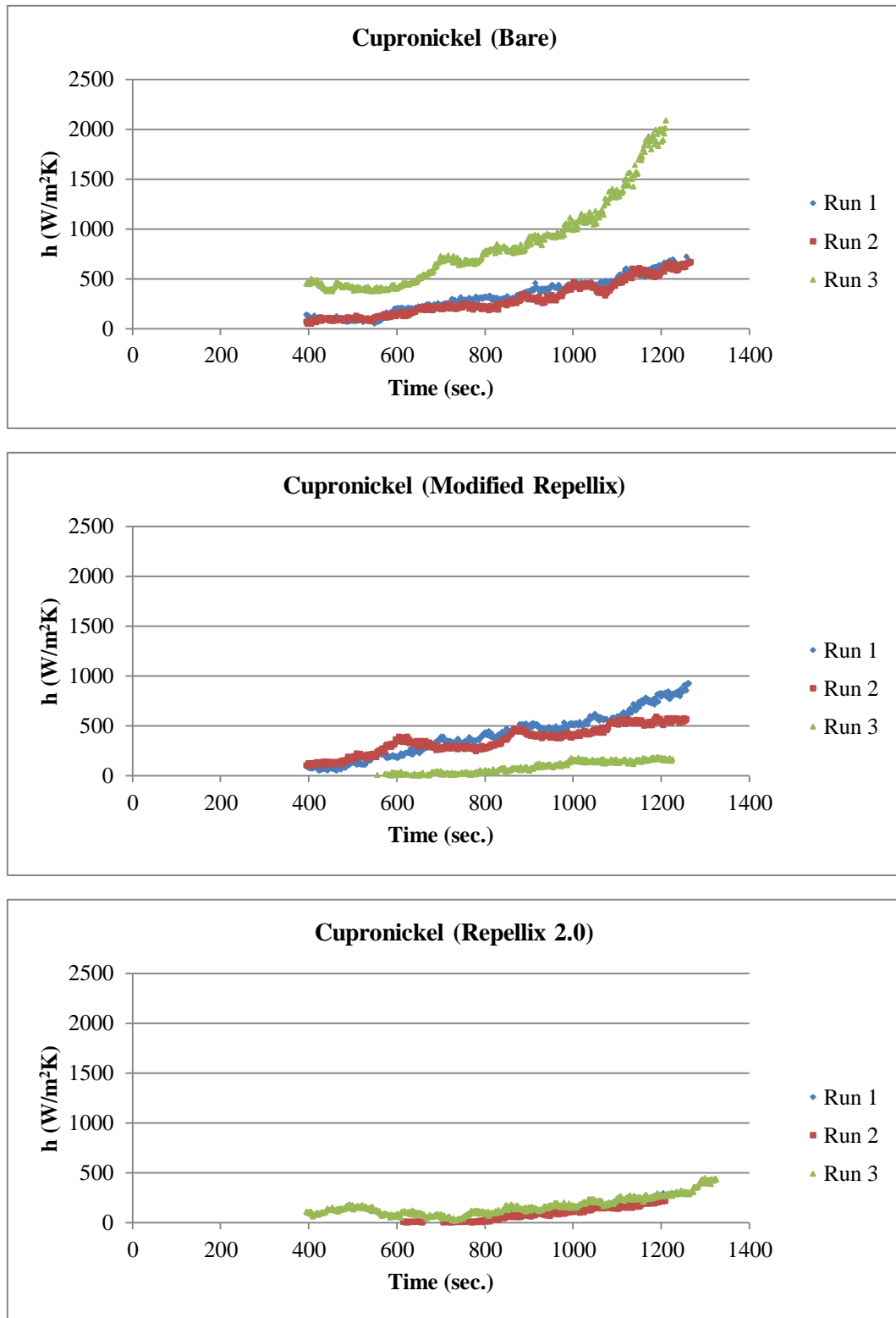


Figure G4: Comparison of Heat transfer coefficient as a function of time on Cupronickel test surfaces for bare, Modified Repellix coated, and Repellix 2.0 coated

### Heat Transfer Coefficient vs. Time on Titanium Test Surfaces

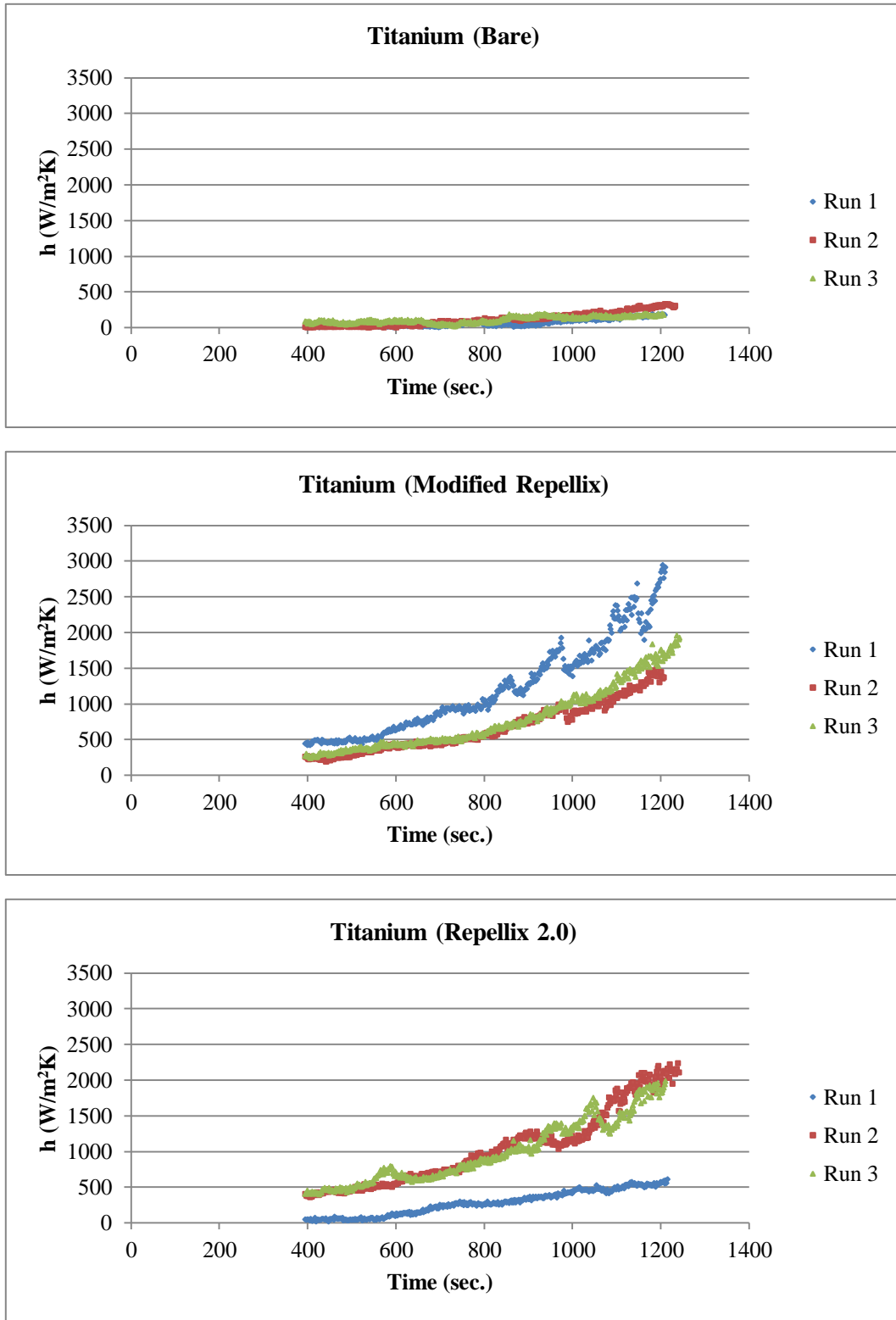


Figure G5: Comparison of Heat transfer coefficient as a function of time on Titanium test surfaces for bare, Modified Repellix coated, and Repellix 2.0 coated

### Heat Transfer Coefficient vs. Time on Sea Cure Test Surfaces

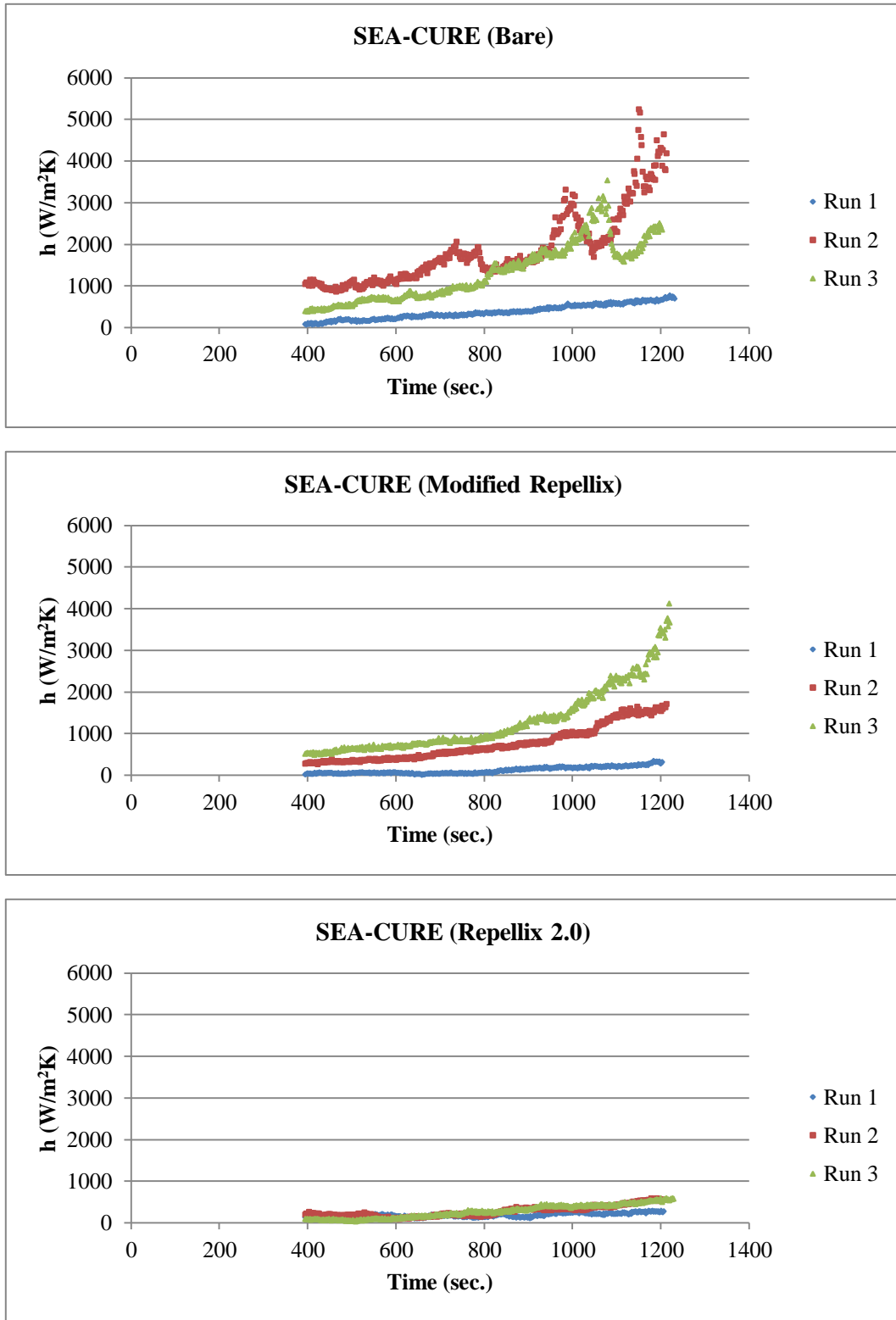


Figure G6: Comparison of Heat transfer coefficient as a function of time on SEA-CURE test surfaces for bare, Modified Repellix coated, and Repellix 2.0 coated

## Appendix H

### Uncertainty Calculation for Heat Transfer Coefficient Values

Detail on the methods and equations used for heat transfer coefficient uncertainty calculations are given in this appendix.

Recall from chapter 2 that the heat transfer coefficients reported in this study are calculated from temperature data gathered from a series of thermocouples in the measurement head and a thermocouple that measures ambient condenser chamber temperature. The temperatures measured by the thermocouples in the measurement head along with their positions in the measurement head are used to calculate a second order temperature distribution within the conducting core of the measurement head for each data collection iteration. These temperature distribution equations then are used to provide the temperature of the top surface of the measurement head's conducting core and the heat flux through the core as shown by the equations below.

The temperature distribution equations are of the form:

$$T = Ax^2 + Bx + C \quad T(0) = C \quad (\text{H.1})$$

Where  $T(0)$  is the temperature at the top surface of the measurement head's conducting core and  $x$  is the distance from the top surface into the conducting core.

Taking the derivative with respect to  $x$  and applying Fourier's Law yields the heat flux through the top surface ( $x=0$ ) of the conducting core.

$$\frac{dT}{dx} = 2Ax + B \quad \frac{dT}{dx}(0) = B \quad (\text{H.2})$$

Fourier's Law:

$$q = -k \frac{dT}{dx} \quad q(0) = -kB \quad (\text{H.3})$$

Where  $q$  is the heat flux and  $k$  is the thermal conductivity of the aluminum conducting core.

The surface temperatures of the test surfaces,  $T_{Test}$ , are calculated using the heat flux calculated above and the average test surface and thermal grease combined thermal resistance  $R$  which was determined experimentally.

$$T_{Test} = q \times R + T(0) \quad (H.4)$$

A rearrangement of Newton's Law of cooling provides an equation for the heat transfer coefficient.

$$h = \frac{q}{(T_{Chamber} - T_{Test})} \quad (H.5)$$

Where  $T_{Chamber}$  is the measured ambient chamber temperature.

Substituting equations H.1, H.3 and H.4 into H.5 yields:

$$h = \frac{-kB}{(T_{Chamber} - ((-kB \times R) + C))} \quad (H.5)$$

The coefficients  $B$  and  $C$  are automatically calculated by the LabVIEW function that generates the temperature distribution equations however their forms were calculated for this analysis:

$$B = \frac{T_2x_1^2 + C(x_2^2 - x_1^2) - T_1x_2^2}{x_2x_1^2 - x_1x_2^2} \quad (H.6)$$

$$C = \frac{(T_3 - T_2)x_1^2(x_2x_1^2 - x_1x_2^2) + T_1[x_2^2(x_3x_1^2 - x_1x_3^2) - x_3^2(x_2x_1^2 - x_1x_2^2)]}{(x_2^2 - x_1^2)(x_3x_1^2 - x_1x_3^2) + (x_1^2 - x_3^2)(x_2x_1^2 - x_1x_2^2)} \quad (H.7)$$

Where  $T_1$ ,  $T_2$ , and  $T_3$  are the temperatures gathered by the thermocouples in the measurement head's conducting core and  $x_1$ ,  $x_2$ , and  $x_3$  are the distance from the top surface at which the thermocouples are installed.  $T_1$  is the thermocouple closest to the top surface and  $T_3$  is the thermocouple furthest from the top surface.

Equations H.5, H.6 and H.7 show that  $h = f(T_1, T_2, T_3, T_{Chamber}, x_1, x_2, x_3, k, R)$ .

The uncertainties of  $x_1$ ,  $x_2$ ,  $x_3$ ,  $k$  and  $R$  are all bias errors that shift all measurements equally so they can be neglected when making comparisons like those presented in chapter 4. Therefore the heat transfer coefficient uncertainty ( $u_h$ ) used to calculate the error bars used in comparison plots is defined by the equation:

$$\frac{u_h}{h} = \sqrt{\left(\frac{u_{T1}}{T_1}\right)^2 + \left(\frac{u_{T2}}{T_2}\right)^2 + \left(\frac{u_{T3}}{T_3}\right)^2 + \left(\frac{u_{Tchamber}}{T_{Chamber}}\right)^2} \quad (\text{H.8})$$

Where  $u_{T1}$ ,  $u_{T2}$ ,  $u_{T3}$  and  $u_{Tchamber}$  are the uncertainties of the temperature measurements  $T_1$ ,  $T_2$ ,  $T_3$ , and  $T_{Chamber}$  respectively. These uncertainties are calculated during calibration and are of the form:

$$u_T = \delta_a T + \delta_b \quad (\text{H.9})$$

Where  $\delta_a$  is the scale uncertainty and  $\delta_b$  is the offset uncertainty. These quantities are calculated using the following equations:

$$\delta_a = \frac{t_{0.025} S_{y/x}}{S_{xx}} \quad (\text{H.10})$$



$$\delta_b = t_{0.025} S_{y/x} \sqrt{\frac{1}{n} + \frac{\bar{x}^2}{S_{xx}}} \quad (\text{H.11})$$

$$S_{xx}^2 = \sum_{i=1}^n (x_i - \bar{x})^2 \quad (\text{H.12})$$

$$S_{y/x} = \sqrt{\frac{\sum_{i=1}^n [y_i - f_{cal}(x_i)]^2}{n - 2}} \quad (\text{H.13})$$

Where  $n$  is the number of measurements taken during calibration,  $t_{0.025}$  is the student's  $t$  table value for 95% confidence intervals,  $\bar{x}$  is the mean of uncalibrated values, and  $f_{cal}(x_i)$  is the calibrated value.

The values of scale and offset uncertainty for the four thermocouples used are given in Table H.1.

Table H.1: Scale and offset uncertainty values for thermocouples

Thermocouple	$\delta_a$	$\delta_b$
T <sub>1</sub>	0.003422031	0.145381077
T <sub>2</sub>	0.003305924	0.140129965
T <sub>3</sub>	0.003483403	0.147168464
T <sub>Chamber</sub>	0.051736767	0.302014013

Inserting the thermocouple uncertainties into equation H.8 and solving for  $u_h$  yields the equation used for calculating heat transfer coefficient uncertainties:

$$u_h = h \sqrt{\left(\frac{0.00342T_1 + 0.145}{T_1}\right)^2 + \left(\frac{0.0033T_2 + 0.14}{T_2}\right)^2 + \left(\frac{0.00348T_3 + .0147}{T_3}\right)^2 + \left(\frac{0.0517T_{chamber} + 0.302}{T_{chamber}}\right)^2} \quad (\text{H.14})$$

Where,  $T_1$ ,  $T_2$ ,  $T_3$ , and  $T_{\text{Chamber}}$  are all measured temperature values and  $h$  is the heat transfer coefficient calculated from the collected data.

A sample calculation is shown below. Figure H.1 shows the data used for the sample calculation.

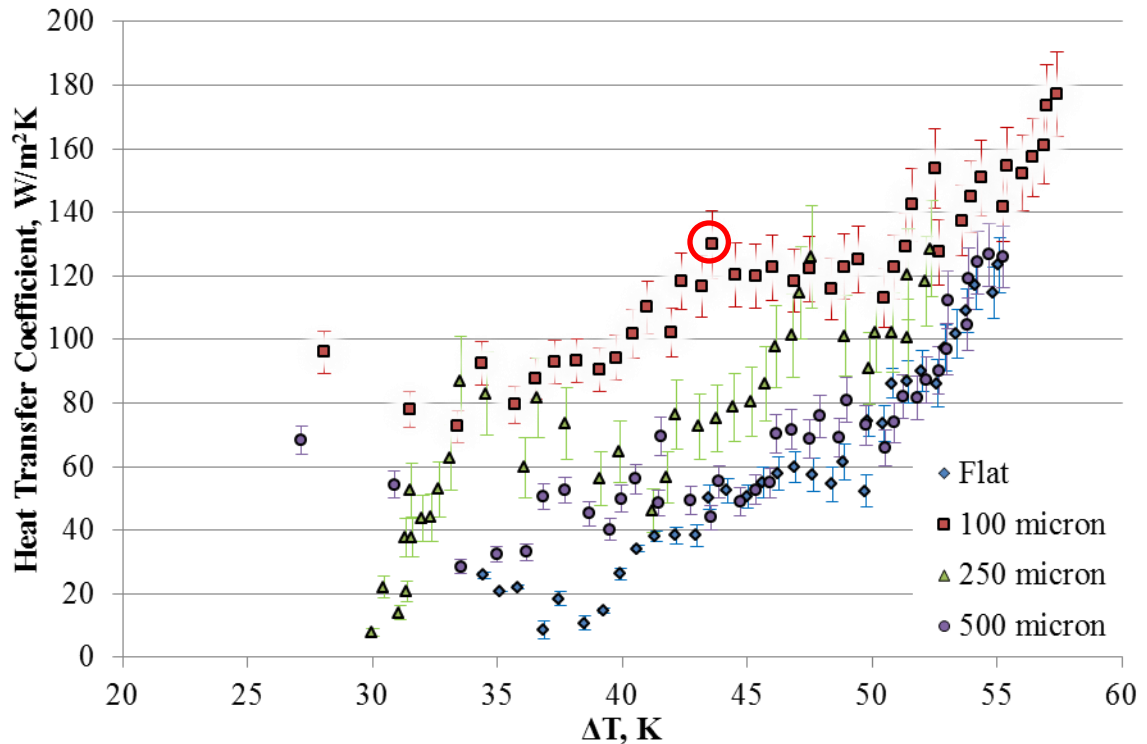


Figure H.1: Condensation heat transfer coefficient as a function of  $\Delta T$  for deionized water on hydrophobic surfaces. Data point used for sample calculation is circled in red.

Table H.2 provides the temperature data and calculated h value for the data point circled in red in Figure H.1. Equation H.15 calculates the uncertainty  $u_h$  for this data point.

Table H.2: Temperature and heat transfer coefficient values for sample calculation

Measurement	Value
$T_1$	5.58 °C
$T_2$	5.03 °C
$T_3$	4.02 °C
$T_{Chamber}$	52.51 °C
$h$	129.85 W/m <sup>2</sup> K

$$u_h = 10.7775 \text{ W/m}^2\text{K} =$$

$$129.85 \frac{W}{m^2K} \sqrt{\left(\frac{0.00342(5.58) + 0.145}{5.58}\right)^2 + \left(\frac{0.0033(5.03) + 0.14}{5.03}\right)^2 + \left(\frac{0.00348(4.02) + .0147}{4.02}\right)^2 + \left(\frac{0.0517(52.51) + 0.302}{52.51}\right)^2} \quad (\text{H.14})$$